ENERGY LABORATORY

MASSACHUSETTS INSTITUTE
OF TECHNOLOGY

ANALYTICAL MODELLING OF HYDROGEN TRANSPORT IN REACTOR CONTAINMENTS

by
Vincent P. Manno and Michael W. Golay

Energy Laboratory Report No. MIT-EL-83-009

October 1983

ANALYTICAL MODELLING OF HYDROGEN TRANSPORT IN REACTOR CONTAINMENTS

by

Vincent P. Manno

and

Michael W. Golay

Energy Laboratory and

Department of Nuclear Engineering

Massachusetts Institute of Technology

Cambridge, MA 02139

MIT-EL-83-009

October 1983

Sponsored by:

Boston Edison Co.
Duke Power Co.
Northeast Utilities Service Corp.
Public Service Electric and Gas Co. of New Jersey

ABSTRACT

ANALYTICAL MODELLING OF HYDROGEN TRANSPORT

IN REACTOR CONTAINMENTS

by

Vincent P. Manno and Michael W. Golay

A versatile computational model of hydrogen transport in nuclear plant containment buildings is developed. The background and significance of hydrogen-related nuclear safety issues are discussed. A computer program is constructed that embodies the analytical models. The thermo-fluid dynamic formulation spans a wide applicability range from rapid two-phase blowdown transients to slow incompressible hydrogen injection. Detailed ancillary models of molecular and turbulent diffusion, mixture transport properties, multi-phase multicomponent thermodynamics and heat sink modelling are addressed. The numerical solution of the continuum equations emphasizes both accuracy and efficiency in the employment of relatively coarse discretization and long time steps. Reducing undesirable numerical diffusion is addressed. Problem geometry options include lumped parameter zones, one dimensional meshes, two dimensional Cartesian or axisymmetric coordinate systems and three dimensional Cartesian or cylindrical regions. An efficient lumped nodal model is included for simulation of events in which spatial resolution is not significant.

Several validation calculations are reported. Demonstration problems include the successful reproduction of analytical or known solutions, simulation of large scale experiments and analyses of "thought experiments" which test the physical reasonableness of the predictions. In particular, simulation of hydrogen transport tests performed at the Battelle Frankfurt Institute and Hanford Engineering Development Laboratory show good agreement with measured hydrogen concentration, temperature and flow fields. The results also indicate that potential areas of improvement are enhanced computational efficiency, further reduction of numerical diffusion and development of containment spray models. Overall, a useful tool applicable to many nuclear safety problems is described.

ACKNOWLEDGEMENTS

This research was conducted under the sponsorship of Boston Edison Co., Duke Power Co., Northeast Utilities Service Corp. and Public Service Electric and Gas Co. of New Jersey. The authors gratefully acknowledge this support. The first author also received partial support from the U.S. Department of Energy. The authors thank all those who assisted them during this research especially Dr. Kang Y. Huh, Dr. Lothar Wolf, Mr. B.K. Riggs, Ms. Cindy Sheeks, Ms. Rachel Morton and Prof. Andrei Schor. The work was expertly typed by Mr. Ted Brand and Ms. Eva Hakala.

TABLE OF CONTENTS

LIST OF FIGURES

LIST OF TABLES

NOMENCLATURE

Some of the variables defined below have more than one meaning. All possible meanings are presented. The correct interpretation is either obvious or stated in the context of the symbol's use. There are a few symbols used in the text which do not appear in this listing. These are used once in a very specific context and are defined at that time.

The following dimensional conventions are utilized: L-length, M-mass, T - temperature, t-time, VD-variable dimension and 0-D-dimensionless. Three listings are presented - symbols, subscripts and superscripts.

SYMBOLS

A - area (L^2) or coefficient (0-D)
B - coefficient (0-D)
C - specific heat (L^2/t^2T), coefficient (0-D) or constant (VD)
c - mass fraction (0-D) or sound speed (L/t)
D - diffusion constant (L^2/t) or coefficient (0-D)
E - coefficient (0-D)
e - specific internal energy (L^2/t^2)
F - degree of implicitness (0-D) or coefficient (0-D)
f - force (ML/t^2)
G - coefficient (0-D)
g - gravitational acceleration (L/t^2)
h - specific enthalpy (L^2/t^2) or heat transfer coefficient (M/L^2tT)
I - junction inertia (1/L)
J - mass phase change rate (M/L^3t)
K - loss coefficient (VD)
k - thermal conductivity (ML/t^2T) or TKE (L^2/t^2)
LHS - left hand side
m - mass flow rate (M/t)
p - pressure (M/Lt^2)
Q - volume flow rate (L^3/t)
R - gas constant (L^2/t^2T)
r - radial dimension (L)
S - source strength (VD)
Sc - Schmidt number (0-D)
SM - mass source strength (M/t)
U - total energy (ML^2/t^2)
u - r direction velocity component (L/t) or velocity (L/t)
V - volume (L^3)
v - axial velocity component (L/t)
W - junction mass flow rate (M/t)
w - θ direction velocity (L/t)
x - dimension (L) or quality (0-D)
z - axial dimension (L)

α - void fraction (0-D) or velocity coefficient (L/t)
β - geometry flag (0-D) or velocity coefficient (L/t)
Γ - diffusivity (L^2/t)
γ - velocity coefficient (L/t)
δ - change (VD) or velocity coefficient (L/t)
ε - small number (VD) or velocity coefficient (L/t)
θ - third dimension (L or 0-D) or angle (radians)
κ - turbulent kinetic energy (L^2/t^2)
λ - third dimension option flag (0-D)
μ - viscosity (M/Lt)
ν - kinematic viscosity (L^2/t)
ξ - dissipation of turbulent kinetic energy (L^2/t^3)
ρ - mass density (M/L^3)
σ - shear stress tensor or velocity coefficient (L/t)
τ - wall shear stress (M/Lt^2)
ϕ - normalized phase change rate (1/t)
Ψ - transported entity (VD)
$\langle\ \rangle$ - ensemble average (VD)

SUBSCRIPTS

a - air
c - condensation
D - drag
E - energy
e - evaporation
f - friction
fg - vaporization
g - gas or gravity
g1 to g3 - gaseous components
h - enthalpy or hydrogen
i - radial or lumped zone index
j - axial or junction index
k - θ cell index
L - lumped region
l - liquid
M - momentum
m - mean
o - blower inlet
r - radial
s - steam
w - water
$\_$ - vector

SUPERSCRIPTS

M or m - molecular
n - time step index
r - radial
T - turbulent
z - axial

θ - third direction
$\hat{}$ - turbulent and molecular
' - fluctuation or perturbation
$\tilde{}$ - approximate value
$^{\circ}$ - old value
$\dot{}$ - time rate of change

1.0 Introduction

1.1 Problem Definition

The potential problems associated with the inadvertent or accidental introduction of combustible gases into nuclear power plant containment buildings have been recognized for many years. Of all the potential constituents, hydrogen gas is of the greatest concern in light water reactor (LWR) safety due to the abundance and potency of its sources in a typical LWR plant. The three principal sources are: production as a byproduct of an exothermic fuel cladding-steam chemical reaction, radiolytic decomposition of water and corrosion of certain metallic species present in the containment. Prior to the Three Mile Island (TMI) accident in March 1979 most nuclear safety analysts believed hydrogen concerns were adequately addressed in the commercial licensing process.

The TMI event and especially the hydrogen ignition which occurred has fostered renewed attention in this area. One important lesson learned is that large amounts of hydrogen can be produced and released to the containment over a wide range of time frames. Further, the potential detrimental consequences of this evolution are strongly determined by the pre-chemical reaction behavior of the various effluent species. In response to this problem, the regulatory authorities have proposed and in some cases required, the installation of various

prevention and/or mitigation schemes including deliberate ignition and ignition prevention systems. In many instances remedies are formulated without the benefit of sufficient analytical support to aid in the assessment of efficacy or desirability.

When one considers the progression of hydrogen behavior in nuclear containments, five general phenomena are identified. The first is hydrogen source definition since its characteristics define both the relevant time frames and bounding compositional end states. The second phenomenological regime involves the pre-chemical reaction flow transient which determines the combustion potential through the specification of local fluid-thermodynamic conditions. As hydrogen concentrations increase, ignition criteria and progression become important. Depending upon the local conditions and strength of the ignition source, either a subsonic deflagration wave (flame) or a detonation wave (shock) will result.

The purpose of this work is to develop analytical methods to treat the pre-chemical reaction thermo-fluid dynamic transient. The analytical methodology is applicable to rapid or slow transients. As models are described their assumptions and limitations are specified. Further, this work unifies these models into a single tool (computer program) for the convenient analysis of a wide range of problems.

Prior to proceeding to the body of this work, a general introductory remark is in order. The overall thrust of this endeavor is to develop a realistic approach to an actual nuclear safety problem. The general lesson that should be ascertained from the TMI experience is that nuclear safety analysis must become more concerned with events that will probably occur over the course of a plant's operating life and less fixated on scenarios of events which have only the smallest possibility of occurrence. Also, the analytical approach must be based on the goal of producing best estimate results with well understood uncertainty bounds. This is indeed in line with the good engineering practice of applying conservatisms after a realistic analysis is performed. In the consideration of complex systems with strong interactions, the prescriptive definition of "conservative" analyses as embodied in the current nuclear regulatory apparatus is intrinsically flawed and worthy of change.

1.2 Historical Background

The inadvertent combustion of volatile elements is a common safety concern in many industrial facilities. In nuclear plant applications these concerns arise during normal operation and unexpected events. The unexpected occurrences are of the greatest significance. Figure 1.1 depicts a particular containment design and is

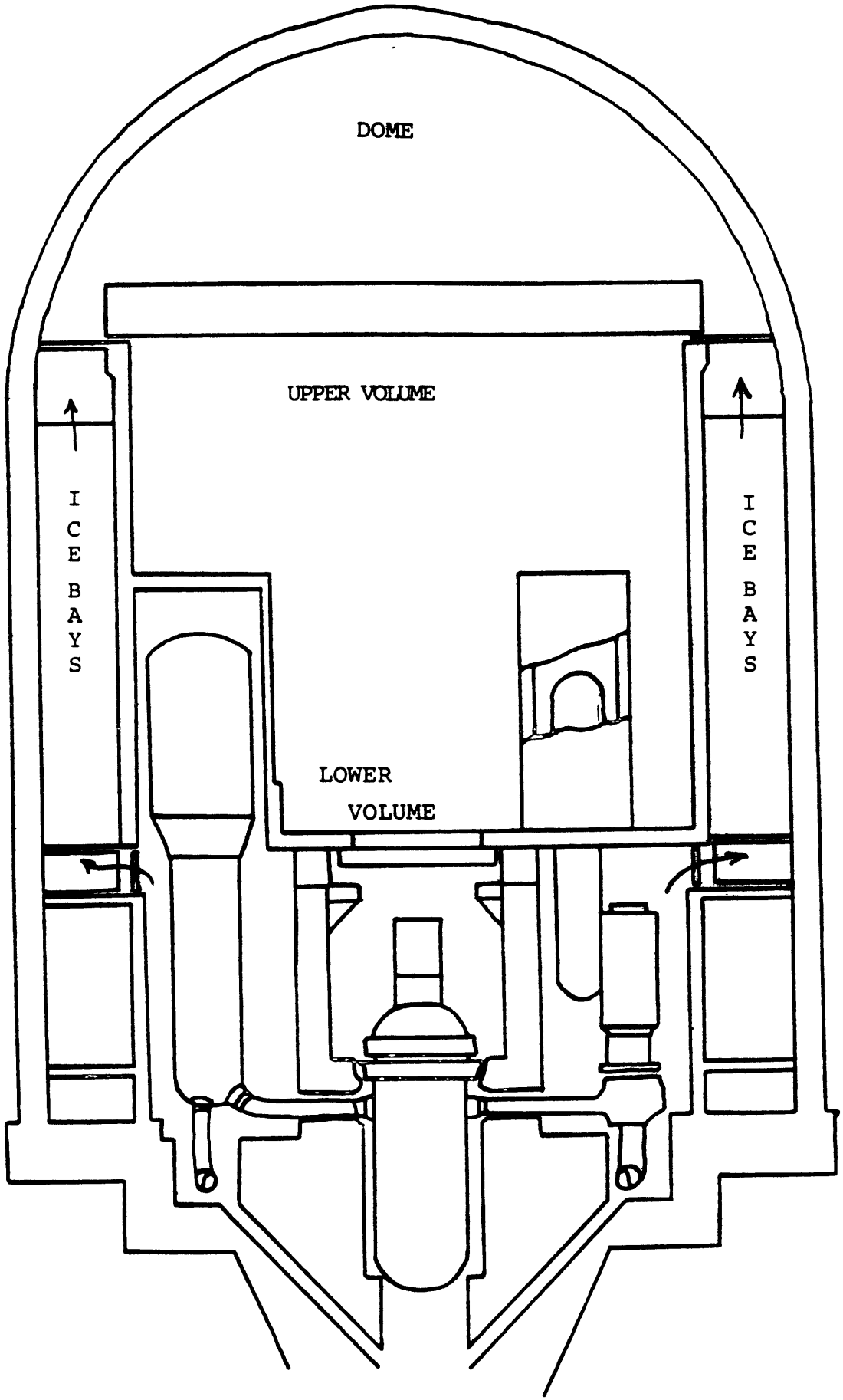

FIGURE 1.1: PWR ICE CONDENSER CONTAINMENT

provided as a physical reference for the problem. The hydrogen damage potential increases precisely when the proper operation of critical safety systems needs to be assured. Equipment damage can result from the impact of detonation waves originating at explosions or from exposure to elevated temperatures or flames.

The most significant hydrogen source is its production as a chemical byproduct of the exothermic zircaloy fuel cladding - high temperature steam reaction which can occur during undercooling events. The reaction has an approximate threshold temperature of 1600°K. The potency of this source is graphically depicted in Figure 1.2. The importance of this figure is noted when one realizes that the nominal flammability limit of hydrogen in air is 4% by volume. In order to "control" this source, the regulatory requirements state that peak cladding temperatures cannot exceed 1480°K and total zircaloy metal reacted cannot exceed 1% of the core inventory during a credible accident. The conformance to this standard is demonstrated through the use of conservative licensing analysis in conjunction with prescribed assumptions as to the performance of man and machines during the postulated events. By using this approach this source is "eliminated".

Radiolytic decomposition of water occurs in both the reactor coolant system (RCS) and containment sump after a postulated loss of coolant. This source

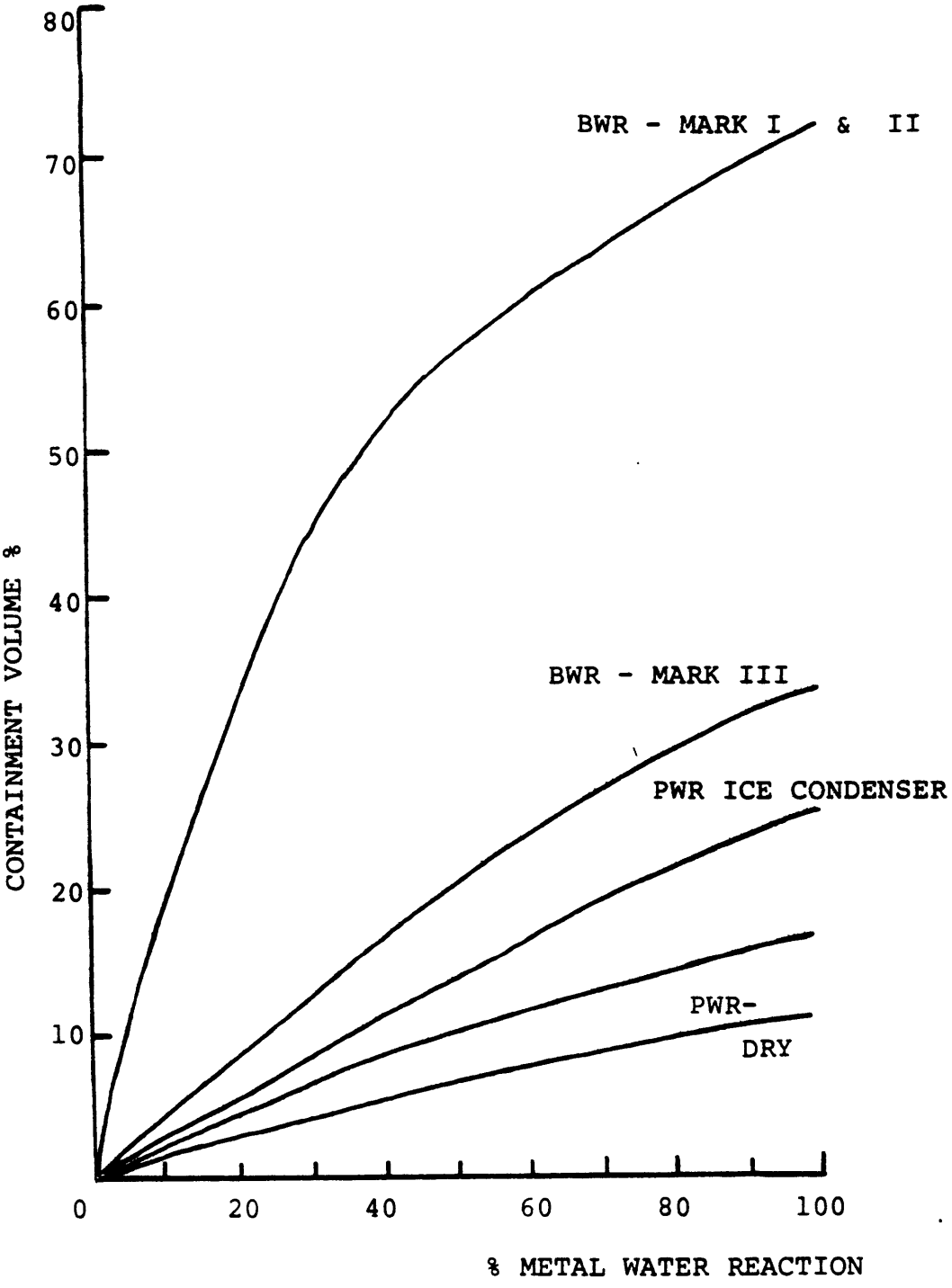

FIGURE 1.2: CONTAINMENT HYDROGEN CONCENTRATION VS METAL WATER REACTION

dominated pre-TMI licensing considerations since it could not be eliminated physically or analytically. While the total amount of hydrogen potentially produced by this source is large, its production rate is relatively low (order of many hours). Hence concentration control can be accomplished through the use of various removal devices such as catalytic recombiners. Hydrogen production due to the corrosion of metallic elements is accelerated in the warm and humid post-accident environment. Two elements of greatest concern are aluminum and zinc (which appears principally in paints and protective coatings). Control of this source is accomplished by strict material accounting procedures.

The TMI accident demonstrated the shortcomings of this overall approach in that the significance of the metal-water reaction hydrogen potential has been underestimated. While hydrogen produced in the reactor and trapped in the coolant system (eg. the infamous "hydrogen bubble" of the TMI accident) has little reaction potential due to the depressed oxygen level in the system, once it is vented from the RCS the containment can easily support an ignition. This indeed occurred at TMI as evidenced by a pressure spike in the containment pressure measurements, depressed containment oxygen content and subsequent visual evidence of equipment damage.

The regulatory reaction to these concerns has focused on the installation of new prevention/mitigation systems. Included among these are inerting strategies (which decrease oxygen concentration but also causes operational concerns when human access is required) and controlled ignition devices which deliberately burn hydrogen at lean, non-detonable, concentrations. In addition, the use of flame suppressants (eg. HALON gas), controlled containment venting (which aggravates radiological releases), water-fogging systems and catalytic absorption systems have been proposed. The basic concern which motivates the present research is that implementation is leading analytical support which calls into question the efficacy or even the desirability of any one or combination of these aforementioned alternatives.

1.3 Scope of Work

There are many phenomena related to this work worthy of study. The scope of this work encompasses the development and testing of analytical methods which accurately predict pre-chemical reaction flow. The hydrogen source strength and introduction mode are assumed to be defined a priori to these analyses. The division of pre- and post-reaction regimes is a logical one since the important physical phenomena as well as the process time scales of each regime are qualitatively distinct. (Appendix C addresses the modelling of

chemical reactions.)

The dynamic domain of interest spans rapid two-phase blowdown transients which are descriptive of jet or relief valve releases to slower near-homogeneous flows which are exemplary of slowly degrading cores or radiolytic sources. The treatment of longer term scenarios are more central to this work since they encompass most of the potential occurrences addressed by the proposed regulatory remedies. The major physical aspects of the problem are: two-phase effects, buoyancy, turbulence, diffusion, heat transfer and condensate behavior. The computational schemes must be both physically and economically appropriate to the problem. An example of physical appropriateness is the proper treatment of diffusion which can be a dominant transport mechanism in a low flow regime. Economical appropriateness relates the computational expense of solving a problem versus the quantity and quality of the information accrued from such an analysis.

Given the stated work scope and acknowledging this to be the initial product of a larger research effort, the particular goal of this work is to develop a basic tool which identifies and treats basic phenomena in a reasonable fashion. Recommendation as to possible areas of improvement are also addressed. Nevertheless, the methodology described herein represents a valid and useful technique.

2.0 Literature Review

Given the large scope of this work, the literature review has the dual purpose of highlighting particularly important work and guiding the reader to more extensive information sources. The survey is divided into three categories - hydrogen related problems in nuclear power plants, relevant computational methods and containment analysis tools.

2.1 Hydrogen Related Problems in Nuclear Power Plants

During normal operation of a nuclear plant combustible gases accumulate in various treatment systems and require careful monitoring. The greatest concerns arise during accident conditions when the available hydrogen sources are orders of magnitude stronger. Hydrogen control was recognized as an important design constraint earlier in the development of large LWR plants. The article of Bergstrom and Chittenden [1] is illuminating in that it documents hydrogen design constraints in containment construction as early as 1959. Keilholtz [2] has assembled an extensive annotated bibliography of hydrogen safety literature through 1977 and is noteworthy as a general reference. The literature in this area can usually be divided into three overlapping categories - generation, behavior and control.

The three principal hydrogen generation mechanisms are metal-water reactions, water radiolysis

and corrosion. All three are enhanced under accident conditions. The reaction of zirconium fuel cladding and steam during core undercooling events is the largest source in terms of both strength and duration. The analytical and empirical study of this reaction is reported in the seminal work of Baker and Just [3]. Their semi-empirical formulation of a finite rate process controlled by steam availability and temperature, characterized by an activation energy, is an important analysis tool. The potential accident dynamics of the reaction in a power reactor core are described by Baker and Ivins [4] and Genco and Raines [5]. In the radiolytic decomposition of water ambient radiation (especially neutron and gamma fluxes) split the water molecules into their elemental parts thus yielding hydrogen. Experimental investigations of radiolysis are reported by Bell et.al. [6] and Zittel [7]. Fletcher et.al.[8] not only investigated radiolysis but also combined the resultant generation rates with assumed metal-water reaction and corrosion to estimate overall containment hydrogen concentrations. In their analysis flammability limits are not reached since only very limited core damage is assumed. The measured radiolysis generation rates are 0.33 H_2 molecules/100 eV absorbed radiation and 0.44 H_2 molecules/100 eV for the sump and core water chemistries, respectively. The difference arises from the higher dissolved H_2 content in the reactor. The chief

corrosion sources are metals either in the structural or protective coating material. For example, Lopata [9] analyzes the generation rate due to zinc paint primers. In core meltdown analyses more exotic sources such as core-concrete interactions and aluminum corrosion become important.

The topic of hydrogen behavior includes pre-chemical reaction mixing, ignition, deflagration and detonation. (The latter three areas are mentioned here but are treated in greater detail in Appendix C.) The TMI 2 accident provides an undesired yet significant empirical demonstration of many aspects of this behavior. A thorough analysis of the TMI hydrogen burn is provided by Henrie and Postma [10]. They calculated an average pre-burn H_2 wet (including steam) volume fraction of 7.9%. The burn was apparently initiated at a lower elevation but propagated through the entire containment height in roughly 10 seconds. Though very high local temperatures occurred (>750°C), equipment thermal excursions were probably limited to 1 or 2 °C. Areas near steam vents showed significantly less fire damage. All these findings are consistent with smaller scale observations.

Two recent large scale hydrogen mixing tests are significant because they are directly applicable to reactor containment analysis and are well instrumented to provide useful data for analytical model validation.

One program was carried out at the Battelle Frankfurt Institute in West Germany. This testing program is described in Chapter 4. Useful resources are the reports of Langer [11] and various data reports issued by the German Federal Ministry for Research and Technology [12]. The second program was performed at the Hanford Engineering Development Laboratory (HEDL) and is also described in Chapter 4. A detailed review of the facility design, operation and results is given by Bloom et.al. [13] and Bloom and Claybrook [14]. Zinnari and Nahum [15] also report a small scale test simulation for BWR containments.

The combustion literature contains innumerable studies of various hydrogen reactions. Sherman et.al.[16] provide a general review of important implications in nuclear safety. Figure 2.1 is abstracted from that work and depicts the parametric dependencies of constituent concentrations and thermodynamic state. Hertzberg and Cashdollar [17] present a review of current theoretical understanding of the size and shape of the flammability limit surface in containment volumes. J. C. Cummings et.al. [18] report work performed at Sandia National Laboratories in which geometrical effects are studied. Jaung et.al. [19] analyze the containment atmosphere system to better understand the transition from deflagration (subsonic propagation - i.e. flame) to detonation (sonic wave propagation). Table 2.1 is

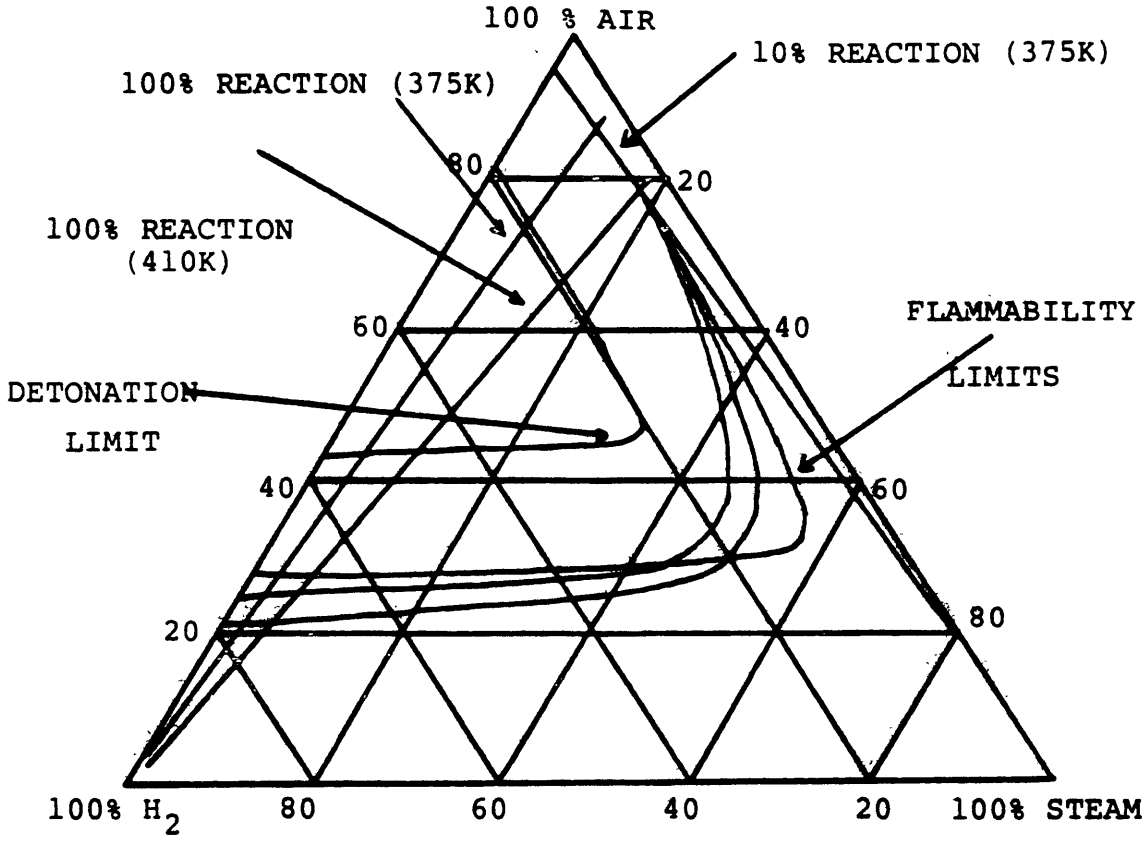

FIGURE 2.1: FLAMMABILITY AND DETONATION LIMITS OF HYROGEN - AIR - STEAM MIXTURES

taken from that work. Finally Kumar et.al.[20] empirically investigated parametric effects at high concentrations including sensitivity to steam concentration and obstacles. Figure 2.2 illustrates on of their more important results. Steam is shown to restrain both the magnitude and extent of the hydrogen reaction.

The issue of post-accident hydrogen control is directly related to the underlying scenario assumptions. If a small core oxidation source is assumed as was required by the regulatory authorities prior to the TMI 2 accident [21], control involved demonstrating conformance analytically through safety analysis and through physical installation of relatively small recombining devices to handle the weaker radiolysis source. The regulatory perspective has distinctly changed after the accident as is evidenced in the presentation of Butler et.al.[22]. The control measures described in this work are classified as either preventive and mitigative. Preventive measures most frequently involve enhanced emergency core cooling systems. This enhancement is sometimes guided by probabalistic risk assessment (PRA) (see Boyd et.al.[23]). Potential mitigative measures include pre-accident inerting, post-accident inerting, deliberate ignition, filtered-vented structures, water-fogging and catalytic absorption. Demonstrating the necessity and efficacy of any of these options is the underlying motivation for this and many other studies

Table 2.1 : Detonation / Deflagration Transition

Regime	Ignition Source	Result
I-near stoi-		
chiometric		
(detonation possible)	Glow plugs	Deflag
	Deflagration	Deton
	Blast wave	Deflag/Deton
	Local explosion	Deflag/Deton
II-transitionally		
reactive	Glow plugs	Deflag
	Deflagration	Deflag/local
	Blast wave	No reaction
	Local explosion	No reaction
	From tube	Deflag or Deton
III-weakly reactive		
	Glow plugs	Deflag
	Deflagration	No reaction
	Blast wave	No reaction
	Local explosion	No reaction

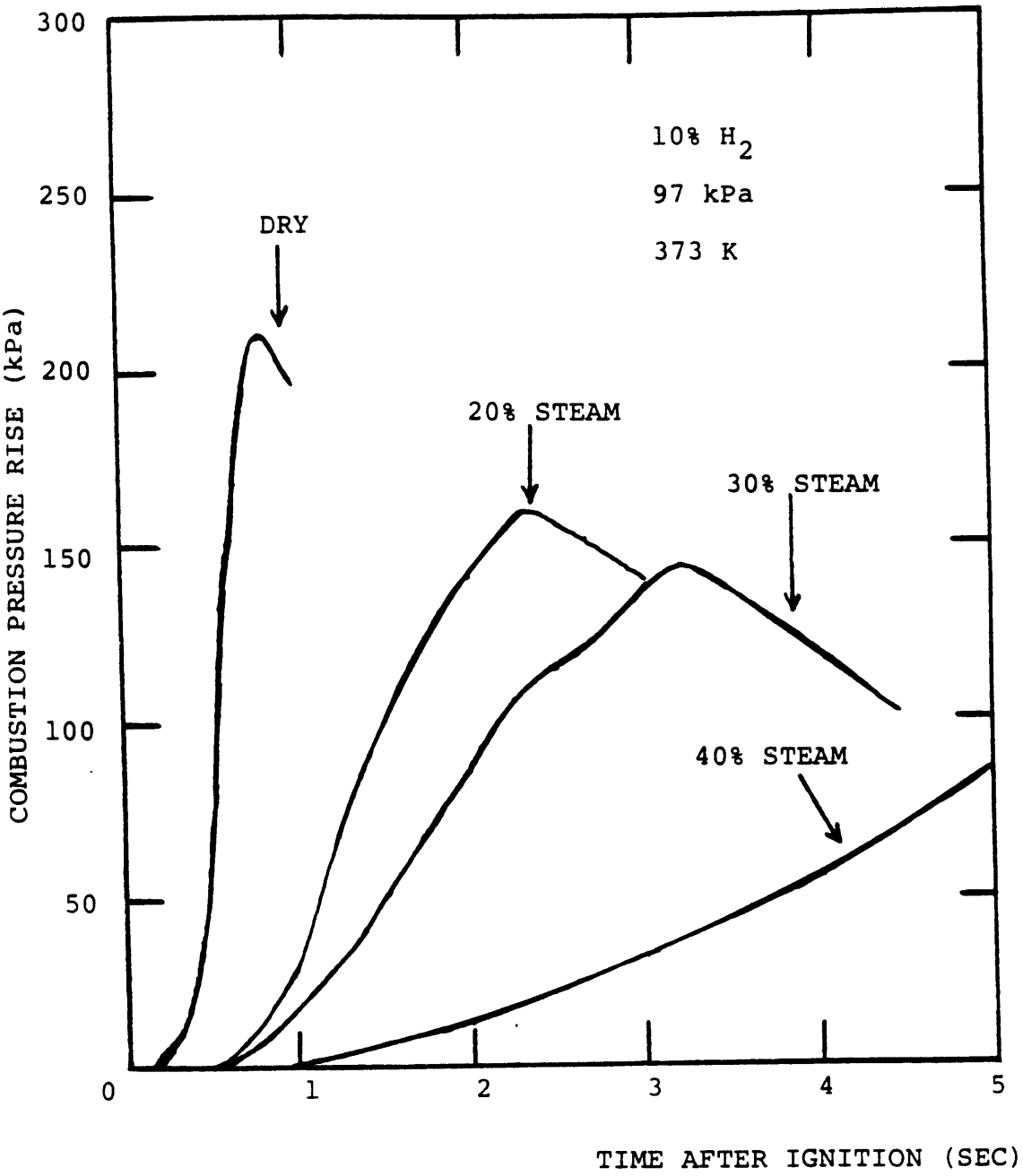

FIGURE 2.2: EFFECT OF STEAM ON H_2 COMBUSTION

(see Thompson [24].)

2.2 Relevant Computational Methods

Prior to the citation of works of narrower scope, a few general references are noted which are used throughout the analytical development. First, the pioneering text of Richtmeyer and Morton [26] addresses the general topic of numerical solution of initial-valued problems. Of particular note are the review of finite difference approximations and their associated accuracy and stability characteristics (see Chapter 8 of that reference). Roache [27] has provided an encyclopedic review of most schemes utilized in the area of computational fluid dynamics. The stability analyses of each scheme provides an excellent overview to aid in the selection of appropriate techniques. The stability analysis of finite difference equations described by Roache is based to a large extent on the work of Hirt [28]. More recently Patankar [29] focuses on a single but quite general flow solution methodolgy (ie. Semi-Implicit Method for Pressure-Linked Equations or SIMPLE) and also provides a basic understanding of the application of finite difference techniques to the solution of fluid and heat transfer problems. Ransom and Trapp [30] have presented a short but thorough review of the use of various computational methods in nuclear thermal hydraulic analysis. Finally, while there are many techniques, most are based on applying the procedures

of numerical analysis, especially of linear systems. In this regard, the text of Isaacson and Keller [31] is useful for the specification of desirable numerical methods such as the inversion of banded matrices.

The solution method used for the solution of the rapid blowdown problems is the Implicit Continuum Eulerian (ICE) technique developed by Harlow and Amsden [32]. The technique allows a stable solution limited by the material Courant time step (ie. $\delta t<\delta x/u$) rather than the full Courant limit ($\delta t<\delta x/u+c$) typical of other compressible flow techniques. Rivard and Torrey [33] applied this technique coupled with a two-phase flow formulation due to Ishii [34] to develop the K-FIX code which was the fluid solution subprogram of the BEACON code. A very efficient method applicable to incompressible problems is the Simplified Marker and Cell or SMAC procedure developed by Amsden and Harlow [35]. It is closely related to the ICE method in both its semi-implicit iterative procedure as well as its discretization logic.

The Courant limitation is rather restrictive in longer duration simulations in which the flow characteristics change slowly in time. In order to eliminate this restriction the use of implicit techniques deserves consideration. The application of completely implicit techniques to pure diffusional problems of the form

$$\frac{\partial \Psi}{\partial t} = \underline{\nabla} \cdot \Gamma \underline{\nabla} \Psi \qquad (2.1)$$

is straightforward. An especially efficient technique is the alternating direction implicit (ADI) method. Important theoretical considerations of this class of methods are provided by Douglas and Gunn [36]. The application of analogous methods to mixed convection/diffusion problems characterized by

$$\frac{\partial \Psi}{\partial t} + \underline{\nabla} \cdot \underline{u} \underline{\nabla} \Psi = \underline{\nabla} \cdot \Gamma \underline{\nabla} \Psi \qquad (2.2)$$

is more complex and not generally amenable to closed form stability and accuracy analysis. Briley and McDonald ([37] and [38]) have analyzed these problems under the general heading of linearized block implicit schemes. They point out that the consistent splitting of the directional sweeps is crucial to a method's success. Nevertheless, the application of the methods described by Briley and McDonald are limited to fully compressible problems since a necessary validity condition is the presence of each dependent variable in a time derivative in at least one equation. In an incompressible problem density does not conform to this constraint.

Stability is not the only computational consideration. Accuracy is of equal importance. This is particularly true in cases when physically diffusive mechanisms are encountered in convective problems. The discretized treatment of convective terms usually gives rise to a computed solution which exhibits an enhanced

diffusional nature. This so-called numerical diffusion must be carefully assessed in order to ensure that the numerical solution technique does not produce an unrealistic physical solution. The work of Huh [39] addresses this problem as it relates to hydrogen transport analysis and it should be consulted for a more thorough treatment of the topic.

Some early higher order techniques are discussed by Roberts and Weiss [40]. The greatest limitation of these early techniques are the prohibitive storage and computing effort associated with correcting convective term inaccuracies. Similar methods are discussed in a review paper by Fromm [41]. More recently, workers have studied Lagrangian-based techniques. Typical among these is the work of Raithby ([42] and [43]) who surveys various upstream differencing techniques and develops an original skewed differencing which he claims can significantly decrease false diffusion in some problems. Chang [44] studied a number of these methods in terms of a method-of-characteristics (MOC) solution. (See Weisman and Tentner [45] for a general review of MOC application to nuclear engineering problems.) Chang emphasizes that the interpolation method used to estimate the upstream path value of the convected entity significantly affects accuracy and physical reasonableness. A related approach termed the tensor viscosity (TV) method has been reported by Dukowicz and

Ramshaw [46].

The numerical solution of turbulent flow problems usually involves simplifying assumptions in order to render the problem tractable. Invariably, higher order correlation functions arising from the expansion of the primitive flow variables into constant and fluctuating components are grouped together to define a reasonable physical characteristic of the average flow. The algebraic eddy viscosity approach is the simplest approximation since no additional conservation equations require solution. Unfortunately, algebraic and first order approaches (such as mixing length hypothesis) are inadequate for recirculating flow analyses. A general introduction to these considerations is provided by Launder and Spalding [47] in a series of published lectures at the Imperial College in England. Second order methods in which additional conservation equations for two turbulence parameters such as turbulent kinetic energy and dissipation are generally accepted as the best current alternative. The review article of Lumley [48] is useful for ascertaining a physical interpretation of second order methods. Rodi [49] presents a number of second order methods applicable to atmospheric transport problems. These models are also useful in the present application since buoyant turbulent production is a significant driving force in both physical regimes.

Most of the computational methods cited above

relate to the solution of continuum problems. Lumped parameter or nodal methods are also very useful analytical tools. The pioneering work of Porsching et al. [50] addresses the stable numerical integration of conservation equations for hydraulic networks. The technique is semi-implicit which is a highly desirable characteristic since an explicit time step stability constraint is quite prohibitive in most problems of this type.

2.3 Containment Analysis Tools

Analytical models of nuclear containment response to accidents have evolved from simple lumped parameter analysis to continuum modelling. The chief application of these tools are the assessment of containment integrity and providing boundary conditions for nuclear steam supply system analysis. The lumped parameter analysis codes are exemplified by the CONTEMPT series of programs (see D. W. Hargroves et.al.[51] for example). As the requirements for accuracy and improved spatial resolution increased, multi-compartment analysis tools were developed. The CONTEMPT4 program described by L. J. Metcalfe et al. [52] addresses the behavior of a wide range of containment designs including dry containments, suppression pool designs, ice condensers and others.

As hydrogen related issues gained importance, basic lumped parameter models were extended to handle

the transport of additional non-condensibles. The RALOC code developed by Jahn ([53] and [54]) is an example of this approach. Some distinguishing characteristics of the RALOC code are its explicit modelling of hydrogen generation rates, treatment of component diffusion and mixed implicit/explicit integration methods. An assessment of this program is reported by Buxton et.al. ([55] and [56]). They conclude that the code produces good qualitative results and fairly stable numerics. Areas worthy of improvement are expansion of base set of components, multiple source injection logic, improved heat slab modelling, removal of the saturation constraint and allowance of user-controlled loss resistances. The last point is particularly salient to the discussion of all lumped parameter tools. These models are very well suited to scoping or global analysis. The application of these methods to the prediction of detailed spatial distributions is hindered by the inability of the basic conservation model to handle local effects. One of the major restrictions is the rather arbitrary specification of junction characteristics such as resistance or inertia when modelling an essentially open space. Fujimoto et.al. [57] report the development of a code named MAPHY (Mixing Analysis Program of Hydrogen) which seems nearly identical to RALOC except for a completely implicit integration logic. Fischer et.al. [58] report the development of the WAVCO program

for the analysis of general non-condensible transport in containments including hydrogen and CO_2 (from core/concrete interactions during meltdown events). The model includes a treatment of sump water dynamics.

The analysis of hydrogen behavior in containments is more complex when chemical reactions are considered. Lumped parameter tools are reasonable in this regard if the analyst is interested in bounding temperatures and pressures. The HECTR code developed by Camp et.al. [59] at Sandia Labs is a recent example of such a program. In addition to the usual nodal flow models, HECTR includes a hydrogen burn and radiative heat transfer models. The burn model is conceptually simple since actual chemical kinetics cannot be modelled in a lumped code due to the dependence of reaction kinetics on local conditions. Deflagration is assumed to be initiated after a user-defined global concentration level is achieved and flame speed is computed using an empirical correlation of the form

$$\text{flame speed} = A\, x_h + B, \quad (2\text{-}3)$$

where: A,B = empirical constants, and

x = mole fraction.

The burn completeness can either be user specified or an additional internal empirical correlation is employed.

If spatial definition is important as is the case in assessing many hydrogen safety questions, a continuum problem must be solved. A one dimensional

formulation is an intermediate step between lumped parameter models and multi-dimensional analyses. It is most appropriate for problems where variations in a preferred direction dominate dynamic effects. Willcutt and Gido [60] and Wilcutt et.al. [61] have discussed application of this approach to hydrogen transport. The flow formulation depends heavily upon boundary layer approximations to define the field. The method is applied to the analysis of radiolytic hydrogen source in a single room. Molecular, turbulent and buoyant effects are treated separately and together in order to assess individual contributions. The application of this method to single region problems with well-defined boundary conditions can accrue the benefits of a more sophisticated multidimensional analysis with considerably reduced computational effort.

Finally, multi-dimensional models are available. The BEACON code described by Broadus et.al. [62] is of central importance to this work. Its basic formulation allows the treatment of fluid regions in terms of zero (lumped), one or two dimensional zones. Two-phase continuum equations describe the multi-dimensional regions from an Eulerian viewpoint. The program includes explicit models for transient heat conduction in solids and condensate film dynamics. This code is more fully described in the next chapter. Other continuum programs are being applied to the hydrogen

problem. Trent [63] and Trent and Eyler [64] have modified the single region TEMPEST code to track hydrogen. This program allows three (or two) dimensional modelling of a single region including heat conducting solids. Turbulence is modelled through the use of a two equation closure model. The HMS (Hydrogen Migration Studies) program developed by Travis ([65] and [66]) is based on a compressible flow solution using the ICE method. Three dimensional single room modelling is employed. Mixing enhancement due to turbulence is handled by an input eddy viscosity. Component diffusion is not taken into account in the species transport equations. Thurgood [67] has applied the two-phase code COBRA-NC to these problems A coupled two-field (gas and liquid) solution is accomplished in continuum regions while a lumped option also exists.

3.0 Analytical Modelling

3.1 Overall Approach

In the interest of efficiency and to minimize the duplication of effort, the starting point of this analytical development is an existing containment code. As noted in Section 2.3, the BEACON code possesses a number of features necessary for the valid simulation of hydrogen transport transients and this program provides the superstructure upon which the overall tool is built. The justification for using BEACON rather than another code or developing a completely new code is first presented in this section. Following this, the two-stage development/modification is described. These discussions demonstrate that the final product is substantially different from the original code.

There are six major characteristics favoring the choice of BEACON. First, it was developed with modelling options such as compartment geometries, input specification and material property data representative of containment problems. Second, the internal code structure is distinctly modular. This feature allows modification of one submodel without serious impact on unrelated models. The computer application discussion of Appendix A further demonstrates this 'top down' programming approach. Third, BEACON's treatment of fluid regions is substantially more versatile than most containment codes in that a region can be modelled as zero-dimensional (lumped parameter), one-dimensional or two-dimensional Eulerian zone. Further, more than one of these options can

be invoked in a single problem such that multi-compartment problems with user specified spatial resolution are possible.

The pre-chemical reaction flow transient as well as the chemical kinetics of hydrogen reactions are strongly influenced by the presence of water. Therefore, the inclusion of condensate film formation and behavior in the original code is a desirable characteristic. Local containment thermal conditions are determined in part by the interaction with structural heat sinks such as walls, gratings and equipment. These structures themselves experience thermal transients over the course of an event. The BEACON code contains a one-dimensional heat conduction model to handle these effects. Finally, the code is available at relatively little expense on a timely basis from the National Energy Software Center.

The requirements of hydrogen analysis in conjunction with the basic deficiencies of the BEACON code specify the required development effort. The basic continuum formulation of the program involves a complex two-phase multi-equation dynamic model with the provision of non-equilibrium inter-phasic mass, momentum and energy transport in a fully compressible format. The original components are water in gaseous or liquid phase and air. Air and water are also the only allowed components of the lumped parameter, condensate film, heat transfer and transport property calculations. These limitations define the first modification step such that hydrogen is consistently included in all the basic models. The resultant product of this first step is a tool

with the ability to handle hydrogen transport during rapid blowdown transients dominated by compressibility and two-phase flow effects.

The inherent limitations of the BEACON program necessitates the development of a completely new slow mixing model. In a slower transient, non-equilibrium thermodynamics, multiphase transport effects and total fluid compressibility are not as important as buoyancy, molecular and turbulent diffusion and compositional changes. The development of an appropriate formulation and solution methodology is detailed in the discussions of section 3.3. The new models are independent of the original BEACON equation set. Particular aspects of the new subcode are: basic model formulation, turbulence modelling, consistent definition of thermodynamic state and detailed consideration of the accuracy and efficiency of the computational scheme. The validity bounds of the new model are also specified.

A substantial amount of time and attention are involved in the acquisition, installation, modification and validation of any large computer program. The work reported here is no exception to this general rule. A number of computer application topics are addressed in Appendix A. This appendix interfaces with the analytical discussions of sections 3.2 and 3.3. More information is contained in the new code's (LIMIT) users manual.

3.2 Modification of the BEACON Code for Rapid Transients

The modification of the BEACON equation set for the analysis of rapid blowdown events is divided into four subtopics. First, the inclusion of hydrogen in the continuum equations and solution logic is described. Second, the treatment of hydrogen in lumped parameter formulations is specified. Following this a number of smaller ancillary model developments are detailed including basic thermodynamics, hydrogen and mixture transport properties, the effect of hydrogen on condensate film dynamics and heat transfer aspects. Finally, the inherent limitations of the modified BEACON equations are set forth. In many instances, the original program documentation is a useful accompanying reference for this section.

3.2.1 Continuum Equations and Their Solution

The original BEACON continuum formulation is best suited for the analysis of rapid transients. The formulation is actually based on the K-FIX code. The model derivation includes non-equilibrium interphasic exchanges. The revised equations are presented below in an abbreviated manner since the exact form of the various exchange functions is not central to this discussion. A thorough treatment of the multifield model equations is provided by Ishii [34].

The major alteration is the addition of a fourth mass balance to represent hydrogen transport. The following mass conservation equations are solved:

$$\frac{\partial \rho_g}{\partial t} + \underline{\nabla} \cdot (\rho_g \underline{u}_g) = J_e - J_c, \tag{3.1}$$

$$\frac{\partial \rho_{g_1}}{\partial t} + \underline{\nabla} \cdot (\rho_g \underline{u}_g) = J_e - J_c, \tag{3.2}$$

$$\frac{\partial \rho_{g_2}}{\partial t} + \underline{\nabla} \cdot (\rho_g \underline{u}_g) = 0, \text{ and} \tag{3.3}$$

$$\frac{\partial \rho_\ell}{\partial t} + \underline{\nabla} \cdot (\rho_\ell \underline{u}_\ell) = J_c - J_e. \tag{3.4}$$

These equations are fully compressible in formulation and the evaporation/condensation source terms are calculated using non-equilibrium thermodynamic models. Diffusional transport of the individual compounds is neglected. In a more conventional formulation the first equation might be replaced with a mass balance for component 3 (air) such as

$$\frac{\partial \rho_{g_3}}{\partial t} + \underline{\nabla} \cdot (\rho_g \underline{u}_g) = 0. \tag{3.5}$$

Nevertheless (3.1) is the sum of equations (3.2) (3.3) and (3.5) and thus represents a consistent formulation.

Each phase is described by its own pair of momentum and energy conservation equations. These equations were not modified and are presented here so that their general structure can be seen and compared to the new slower mixing model. The time momentum balances are:

$$\frac{\partial \rho_g \underline{u}_g}{\partial t} + \underline{\nabla} \cdot (\rho_g \underline{u}_g \underline{u}_g) =$$

$$- \alpha \underline{\nabla} P + \underline{\nabla} \cdot \alpha \underline{\sigma}_g + \rho_g \underline{f} + \underline{f}_M (\underline{u}_g, \underline{u}_\ell, J_e - J_c), \quad (3.6)$$

and

$$\frac{\partial \rho_\ell \underline{u}_\ell}{\partial t} + \underline{\nabla} \cdot (\rho_\ell \underline{u}_\ell \underline{u}_\ell) =$$

$$(\alpha - 1) \underline{\nabla} P + \underline{\nabla} \cdot (1-\alpha) \underline{\sigma}_\ell + \rho_\ell \underline{f} - \underline{f}_M (\underline{u}_g, \underline{u}_\ell, J_e - J_c). \quad (3.7)$$

The $\underline{f}_M$ function represents non-equilibrium interphasic momentum exchange due to velocity slip and phase change. The shear stress tensor embodies only molecular effects including bulk viscosity using Stoke's hypothesis. The neglect of turbulent-enhanced viscosity is a reasonable simplification in blowdown calculations. $\underline{f}$ represents body forces such as gravity.

The two energy equations are:

$$\frac{\partial \rho_g e_g}{\partial t} + \underline{\nabla} \cdot (\rho_g e_g \underline{u}_g) = -P \left[\frac{\partial \alpha}{\partial t} + \underline{\nabla} \cdot \alpha \underline{u}_g\right] + \alpha \underline{\sigma}_g : \underline{\nabla u}_g$$

$$+ \underline{\nabla} \cdot k_g \underline{\nabla T}_g + f_E (\underline{u}_g, \underline{u}_\ell, J_e - J_c, T_g - T_\ell, e_{fg}),$$

and (3.8)

$$\frac{\partial \rho_\ell e_\ell}{\partial t} + \underline{\nabla} \cdot (\rho_\ell e_\ell \underline{u}_\ell) = -P \left[\frac{\partial (1-\alpha)}{\partial t} + \nabla \cdot (1-\alpha)\, \underline{u}_\ell\right]$$

$$+ (1-\alpha) \underline{\sigma}_\ell : \nabla \underline{u}_\ell + \underline{\nabla} \cdot k_\ell \underline{\nabla T}_\ell$$

$$- f_E (\underline{u}_g - \underline{u}_\ell, J_e - J_c, T_g - T_\ell, e_{fg}), \qquad (3.9)$$

where

$$\sigma_i : \nabla \underline{u}_i \equiv \sum_i \sum_j \sigma_{ij} \frac{\partial u_i}{\partial x_j} \quad \text{(tensor notation)}.$$

In analogy to $\underline{f}_M$, f_E describes the non-equilibrium interphasic exchange. A number of possible exchange models are available as options but the analyst should be cautioned that all models save for the model of Crowe et al. [68] do not account for the presence of an inert gas such as hydrogen or air at the interface. As such, option choice must be based on the conformance of the problem to the constraints of the exchange model. As a general remark, it is felt that any of these rather complex, semi-empirical and restricted scope models are of limited usefulness to hydrogen-related questions.

The basic numerical solution methodology of this modified equation set is not changed. The code allows different computational time step sizes for different regions and processes. The basic time advancement logic is shown in Figure 3.1. As such time steps in lumped parameter regions and solid heat sinks of reasonable thicknesses are usually larger than those of the Eulerian fluid regions. The fluid solution technique involves casting the differential equations into a finite difference staggered mesh (see section 3.3) and solving the resulting coupled algebraic equations by an implicit point relaxation scheme. Due to the coupling logic used to relate the momentum and mass equations the stability limitation of the time step is independent of sound speed but constrained by the material Courant-Freidrichs-Levy (CFL or Courant) condition of

$$\delta t \leq \left| \frac{\delta x_i}{u_i} \right|_{max} \tag{3.10}$$

Due to the coupled nature of the conservation equations, a number of nested iterative operations are required to arrive at a converged solution. A more detailed treatment of this technique, which is named Implicit Multifield (or IMF), is provided by Harlow and Amsden [69].

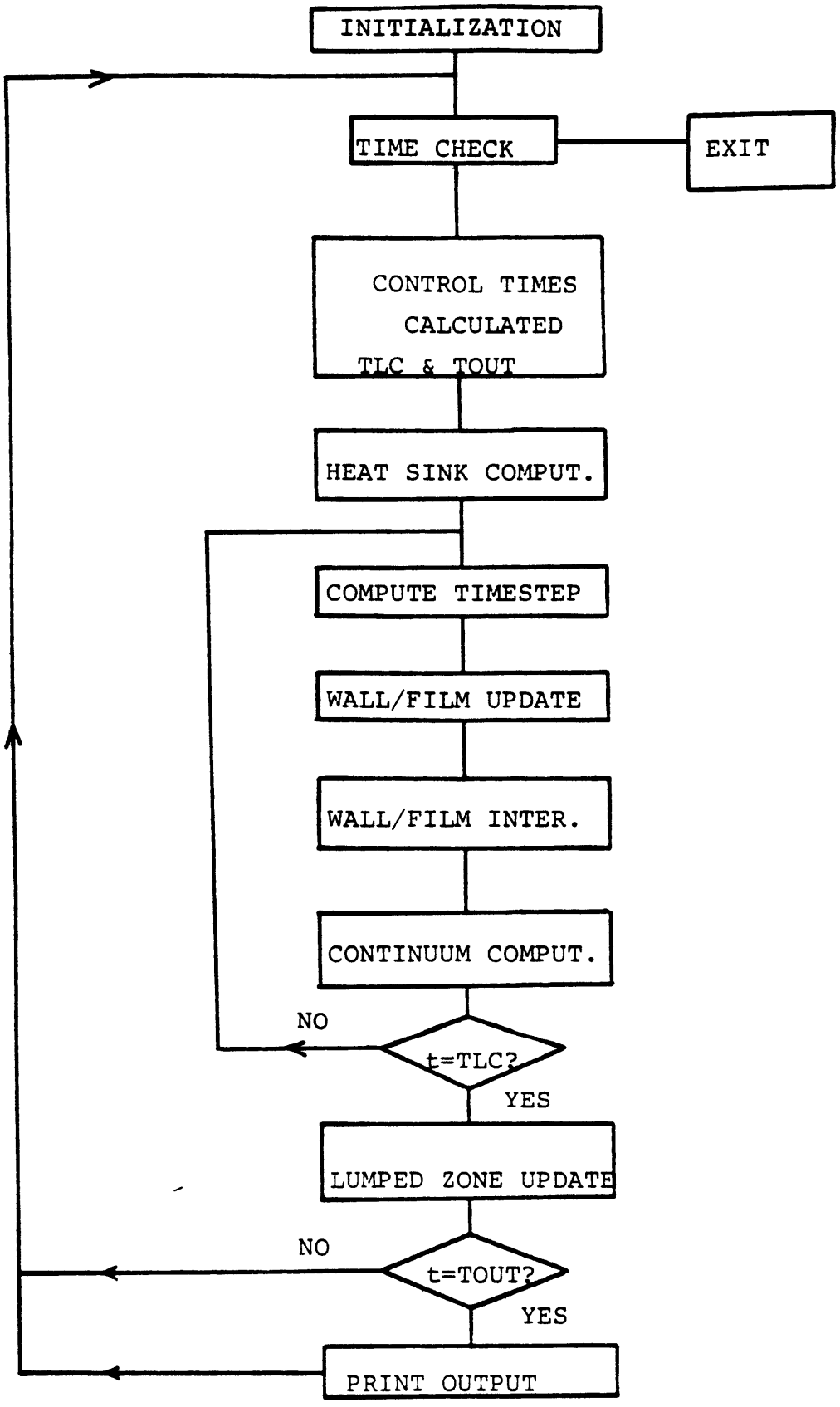

FIGURE 3.1: BASIC TIME ADVANCEMENT LOGIC

FIGURE 3.2: COORDINATE SYSTEMS DEFINITIONS FOR CONTINUUM REGIONS

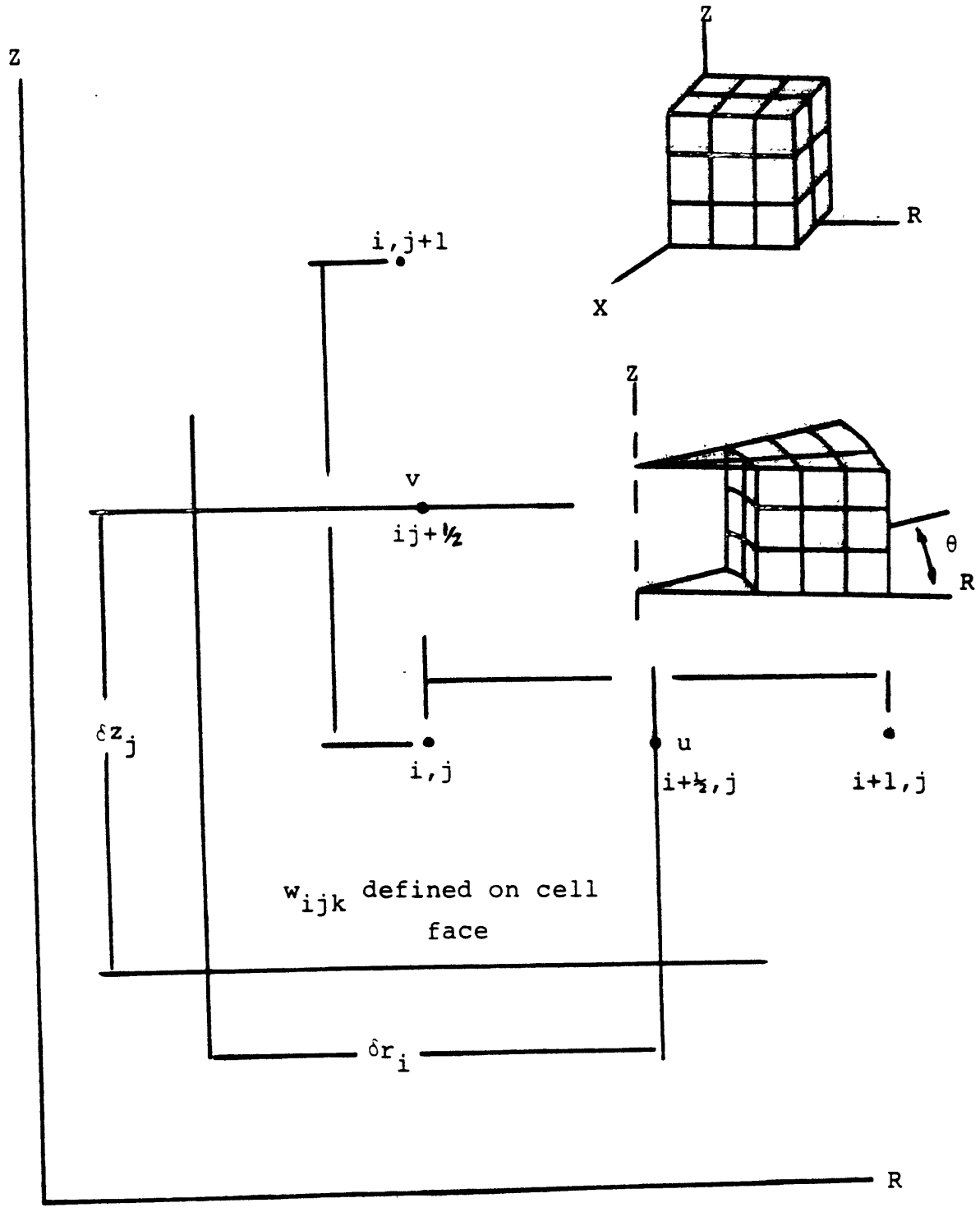

3.2.2 Lumped Parameter Zones

The original program possessed the capability of treating large regions in which spatial variations are not important as zero-dimensional or lumped parameter zones. The regions are assumed to be perfectly mixed and mass and energy are balanced on a control volume basis. Flows to and from these zones are computed by modelling the connecting junction as a one-dimensional Eulerian region. This approach is restrictive for two reasons. First it necessitates employing a continuum model when merely average junction flows are required. Second, the balance equations are solved explicitly in time which makes long term computations costly. Therefore two lumped parameter related developments are described. First the existing BEACON approach is extended to handle hydrogen and second, an entirely new treatment which requires no continuum solution and is completely implicit in solution formulation is added as an additional option.

3.2.2.1 Inclusion of Hydrogen in Existing Formulation

A balance equation for hydrogen of the following form is added

$$V_L \frac{d}{dt} \rho_{g_2} = \sum_{\substack{i=\text{all boundaries}}} (\rho_{g_2} \bar{u}_g A)_i + \sum_{\substack{j=\text{all sources}}} (\dot{m}_{g_2})_j \cdot \qquad (3.11)$$

The remaining energy balances are modified to account for flow energy transfer due to hydrogen transport. An additional

limitation of the original formulation is that the nodal balances are specified as to be compatible with the two-phase non-equilibrium model and as such the lumped parameter state solution exhibits the same limitations as the continuum solution.

3.2.2.2 Model Improvement

In light of the limitations elucidated above, a new lumped parameter model is developed. The formulation presented is based on the well-established nodal solution methodology used in the RELAP and FLASH programs and as such only the essential points are presented. Three nodal mass balances are used.

$$\frac{d}{dt} M_{ik} = \underset{j=\text{to junctions}}{\Sigma \frac{\rho_{ij}}{\rho_j} W_j} - \underset{j=\text{from junctions}}{\Sigma \frac{\rho_{ij}}{\rho_j} W_j} + SM_{ik}, \tag{3.12}$$

where: k = air, hydrogen and water and

i = node.

The nodal energy conservation equation is

$$\frac{d}{dt} U_i = \underset{j=\text{to junctions}}{\Sigma h_j W_j} - \underset{j=\text{from junctions}}{\Sigma h_i W_j} + \underset{k=1,3}{\Sigma SM_{ik}} h_{sk}, \tag{3.13}$$

where: $h = \frac{1}{M}[U+pV]$ and

h_{sk} = source enthalpy.

Momentum is conserved using a junction to describe the flow from node K to node L. Junction inertia, differential nodal pressure, frictional resistance and elevation differences describe the junctions' temporal behavior.

$$I_j \frac{d}{dt} W_j = [(P_K - P_L) - \frac{K_j \, \text{Sign}(W_j) W_j^2}{2A_j^2 \rho_j} + \rho_j g \delta z_j] \quad . \quad (3.14)$$

This model formulation requires the solution of 4 ordinary differential equations (ODE) for each node and one ODE for each junction such that a system of I nodes and J junctions requires the simultaneous solution of $4I + J$ coupled rather stiff differential equations. The strong coupling suggests an implicit method is required in order to attain a stable solution. The particular implicit solution procedure was first introduced by Porsching et.al. The $4I + J$ system is formulated in a vector fashion with a state vector defined as follows:

$$\underline{y} = \begin{bmatrix} W_1 \\ \vdots \\ W_J \\ M_{a1} \\ \vdots \\ M_{aI} \\ M_{h1} \\ \vdots \\ M_{hI} \\ M_{w1} \\ \vdots \\ M_{wI} \\ U_1 \\ \vdots \\ U_I \end{bmatrix} . \tag{3.15}$$

and the system is described by:

$$\frac{d\underline{y}}{dt} = \underline{f}(\underline{y},t) . \tag{3.16}$$

A Taylor series expansion of the vector function, $\underline{f}$, including only first order terms and assuming a forward time difference for the left hand side is

$$\frac{\underline{y}^{n+1} - \underline{y}^{n}}{\delta t} = \underline{f}(\underline{y}^{n},t^{n}) + \frac{\partial \underline{f}}{\partial \underline{y}}\Big|_{\underline{y}^{n},t^{n}} (\underline{y}^{n+1} - \underline{y}^{n}) . \tag{3.17}$$

The terms of the Jacobian matrix are evaluated assuming the state variables are independent of each other. Under this constraint, the junction mass flow difference equation is

$$\frac{W_j^{n+1} - W_j^n}{\delta t} = \left[\frac{K_j \, \text{Sign}(W_j^n) w_j^n}{2A_j^2 I_j \rho_j^n}\right] (W_j^{n+1} - W_j^n)$$

$$+ \frac{1}{I_j}\left[\left(\frac{\partial P}{\partial M}\right)_K (M_K^{n+1} - M_K^n) - \left(\frac{\partial P}{\partial M}\right)_L (M_L^{n+1} - M_L^n)\right.$$

$$\left. + \left(\frac{\partial P}{\partial U}\right)_K (U_K^{n+1} - U_K^n) - \left(\frac{\partial P}{\partial U}\right)_L (U_L^{n+1} - U_L^n)\right]$$

$$+ \frac{1}{I_j}\left[P_K^n - P_L^n - \frac{K_j W_j^n |W_j^n|}{2A_j^2 \rho_j^n}\right] + \frac{\rho_j g \delta z_j}{I_j} \quad . \qquad (3.18)$$

The nodal mass and energy balances are of the form

$$\frac{M_i^{n+1} - M_i^n}{\delta t} = \sum_{j=\text{to junctions}} [(W_j^{n+1} - W_j^n) + W_j^n] - \sum_{j=\text{from junctions}} [(W_j^{n+1} - W_j^n) + W_j^n]$$

$$+ SM_i \qquad (3.19)$$

and

$$\frac{U_i^{n+1} - U_i^n}{\delta t} = \sum_{j=\text{to junctions}} [(W_j^{n+1} - W_j^n) + W_j^n] h_j -$$

$$- \sum_{j=\text{from junctions}} [(W_j^{n+1} - W_j^n) + W_j^n] h_i + SM_i h_s \quad . \qquad (3.20)$$

The mass and energy balances can be substituted into the junction equations to reduce the system to order J. The resulting matrix equation is

$$\underline{A}^n \, \underline{\Delta W}^n = \underline{B}^n \qquad (3.21)$$

where $\underline{A}$ is a J×J square coefficient matrix and $\underline{\Delta W}$ (= $\underline{W}^{n+1}-\underline{W}^{n}$) and $\underline{B}$ are vectors of length J. The matrix elements are

$$A_{jj} = 1 - \delta t\, F_j^n + \frac{\text{Sign}(W_j^n)\,\delta t^2}{I_j}\left[\left(\frac{\partial P}{\partial M}\right)_K + \left(\frac{\partial P}{\partial M}\right)_L + \left(\frac{\partial P}{\partial U}\right)_K h_j + \left(\frac{\partial P}{\partial U}\right)_L h_j\right], \qquad (3.22)$$

where $F_j^n = \left[\frac{K_j\ \text{sign}(W_j)\,W_j}{2\rho_j I_j A_j^2}\right]^n$ and

$$h_j = \begin{cases} h_K^n & \text{if } W_j^n \geq 0 \\ h_L^n & \text{if } W_j^n < 0 \end{cases}$$

$$A_{ij}\ _{i\neq j} = \frac{\delta t^2}{I_j}\left[F1\left(\left(\frac{\partial P}{\partial M}\right)_K + \left(\frac{\partial P}{\partial U}\right)_K h_{iK}\right) + F2\left(\left(\frac{\partial P}{\partial M}\right)_L + \left(\frac{\partial P}{\partial U}\right)_L h_{ik}\right)\right] \qquad (3.23)$$

where

$$F1 = \begin{cases} 0 \text{ if } W_i^n \text{ is not to or from K} \\ 1 \text{ if } W_i^n \text{ is from K} \\ -1 \text{ if } W_i^n \text{ is to K,} \end{cases}$$

$$F2 = \begin{cases} 0 \text{ if } W_i^n \text{ is not to or from L} \\ 1 \text{ if } W_i^n \text{ is to L} \\ -1 \text{ if } W_i^n \text{ is from L,} \end{cases}$$

$h_{iK} = \frac{1}{2}\left[(1+F1)h_K^n + (1-F1)\,h_L^n \text{ of junction i}\right]$ and

$h_{iL} = \frac{1}{2}\left[(1+F2)h_K^n \text{ of junction i} + (1-F2)h_L^n\right]$.

$$B_j = \frac{\delta t}{I_j}\left[P_K^n - P_L^n - \frac{K_j|W_j^n|W_j^n}{2\rho_j^n A_j^2} + \rho_j^n g\ \delta z_j\right]$$

$$+ \frac{\delta t^2}{I_j}\left[F_{1K} + F_{2K} - F_{1L} - F_{2L}\right] , \qquad (3.24)$$

where

$$F_{1x} = \sum_{k=1}^{3} \frac{\partial P_{xk}}{\partial M_{xk}} \left(SM_{xk} + \sum_{j=\text{to junctions}} x_{kj} W_j^n - \sum_{j=\text{from junctions}} x_{kj} W_j^n\right) ,$$

and

$$F_{2x} = \sum_{k=1}^{3} \frac{\partial P_{xk}}{\partial U_{xk}} \left(SM_{xk} h_{sxk} + \sum_{j=\text{to junctions}} x_{kj} W_j^n h_{jk}^n \right.$$

$$\left. - \sum_{j=\text{from junctions}} x_{jh} W_j^n h_{jkx}^n\right) .$$

The equation set must be closed with state relations in order to evaluate the various partial derivations of pressure. A mixture perfect gas law coupled with an assumption of a saturated liquid state leads to the following representative relations:

$$\left(\frac{\partial P}{\partial M}\right)_x = \frac{\partial}{\partial M_x} \frac{x_{gx} M_x R_x T_x}{V_{gx}} = \frac{x_{gx} R_x T_x}{V_{gx}} , \qquad (3.25)$$

$$x_{gx} \equiv \left[\frac{\rho_g}{\rho_g + \rho_\ell}\right]_x , \qquad (3.26)$$

$$R_x = x_{xa} R_a + x_{xh} R_h + x_{xs} R_s \qquad (3.27)$$

$$V_{gx} = V_x - \frac{\rho_{\ell x} V_x}{\rho_{fx}} = V_x[1 - \frac{\rho_{\ell x}}{\rho_{fx}}] \ , \tag{3.28}$$

$$(\frac{\partial P}{\partial U})_x = \frac{\partial}{\partial U_x} \frac{x_{gx} M_x R_x T_x}{V_{gx}} \ , \tag{3.29}$$

but we know

$$U_x = M_x[x_{xg} e_g + (1 - x_{xg}) e_\ell]$$

$$= M_x[x_g(x_a C_a T + x_h C_h T + x_s C_s T) + (1 - x_g)(e_{fo} + C_\ell T)]_x, \tag{3.30}$$

or

$$T_x = [\frac{U}{M} - (1 - x_g) e_{fo}]_x [x_g(x_a C_a + x_h C_h + x_s C_s - C_\ell) + C_\ell]_x^{-1}. \tag{3.31}$$

Hence the partial derivatives of P in relation U may be evaluated as

$$(\frac{\partial P}{\partial U})_x = \frac{x_{xg} R_x}{V_{gx}} [x_g(x_a C_a + x_h C_h + x_s C_s - C_\ell) + C_\ell]_x^{-1}. \tag{3.32}$$

The coefficient matrix assumes a general structure that need not be diagonally dominant and is therefore not amenable to iterative solution. In the case of a chain of nodes where one volume is connected to only its up and downstream neighbor the matrix takes on a block-like structure but in general containment problems the solution must rely on direct inversion using Gaussian elimination. The outcome of this calculation are the respective ΔW_j for each junction which

can be back-substituted into the nodal mass and energy balances to arrive at the updated nodal densities and temperatures. The definition of the actual nodal state given the possible presence of steam and water deserves additional comment but this discussion is delayed until the slower mixing transient model derivation.

3.2.3 Ancillary Model Development

Numerous additional models are required to fully define the problem solution. One is the ability to model hydrogen as a possible source material. This addition is dependent upon defining the thermodynamic characteristics of hydrogen. Once hydrogen is introduced, its effect on the mixture transport parameters such as thermal conductivity and viscosity must be considered. Development and definition of these properties are presented below. Following this discussion the effect of hydrogen on condensate film behavior as well as reasonable heat transfer modelling of this flow regime is addressed.

3.2.3.1 Thermodynamic and Transport Properties

Given that the state relations are based on a mixture of perfect gases, the required hydrogen thermodynamic values are molecular weight and relation between the specific heat and the gas constant. The molecular weight of hydrogen used is 2.0158 AMU which leads to a gas constant

of

$$R_H = \frac{R}{M_{H_2}} = 4124.58 \text{ m}^2/\text{sec}^2\text{°K} . \qquad (3.33)$$

The ratio C_p/R_H for hydrogen varies from 3.451 to 3.519 over a temperature range of 280 to 500°K according to Reference 70 and hence a value of 3.47 is utilized. Specific heat at constant volume is taken as 2.47 R (i.e. $C_p - R = C_v$). In accordance with the law of partial pressures, the overall state definition (assuming uniform temperatures) is

$$P = (\sum_i \rho_i R_i)T \quad \text{where } i = \text{gaseous components} \qquad (3.34)$$

The two transport parameters are molecular viscosity and thermal conductivity. The two properties are expressed as linear functions of temperature. The two curve fits based on a linear regression of experimental data are:

$$k_H^M = 0.03437 + 4.892 \times 10^{-4} \text{ T (W/m°K), and} \qquad (3.35)$$

$$\mu_H^M = 2.942 \times 10^{-6} + 2.002 \times 10^{-8} \text{ T (kg/m sec).} \qquad (3.36)$$

A comparison of these functional approximations and the actual data is provided in Table 3.1. As is seen the agreement is quite acceptable especially in the expected containment temperature range below 400°K (260°F).

3.2.3.2 Condensate Film and Heat Transfer

Very detailed condensate film modelling is available

TABLE 3.1: Comparison of Property Approximations vs. Data [70]

T (^{o}K)	k_H^M (W/m ^{o}K)		$\mu_H^M \times 10^6$ (kg/m sec)	
	EQUATION	DATA	EQUATION	DATA
280	0.171	0.171	8.548	8.554
300	0.181	0.181	8.948	8.958
350	0.206	0.205	9.949	9.942
500	0.279	0.272	12.952	12.242
AVERAGE ERROR	±1.3%		±1.2%	
AVERAGE ERROR w/o 500^{o}K DATA	±0.2%		±0.1%	

in BEACON such that the time dependent flow behavior of a film travelling along a solid surface can be predicted. The transfer of mass and energy at the film/bulk fluid interface is strongly determined by the local component profiles. As such the original film model is modified to account for the presence of hydrogen in this interfacial region. If the film model is employed, the heat transfer at the film/fluid boundary is computed on the basis of a mass/heat transfer analogy and the heat transfer at the boundary is computed using a film Nusselt number correlation. If a film is not modelled explicitly, the original code allows the use of three options -- input constant coefficients, coefficients based on vapor content or temperature or using a Stanton number correlation for a flat plate of the form:

$$St = \frac{(f/2)^{1/2}}{5P_r + 5\ell n(5P_r + 1) + (f/2)^{-1/2} - 14} . \qquad (3.37)$$

This overall approach seems too complex in the film modelling and oversimplified for heat transfer calculations. A more useful approach might be to include a heat transfer computation logic which is more typical of the expected regimes that incorporates condensation effects without resorting to a detailed film model. One promising approach is discussed by Covelli et al. [72] who propose a heat transfer coefficient which embodies both natural circulation and

condensation. The general form of this expression is

$$h = h_{NC} + C^{*}h_{C} \tag{3.38}$$

where C^{*} = function of condensation rate. Corradini [71] also reports a condensation model for both forced and natural convection based on extending the Reynolds-Colburn analogy to mass and momentum transfer.

3.2.4 Inherent Limitations of the Modified Code

A comparison of the desired capabilities of a hydrogen transport code with the characteristics of the program after this first series of modifications demonstrates that substantially more development is required. The so-called modified BEACON equation set can handle hydrogen as a third gaseous component but still subject to the overall assumptions and limitations of the original code. The use of these analytical models is restricted to rapid two-phase transients. The use of non-equilibrium thermodynamics is unwarranted in slower mixing transients and leads to inordinate amounts of computational effort. Clearly, the nested iteration aspects of a compressible flow solution should only be used when the problem demands it. Nevertheless, the model at this stage of development addresses important parts of the hydrogen scenario spectrum in its appropriate application to two-phase jet-like releases such as might occur from a pressure relief valve or the study of large interconnected rooms using a lumped-parameter approach.

The limitations of the modified code define the requirements for the slow mixing model described in the next section. Also addressed in the following discussions is the boundary of applicability between the two analytical models of continuum regions.

3.3 Longer Term Transient Modelling - MITHYD

While blowdown transients are dominated by two-phase compressibility effects, longer term transients, which involve the gradual build-up of hydrogen over an extended period (e.g. degrading core or radiolytic decomposition), are characterized by a nearly incompressible multi-component homogeneous flow field. The model formulation described in this section is based on this physical regime. Important effects include molecular and turbulent-driven transport as well as buoyancy-driven convection.

The basic theoretical formulation is first derived and specialized to the problems of interest. The model is based on a primitive variable formulation augmented by turbulence transport equations. The turbulence modelling is based on a 2 equation k-ε formulation employing seven empirically-derived closure constraints. The problem is complicated by the presence of a condensible species-water. Consistent thermodynamic state determination must be carefully considered. An assumption of interphasic equilibrium is made to formulate this approach.

The definition of the overall equation set is the first step in creating a model. The coupled set of non-linear partial differential equations is clearly not amenable to analytic closed form solution and hence a numerical technique is required. The solution scheme is based on a finite difference discretization of the continuum equations using a staggered computational grid. Given that physically diffusive phenomena are important, the numerical scheme should not introduce false diffusion. This usually arises from the treatment of convective terms in the conservation equations and hence a proper limited diffusion technique is needed.

The nearly incompressible assumption allows the solution of the momentum/continuity equations independently of the energy equation save for the feedback of buoyancy effects. At first glance one would assume that this allows the straightforward application of an established technique such as the SMAC method. However in buoyancy-dominated flow closer attention to the coupling is necessary. Once the flow field is computed, the remaining mass transport energy and turbulence equations must be solved. The solution of these equations involve accurate models of mass diffusion and nodal phase changes as well as reference state definition. A complete problem definition involves not only the prescription of the controlling equations but also a complete and consistent specification of initial and boundary conditions.

This is especially so in a discretized solution regime. Finally the underlying assumptions, especially that of incompressibility, need to be monitored in order to assure the solution remains within the appropriate physical bounds.

The following subsections elaborate in detail upon the points made above. The model has been implemented in a subcode named MITHYD. The MITHYD subcode is modular in structure as is further described in Appendix A. The computational coupling to the overall code is analogous to the role played by the K-FIX two phase flow subcode. In effect insofar as the slower mixing computations are concerned, the MITHYD subprogram uses the remaining portions of the code for data processing, ancillary effects calculations and input/output processing.

3.3.1 Basic Equation Formulation

The basic thermo-fluid dynamic equation set which constitutes the theoretical foundation of the slow mixing model is presented. Detailed equation derivations are omitted but may be found in standard transport phenomena texts such as Bird et al. [73]. The equations are presented first in vector notation so that individual terms can be addressed from a physical standpoint. They are then specialized to a 3-D cylindrical/Cartesian coordinate system. The equations are formulated such that a 2-D system can be solved. A 2-D formulation is compatible with the rapid transient

model and is expected to be used in the majority of applications. The three dimensional option is provided for problems in which such modelling complexity and computational effort is required.

The general fully compressible mass conservation or continuity equation without source effects is

$$\frac{\partial \rho}{\partial t} + \underline{\nabla}\cdot(\rho \underline{u}) = 0 \ . \tag{3.39}$$

If the incompressibility assumption is made, (3.39) may be simplified to

$$\cancelto{0}{\frac{\partial \rho}{\partial t}} + \rho \underline{\nabla}\cdot\underline{u} + \underline{u}\cancelto{0}{\underline{\nabla}\rho} = 0 \quad \text{or} \quad \underline{\nabla}\cdot\underline{u} = 0 \ . \tag{3.40}$$

The momentum equation is

$$\rho_r \left[\frac{\partial \underline{u}}{\partial t} + \underline{\nabla}\cdot(\underline{u}\,\underline{u}) \right] = - \underline{\nabla} P + \underline{\nabla}\cdot\hat{\underline{\sigma}} + \rho \underline{f} + f_D \ , \tag{3.41}$$

where $\hat{\underline{\sigma}} = \underline{\sigma}^M + \underline{\sigma}^T$.

The reference state density formulation is typical of the Boussinesq approximation. Physically the lefthand side (LHS) are the time rate of change of momentum and the convective momentum transport, respectively. The first right hand side (RHS) term is the pressure field gradient. The second term is the shear stress which embodies both molecular and turbulent mixing effects. The third term represents body forces which in this application are limited to gravity while the final term involves frictional and form losses

due to objects within the flow field. This term is included to account for gratings, small obstacles, structural members, etc.

The fully compressible mixture internal energy conservation equation is

$$\frac{\partial \rho e}{\partial t} + \underline{\nabla} \cdot \rho \underline{u} e = \underline{\nabla} \cdot \hat{k} \underline{\nabla} T - p \underline{\nabla} \cdot \underline{u} + \mu \Phi \ , \tag{3.42}$$

where $\hat{k} = k^M + k^T$, and

$\mu\Phi$ = viscous dissipation.

The incompressible formulation of the momentum equation leads to the neglection of the flow work term. The viscous dissipation term is assumed negligible in problems of interest. Omitting the flow work contribution is a reasonable approximation for situations in which convection is dominant and forces on the fluid are dominated by mass transport induced buoyancy (e.g. introduction of a light gas) or momentum sources (jet effects). Both conditions are satisfied in the slow mixing analysis. Therefore, the actual mixture energy equation utilized in the model is

$$\frac{\partial \rho e}{\partial t} + \underline{\nabla} \cdot \rho \underline{u} e = \underline{\nabla} \cdot \hat{k} \underline{\nabla} T \ . \tag{3.43}$$

The substantive derivative is kept in a conservative form to more accurately track the convective transport. In comparison with the BEACON energy equations, compressive work, viscous dissipation and non-equilibrium interphasic

transport are neglected. It may also be noted that if separate gaseous and liquid phase energy equations were used in the slow mixing model, an additional source term due to phase change energy absorption or liberation would have been required.

The single continuity equation is inadequate for tracking the transport of the individual species. Hence four additional mass transport equations are introduced. The general equation form equates the species substantive derivative to diffusion, source and phase change effects and has the form

$$\frac{\partial c_i}{\partial t} + \underline{\nabla}\cdot(\underline{u}c_i) = \underline{\nabla}\cdot\hat{D}_i\nabla c_i + \phi_i \ , \qquad (3.44)$$

where i = air, hydrogen, steam and liquid,

$D_i = D_i^M + D^T$, and

ϕ_i = phase change rate (for steam and water only).

The appropriateness of this equation for the three gaseous components is well-established. The phase change rate is calculated on the basis of a thermodynamic equilibrium assumption. The proper treatment of multi-component molecular diffusion is addressed below. Nevertheless the application of an equation of this form to liquid transport which would actually involve a spectrum of droplet sizes and speeds is not truly appropriate. It is used here as a first approximation and in anticipation of the development

of a more accurate spray model. This equation is valid if a no-slip assumption is made and diffusional effects are neglected (i.e., $\hat{D}_\ell = 0$). The discussion of computing turbulence effects is postponed until the next section. Clearly some prescription of this augmentation effect is required to partially close the analytical problem definition.

A pseudo-local mixture density is calculated using the saturated liquid density and the perfect gas law in the following form:

$$\tilde{\rho}_m = c_\ell \rho_f(T) + \frac{P_r}{T \sum_{i=\text{steam},H_2,\text{air}} R_i c_i} \tag{3.45}$$

This mixture density is only used to compute the relative buoyancy force due to compositional and temperature differences. It is not necessarily equal to the sum of local component densities which defines the true local density, i.e.

$$\rho_m = \rho_\ell + \rho_s + \rho_H + \rho_a \ . \tag{3.46}$$

The inconsistency arises from the perturbation nature of the Boussinesq or nearly incompressible assumption in which local density is calculated on the basis of a reference state. If the reference state was updated continuously to account for local state changes, the two mixture density definitions would be identical. However this would also imply that the momentum and energy equations must be

solved simultaneously completing the path back to a fully compressible formulation. The advantage of allowing this degree of inaccuracy is the ability to solve the two equations (and the individual component equations) independently. The error in the buoyancy term increases as the actual state departs from the assumed reference state. Periodic redefinition of the reference state can limit the magnitude of this error and is discussed in greater detail in the solution scheme subsection.

The fluid dynamic equations are now presented in a generalized 3-D formulation. The parameter β allows the equations to be descriptive of either cylindrical or Cartesian coordinates while the parameter λ is used to specialize the equations to either a 2 or 3 dimensional form. The logic of this specification is

λ \ β	0	1
0	2-D Cartesian	2-D axisymmetric
1	3-D Cartesian	3-D cylindrical

The coordinate system is shown in Figure 3.2.

The continuity equation is

$$\frac{1}{r^{\beta}} \frac{\partial}{\partial r} r^{\beta} u + \frac{\partial}{\partial t} v + \lambda \frac{1}{r^{\beta}} \frac{\partial w}{\partial \theta} = 0 \ . \qquad (3.47)$$

The vector momentum equation is decomposed into three scalar relations representing force balances along the principal axes of the appropriate coordinate system. The radial momentum equation is

$$\rho_r \left[\frac{\partial u}{\partial t} + \frac{\partial}{\partial r} u^2 + \frac{\partial}{\partial z} uv + \frac{\beta u^2}{r^\beta} + \frac{\lambda}{r^\beta} \frac{\partial}{\partial \theta} uw - \frac{\lambda \beta w^2}{r^\beta} \right] =$$

$$- \frac{\partial P}{\partial r} + \rho g_r + f_{Dr} + \frac{1}{r^\beta} \frac{\partial}{\partial r} \hat{\mu} r^\beta \frac{\partial u}{\partial r} + \frac{\partial}{\partial z} \hat{\mu} \frac{\partial u}{\partial z} + \frac{\partial \hat{\mu}}{\partial r} \frac{\partial u}{\partial r}$$

$$+ \frac{\partial \hat{\mu}}{\partial z} \frac{\partial v}{\partial r} - \frac{\beta \hat{\mu} u}{r^{2\beta}}$$

$$+ \lambda \left[\frac{1}{r^{2\beta}} \frac{\partial}{\partial \theta} \hat{\mu} \frac{\partial u}{\partial \theta} + \frac{1}{r^\beta} \frac{\partial \hat{\mu}}{\partial \theta} \left(\frac{\partial w}{\partial r} - \frac{\beta w}{r^\beta} \right) - \frac{2\beta \hat{\mu}}{r^{2\beta}} \frac{\partial w}{\partial \theta} \right]. \quad (3.48)$$

The formulation also accounts for spatial variation in viscosity. The axial or z-momentum balance is

$$\rho_r \left[\frac{\partial v}{\partial t} + \frac{\partial}{\partial r} uv + \frac{\partial}{\partial z} v^2 + \frac{\beta uv}{r^\beta} + \frac{\lambda}{r^\beta} \frac{\partial}{\partial \theta} vw \right] = - \frac{\partial P}{\partial z} + \rho g_z$$

$$+ f_{Dz} + \frac{1}{r^\beta} \frac{\partial}{\partial r} \hat{\mu} r^\beta \frac{\partial v}{\partial r} + \frac{\partial}{\partial z} \hat{\mu} \frac{\partial v}{\partial z} + \frac{\partial \hat{\mu}}{\partial r} \frac{\partial u}{\partial z} + \frac{\partial \hat{\mu}}{\partial z} \frac{\partial v}{\partial z}$$

$$+ \lambda \left[\frac{1}{r^{2\beta}} \frac{\partial}{\partial \theta} \hat{\mu} \frac{\partial v}{\partial \theta} + \frac{1}{r^\beta} \frac{\partial \hat{\mu}}{\partial \theta} \frac{\partial w}{\partial z} \right]. \quad (3.49)$$

Finally the optional third dimensional equation is

$$\lambda\rho_r \left[\frac{\partial w}{\partial t} + \frac{\partial}{\partial r} uw + \frac{1}{r^\beta} \frac{\partial}{\partial \theta} w^2 + \frac{\partial}{\partial z} wv + \frac{2\beta uw}{r^\beta} \right] =$$

$$\lambda \left\{ - \frac{1}{r^\beta} \frac{\partial P}{\partial \theta} + f_{D\theta} + \frac{1}{r^\beta} \frac{\partial}{\partial r} r^\beta \hat{\mu} \frac{\partial w}{\partial r} + \frac{1}{r^{2\beta}} \frac{\partial}{\partial \theta} \hat{\mu} \frac{\partial w}{\partial \theta} \right.$$

$$+ \frac{\partial}{\partial z} \hat{\mu} \frac{\partial w}{\partial z} + \frac{\beta \hat{\mu}}{r^{2\beta}} \left(2\frac{\partial u}{\partial \theta} - w\right) + \frac{1}{r^\beta} \frac{\partial \hat{\mu}}{\partial r} \left(\frac{\partial \hat{\mu}}{\partial \theta} - \beta w\right)$$

$$\left. + \frac{1}{r^{2\beta}} \frac{\partial \hat{\mu}}{\partial \theta} \left(\frac{\partial w}{\partial \theta} + 2\beta u\right) + \frac{1}{r^\beta} \frac{\partial \hat{\mu}}{\partial z} \frac{\partial v}{\partial \theta} \right\} . \qquad (3.50)$$

The θ-momentum equation does not contain a gravitational term since normal orientations are expected to be typical of containment problems. The energy and other transport equation can all be described by the following generalized form

$$\left[\frac{\partial \psi}{\partial t} + \frac{1}{r^\beta} \frac{\partial}{\partial r} r^\beta u\psi + \frac{\partial}{\partial z} v\psi + \frac{\lambda}{r^\beta} \frac{\partial}{\partial \theta} w\psi \right] =$$

$$\frac{1}{r^\beta} \frac{\partial}{\partial r} r^\beta \hat{\Gamma} \frac{\partial \psi}{\partial r} + \frac{\partial}{\partial z} \hat{\Gamma} \frac{\partial \psi}{\partial z} + \frac{\lambda}{r^{2\beta}} \frac{\partial}{\partial \theta} \hat{\Gamma} \frac{\partial \psi}{\partial \theta} + S_\psi . \qquad (3.51)$$

3.3.2 Turbulence Effects

Turbulent transport processes are a significant physical effect that must be addressed in slower mixing transients. The selection of a turbulence model is not a trivial task especially in this application. The multicomponent flow field is affected by buoyancy induced

convection arising from both local temperature and concentration perturbations. Also, the flow fields typical of enclosed region problems exhibit recirculating flow and local relaminarization or transitional flows. The general approach taken in this work is to utilize a so-called 'two-equation' turbulence model. These additional closure equations arise from the resolution of the Navier-Stokes equations into constant and time-varying components. The resultant new terms arise from the non-zero ensemble averaging of correlation functions. The reader is referred to a turbulence text such as Hinze [74] for more detailed derivations.

The form of the turbulence model used in this model is already suggested by the diffusion terms in the various conservation equations in which the molecular transport coefficient is augmented by an effective turbulent diffusivity. The implicit assumption is that turbulent transport can be related to the gradient of the transported property as is the case for molecular effects. Early attempts at computing the value of this turbulent or eddy diffusivity employed either constants based on the pioneering arguments of Boussinesq or a single equation model such as Prandtl's mixing length. Though simplicity and reduced reliance on empiricism are attractive features of a mixing length argument, the actual definition of a single length scale descriptive of transport through a recircu-

lating flow is physically unrealizable. Most current models utilize two-equation closure models as an acceptable compromise between accuracy and effort. There are much more complex models which basically involve transport equations for higher order correlation functions. Unfortunately utilization of such models requires even more empirically derived closure constants which in turn render the model less general. Further the computational effort increases unboundedly. To quote Launder and Spalding: 'the proponents of the most detailed turbulence models have themselves been armchair explorers.'

Numerous two-equation models have been proposed. Most involve the behavior of the turbulent kinetic energy and turbulent viscosity (k-σ models) or turbulent kinetic energy and its dissipation (k-ε models). Launder and Spalding argue from a physical standpoint that the k-ε models are more appropriate but both classes of models seem to be useful. As alluded to above, turbulent kinetic energy and its dissipation are analytical constructs of correlation terms originating from the Navier-Stokes equations. In terms of the primitive variables the two turbulence parameters are

$$k \equiv \frac{1}{2} < u'u' >, \text{ and} \tag{3.52}$$

$$\xi \equiv \frac{\mu^M}{\rho} < \frac{\partial u_i}{\partial x_k} \frac{\partial u_i}{\partial x_k} > . \tag{3.53}$$

Lumley [48] comments that the name, dissipation, is

somewhat misleading since the quantity embodied in this correlation is only incidentally the dissipation. It is more correctly the rate at which energy enters the spectrum of smaller scale eddies which eventually decay via molecular processes.

The two closure equations along with the assumed closure constants are essentially based on the previously referenced work of Launder and Spalding but augmented in terms of buoyant production using a formulation suggested by Rodi [49]. The turbulent kinetic energy equation is

$$\rho_r\left[\frac{\partial k}{\partial t} + \underline{\nabla}\cdot\underline{u}k\right] = P_k + G_k + D_k - \rho\xi \ , \qquad (3.54)$$

where P_k = shear production

$$= \mu^T\left[2\left(\frac{\partial u_i}{\partial x_i}\right)^2 + \left(\frac{\partial u_i}{\partial x_j}\right)^2\right] \text{ (tensor notation)}$$

$$\text{or} = \mu^T\Bigg\{2\left[\left(\frac{\partial u}{\partial r}\right)^2 + \left(\frac{\partial v}{\partial z}\right)^2 + \left(\frac{\lambda}{r^\beta}\frac{\partial w}{\partial \theta} + \frac{\beta u}{r^\beta}\right)^2\right]$$

$$+ \left(\frac{\partial u}{\partial z} + \frac{\partial v}{\partial r}\right)^2 + \lambda\left[\left(\frac{1}{r^\beta}\frac{\partial u}{\partial \theta} + \frac{\partial w}{\partial r} - \frac{\beta w}{r^\beta}\right)^2\right.$$

$$\left. + \left(\frac{\partial w}{\partial z} + \frac{1}{r^\beta}\frac{\partial w}{\partial \theta}\right)^2\right]\Bigg\} \text{ (cylindrical coordinates)}$$

$$G_k = \text{buoyant production} = g f_i \mu^T (Sc^T)^{-1} \frac{\partial \bar{\rho}}{\partial x_i}$$

$$= g_r \frac{\mu^T}{Sc^T}\left[g_r \frac{\partial \rho}{\partial r} + g_z \frac{\partial \rho}{\partial z} + g_\theta \frac{\partial \rho}{r^\beta \partial \theta}\right] \ , \text{ and}$$

$$D_k = \text{diffusion of } k = \underline{\nabla}\cdot(\mu^M + \frac{\mu^T}{\sigma_k})\underline{\nabla}k, \text{ or}$$

$$= \frac{1}{r^\beta}\frac{\partial}{\partial r} r^\beta(\mu^M + \frac{\mu^T}{\sigma_k})\frac{\partial k}{\partial r} + \frac{\partial}{\partial z}(\mu^M + \frac{\mu^T}{\sigma_k})\frac{\partial k}{\partial z}$$

$$+ \frac{\lambda}{r^2\beta}\frac{\partial}{\partial\theta}(\mu^M + \frac{\mu^T}{\sigma_k})\frac{\partial k}{\partial\theta} .$$

The buoyant production term is not the standard expression found in single component k-ε models. The standard approach is to use the temperature gradients as a surrogate for density gradients. The method proposed here is more correct since the multicomponent nature of the field is taken into account. Due to the lack of experimental evidence a turbulent Sc of 1.0 is suggested.

The dissipation equation is

$$\rho_r\left[\frac{\partial\xi}{\partial t} + \underline{\nabla}\cdot\underline{u}\xi\right] = \frac{\xi}{k}(C_{\xi 1}P_k + C_{\xi 3}G_k) - \rho C_{\xi 2}\frac{\xi^2}{k} + D_\xi, \quad (3.55)$$

$$\text{where } D_\xi = \text{diffusion of } \xi = \underline{\nabla}\cdot(\mu^M + \frac{\mu^T}{\sigma_\xi})\underline{\nabla}\xi$$

$$\text{or} = \frac{1}{r^2\beta}\frac{\partial}{\partial r} r^\beta(\mu^M + \frac{\mu^T}{\sigma_\xi})\frac{\partial\xi}{\partial r} + \frac{\partial}{\partial z}(\mu^M + \frac{\mu^T}{\xi})\frac{\partial\xi}{\partial z}$$

$$+ \frac{\lambda}{r^2\beta}\frac{\partial}{\partial\theta}(\mu^M + \frac{\mu^T}{\sigma_\xi})\frac{\partial\xi}{\partial\theta} .$$

Six free constants requi_e definition in order to close the model and they are specified in Table 3.2.

TABLE 3.2 Turbulence Model Constants

$\sigma_T = 0.9$	$C_{\xi_1} = 1.44$
$\sigma_K = 1.0$	$C_{\xi_2} = 1.92$
$\sigma_\xi = 1.3$	$C_{\xi_3} = 1.44$

The eddy diffusivity is computed using the Prandtl-Kolmolgorov hypothesis:

$$\mu^T = \frac{C_\mu \rho k^2}{\xi} \quad , \tag{3.56}$$

where C_μ is assumed to be 0.09. The mass and energy transport coefficients are computed using user-defined turbulent Prandtl and Schmidt numbers.

3.3.3 Mass Diffusion

The multicomponent flow field necessitates the accurate modelling of diffusional mass transport. The component diffusivities are composed of both molecular and turbulent factors such that

$$\hat{D}_i = D_i^M + D^T \quad . \tag{3.57}$$

The turbulent mass diffusivity is independent of component type since turbulent transport is a property of the flow field not the species. According to the formulation of Wilke [75], the multicomponent molecular diffusion constant for a mixture of gases is described by

$$D_i^M = \frac{1 - C_i}{\sum_{j \neq i} C_j / D_{ji}^M} . \qquad (3.58)$$

Bird et al. provide the following prescription for the binary diffusion constants.

$$D_{ji}^M = \frac{1.8583 \times 10^{-7} \sqrt{T^3 \left(\frac{1}{M_j} + \frac{1}{M_i}\right)}}{p \sigma_{ji}^2 \, \Omega_{D,ji}} \qquad (3.59)$$

where $D_{ji}^M = m^2/sec$,

M = molecular weight,

p = pressure (atm),

T = temperature (^oK), and

Ω = empirical constant, function of temperature and binary components

Using the applicable factors for the three possible binary combinations (air-hydrogen, steam-hydrogen and steam-air) the binary coefficients were fit to curves of the following functional form:

$$D_{ah} = 4.9492 \times 10^{-5} \, T^{1.6947} , \qquad (3.60)$$

$$D_{hs} = 2.8916 \times 10^{-5} \, T^{1.8144} , \text{ and} \qquad (3.61)$$

$$D_{as} = 4.681 \times 10^{-6} \, T^{1.9035} . \qquad (3.62)$$

These approximate curves are compared with the analytical values in Figure 3.3. The agreement is quite good over the expected temperature range. In problems in which

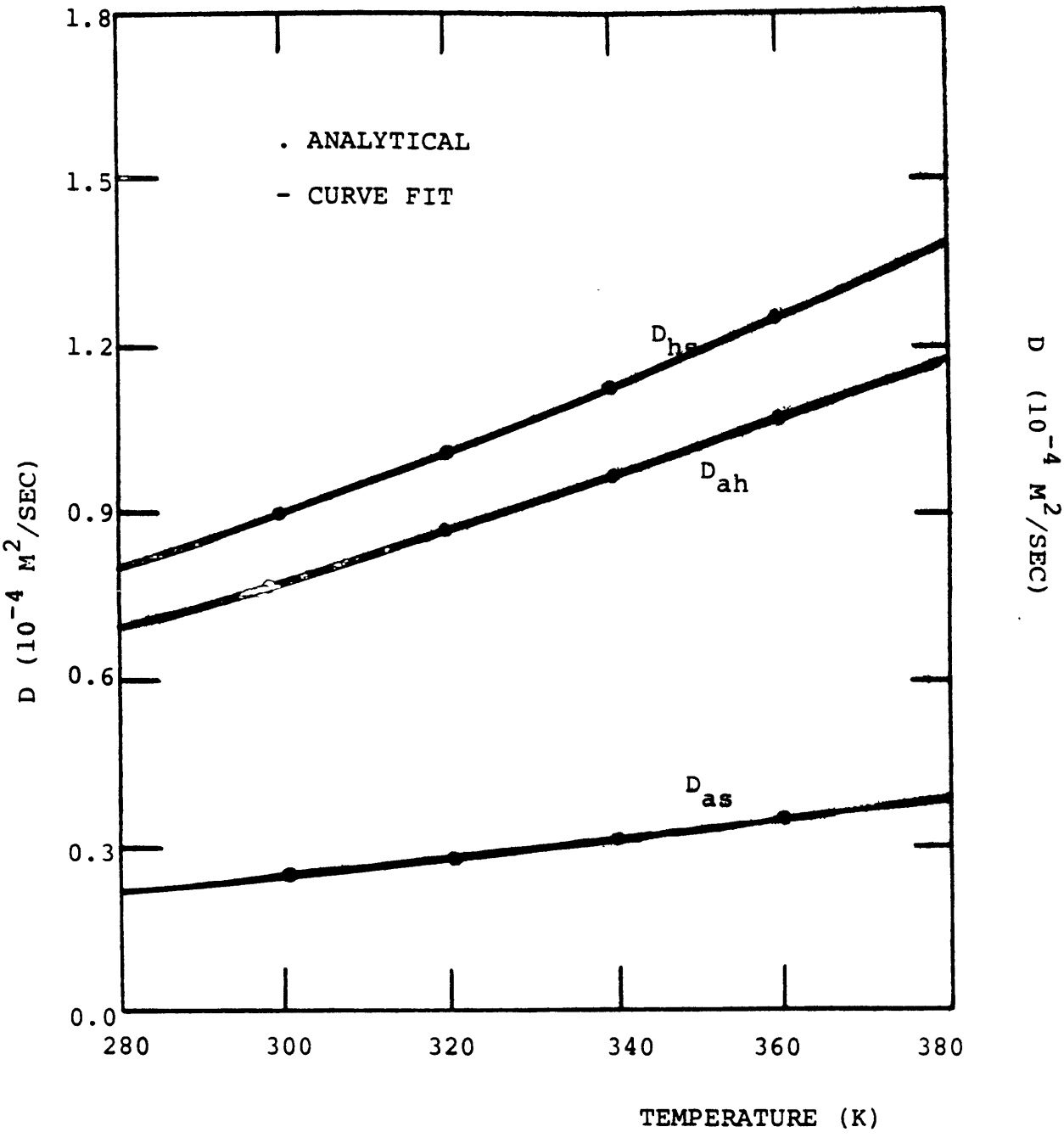

FIGURE 3.3: MOLECULAR BINARY DIFFUSIVITIES AT ATMOSPHERIC PRESSURE

molecular effects are unimportant a constant component-specific diffusion constant may be employed.

As stated in the turbulence modelling discussion, turbulent mass diffusivity is computed on the basis of the turbulent viscosity and a user-supplied reciprocal turbulent Schmidt number. (1.0 is the suggested value for most simulations.) This leads to

$$D^T = (Sc^T)^{-1} \nu^T = \frac{1}{\rho Sc^T} \frac{\rho C_\mu k^2}{\xi}$$

or

$$D^T = \frac{C_\mu k^2}{Sc^T \xi} . \qquad (3.63)$$

3.3.4 Solution Scheme

The set of non-linear partial differential equations and constituent relations which define the slower mixing analytical model are not amenable to closed form solution without substantial simplification. Therefore a numerical solution technique is formulated. An overview of the solution scheme is provided in Figure 3.4. The continuum is discretized into a computational mesh exemplified by Figure 3.2. This staggered mesh arrangement of variable definition in which all cell parameters except momentum are cell-centered while the cell momenta fluxes are defined at cell boundaries is typical of Marker and Cell (MAC) type algorithms.

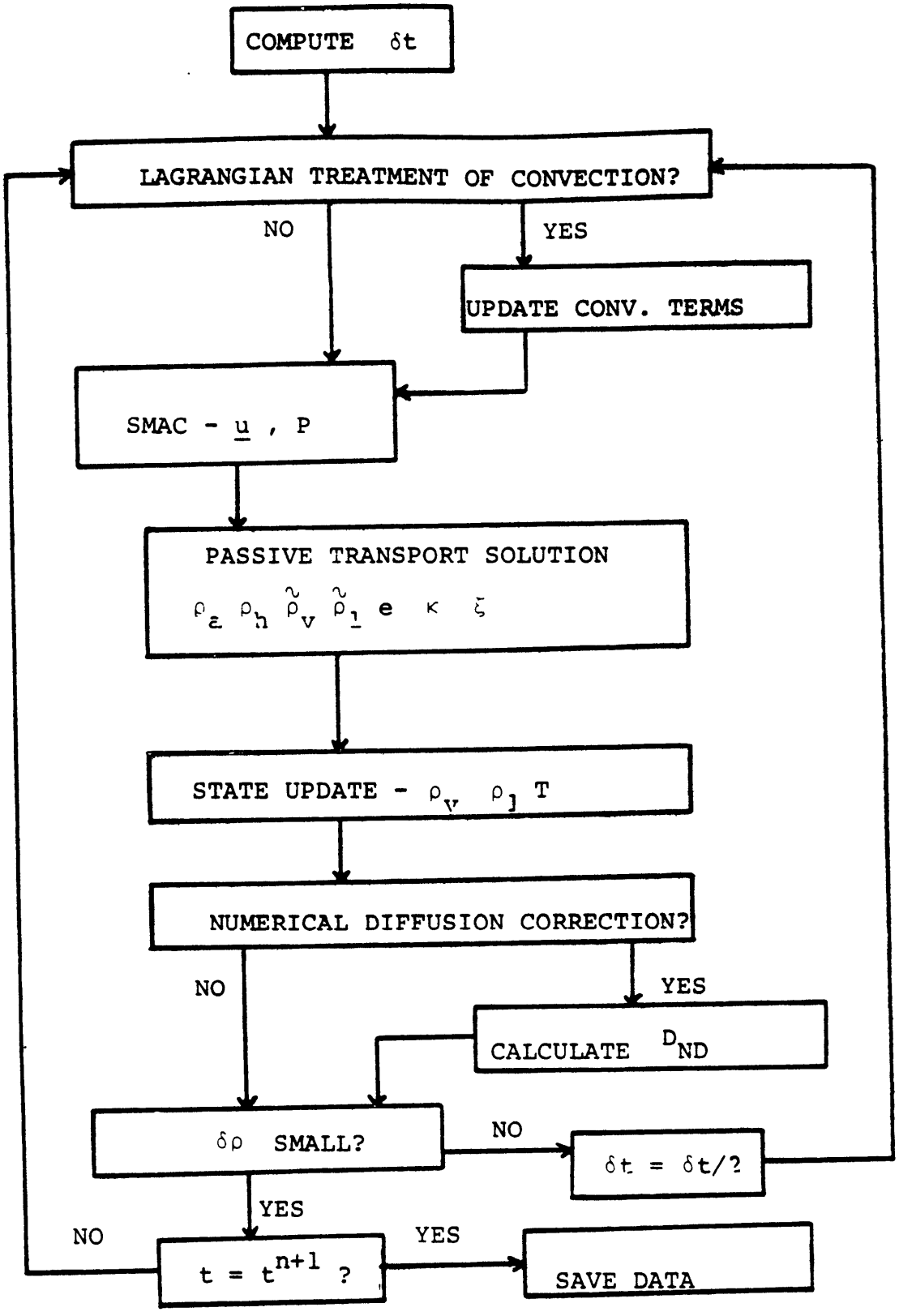

FIGURE 3.4: BASIC SLOW MIXING SOLUTION LOGIC

Given that the pertinent transients are such that physically diffusive mechanisms are important, the numerical scheme should not introduce false diffusion due to its discretization. The convective terms are most susceptible to this limitation and must be formulated accordingly. Irregardless of the convective treatment, the incompressible assumption allows the nearly decoupled solution of the conservation equations. The continuity/momentum solution is accomplished using a 3-D form of the modified Simplified Marker and Cell (SMAC) method. Once the updated velocity and local pressure fields are computed, the remaining conservation equations can be solved. These equations are solved with either an explicit or implicit technique depending upon particular stability constraints. The liquid and steam transport equations must be solved neglecting the condensation/evaporation contribution since the value of this term is determined by the local state which itself depends upon the local mass fractions. The knowledge of the local mixture energy and total mass density coupled with a thermodynamic state constraint is used to define the local temperature and phase change rate.

The solution of any set of partial differential equations requires the complete and consistent definition of initial and boundary conditions. With the addition of new flow variables such as turbulent parameters, proper initial condition definition must be addressed. New boundary conditions

for the turbulence parameters and the optional three dimensional flow field need definition. Finally, given the underlying incompressibility assumption, the solution methodology should have internal validity checks to assure the physical appropriateness of the technique. These various facets of the scheme are now described in more detail.

3.3.4.1 Treatment of Convection and Numerical Diffusion

The discretization of the continuum equations gives rise to inaccuracies in the computed solution when compared to exact analytical results. One important source of error is false or numerical diffusion. This false diffusion arises from the treatment of advection terms and manifests itself by producing distributions in which the entity is transported further in the normal direction (to the flow) than can be accounted for by physical processes. The donor cell treatment of convection exhibits significant numerical diffusion. The donor cell logic is described by

$$\frac{\partial u\psi}{\partial x} \simeq \frac{u_+\psi^* - u_-\psi^{**}}{\delta x} , \tag{3.64}$$

where u_+, u_- = velocities defined at cell boundaries,

$$\psi^* = \begin{cases} \psi \text{ of the cell if } u_+ \geq 0 \\ \psi \text{ of the right cell if } u_+ < 0, \text{ and} \end{cases}$$

$$\psi^{**} = \begin{cases} \psi \text{ of the left cell if } u_{-} \geq 0 \\ \psi \text{ of the cell if } u_{-} < 0. \end{cases}$$

Huh [39] has described the errors associated with this approach in terms of truncation and cross-flow errors. Crossflow diffusion is especially important in recirculation problems when velocity vectors problems where velocity vectors substantially deviate from the orthogonal mesh coordinate system. Huh has quantified the equivalent diffusion constant due to the donor cell treatment as follows:

$$D_r = u\ \delta r\ (1 - P_r)\ , \tag{3.65}$$

$$D_z = v\ \delta z\ (1 - P_z)\ , \tag{3.66}$$

$$D_\theta = w\ r^{\beta} \delta\theta\ (1 - P_\theta)\ , \tag{3.67}$$

where

D_i = directional diffusivity,

P_i = directional cell Peclet number

$$= \frac{u_i/\delta x_i}{\sum_{i=1}^{3} u_i/\delta x_i}$$

The donor cell treatment is seen to increase in accuracy as cell spacing is decreased.

The good stability characteristics and the conservative nature of the donor cell treatment makes it the primary treatment of convection. Nevertheless, applications may arise in which coarser nodalizations are desirable. For such situations, two possible corrective schemes are

proposed. The first and most appropriate for transient problems is to subtract the local numerical diffusion constant from the local physical diffusivity. The reader is referred to the original work for a detailed consideration of the stability constraints of this approach. In brief, not all the numerical diffusion can be corrected and the approximate correction made is

$$D_{total} = D_{physical} - SF\ D_{ND}\ , \tag{3.68}$$

where

SF = safety factor.

A second alternative is provided but its application to transient problems is not recommended. The technique treats the convection terms in a Lagrangian manner while the remaining diffusive and source terms are treated in a Eulerian orientation. This work is related to that of Raithby [43] and Stukley et al. [76]. In effect each conservation equation is solved in a two step fashion as depicted by the following generalized formulation.

$$\frac{\partial \psi}{\partial t} + \underline{\nabla}\cdot\underline{u}\psi = \underline{\nabla}\cdot\hat{\Gamma}\underline{\nabla}\psi + S_{\psi} \tag{3.69}$$

is replaced by

$$\frac{\tilde{\psi} - \psi^{n}}{\delta t} + \underline{\nabla}\cdot\underline{u}\psi = 0 \quad \text{and} \tag{3.70}$$

$$\frac{\psi^{n+1} - \tilde{\psi}}{\delta t} = \underline{\nabla}\cdot\hat{\Gamma}\underline{\nabla}\psi + S_{\psi}\ . \tag{3.71}$$

The first equation which is purely convective

is solved using the new scheme while the solution of the second class of equations is accomplished using the explicit/implicit method described below.

The Lagrangian scheme intuitively involves a coordinate transformation to the trajectory of the convected entity over the time step. This trajectory will nearly always intersect a location for which the entity is not defined and therefore some sort of spatial interpolation to arrive at a useable value. Of course in situations in which the intersecting location lies outside the physical domain, the donor cell scheme is used. This is not a major weakness since in this boundary region flows more closely follow grid directions. The most significant weakness of this type of Lagrangian approach is its non-conservative nature. A complete understanding of the inaccuracies arising from utilizing such an approach are not fully appreciated at this time.

3.3.4.2 Flow and Pressure Fields

The Simplified Marker and Cell (SMAC) method introduced by Harlow and Amsden is used to solve the momentum/continuity equation set. The exact form of the solution scheme is described in some detail herein because the complete formulation of the technique applicable to a general non-uniform three dimensional cylindrical mesh is derived. Most available references on the SMAC method

are usually limited to uniform 2-D meshes.

The first step in the method is computation of an estimated or 'tilde' velocity field based on a completely explicit advancement of the component momentum equations. The form of the drag term is assumed to be

$$f_{DX} = -K_x |u_x|^n u_x^{n+1} . \tag{3.72}$$

Using this form the three tilde velocities are specified. In order to streamline the notation the following subscripting logic is employed:

if no subscript $u \rightarrow u_{i+\frac{1}{2}jk}$,

$v \rightarrow v_{ij+\frac{1}{2}k}$,

$w \rightarrow w_{ijk+\frac{1}{2}}$, and

$\psi \rightarrow \psi_{ijk}$

Only deviations from this are shown

e.g. $u_{i-\frac{1}{2}} = u_{i-\frac{1}{2}jk}$.

The r-direction tilde velocity is

$$\tilde{u} = \frac{1}{1 + \frac{\delta t K_r |u|^n}{\rho_r}} \left\{ u^n + \frac{\delta t}{\rho_r}\left[- \frac{\partial P}{\partial r} + \rho g_r + \frac{1}{r^\beta} \frac{\partial}{\partial r} \hat{\mu} r^\beta \frac{\partial u}{\partial r} + \frac{\partial}{\partial z} \hat{\mu} \frac{\partial u}{\partial z} \right.\right.$$

$$+ \frac{\partial \hat{\mu}}{\partial r} \frac{\partial u}{\partial r} + \frac{\partial \hat{\mu}}{\partial z} \frac{\partial v}{\partial r} - \frac{\beta \hat{\mu} u}{r^{2\beta}} + \frac{\lambda}{r^{2\beta}} \frac{\partial}{\partial \theta} \hat{\mu} \frac{\partial u}{\partial \theta} + \frac{\lambda}{r^\beta} \frac{\partial \hat{\mu}}{\partial \theta} \left(\frac{\partial w}{\partial r} - \frac{\beta w}{r^\beta}\right)$$

$$\left. - \frac{2\beta \hat{\mu} \lambda}{r^{2\beta}} \frac{\partial w}{\partial \theta} - \frac{\rho_r \beta u^2}{r^\beta} + \frac{\lambda \rho_r \beta w^2}{r^\beta} \right]^n - \delta t \left[\frac{\partial}{\partial r} u^2 + \frac{\partial}{\partial z} uv \right.$$

$$\left. \left. + \frac{\lambda}{r^\beta} \frac{\partial}{\partial \theta} uw \right]^n \right\} , \tag{3.73}$$

where

$$-\frac{\partial P}{\partial r} \simeq \frac{2}{\delta r_+}(P-P_{i+1}) \quad , \tag{3.74}$$

$$\rho g_r \simeq \frac{\rho_{i+1}+\rho-2\rho_r}{2} g \quad , \tag{3.75}$$

$$\frac{1}{r^\beta}\frac{\partial}{\partial r}\hat{\mu} r^\beta \frac{\partial u}{\partial r} \simeq \frac{2}{\delta r_+ (r+\frac{\partial r}{2})}\left[\frac{\hat{\mu}_{i+1} r^\beta_{i+1}(u_{i+\frac{3}{2}}-u)}{\delta r_{i+1}} - \frac{\mu r^\beta (u-u_{i-\frac{1}{2}})}{\delta r}\right], \tag{3.76}$$

$$\frac{\partial}{\partial z}\hat{\mu}\frac{\partial u}{\partial z} \simeq \frac{1}{\delta z}\left[\frac{(\hat{\mu}_{i+1}+\hat{\mu})(u_{j+1}-u)}{\delta z_+} - \frac{(\hat{\mu}+\hat{\mu}_{i-1})(u-u_{j-1})}{\delta z_-}\right], \tag{3.77}$$

$$\frac{\partial \hat{\mu}}{\partial r}\frac{\partial u}{\partial r} \simeq \frac{\hat{\mu}_{i+1}-\hat{\mu}}{\delta r_+}\left[\frac{u_{i+\frac{3}{2}}-u}{\delta r_{i+1}} + \frac{u-u_{i-\frac{1}{2}}}{\delta r}\right] \quad , \tag{3.78}$$

$$\frac{\partial \hat{\mu}}{\partial z}\frac{\partial v}{\partial r} \simeq \frac{1}{4\delta z}\left[\frac{1}{\delta r_+}(v_{i+1}-v+v_{i+1j-\frac{1}{2}}-v_{j-\frac{1}{2}}) \cdot (\hat{\mu}_{j+1}+\hat{\mu}_{i+1j+1}-\hat{\mu}_{i-1j}-\hat{\mu}_{i+1j-1})\right] \quad , \tag{3.79}$$

$$\frac{-\beta\hat{\mu}u}{r^{2\beta}} \simeq \frac{-\beta u}{(r+\frac{\delta r}{2})^{2\beta}}\left[\frac{\hat{\mu}_{i+1}+\hat{\mu}}{2}\right] \quad , \tag{3.80}$$

$$\frac{\lambda}{r^{2\beta}}\frac{\partial}{\partial\theta}\hat{\mu}\frac{\partial u}{\delta\theta} \simeq \frac{2\lambda}{(r+\frac{\delta r}{2})^{2\beta}\delta\theta}\left[\frac{\hat{\mu}(u_{k+1}-u_k)}{\delta\theta_+} - \frac{\hat{\mu}_{k-1}(u-u_{k-1})}{\delta\theta_-}\right] \tag{3.81}$$

$$\frac{\lambda}{r^{\beta}}\frac{\partial\hat{\mu}}{\partial\theta}\left(\frac{\partial w}{\partial r}-\frac{\beta w}{r^{\beta}}\right) \simeq \left[\frac{\lambda(\hat{\mu}-\hat{\mu}_{k-1})}{(r+\frac{\delta r}{2})^{\beta}\delta\theta}\right.\quad \frac{(w_{i+1}+w_{i+1k-\frac{1}{2}})-(w+w_{k-\frac{1}{2}})}{\delta r_{+}}$$

$$\left.-\frac{\beta}{2(r+\frac{\delta r}{2})^{\beta}}\quad SR2(w_{i+1}-w_{i+1k-\frac{1}{2}})+SR1(w+w_{k-\frac{1}{2}})\right], \quad (3.82)$$

$$\frac{2\beta\hat{\mu}\lambda}{r^{2\beta}}\frac{\partial w}{\delta\theta} \simeq \frac{\lambda\beta(\hat{\mu}+\hat{\mu}_{j-1})}{(r+\frac{\delta r}{2})^{\beta}\delta\theta}\left[\ SR2(w_{i+1}-w_{i+1k-\frac{1}{2}})+SR1(w-w_{k-\frac{1}{2}})\right] ,$$

(3.83)

$$-\frac{\rho_r\beta u^2}{r^{\beta}} \simeq -\frac{\beta\rho_r u^2}{r^{\beta}} , \quad (3.84)$$

$$-\frac{\lambda\rho_r\beta w^2}{r^{\beta}} \simeq \frac{\lambda\rho_r\beta}{(r+\frac{\delta r}{2})^{\beta}}\left[\ SR2(w_{i+1k-\frac{1}{2}}+w_{i+1})+SR1(w_{k-\frac{1}{2}}+w)\ \right]^2 ,$$

(3.85)

$$\frac{\partial}{\partial r}u^2 \simeq \frac{1}{2\delta r_{+}}\left[\ \left|u_{i+\frac{3}{2}}+u\right|(u-u_{i+\frac{3}{2}}) + \left|u_{i-\frac{1}{2}}+u\right|(u-u_{i-\frac{1}{2}})\right.$$

$$\left.+\ u^2_{i+\frac{3}{2}} - u^2_{i-\frac{1}{2}} + 2u(u_{i+\frac{3}{2}}-u_{i-\frac{1}{2}})\ \right] , \quad (3.86)$$

$$\frac{\partial}{\partial z}uv \simeq \frac{1}{2\delta z}\quad \left|SR2v_{i+1}+SR1v\right|(u-u_{j+1})$$

$$+\ \left|SR2v_{i+1j-\frac{1}{2}}SR1v_{j-\frac{1}{2}}\right|(u-u_{j-1})$$

$$+\ (SR2v_{i+1}+SR1v)(u+u_{j+1})$$

$$-\ (SR2v_{i+1j-\frac{1}{2}}+SR1v_{j-\frac{1}{2}})(u+u_{j-1})\ ] , \quad (3.87)$$

$$\frac{\lambda}{r^{\beta}}\frac{\partial}{\partial\theta}uw \simeq \frac{\lambda}{(r+\frac{\delta r}{2})^{\beta}}\Big[\Big|SR2w_{i+1}+SRw\Big|(u-u_{k+1})$$

$$+\Big|SR2w_{i+1k-\frac{1}{2}}+SR1w_{k-\frac{1}{2}}\Big|(u-u_{k-1})$$

$$+\ (SR2w_{i+1}+SR1w)(u+u_{k+1})$$

$$-\ (SR2w_{i+1k-\frac{1}{2}}+SR1w_{k-\frac{1}{2}})(u+u_{k-1})\ \Big]\ , \qquad (3.88)$$

$$\delta x_{+/-} = \delta x + \delta x_{i+1/i-1}\ , \qquad (3.89)$$

$$SR1 = \delta r_{i+1}/\delta r_{+}\ , \qquad (3.90)$$

and

$$SR2 = \delta r/\delta r_{+}\ . \qquad (3.91)$$

The z-direction tilde velocity estimate is

$$\tilde{v} = \frac{1}{1+\frac{\delta t k^{z}|v|^{n}}{\rho_r}}\Bigg\{v^{n} + \frac{\delta t}{\rho_r}\Big[-\frac{\partial P}{\partial z} + \rho g_z + \frac{1}{r^{\beta}}\frac{\partial}{\partial r}r^{\beta}\hat{\mu}\frac{\partial v}{\partial r} + \frac{\partial}{\partial z}\hat{\mu}\frac{\partial v}{\partial z}$$

$$+\ \frac{\partial\hat{\mu}}{\partial r}\frac{\partial u}{\partial z} + \frac{\partial\hat{\mu}}{\partial z}\frac{\partial v}{\partial z} + \frac{\lambda}{r^{2\beta}}\frac{\partial}{\partial\theta}\hat{\mu}\frac{\partial v}{\partial\theta} + \frac{\lambda}{r^{\beta}}\frac{\partial\hat{\mu}}{\partial\theta}\frac{\partial w}{\partial z} - \frac{\rho_r\beta uv}{r^{\beta}}\Big]^{n}$$

$$-\ \delta t\Big[\frac{\partial}{\partial r}uv + \frac{\partial}{\partial z}v^{2} + \frac{\lambda}{r^{\beta}}\frac{\partial}{\partial\theta}vw\Big]^{n}\Bigg\}\ , \qquad (3.92)$$

where

$$-\frac{\partial P}{\partial z} \simeq -\frac{2}{\delta z_{+}}\ [P-P_{j+1}]\ , \qquad (3.93)$$

$$f_{gz} \simeq\ [\rho_{j+1}+\rho-2\rho_r]\ \frac{g}{2}\ , \qquad (3.94)$$

$$\frac{1}{r^{\beta}}\frac{\partial}{\partial r}r^{\beta}\hat{\mu}\frac{\partial v}{\partial r} \simeq \frac{2(r+\frac{\delta r}{2})^{\beta}}{r^{\beta}\delta r}\Big[\frac{\hat{\mu}^{+}(v_{i+1}-v)}{\delta r_{+}} - \frac{\hat{\mu}^{-}(v-v_{i-1})}{\delta r_{-}}\Big], \qquad (3.95)$$

$$\mu^{+} = \tfrac{1}{4}[\hat{\mu}+\hat{\mu}_{j+1}+\hat{\mu}_{i+1j+1}+\hat{\mu}_{i+1}] \ , \tag{3.96}$$

$$\mu^{-} = \tfrac{1}{4}[\hat{\mu}+\hat{\mu}_{j+1}+\hat{\mu}_{i-1j+1}+\hat{\mu}_{i-1j}] , \tag{3.97}$$

$$\frac{\partial}{\partial z}\hat{\mu}\frac{\partial v}{\partial z} \simeq \frac{2}{\delta z_{+}} \left[\frac{\hat{\mu}_{j+1}(v_{j+\frac{3}{2}}-v)}{\delta z_{j+1}} - \frac{\hat{\mu}(v-v_{j-\frac{1}{2}})}{\delta z} \right] , \tag{3.98}$$

$$\frac{\partial \hat{\mu}}{\partial r}\frac{\partial u}{\partial z} \simeq \frac{2}{\delta z_{+}} \left[(u_{j+1}-u+u_{i-\frac{1}{2}j+1}-u_{i-\frac{1}{2}}) \cdot \left(\frac{\hat{\mu}_{i+1j+1}+\hat{\mu}_{i+1}-\hat{\mu}_{j+1}-\hat{\mu}}{\delta r_{+}} - \frac{\hat{\mu}+\hat{\mu}_{j+1}-\hat{\mu}_{i-1j+1}-\hat{\mu}_{i-1j}}{\delta r_{-}}\right)\right] , \tag{3.99}$$

$$\frac{\partial v}{\partial z}\frac{\partial \hat{\mu}}{\partial z} \simeq \frac{2}{\delta z_{+}^{2}}(v_{j+\frac{3}{2}}-v_{j-\frac{1}{2}})(\hat{\mu}_{j+1}-\hat{\mu}) \ , \tag{3.100}$$

$$\frac{\lambda}{r^{2\beta}}\frac{\partial}{\partial \theta}\hat{\mu}\frac{\partial v}{\partial \theta} \simeq \frac{\lambda 2}{r^{2\beta}\delta\theta}\left[\frac{\hat{\mu}(v_{k+1}-v)}{\delta\theta_{+}} - \frac{\hat{\mu}_{k-1}(v-v_{k-1})}{\delta\theta_{-}}\right] , \tag{3.101}$$

$$\frac{\lambda}{r^{\beta}}\frac{\partial \hat{\mu}}{\partial \theta}\frac{\partial w}{\partial z} \simeq \frac{\mu-\mu_{k-1}}{r^{\beta}\delta\theta}\left[\frac{w_{j+1}+w_{j+1k-\frac{1}{2}}-w-w_{k-\frac{1}{2}}}{\delta z_{+}}\right] , \tag{3.102}$$

$$-\frac{\rho_r \beta uv}{r^{\beta}} \simeq -\frac{\rho_r \beta}{4} v[u+u_{j+1}+u_{i-\frac{1}{2}j+1}+u_{i-\frac{1}{2}}] , \tag{3.103}$$

$$\begin{aligned}\frac{\partial}{\partial r}uv \simeq \frac{1}{2\delta r}[& \left|Sz2u_{j+1}+Szlu\right|(v-v_{i+1}) \\ & + \left|Sz2u_{i-\frac{1}{2}j+1}+Szlu_{i-\frac{1}{2}}\right|(v-v_{i-1}) \\ & + (Sz2u_{j+1}+Szlu)(v+v_{i+1}) \\ & - (Sz2u_{i-\frac{1}{2}j+1}+Szlu_{i-\frac{1}{2}})(v+v_{i-1})] \ ,\end{aligned} \tag{3.104}$$

$$\frac{\partial}{\partial z}v^2 \simeq \frac{1}{2\delta z_+}\left[\left|v_{j+\frac{3}{2}}+v\right|(v-v_{j+\frac{3}{2}}) + \left|v_{j-\frac{1}{2}}+v\right|(v-v_{j-\frac{1}{2}}) + v^2_{j+\frac{3}{2}} - v^2_{j-\frac{1}{2}} + 2v(v_{j+\frac{3}{2}}-v_{j-\frac{1}{2}})\right] , \tag{3.105}$$

$$\frac{\lambda}{r^\beta}\frac{\partial}{\partial\theta}vw \simeq \frac{\lambda}{2r^\beta\delta\theta}\left[\left|Sz2w_{j+1}+Szlw\right|(v-v_{k+1}) + \left|Sz2w_{j+1k-\frac{1}{2}}+Szlw_{j-1}\right|(v-v_{k-1}) + (Sz2w_{j+1}+Szlw)(v+v_{k+1}) - (Sz2w_{j+1k-\frac{1}{2}}+Szlw_{j-1})(v+v_{k-1})\right] , \tag{3.106}$$

$$Szl \simeq \delta z_{j+1}/\delta z_+ , \tag{3.107}$$

and

$$Sz2 \simeq \delta z_j/\delta z_+ . \tag{3.108}$$

Finally, the optional third dimension tilde velocity is

$$\tilde{w} = \frac{\lambda}{1+\frac{\delta t k^\theta |w|^n}{\rho_r}}\left\{w^n + \frac{\delta t}{\rho_r}\left[-\frac{1}{r}\frac{\partial P}{\partial\theta} + \frac{1}{r^\beta}\frac{\partial}{\partial r}r^\beta\hat{\mu}\frac{\partial w}{\partial r} + \frac{1}{r^{2\beta}}\frac{\partial}{\partial\theta}\hat{\mu}\frac{\partial w}{\partial\theta} + \frac{\partial}{\partial z}\hat{\mu}\frac{\partial w}{\partial z} + \frac{\beta\hat{\mu}}{r^{2\beta}}(2\frac{\partial u}{\partial\theta}-w) + \frac{1}{r^\beta}\frac{\partial\hat{\mu}}{\partial r}(\frac{\partial u}{\partial\theta}-\beta w) + \frac{1}{r^{2\beta}}\frac{\partial\hat{\mu}}{\partial\theta}(\frac{\partial w}{\partial\theta} + 2\beta u) + \frac{1}{r^\beta}\frac{\partial\hat{\mu}}{\partial z}\frac{\partial v}{\partial\theta} - \frac{2\rho_r\beta uw}{r^\beta}\right]^n - \delta t\left[\frac{\partial}{\partial r}uw + \frac{1}{r^\beta}\frac{\partial}{\partial\theta}w^2 + \frac{\partial}{\partial z}vw\right]^n\right\}, \tag{3.109}$$

where $$\frac{1}{r^\beta}\frac{\partial P}{\partial\theta} \simeq \frac{2}{r^\beta\delta\theta_+}\left[P_{k+1}-P\right] , \tag{3.110}$$

$$\frac{1}{r^{\beta}}\frac{\partial}{\partial r}r^{\beta}\hat{\mu}\frac{\partial w}{\partial \theta} \simeq \frac{2}{r^{\beta}\delta r}\left[\frac{\hat{\mu}(r+\frac{\delta r}{2})^{\beta}(w_{i+1}-w)}{\delta r_{+}} - \frac{\hat{\mu}_{i-1}(r-\frac{\delta r}{2})^{\beta}(w-w_{i-1})}{\delta r_{-}}\right] \tag{3.111}$$

$$\frac{1}{r^{2\beta}}\frac{\partial}{\partial \theta}\hat{\mu}\frac{\partial w}{\partial \theta} \simeq \frac{2}{r^{2\beta}\delta\theta_{+}}\left[\frac{\hat{\mu}_{k+1}(w_{k+\frac{3}{2}}-w)}{\delta\theta_{k+1}} - \frac{\hat{\mu}(w-w_{k-\frac{1}{2}})}{\delta\theta}\right], \tag{3.112}$$

$$\frac{\partial}{\partial z}\hat{\mu}\frac{\partial w}{\partial z} \simeq \frac{2}{\partial z}\left[\frac{\hat{\mu}(w_{j+1}-w)}{\delta z_{+}} - \frac{\hat{\mu}_{j-1}(w-w_{j-1})}{\delta z_{-}}\right], \tag{3.113}$$

$$\frac{\beta\hat{\mu}}{r^{2\beta}}(2\frac{\partial u}{\partial \theta}-w) \simeq \frac{\beta(\hat{\mu}+\hat{\mu}_{i-1})}{r^{2\beta}}\left[\frac{(u_{k+1}+u_{i-\frac{1}{2}k+1}-u-u_{i-\frac{1}{2}})}{\delta\theta_{+}} - \frac{w}{2}\right] \tag{3.114}$$

$$\frac{1}{r^{\beta}}\frac{\partial\hat{\mu}}{\partial r}(\frac{\partial u}{\partial \theta}-\beta w) \simeq \frac{(\hat{\mu}+\hat{\mu}_{i-1})}{r^{\beta}\delta r}\left[\frac{u_{k+1}+u_{i-\frac{1}{2}k+1}-u-u_{i-\frac{1}{2}}}{\delta\theta_{+}} - \beta w\right] \tag{3.115}$$

$$\frac{1}{r^{2\beta}}(\frac{\partial w}{\partial \theta}+2\beta u)\frac{\partial\hat{\mu}}{\partial\theta} \simeq \frac{2(\hat{\mu}_{j+1}-\hat{\mu})}{r^{2\beta}\delta\theta_{+}}\left(\frac{S\theta 2 w_{k+\frac{3}{2}}}{\delta\theta_{k+1}} - \frac{S\theta 1 w_{k-\frac{1}{2}}}{\delta\theta} - \frac{S\theta_{k+1}-S\theta_{k}}{\delta\theta_{k+1}\delta\theta_{k}}w\right)$$
$$+ \beta(S\theta 2(u_{k+1}+u_{i-\frac{1}{2}k+1}) + S\theta 1(u+u_{i+\frac{1}{2}})), \tag{3.116}$$

$$\frac{1}{r^{\beta}}\frac{\partial\hat{\mu}}{\partial z}\frac{\partial v}{\partial\theta} \simeq \frac{\mu-\mu_{j-1}}{r^{\beta}\partial z}\left[\frac{v_{k+1}+v_{j-\frac{1}{2}k+1}-v-v_{j-\frac{1}{2}}}{\delta\theta_{+}}\right], \tag{3.117}$$

$$\frac{2\rho_{r}\beta uw}{r^{\beta}} \simeq \frac{w\rho_{r}\beta}{r^{\beta}}[S\theta 2(u_{k+1}+u_{i-\frac{1}{2}k+1}) + S\theta 1(u+u_{i-\frac{1}{2}})], \tag{3.118}$$

$$\frac{\partial}{\partial r}uw \simeq \frac{1}{2\partial r}[\left|S\theta 2u_{k+1}+S\theta 1u\right|(w-w_{i+1})$$
$$+ \left|S\theta 2u_{i-\frac{1}{2}k+1}+S\theta 1u_{i-\frac{1}{2}}\right|(w-w_{i-1})$$
$$+ (S\theta 2u_{k+1}+S\theta 1u)(w+w_{i+1})$$
$$- (S\theta 2u_{i-\frac{1}{2}k+1}+S\theta 1u_{i-\frac{1}{2}})\ (w+w_{i-1})\ ]\ , \qquad (3.119)$$

$$\frac{1}{r^{\beta}}\frac{\partial}{\partial\theta}w^2 \simeq \frac{1}{2r^{\beta}\delta\theta_{+}}[\left|w_{k+\frac{3}{2}}+w\right|(w-w_{k+\frac{3}{2}}) + \left|w_{k-\frac{1}{2}}+w\right|(w-w_{k-\frac{1}{2}})$$
$$+ w^2_{k+\frac{3}{2}} - w^2_{k-\frac{1}{2}} + 2w(w_{k+\frac{3}{2}}-w_{k-\frac{1}{2}})\ ], \qquad (3.120)$$

$$\frac{\partial}{\partial z}vw \simeq \frac{1}{2\delta z}\ [\left|S\theta 2v_{k+1}+S\theta 1v\right|(w-w_{j+1})$$
$$+ \left|S\theta 2v_{j-\frac{1}{2}k+1}+S\theta 1v_{j-\frac{1}{2}}\right|(w-w_{j-1})$$
$$+ (S\theta 2v_{k+1}+S\theta 1v)(w+w_{j+1})$$
$$- (S\theta 2v_{j-\frac{1}{2}k+1}+S\theta 1v_{j-\frac{1}{2}})(w+w_{j-1})\ ]\ , \qquad (3.121)$$

$$S\theta 1 = \delta\theta_{k+1}/\delta\theta_{+}\ \text{, and} \qquad (3.122)$$

$$S\theta 2 = \delta\theta/\delta\theta_{+}\ . \qquad (3.123)$$

These difference equations are for an internal mesh point. A discussion of the treatment of boundary cells is postponed until section 3.3.4.5.

The resultant tilde velocity field will not usually satisfy the continuity constraint, i.e.,

$$D \equiv \underline{\nabla}\cdot\underline{u} \simeq \frac{(r+\frac{\delta r}{2})^{\beta}\tilde{u}-(r-\frac{\delta r}{2})^{\beta}\tilde{u}_{i-\frac{1}{2}}}{r^{\beta}\delta r} + \frac{\tilde{v}-\tilde{v}_{j-\frac{1}{2}}}{\delta z}$$

$$+ \frac{\lambda(w-w_{k-\frac{1}{2}})}{r^{\beta}\delta\theta} \neq 0 \ . \qquad (3.124)$$

The velocity field is modified by adjusting the local pressure to produce a zero divergence (actually a small non-zero value) field. This pressure correction is formulated in the following manner. First if the gradient of the vector momentum equation is taken and viscous and higher order velocity derivatives are neglected, the resulting equation is

$$\underline{\nabla}\cdot\frac{\partial\underline{u}}{\partial t} = -\frac{1}{\rho}\nabla^2 P$$

or

$$\frac{\partial}{\partial t}\underline{\nabla}\cdot\underline{u} = -\frac{1}{\rho}\nabla^2 P$$

or

$$\frac{\partial D}{\partial t} = -\frac{1}{\rho}\nabla^2 P \ . \qquad (3.125)$$

Rewriting (3.125) in a finite difference formulation yields

$$\rho\frac{D^n-D^{n+1}}{\partial t} = \frac{2}{r^{\beta}\delta r}\left[\frac{r^{\beta}_{i+\frac{1}{2}}(P_{i+1}-P)}{\delta r_+} - \frac{r^{\beta}_{i-\frac{1}{2}}(P-P_{i-1})}{\delta r_-}\right]$$

$$+ \frac{2}{\delta z}\left[\frac{P_{j+1}-P}{\delta z_+} - \frac{P-P_{j-1}}{\delta z_-}\right] + \frac{2\lambda}{r^{2\beta}}\left[\frac{P_{k+1}-P}{\delta\theta_+} - \frac{P-P_{k-1}}{\delta\theta_-}\right] \ . \qquad (3.126)$$

(Here n represents iteration number.)

An iterative correction scheme is established by assuming that only a pressure correction for the (i,j,k) cell is computed and setting D^{n+1} equal to zero; this yields

$$\delta P\, \delta t = -\rho B D^{n} , \tag{3.127}$$

where

$$B = 2 \left[\frac{1}{\delta r} \frac{r^{\beta}_{i+\frac{1}{2}} \delta r_{-} + r^{\beta}_{i-\frac{1}{2}} \delta r_{+}}{r^{\beta} \delta r_{+} \delta r_{-}} + \frac{1}{\delta z} \frac{\delta z_{-} + \delta z_{+}}{\delta z_{+} \delta z_{-}} + \frac{1}{r^{2\beta} \delta\theta} \frac{\delta\theta_{-} + \delta\theta_{+}}{\delta\theta_{-} \delta\theta_{+}} \right]^{-1} \tag{3.128}$$

The iteration can usually be made more quickly convergent by utilizing a selective over-relaxation procedure such that B is multiplied by a factor ranging from 1 to 2. The velocity components are iteratively corrected using the pressure field corrections using the following algorithm:

$$\tilde{u} = \tilde{u} - \frac{2}{\rho \delta r_{+}} \frac{\delta P \delta t}{1+\delta t K^{r} |u|} , \tag{3.129}$$

$$\tilde{v} = \tilde{v} - \frac{2}{\rho \delta z_{+}} \frac{\delta P \delta t}{1+\delta t K^{z} |v|} , \text{ and} \tag{3.130}$$

$$\tilde{w} = \tilde{w} - \frac{2}{r^{\beta} \rho \delta\theta_{+}} \frac{\delta P \delta t}{1+\delta t K^{\theta} |w|} . \tag{3.131}$$

The iteration is continued until the condition

$$\max|D_{ijk}| < \varepsilon \qquad (3.132)$$

is satisfied where ε is a user specified small number.

3.3.4.3 Transport Equations

Once the velocity field at the new time is ascertained, the remaining transport equations are solved. The accurate and efficient solution of these equations is particularly important because of their coupling to the momentum equation through the body force term. Before proceeding to the exact form of the solution procedure, an important but subtle aspect of the equation coupling is addressed.

A simplified form of the incompressible conservation equation describing the transport of a passive entity is

$$\rho_r \left[\frac{\partial \psi}{\partial t} + \underline{\nabla} \cdot \underline{u} \psi \right] = (\mathrm{LHS})_\psi \quad , \qquad (3.133)$$

which upon expansion yields

$$\rho_r \left[\frac{\partial \psi}{\partial t} + \underline{u} \underline{\nabla} \psi \right] = (\mathrm{LHS})_\psi - \rho_r \psi (\underline{\nabla} \cdot \underline{u}) \quad . \qquad (3.134)$$

In a completely divergence free velocity field the final term would be exactly zero. Unfortunately, the SMAC procedure yields a flow field that exhibits small cell divergences such that an error of order $\rho_r \psi \varepsilon$ results. In most applications this is not significant but in problems involving a slowly changing density field must be

considered. Consider that an ε of 10^{-4} causes a buoyancy error equivalent to a velocity of 10^{-3} m/sec in an air environment. This can easily be of the same order of magnitude as a slowly injected hydrogen source.

The solution of course is to reduce the error until it becomes insignificant. One option is to set a tight convergence criterion (i.e., small $|\varepsilon|$) in the SMAC solution. However, there are physical situations in which this is not possible. For example, in a problem involving a net volumetric inflow, the absolute value of the total field divergence is equal to the net inflow as the following development demonstrates.

$$\int_V D \, dV = \int_V (\underline{\nabla} \cdot \underline{u}) dV = \int_{SA} \underline{u} \cdot d\underline{A} = \text{NET INFLOW} \ , \qquad (3.135)$$

or in discrete terms, the SMAC iteration has a lower bound such that

$$\sum_{\text{all cells}} D_{\text{cell}} \, V_{\text{cell}} \geq \text{NET INFLOW} \ . \qquad (3.136)$$

Further the computational effort of attaining very small divergences may be substantial. These considerations motivate the development of an alternative.

First, consider the fully compressible transport equation

$$\frac{\partial \rho \psi}{\partial t} + \underline{\nabla} \cdot \rho \psi \underline{u} = (\text{LHS})_{\psi} \ . \qquad (3.137)$$

Assume ρ and ψ can be described by a perturbation analysis which is reasonable in these nearly incompressible

flows, i.e.,

$$\rho = \rho_r + \rho' \text{ , and} \tag{3.138}$$

$$\psi = \psi_r + \psi' \text{ .} \tag{3.139}$$

Substitution yields

$$\frac{\partial}{\partial t}\rho_r\psi_r + \frac{\partial}{\partial t}\rho_r\psi' + \frac{\partial}{\partial t}\rho'\psi_r + \frac{\partial}{\partial t}\rho'\psi' +$$
$$(\rho_r\psi_r + \rho'\psi_r + \rho_r\psi' + \rho'\psi')\underline{\nabla}\cdot\underline{u} +$$
$$\underline{u}(\underline{\nabla}\rho_r\psi_r + \underline{\nabla}\rho'\psi_r + \underline{\nabla}\rho_r\psi' + \underline{\nabla}\rho'\psi') = (\text{LHS})_\psi \text{ .} \tag{3.140}$$

Ignoring the products of perturbations, taking into account the spatial independence of reference conditions and simplifying results in the expression:

$$\rho_r \frac{\partial\psi'}{\partial t} + \underline{\nabla}\cdot\underline{u}\psi' = (\text{LHS})_\psi - \frac{\partial}{\partial t}\psi_r(\rho_r+\rho') - \psi'\frac{\partial\rho'}{\partial t}$$
$$- \psi_r[(\rho_r+\rho')\underline{\nabla}\cdot\underline{u} + \underline{u}\underline{\nabla}\rho'] \text{ .} \tag{3.141}$$

This equation can be further simplified by using a perturbation analysis of the fully compressible continuity equation.

$$\frac{\partial\rho}{\partial t} + \underline{\nabla}\cdot\rho\underline{u} = 0 \text{ ,} \tag{3.142}$$

which after simplification yields:

$$\underline{\nabla}\cdot\underline{u} = \frac{1}{\rho_r+\rho'}\frac{\partial\rho_r}{\partial t} + \frac{\partial\rho'}{\partial t} + \underline{u}\nabla\rho' \text{ .} \tag{3.143}$$

Using this relation and the identity $\psi' = \psi - \psi_r$ in (3.141)

results in

$$\rho_r \left[\frac{\partial \psi}{\partial t} + \underline{\nabla} \cdot \underline{u} \psi \right] = (\text{LHS})_\psi + \rho_r \psi_r \underline{\nabla} \cdot \underline{u} - \rho' \frac{\partial \psi_r}{\partial t} - \psi' \frac{\partial \rho_r}{\partial t} \quad . \tag{3.144}$$

The form of this equation suggests a correction may be added to the original incompressible equation to counteract the non-zero divergence. In most problems only the first correction is required and hence the actual equations to be solved are of the form

$$\rho_r \left[\frac{\partial \psi}{\partial t} + \underline{\nabla} \cdot \underline{u} \psi \right] = (\text{LHS})_\psi + \rho_r \psi_r (\underline{\nabla} \cdot \underline{u}) \quad , \tag{3.145}$$

where the final term is treated as a source term in the solution procedure since the divergence is already known at the time of the conservation equation solution. There are problems in which this first order correction is not sufficient but these problems are truly compressible in nature and should be solved accordingly.

The solution procedure is described for a general equation form which can be easily specialized to the entity of interest:[1]

$$\rho_r \left[\frac{\partial \psi}{\partial t} + \frac{\partial}{\partial r} u\psi + \frac{\partial}{\partial z} v\psi + \frac{\lambda}{r^\beta} \frac{\partial}{\partial \theta} w\psi + \frac{\beta u \psi}{r^\beta} \right] =$$

$$\frac{1}{r^\beta} \frac{\partial}{\partial r} r^\beta \hat{\Gamma} \frac{\partial \psi}{\partial r} + \frac{\partial}{\partial z} \hat{\Gamma} \frac{\partial \psi}{\partial z} + \frac{\lambda}{r^{2\beta}} \frac{\partial}{\partial \theta} \hat{\Gamma} \frac{\partial \psi}{\partial \theta} + S_\psi \quad . \tag{3.146}$$

This equation is cast into a discrete form utilizing the following information. First, if the Lagrangian treatment

[1] Appendix E addresses the energy equation solution.

of convection is utilized prior to this step in the procedure, the advective terms are dropped and the previous value of a parameter is described by

$$\text{old value} \equiv \overset{\circ}{\psi} = (1-C)\psi^n + C\tilde{\psi} \ , \tag{3.147}$$

where $C = 0$ if donor cell logic is employed, and

$\tilde{\psi}$ = value of ψ calculated in Lagrangian step.

Second, the donor cell logic implies the following definitions:

$$\frac{\partial}{\partial r}u\psi \simeq \frac{1}{2\delta r}\left[u\left[\left(1+\frac{u}{|u|}\right)\psi + \left(1-\frac{u}{|u|}\right)\psi_{i+1}\right] - u_{i-\frac{1}{2}}\left[\left(1+\frac{u_{i-\frac{1}{2}}}{|u_{i-\frac{1}{2}}|}\right)\psi_{i-1} + \left(1-\frac{u_{i-\frac{1}{2}}}{|u_{i-\frac{1}{2}}|}\right)\psi\right]\right] , \tag{3.148}$$

$$\frac{\partial}{\partial z}v\psi \simeq \frac{1}{2\delta z}\left[v\left[\left(1+\frac{v}{|v|}\right)\psi + \left(1-\frac{v}{|v|}\right)\psi_{j+1}\right] - v_{j-\frac{1}{2}}\left[\left(1+\frac{v_{j-\frac{1}{2}}}{|v_{j-\frac{1}{2}}|}\right)\psi_{j-1} + \left(1-\frac{v_{j-\frac{1}{2}}}{|v_{j-\frac{1}{2}}|}\right)\psi\right]\right] , \tag{3.149}$$

and

$$\frac{1}{r^\beta}\frac{\partial w\psi}{\partial \theta} \simeq \frac{1}{2r^\beta\delta\theta}\left[w\left[\left(1+\frac{w}{|w|}\right)\psi + \left(1-\frac{w}{|w|}\right)\psi_{k+1}\right] - w_{k-\frac{1}{2}}\left[\left(1+\frac{w_{k-\frac{1}{2}}}{|w_{k-\frac{1}{2}}|}\right)\psi_{k-1} + \left(1-\frac{w_{k-\frac{1}{2}}}{|w_{k-\frac{1}{2}}|}\right)\psi\right]\right] . \tag{3.150}$$

Third, the diffusional terms are represented by

$$\frac{1}{r^{\beta}}\frac{\partial}{\partial r}r^{\beta}\hat{\Gamma}\frac{\partial\psi}{\partial r} \simeq \frac{1}{r^{\beta}\delta r}\left[\frac{(r+\frac{\delta r}{2})^{\beta}(\hat{\Gamma}_{i+1}+\hat{\Gamma})(\psi_{i+1}-\psi)}{\delta r_{+}}\right.$$

$$\left. - \frac{(r-\frac{\delta r}{2})^{\beta}(\hat{\Gamma}+\hat{\Gamma}_{i-1})^{\beta}(\psi-\psi_{i-1})}{\delta r_{-}}\right] , \qquad (3.151)$$

$$\frac{\partial}{\partial z}\hat{\Gamma}\frac{\partial\psi}{\partial r} \simeq \frac{1}{\delta z}\left[\frac{(\hat{\Gamma}_{j+1}+\hat{\Gamma})(\psi_{j+1}-\psi)}{\delta z_{+}} - \frac{(\hat{\Gamma}+\hat{\Gamma}_{j-1})(\psi-\psi_{j-1})}{\delta z_{-}}\right], \qquad (3.152)$$

and

$$\frac{\lambda}{r^{2\beta}}\frac{\partial}{\partial\theta}\hat{\Gamma}\frac{\partial\psi}{\partial\theta} \simeq \frac{\lambda}{r^{2\beta}\delta\theta}\left[\frac{(\hat{\Gamma}_{k+1}+\hat{\Gamma}_{k})(\psi_{k+1}-\psi)}{\delta\theta_{+}} - \frac{(\hat{\Gamma}+\hat{\Gamma}_{k-1})(\psi-\psi_{k-1})}{\delta\theta_{-}}\right] . \qquad (3.153)$$

Finally, each value of ψ is treated in a variable implicit/explicit manner such that

$$\psi = F\psi^{n+1} + (1-F)\overset{\circ}{\psi} , \qquad (3.154)$$

where F = degree of implicitness ($0 \leq F \leq 1$).

Using these prescriptions, the generalized conservation equation's discrete form is

$$\rho_{r}\left[\frac{\psi^{n+1}-\overset{\circ}{\psi}}{\delta t} + (1-C)\left[\frac{1}{\delta r}[\alpha_{+}F\psi^{n+1} + \alpha_{+}(1-F)\psi^{n} + \beta_{+}F\psi^{n+1}_{i+1}\right.\right.$$

$$+ \beta_{+}(1-F)\psi^{n}_{i+1} - \alpha_{-}F\psi^{n+1}_{i-1} - \gamma_{-}(1-F)\psi^{n}_{i-1} - \beta_{-}F\psi^{n+1} + \beta_{-}(1-F)\psi^{n}]$$

$$+ \frac{1}{\delta z}[\gamma_{+}F\psi^{n+1} + \gamma_{+}(1-F)\psi^{n} + \delta_{+}F\psi^{n+1}_{j+1} + \delta_{+}(1-F)\psi^{n}_{j+1}$$

$$\left.\left. - \gamma_{-}F\psi^{n+1}_{j-1} - \gamma_{-}(1-F)\psi^{n}_{j-1} - \delta_{-}F\psi^{n+1} - \delta_{-}(1-F)\psi^{n}] +\right.\right.$$

$$+ \frac{1}{r^{\beta}\delta\theta}\left[\varepsilon_+ F\psi^{n+1} + \varepsilon_+(1-F)\psi^n + \sigma_+ F\psi^{n+1}_{k+1} + \sigma_+(1-F)\psi^n_{k+1}\right.$$

$$- \varepsilon_- F\psi^{n+1}_{k-1} - \varepsilon_-(1-F)\psi^n_{k-1} - \sigma_- F\psi^{n+1} - \sigma_-(1-F)\psi^n]$$

$$+ \frac{\beta}{2r^{\beta}}\left[F(\alpha_+ + \beta_-)\psi^{n+1} + (1-F)(\alpha_+ + \beta_-)\psi^n + F\beta_+\psi^{n+1}_{i+1}\right.$$

$$\left.\left. + (1-F)\beta_+\psi^n_{i+1} + F\alpha_-\psi^{n+1}_{i-1} + (1-F)\alpha_-\psi^n_{i-1}]\right]\right] =$$

$$\Delta\Gamma_{r+}[F\psi^{n+1}_{i+1} + (1-F)\mathring{\psi}_{i+1} - F\psi^{n+1} - (1-F)\mathring{\psi}]$$

$$- \Delta\Gamma_{r-}[F\psi^{n+1} + (1-F)\mathring{\psi} - F\psi^{n+1}_{i-1} - (1-F)\mathring{\psi}_{i-1}]$$

$$+ \Delta\Gamma_{z+}[F\psi^{n+1}_{j+1} + (1-F)\mathring{\psi}_{j+1} - F\psi^{n+1} - (1-F)\mathring{\psi}]$$

$$- \Delta\Gamma_{z-}[F\psi^{n+1} + (1-F)\mathring{\psi} - F\psi^{n+1}_{j-1} - (1-F)\mathring{\psi}_{j-1}]$$

$$+ \lambda\Delta\Gamma_{\theta+}[F\psi^{n+1}_{k+1} + (1-F)\mathring{\psi}_{k+1} - F\psi^{n+1} - (1-F)\mathring{\psi}]$$

$$- \lambda\Delta\Gamma_{\theta-}[F\psi^{n+1} + (1-F)\mathring{\psi} - F\psi^{n+1}_{k-1} - (1-F)\mathring{\psi}_{k-1}] + S^n_{\psi} \quad , \qquad (3.155)$$

where

$$\alpha_{\pm} = \tfrac{1}{2}u_{i\pm\frac{1}{2}}\left(1+\frac{u_{i\pm\frac{1}{2}}}{|u_{i\pm\frac{1}{2}}|}\right) \quad , \qquad (3.156)$$

$$\beta_{\pm} = \tfrac{1}{2}u_{i\pm\frac{1}{2}}\left(1-\frac{u_{i\pm\frac{1}{2}}}{|u_{i\pm\frac{1}{2}}|}\right) \quad , \qquad (3.157)$$

$$\gamma_{\pm} = \tfrac{1}{2}v_{j\pm\frac{1}{2}}\left(1+\frac{v_{j\pm\frac{1}{2}}}{|v_{j\pm\frac{1}{2}}|}\right) \quad , \qquad (3.158)$$

$$\delta_{\pm} = \tfrac{1}{2}v_{j\pm\frac{1}{2}}\left(1-\frac{v_{j\pm\frac{1}{2}}}{|v_{j\pm\frac{1}{2}}|}\right) \quad , \qquad (3.159)$$

$$\varepsilon_{\pm} = w_{k\pm\frac{1}{2}}\left(1+\frac{w_{k\pm\frac{1}{2}}}{|w_{k\pm\frac{1}{2}}|}\right) , \tag{3.160}$$

$$\sigma_{\pm} = w_{k\pm\frac{1}{2}}\left(1-\frac{w_{k\pm\frac{1}{2}}}{|w_{k\pm\frac{1}{2}}|}\right) , \tag{3.161}$$

$$\Delta\Gamma_{r+} = \frac{\left(r+\frac{\delta r}{2}\right)^{\beta}\left(\hat{\Gamma}+\hat{\Gamma}_{i+1}\right)}{\delta r\ r^{\beta}} , \tag{3.162}$$

$$\Delta\Gamma_{r-} = \frac{\left(r-\frac{\delta r}{2}\right)^{\beta}\left(\hat{\Gamma}+\hat{\Gamma}_{i-1}\right)}{\delta r\ r^{\beta}} , \tag{3.163}$$

$$\Delta\Gamma_{z+/-} = \left(\hat{\Gamma}+\hat{\Gamma}_{j\pm1}\right)/\delta z \text{ , and} \tag{3.164}$$

$$\Delta\Gamma_{\theta+/-} = \left(\hat{\Gamma}+\hat{\Gamma}_{k\pm1}\right)/\delta\theta r^{2\beta} \tag{3.165}$$

The next steps in this development cast the difference equations into a format which allows solution using either a fully explicit or implicit approach. The implicit solution is accomplished using the alternating direction implicit (ADI) method originated by Douglas and Gunn [36]. The particular form used herein where the problem solution yields relative changes rather than absolute magnitudes was suggested by Trent [63] in his formulation of the TEMPEST program. First, using the definition

$$\Delta\psi \equiv \psi^{n+1} - (1-C)\psi^{n} - C\tilde{\psi} \tag{3.166}$$

in the complete discrete equations allows it to be written

in the following concise form

$$\Delta\psi = F\,[\,A\Delta\psi_{i+1} + B\Delta\psi_{j+1} + H\Delta\psi_{k+1} + (C^r+C^\theta+C^z)\Delta\psi + G\Delta\psi_{k-1} + D\Delta\psi_{j-1} + E\Delta\psi_{i-1}\,] + \Delta\psi_E\ , \tag{3.167}$$

where

$$A = \delta t\,[\,\frac{\Delta\Gamma_{r+}}{\rho_r} - (1-C)\,\beta_+\,(\frac{1}{\delta r} + \frac{\beta}{2r^\beta})\,]\,, \tag{3.168}$$

$$B = \delta t\,[\,\frac{\Delta\Gamma_{z+}}{\rho_r} - (1-C)\,\frac{\delta_+}{\delta z}\,]\,, \tag{3.169}$$

$$C^r = \delta t\,[\,-\frac{1}{\rho_r}(\Delta\Gamma_{r+}+\Delta\Gamma_{r-}) - (1-C)\,(\frac{\alpha_+-\beta_-}{\delta r} + \frac{\beta(\alpha_++\beta_-)}{2r^\beta})\,]\,, \tag{3.170}$$

$$C^\theta = \lambda\delta t\,[\,-\frac{1}{\rho_r}(\Delta\Gamma_{\theta+}+\Delta\Gamma_{\theta-}) - (1-C)\,(\frac{\varepsilon_+-\sigma_-}{r^\beta\delta\theta})\,]\ , \tag{3.171}$$

$$C^z = \delta t\,[\,-\frac{1}{\rho_r}(\Delta\Gamma_{z+}+\Delta\Gamma_{z-}) - (1-C)\,(\frac{\gamma_+-\delta_-}{\delta z})\,]\ , \tag{3.172}$$

$$D = \delta t\,[\,\frac{\Delta\Gamma_{z-}}{\rho_r} + (1-C)\,\frac{\gamma_-}{\delta z}\,]\,, \tag{3.173}$$

$$E = \delta t\,[\,\frac{\Delta\Gamma_{r-}}{\rho_r} + (1-C)\,\alpha_-\,(\frac{1}{\delta r} + \frac{\beta}{2r^\beta})\,]\,, \tag{3.174}$$

$$G = \lambda\delta t\,[\,\frac{\Delta\Gamma_{\theta-}}{\rho_r} + (1-C)\,\frac{\alpha_-}{r^\beta\delta\theta}\,]\,, \tag{3.175}$$

$$H = \lambda\delta t\,[\,\frac{\Delta\Gamma_{\theta+}}{\rho_r} - (1-C)\,\frac{\sigma_+}{r^\beta\delta\theta}\,]\ , \text{ and} \tag{3.176}$$

$$\Delta\psi_E = A\overset{\circ}{\psi}_{i+1} + B\overset{\circ}{\psi}_{j+1} + H\overset{\circ}{\psi}_{k+1} + (C^r+C^\theta+C^z)\overset{\circ}{\psi}$$
$$+ G\overset{\circ}{\psi}_{k-1} + D\overset{\circ}{\psi}_{j-1} + E\overset{\circ}{\psi}_{i-1} + S^n_\psi \ \delta t \ . \qquad (3.177)$$

The $\Delta\psi_E$ is noted as completely explicit in time and represents the fully explicit solution since all other terms are dropped if F is set to zero. The choice of which solution procedure to utilize can be made on the basis of a stability argument. The overall problem time step is limited by the SMAC procedure to the material Courant limit, i.e.,

$$\delta t_{SMAC} \leq \min_{\text{all ijk}} \left(\left|\frac{\delta r}{u}\right|, \left|\frac{\delta z}{v}\right|, \lambda\left|\frac{r\delta\theta}{w}\right|\right) \ . \qquad (3.178)$$

In most cases this inequality is satisfied with additional margin through the use of an arbitrary multiplier. The explicit stability constraint of these transport equations is suggested by Roache [27] and is of the form

$$\delta t \leq \min_{\text{all cells}} \left[\left(C\left(\left|\frac{u}{\delta r}\right| + \left|\frac{v}{\delta z}\right| + \left|\frac{w}{r\delta\theta}\right|\right)\right.$$
$$\left. + 2\hat{\Gamma}\left(\frac{1}{\delta r^2} + \frac{1}{\delta z^2} + \frac{\lambda}{r^{2\beta}\delta\theta^2}\right)\right]^{-1} \ . \qquad (3.179)$$

If the stability test is not satisfied, the ADI method is employed. The scheme involves a three pass implicit solution of the following equation set.

$$\Delta\psi^1 = F[A\Delta\psi^1_{i+1} + C^r\Delta\psi^1 + E\Delta\psi^1_{i-1}] + \Delta\psi^E \ , \qquad (3.180)$$

$$\Delta\psi^2 = F[B\Delta\psi^2_{j+1} + C^z\Delta\psi^2 + D\Delta\psi^2_{j-1}] + \Delta\psi^1 \ , \qquad (3.181)$$

and

$$\Delta\psi = F[H\Delta\psi_{k+1} + C^\theta\Delta\psi + G\Delta\psi_{k-1}] + \Delta\psi^2 \ . \qquad (3.182)$$

The solution of each directional pass can be accomplished using an efficient elimination quadrature given the simple banded structure of the coefficient matrices.

All conservation equations are solved using this versatile explicit/implicit technique. The turbulence equations contain LHS source terms which involve the primitive variables. These source terms are evaluated completely explicitly since their variation over a single computational time step should not be significant. Once the solutions are computed, the absolute magnitude of the variable of interest is evaluated using

$$\psi^{n+1} = \overset{\circ}{\psi} + \Delta\psi. \qquad (3.183)$$

3.3.4.4 Information Update and State Determination

The solution of the conservation euqations does not complete the computational cycle. Three additional tasks require completion. One is the complete specification of the local thermodynamic state. The component and energy conservation equations specify the cell total mass density and mixture energy but temperature and liquid content have yet to be computed. Second, various useful

data such as hydrogen mass and volume fractions, void fraction and density change rate must be calculated. Finally, the redefinition of the reference state can be accomplished in the interest of improving the physical accuracy of the incompressible assumption.

The basic goal of the state definition is finding the component densities and temperatures once the total density and mixture energy are known. The analysis begins with this simple total cell energy calculation

$$\rho^{n+1}e^{n+1} = \sum_{\text{i=all components}} \rho_i^{n+1}e_i^{n+1} \quad . \tag{3.184}$$

This can be expanded if the assumptions of thermodynamic equilibrium (all temperatures are equal), saturated liquid and perfect gas description of non-condensibles are made. Hence,

$$\rho^{n+1}e^{n+1} = \rho_a^{n+1}C_aT^{n+1} + \rho_h^{n+1}C_hT^{n+1} + \rho_w^{n+1}e_w^{n+1} . \tag{3.185}$$

In cases where no water is present, this equation can be solved directly to yield

$$T^{n+1} = \rho^{n+1}e^{n+1}/(\rho_a^{n+1}C_a + \rho_h^{n+1}C_h) \quad , \tag{3.186}$$

and

$$\chi_w = \frac{\text{steam mass}}{\text{liquid mass}} = 0 \quad . \tag{3.187}$$

The total water density is known but the liquid and vapor fractions are not. If saturated conditions exist,

the water specific internal energy is described by

$$e_w = e_f + \chi_w e_{fg} \ . \tag{3.188}$$

Both e_f and e_{fg} can be approximated in the temperature range of interest by

$$e_f \simeq e_{f0} + C_l T = -1143624.4 + 4186.8\ T\ (J/kg), \tag{3.189}$$

and

$$e_{fg} \simeq e_{fg0} - BT = 3177400 - 2920.5\ T\ (J/kg) \ . \tag{3.190}$$

Given these definitions equation (3.185) is rewritten such that

$$\rho^{n+1}e^{n+1} = (\rho_a^{n+1}C_a + \rho_h^{n+1}C_h + \rho_w^{n+1}C_\ell)T^{n+1} + \rho_w^{n+1}e_{f0} + \rho_g^{n+1}(e_{fg0}-BT^{n+1}) \ . \tag{3.191}$$

The updated steam density remains as the sole undefined variable (besides local temperature). The saturated steam density is well represented by

$$\rho_g = \frac{P_s(T)}{TR_s(T)} \tag{3.192}$$

where

$$P_s(T) \simeq AT^{\alpha}e^{\beta/T} = 6.0573 \times 10^{26}T^{-5.3512}e^{-6890.81/T}\ (N/m^2),$$

and

$$R_s(T) \simeq R_{s0} - YT = 485.27-.07966T \text{ N-m/kg°K} ,$$

or

$$\rho_g^{n+1} \simeq A(T^{n+1})^{\alpha} e^{\beta/T^{n+1}} / T^{n+1}(R_{s0}-YT^{n+1}) . \qquad (3.193)$$

Thus, there are two equations (3.191 and 3.193) and two unknowns (ρ_g,T). Since the vapor density equation is transcendental, a closed form algebraic solution is impossible. However a rapidly convergent iterative solution can be accomplished by substituting the density expression into the energy constraint and solving for the temperature in the exponential which is

$$T^{new} = \beta/\ln\left[\frac{(\rho e-\rho_w e_{f0}-T\Sigma\rho_i C_i)(R_0-YT)}{(e_{fg0}-BT)AT^{\alpha-1}} \right] . \qquad (3.194)$$

The new temperature estimate may yield a vapor density greater than the total water density. If this occurs, a superheated steam condition is possible. If this is the case, the temperature can be computed directly using

$$T/= \underset{\text{steam}}{\text{superheated}} \quad \frac{\rho e-\rho_w(e_{f0}+e_{fg0}+T_s(C_l-C_s-B)}{\Sigma\rho_i C_i + \rho_w C_s} , \qquad (3.195)$$

where

T_s = saturation temperature,

C_s = steam specific heat, and

$\Sigma\rho_i C_i = \rho_a C_a + \rho_h C_{..}$.

If this temperature also yields a larger saturated vapor density than the total density, the solution is complete.

If not, the saturation iteration is recommenced. Finally, the vapor and liquid densities are defined by

$$\rho_s^{n+1} = \begin{cases} \rho_g(T^{n+1}) & \text{if } \rho_g \leq \rho_w \\ \rho_w^{n+1} & \text{if } \rho_g > \rho_w \end{cases}, \text{ and}$$

$$\rho_\ell^{n+1} = \rho_w^{n+1} - \rho_s^{n+1} . \qquad (3.196)$$

The overall state calculation is summarized in the following stepwise prescription:

1. Is $\rho_w^{n+1}=0$. If so, solve directly using perfect gas and $\chi_w = 0$. If not, continue;
2. guess T, best guess is T^n.
3. evaluate $(\rho e-\rho_w e_{f0}-T\Sigma\rho_i C_i)$. If > 0, continue. If < 0, reduce guess and continue;
4. calculate T^{new} and evaluate $\rho_g(T^{new})$;
5. Is $\rho_g>\rho_w$. If so, go to step 7. If not, go to 6.
6. Is $|T^{new}-T^{old}| \leq \varepsilon$, if yes, solution complete, densities can be evaluated and $T^{n+1}=T^{new}$. If not, $T=T^{new}$ and go to 3.
7. calculate T with superheat. Is T > 273.15°K. If yes, continue. If not, reduce T and go back to 3.
8. Evaluate ρ_g. Is $\rho_g > \rho_w$. If yes, solution complete. If no, go back to 3.

The iteration usually converges to an error of 0.001°K in roughly 5 iterations. The most difficult convergence is encountered near saturation as the iteration in Table 3.3 illustrates. Finally, the curve fits of the thermodynamic properties previously specified are plotted in Figure 3.5. Good agreement is observed.

Many additional useful data are calculated once the state and quality are defined. Three which merit additional comment are hydrogen volume fraction, void fraction and change of density with temperature. Hydrogen volume fraction is usually the most important datum in this application and is computed assuming the cell volume occupied by liquid is negligible and the perfect gas law is applicable. As such

$$f_H = \frac{x_h}{x_h + \frac{(mw)_h}{(mw)_a} x_a + \frac{(mw)_h}{(mw)_s} x_s} \tag{3.197}$$

where x_i = mass fraction,

$(mw)_i/(mw)_j$ = ratio of molecular weights.

The void fraction is computed assuming the liquid density is that of saturated water.

$$\alpha = \text{void fraction} = \frac{\rho^{n+1} - \rho_f}{\rho^{n+1}_\ell - \rho_f} \,. \tag{3.198}$$

The final task in the computational cycle is an optional reference state update. The frequency of this

Table 3.3

State Determination Example Near Saturation Line

Given: $e = 7.3 \times 10^5$ J/kg, $\rho_a = 1.0$ kg/m^3

$\rho_h = .05$ kg/m^3, $\rho_w = .2$ kg/m^3

Guess T = 344°K

Old estimate (°K)	New estimate (°K)	Vapor density (kg/m^3)
344	343.434	0.2004
$\rho_g > \rho_w \rightarrow$ try superheat assumption		
343.434	341.583	0.186
$\rho_g > \rho_w \rightarrow$ try saturated assumption		
341.583	343.144	0.1981
343.144	343.217	0.1987
343.217	343.235	0.1988
343.235	343.230	0.1988
343.240	343.241	0.1989

$\therefore$ after 7 iterations

T = 343.241 $\rho_v = 0.1989$ $\rho_\ell = 0.0011$ $\chi = 99.45\%$

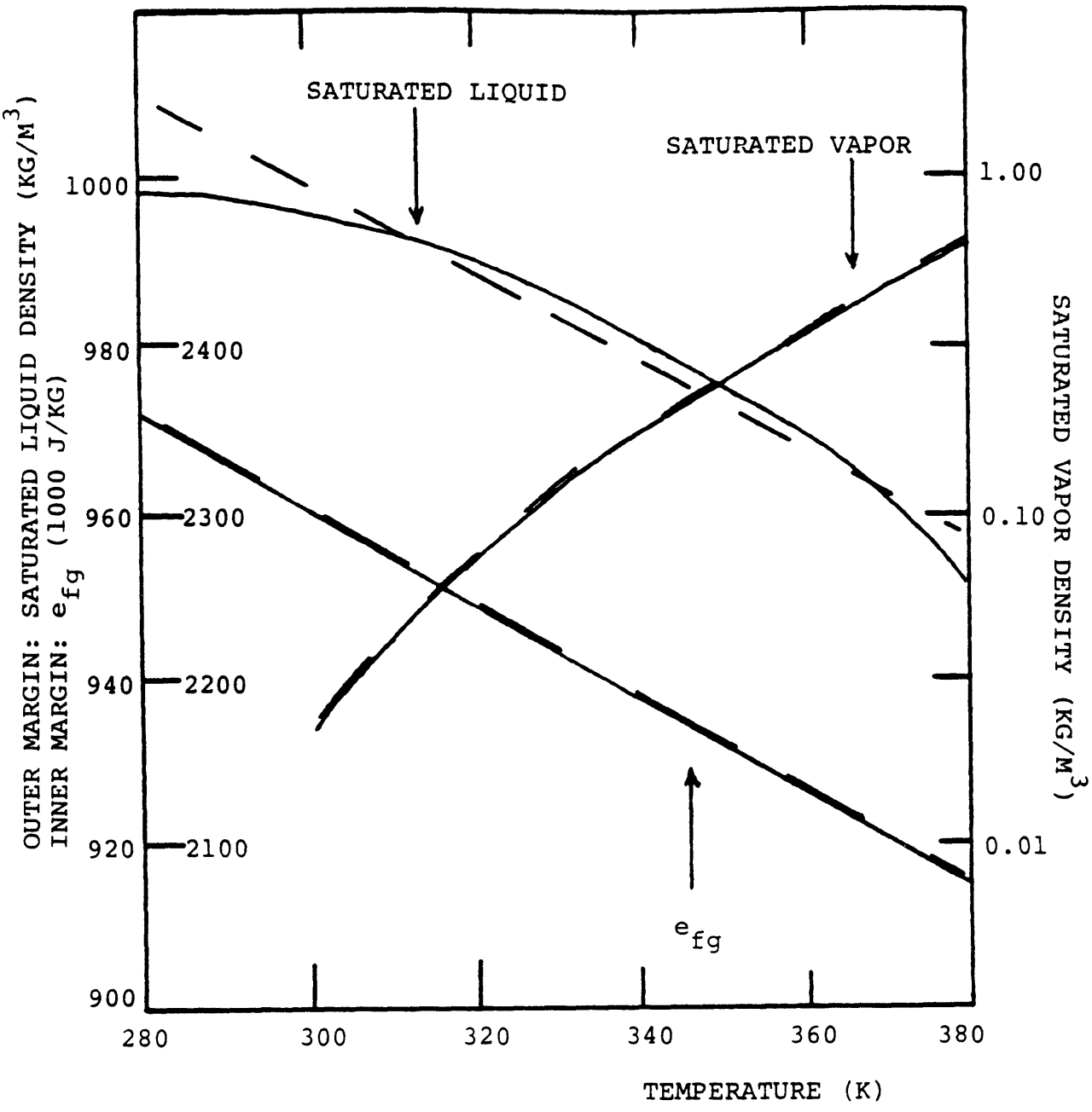

FIGURE 3.5: SATURATION PROPERTIES OF WATER

update is user-defined with the greater frequency yielding increased accuracy at the cost of additional computation. The procedure consists of adding all the mass in a region, evaluating the new reference density, gas density, average temperature and gas constant, and redefining a new reference pressure.

3.3.4.5 Boundary and Initial Conditions

The boundary and initial condition options of the original code remain unaltered by the new model additions. Two restrictions in utilizing three dimensional modelling are that it is only valid for the slower mixing option and connected continuum regions cannot be defined. The new model formulations have introduced the need to specify additional conditions for a complete problem definition.

Boundary conditions for the two theta-direction bounding surfaces must be specified in all 3-D problems except those involving a complete cylinder in which case there are no intervening solid surfaces. The no-slip boundary option for solid surfaces has additional ramifications when the turbulence model is employed. This boundary condition should only be employed in problems where the near-wall mesh spacing is on the same scale as the boundary layer thickness such that purely molecular effects are significant. If such is the case

a modified "law of the wall" is utilized (see Launder and Spalding).

The logarithmic law of the wall approximation is illustrated for a boundary on the right-most fluid cell.

$$\frac{v}{(\tau/\rho)_w}[C_\mu^{\frac{1}{2}}k]^{\frac{1}{2}} = \frac{1}{K}\ln[E\frac{\delta r}{2}\frac{\rho[C_\mu^{\frac{1}{2}}k]^{\frac{1}{2}}}{\mu^m}] \quad , \tag{3.199}$$

where K = von Karman's constant = 0.42, and

E = 9.793 .

Near the wall

$$(\tau/\rho)_w \simeq [C_\mu^{\frac{1}{2}}k] \tag{3.200}$$

and we call approximate v by

$$v \simeq \frac{v + v_{j-\frac{1}{2}}}{2} \tag{3.201}$$

Substitution yields

$$\ln k + 2\beta_k - \frac{2\alpha_k}{\sqrt{k}} = 0 \quad , \tag{3.202}$$

where $\beta_k \equiv \ln[\frac{E\delta r\rho C_\mu^{\frac{1}{4}}}{2\mu^m}]$, and

$\alpha_k \equiv K(v+v_{j-\frac{1}{2}})/2C_\mu^{\frac{1}{4}}$.

The defining transcendental equation can be solved using Newton's method. Once the boundary cell turbulent kinetic energy is calculated, the dissipation level is computed using the following prescription:

$$g = \frac{C_\mu^{\frac{3}{4}} k^{\frac{3}{2}}}{K\frac{\delta r}{2}} \quad . \tag{3.203}$$

The turbulence model also necessitates the specification of initial turbulence levels. Recall the eddy viscosity is

$$\mu^T = \frac{\rho C_\mu k^2}{\xi} \tag{3.204}$$

Since turbulent velocity components usually experience fluctuations less than the absolute magnitude of the mean velocity, a reasonable initial k is the square of the maximum expected velocity. The authors of the VARR-II code suggest an initial dissipation level of

$$\xi_{initial} = \frac{C_\mu u_{max}^3}{\delta x} \quad . \tag{3.205}$$

Finally, the reference density definition should be computed as follows,

$$\rho_r = \frac{P_0}{R_0 T_0} + \bar{\rho}_\ell \quad . \tag{3.206}$$

3.3.4.6 Incompressibility Check

The underlying assumption of the slow mixing model is incompressibility. Local densities are computed on the basis of a reference pressure and are assumed to be

close enough to the reference density to be considered perturbations. In order to conform to this requirement local changes should not be large during a computational cycle. This limit is implemented by checking local density changes such that

$$\max_{\text{all cells}} \left| \frac{\rho^{n+1} - \rho^{n}}{\rho^{n}} \right| < \text{small number} \; . \tag{3.207}$$

The limiting criterion is user-specified and 1% seems to be a conservative value. If this test is not satisfied, the computational time step is halved and the calculation is redone until the incompressibility check is satisfied. This procedure coupled with judicious reference state updating can substantially broaden the range of applicability for this basically incompressible formulation.

3.3.5 Physical and Computational Interfacing Between MITHYD and the Overall Code

Given that the MITHYD subcode introduces a new fluid dynamic model, the question of interfacing with existing models in the code arises. These interface considerations can be grouped into two categories--physical and computational. The physical aspects relate to deciding what is the correct phenomenological model for the problem of interest. This may be apparent to the analyst a priori and hence the user is allowed to specify which model to use. However, a problem could involve flows which at

various times or places require both models. One example is a situation in which hydrogen is introduced as part of a steam jet which is of significant size when compared to the flow domain. This problem is best treated using the two-phase modified BEACON equation set. If the jet ceases after some time as could be the case if a relief valve reseated, the flow problem is then best described by the slower mixing equation set.

The exemplary scenario described is treated by an internal checking logic in the code. The most basic distinction between the two fluid models is the treatment of compressibility effects. Therefore a compressibility check is performed and the code can automatically switch to the slower mixing model from the BEACON model. Only this switching mode (not the reverse from MITHYD to BEACON) is allowed. Further, this switching is limited to one occurrence in each flow mesh. The rationale for these restrictions arises from the desire to minimize computational complexity. The next logical step in computational interfacing could be based on combining the two models into a single scheme. This seems to be a preferable alternative to devising a more complex switching logic. Nevertheless, the simplicity of the present formulation provides the analyst with significant latitude.

Computational aspects address the computer programming interface problem. These are addressed in detail in

Appendix A. In brief, the new models are formulated to be completely compatible with the variables utilized in the original formulations. The MITHYD subcode utilizes existing software for data management, input/output processing and ancillary calculations. Structurally, it is attached to the larger code in a highly modular fashion which allows for easy modification and understanding.

4.0 Results and Discussion

The development of analytical models as exemplified by the previous chapter is only part of the process. The successful implementation of these models can only be demonstrated by performing computer computations. The underlying framework of demonstrating a code's validity relies on comparing predictions to measured data (or at least other reliable calculations). This chapter details a number of validation calculations which demonstrate the capabilities and limitations of this tool. After results are presented, an analysis of their implications is undertaken. The results must be considered not only for their accuracy but also the computational effort involved in achieving them. Therefore, the final sections of this chapter compare the capabilities of this methodology versus other approaches.

4.1 Validation Methodology

The program possesses three major computational options. The first is the modified BEACON equation set which is most appropriate for detailed simulations of flows driven by compressible two phase effects. The basic code capability in this area is already demonstrated by the developers and subsequent users and hence is not a necessary part of this validation effort. The ability to handle

hydrogen transport during such transients however is a required task. The approach taken is to revise existing sample problems with known results and comparing code predictions with them. Attempts at using the modified BEACON equation set for longer transients are also reported in order to demonstrate its inadequacies of treating such events.

The bulk of the validation effort is focused upon the simulation of longer mixing transients using the MITHYD subcode. Two large scale experimental programs are the source of validation case studies. The first and largest simulation effort utilizes data from a series of single phase experiments performed at the Battelle-Frankfurt (BF) Institute in the Federal Republic of Germany. These tests are chosen because of their extensive documentation, simple structure, range of testing and direct applicability. The second source of empirical information originates from a series of multicomponent and two phase tests performed at the Handford Engineering Development Laboratory (HEDL). These tests involve complex geometries and flow regimes, and are considered to be the most challenging from a simulation standpoint. These simulations demonstrate the limitations of the MITHYD methodology.

Finally, lumped parameter model validation is reported. The new junction and node model described in Chapter 3 is used to simulate a number of problems including some of the

more complex multiroom BF tests. The simulations not only demonstrate the enhanced capability afforded by this addition but also illustrate the importance of input data such as time step size and junction characteristics. The input data decks for all simulations reported in this chapter are included in Appendix B.

4.2 Results Using the Modified BEACON Equation Set

Four simulations are reported in this section. The first problem which involves the rapid injection of an air/water flow into an initially stagnant region is identical to a reported BEACON sample problem. The results demonstrate that original code's capabilities have not been compromised during the development process.

The second problem is similar to the first except hydrogen is substituted for air in the incoming flow. This simulation addresses the issue of tracking hydrogen and is easily compared to the first problem. The ability (or inability) of the code to handle slower single phase transients was not known a priori. The third result discussion involves various attempts at simulating one of the more simple BF tests. A successful simulation is never achieved. Finally, the computational transition from the BEACON equations to the slower mixing model is tested in the final subsection.

4.2.1 Air and Water Blowdown

The geometry for this problem is shown in Figure 4.1 which depicts a single compartment in a Cartesian geometry with internal flow obstacles. Initially, the room consists of a uniform distribution of 90% air and 10% water (liquid) by volume which is stagnant and at atmospheric pressure and 333°K. The incoming flow is a 333°K mixture of 50% air/50% water by volume entering the left bottom boundary 3.05 m/sec. Gravity is not considered. Non-equilibrium interphasic momentum and energy exchanges are modelled but solid heat transfer and detailed condensate film formation are not considered. All solid surfaces are considered to be no-slip boundaries.

Figure 4.2 depicts the gas phase (air) flow field at 0.10 seconds into the transient. These results are identical to those presented in the original BEACON documentation. A physically reasonable velocity field is predicted with the solid walls producing the expected flow diversion. Figure 4.3 is a plot of the void fraction transient at five different locations. The location indexing is provided in Figure 4.1. This plot illustrates the progression of the lower void fraction inlet flow as it penetrates the field. Though it is not easily seen in this plot the data of points 3 and 4 are interesting in that the difference between the two actually reaches a maximum at about 0.08 seconds and if one extrapolates the results the void fraction at 3 will

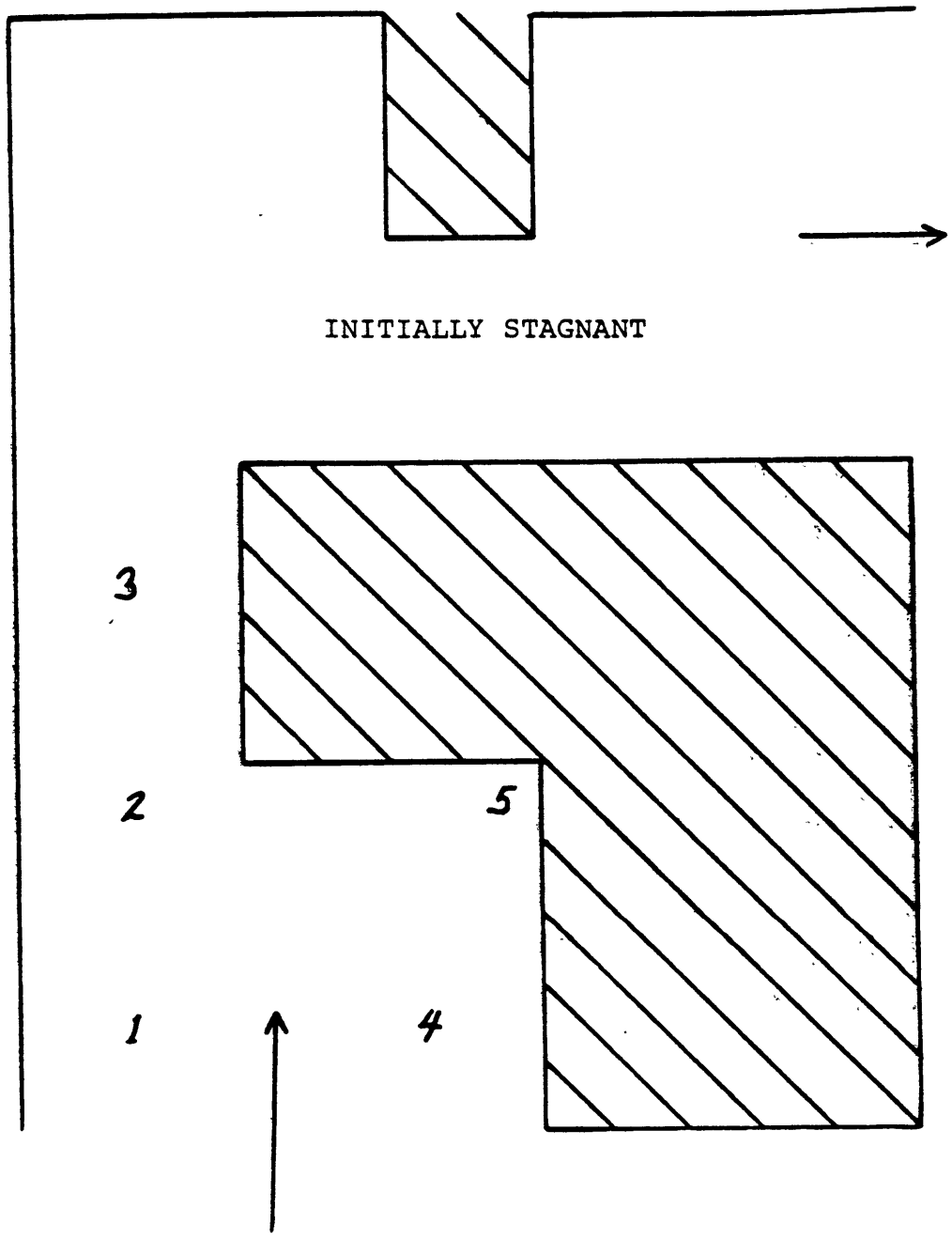

FIGURE 4.1: BEACON SAMPLE PROBLEM GEOMETRY

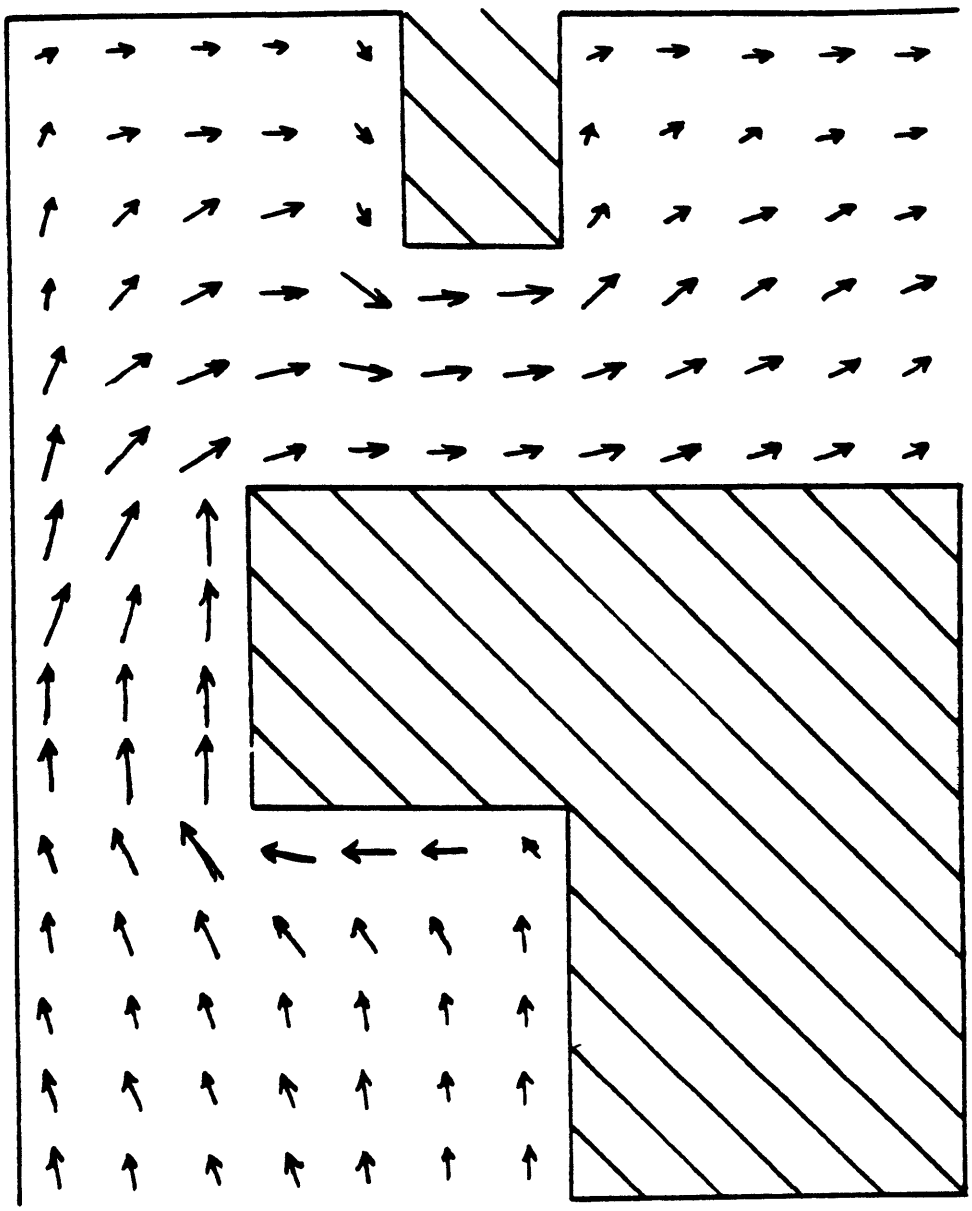

FIGURE 4.2: GAS VELOCITY FIELD AT 0.1 SECOND

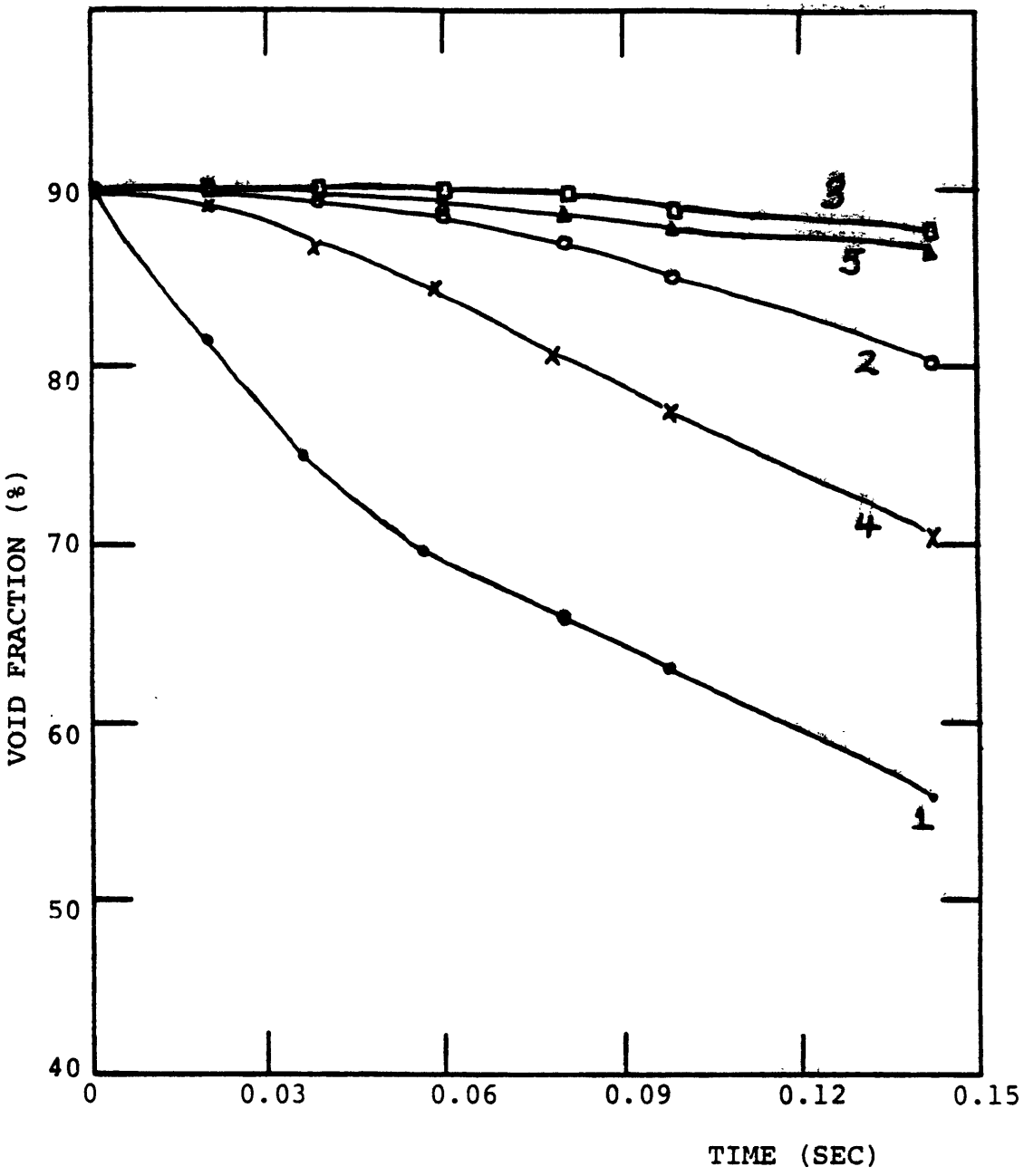

FIGURE 4.3: VOID FRACTION TRANSIENTS

in fact become lower than that of 5 at some later time. This is consistent with the hydrogen transport results reported in the next subsection. In all, a satisfactory result is accomplished for this case and the original capability remains intact.

4.2.2 Hydrogen and Water Blowdown

This problem is similar to the previous simulation save for the fact that hydrogen is now the inflow gaseous component. The resultant velocity profile of the gaseous phase was nearly the same as the previous problem. The only significant difference was the velocity profile developed a bit faster in this simulation. As a quantitative illustration, the velocity vectors at point 3 in the field at 0.1 seconds were 5.31 m/sec (-5° from vertical) and 5.62 m/sec (-5° from vertical), respectively for the two transients.

Figure 4.4 illustrates both the gas velocity and concentration field at 0.1 seconds into the transient. The velocity profile has not yet fully developed as can be seen by comparing this figure to Figure 4.5 which shows these fields at 0.20 seconds. The effect of the sharp corner of the central obstacle is to retard the flow and hence inhibit the convective transport of the hydrogen in this area. The time history of the H_2 volume fraction at the 5 calculational points discussed previously are shown in Figure 4.6. The 4% line is drawn on this figure since it represents a

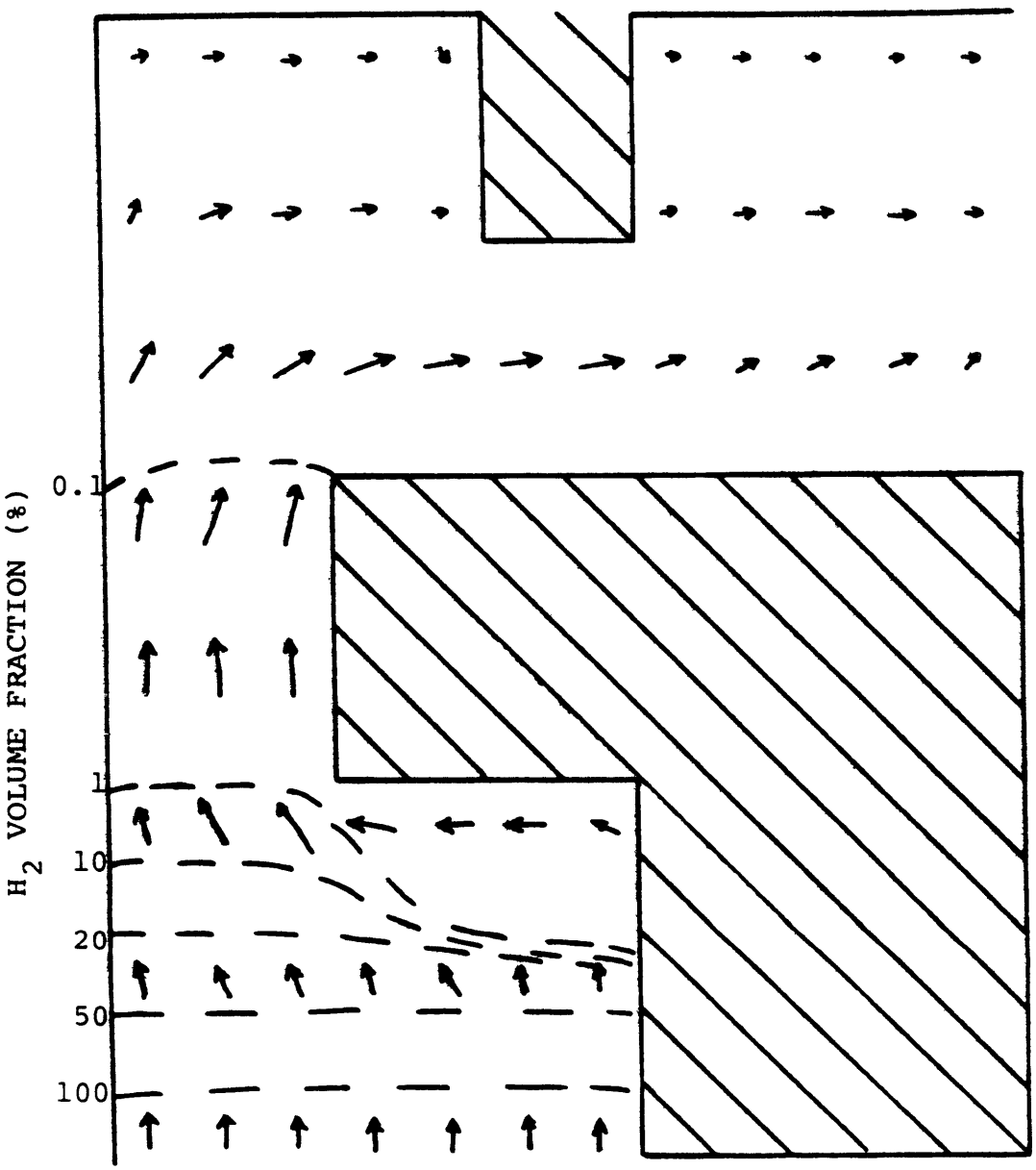

FIGURE 4.4: VELOCITY AND HYDROGEN CONCENTRATION FIELDS AT 0.1 SECOND

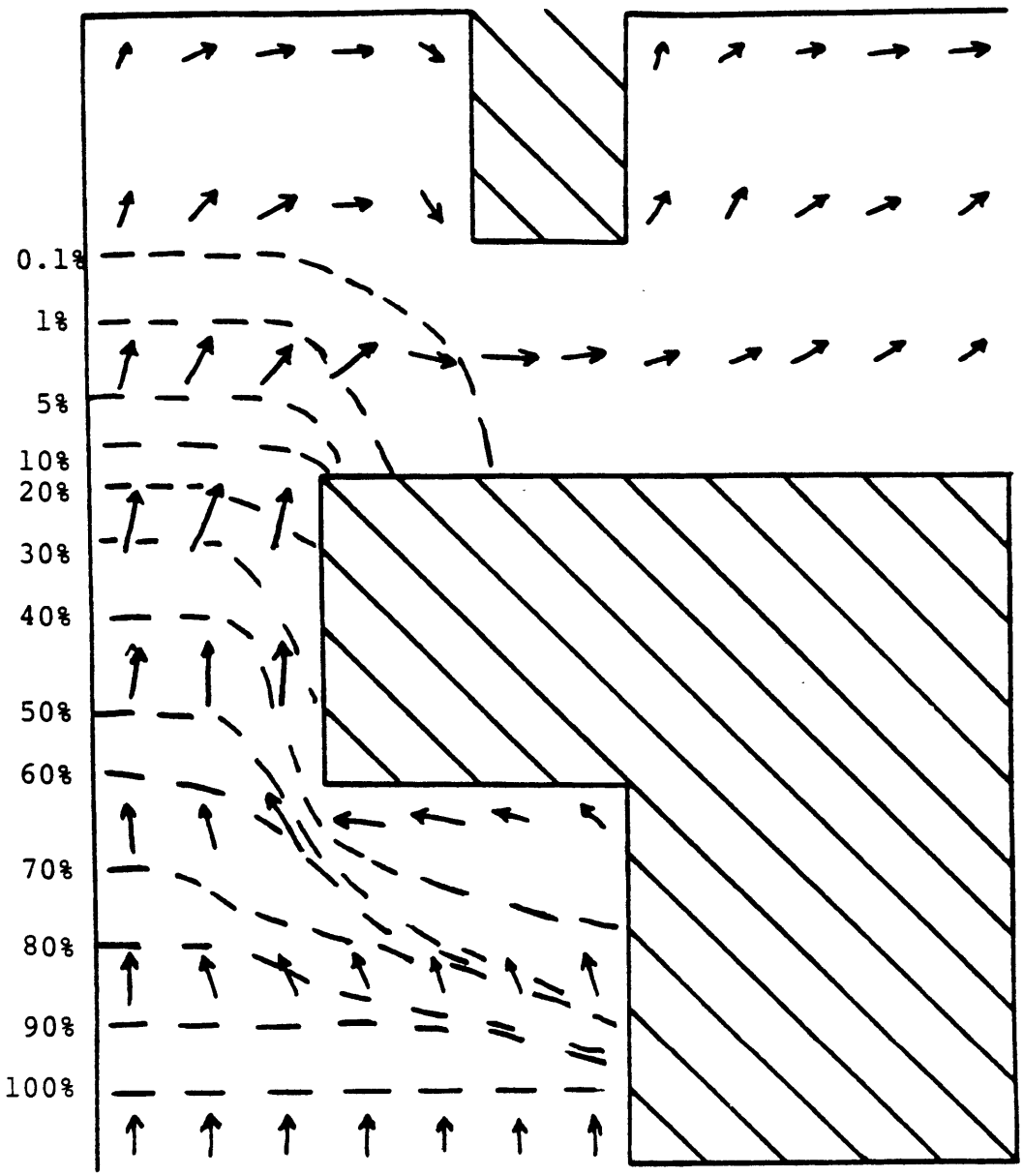

FIGURE 4.5: VELOCITY AND HYDROGEN CONCENTRATION FIELDS AT 0.2 SECOND

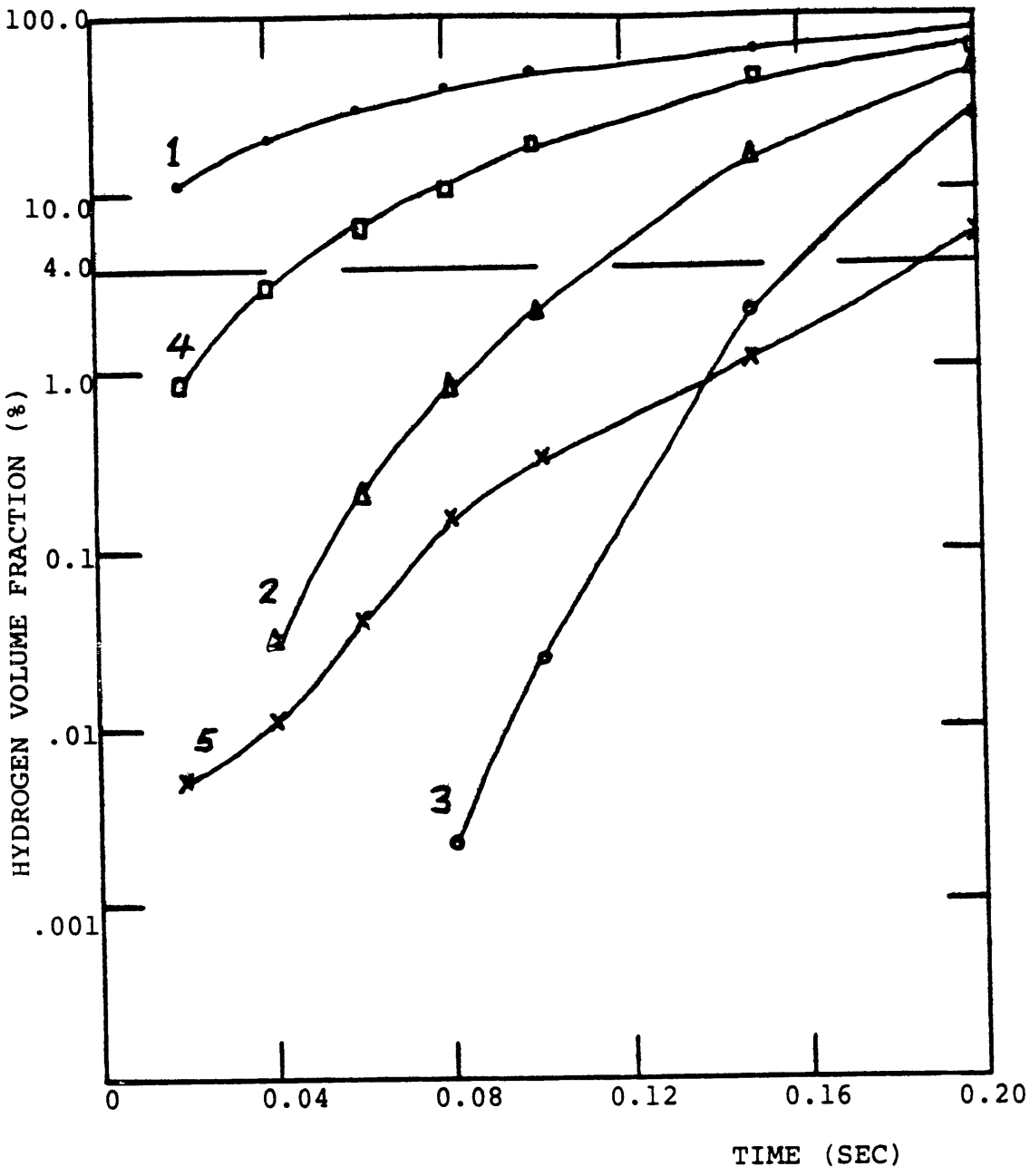

FIGURE 4.6: HYDROGEN CONCENTRATION TRANSIENTS

nominal ignition lower bound. An additional point to be observed in this figure is the intersection of the curves for points 3 and 5. This is analogous to the void fraction behavior reported in the previous subsection.

Taken together with the air/water blowdown transient, these results demonstrate the capability of the modified equations set to handle rapid transients. The time step size during these calculations were on the order of 0.001 seconds. The number of iterations required to converge the continuity constraint to 10^{-5} (0. being completely divergent free) was on the order of 10.

4.2.3 Analysis of Slower Transients

Simulation of a longer term transient is attempted in order to test the limitations of this analytical model. Test No. 2 of the Battelle Frankfurt series (see 4.3.1) is used as the test case. This experiment involves the introduction of a hydrogen/nitrogen mixture into a closed air-filled vessel with internal flow orificing. The experiment is characterised by a very slow injection rate. An abbreviated specification of this experiment is provided in Table 4.1. Figure 4.7 illustrates the basic geometry and the coarse nodalization used in the baseline simulation.

Numerous attempts of performing this calculation failed and a successful simulation beyond a few seconds is never achieved. The reasons for this lack of success are now

Table 4.1

Abbreviated Specifications of BF Test No. 2

Duration	3 hr 47 min (13620 sec)
Source Mixture (Volume %)	34% N_2* / 66% H_2
Source Flow	1.19 m^3/hr
Free Volume	71.9 m^3
Initial Compartment Temperature	17 °C
Mean Source Temperature	19 °C
Orifice Diameter	1.13 m

*Nitrogen modelled as air.

addressed. There are several significant differences between this problem and the previous two. Time scale is the most important of these distinctions. The blowdown events involved total problem times of less than a second with Courant time step sizes on the order of 10^{-3} to 10^{-2} seconds. This BF-based simulation involves an event which lasted over 13600 seconds and the expected Courant limit time steps are 1-10 seconds. Second, liquid phase water is not involved in the Battelle test. Given the absence of the liquid phase, interphasic effects are inappropriate and should not be included.

In lieu of providing a very detailed account of the problems encountered, Table 4.2 is presented as a summary of events. A close investigation of these attempts leads to the conclusion that the overall solution methodology is ill-suited for problems involving long time steps and no liquid phase at all. The non-equilibrium interphasic exchange formulation is particularly destabilizing in low convection flows when the usually small non-equilibrium exchanges become significant. One disturbing aspect of the existing BEACON computational logic is that interphasic exchanges cannot be neglected since the input specification of null coefficients causes the code to completely bypass the energy equations' solution. This is noted in the table under the entry labelled Attempt 4. Secondly, the code is unable to handle zero or unity void fraction flows. This

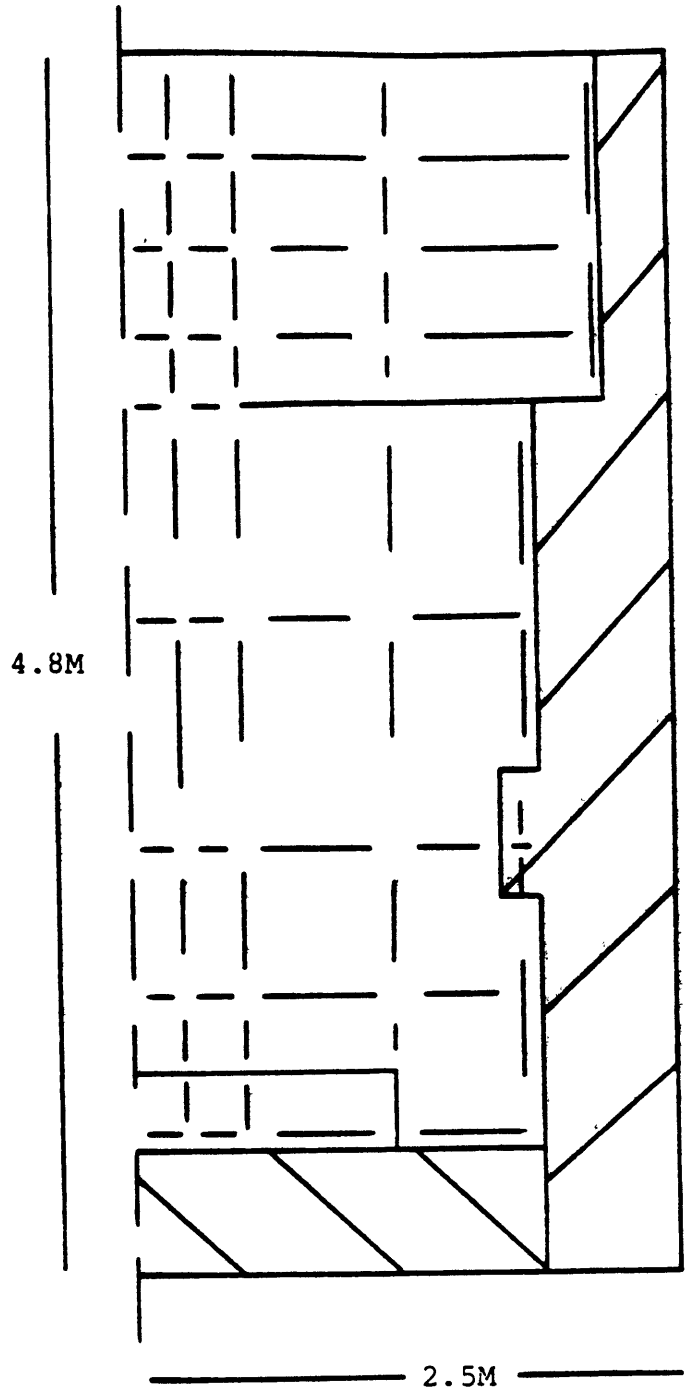

FIGURE 4.7: 32 NODE MESH USED IN BEACON EQUATION SET SLOW MIXING TRIAL RUNS

Table 4.2

Synopsis of Attempts at Simulating BF2 Using the BEACON Equation Set

Attempt			
1	Base case, no liquid, best estimate interphasic exchange, 16 nodes, initial Δt=1 second.	No convergence, erratic energy conservation leading to non-physical state.	Demonstrates underlying difficulties.
2	32 nodes, negligible user-defined interphasic parameters.	No convergence, similar to Attempt 1.	Nodalization did not affect solution. Erratic energy conservation seems to arise from non-conservative velocity field and interphasic exchange calculations.
3	16 nodes, even smaller interphasic constants.	Simulation to 5300 seconds, erratic convergence and non-physical results.	Convergence achieved temporarily but lost as Δt increased.
4	16 nodes, interphasic constants set to 0.	Simulation to 3 seconds, no convergence.	Δt's $\leq$ 0.1 seconds. Energy equations not solved.
5	16 nodes, small interphasic exchange and some liquid in initial	Better convergence behavior.	Demonstrates solution, requires some liquid and small Δt's.

limitation is also reported by Gido et al. [77]. Finally, the stability limit seems to be quite a bit below the expected Courant constraint (less than 10% of the CFL limit).

In short, the modified BEACON equation set is shown to be ill-suited for longer simulations. An approximate calculation would probably be successful if a fictitious liquid field is assumed and a very limiting time step constraint is utilized. However, the computational cost of performing such a calculation is unreasonable. For example, a simulation of a 10000 second (real time) event using 0.010 second time steps with perhaps 20 iterations per calculation cycle would involve over 300 million calculational passes and many tens of hours of computer time. Further, the resultant solution would not address turbulence or multicomponent diffusion. Clearly, another methodology is required for such analysis.

4.2.4 Transition to the Slower Mixing Model

The analytical aspects of the interfacing between the two continuum models is discussed in 3.3.5. A simple simulation is reported which demonstrates the code's ability to perform such a switch. The problem geometry is a simple 6 m^3 2-D Cartesian region divided into 6 mesh cells. Hydrogen is introduced into the lower left cell at a rate of 10^{-4} kg/sec (equivalent to 4 m^3/hr) for a period of 10 seconds (total injection = .011 m^3). The BEACON equation set is initially solved using a time step of 0.5 seconds. After 2

computational cycles, the code switched to the slower mixing model. Figure 4.8 depicts both the problem geometry and the convergence behavior of the simulation. The switching point is clearly evident at the end of 1 second of simulation. The poor convergence behavior of the BEACON model is not surprising given the similarity of this problem to the attempts described in 4.2.3. The slower mixing model handles this transient very well with an average 6 iterations per time step.

Figure 4.9 contains time history plots of the developing velocity and hydrogen fields. Physically reasonable results are observed and the traces show no sign of instability or discontinuity. Finally, Figure 4.10 provides schematic representations of the flow and concentration fields at both 1 and 10 seconds. The profiles at one second indicate that the BEACON models predict reasonable fields even though complete convergence is not achieved. In summary, the code is shown to successfully execute the desired computational transition.

4.3 Longer Mixing Transients Using MITHYD

The results reported in the previous section demonstrate the need for the longer term mixing model detailed in Chapter 3 and embodied in the MITHYD subcode. The extensive development effort which involves transforming the equations and assumptions of Chapter 3 into a working and (nearly)

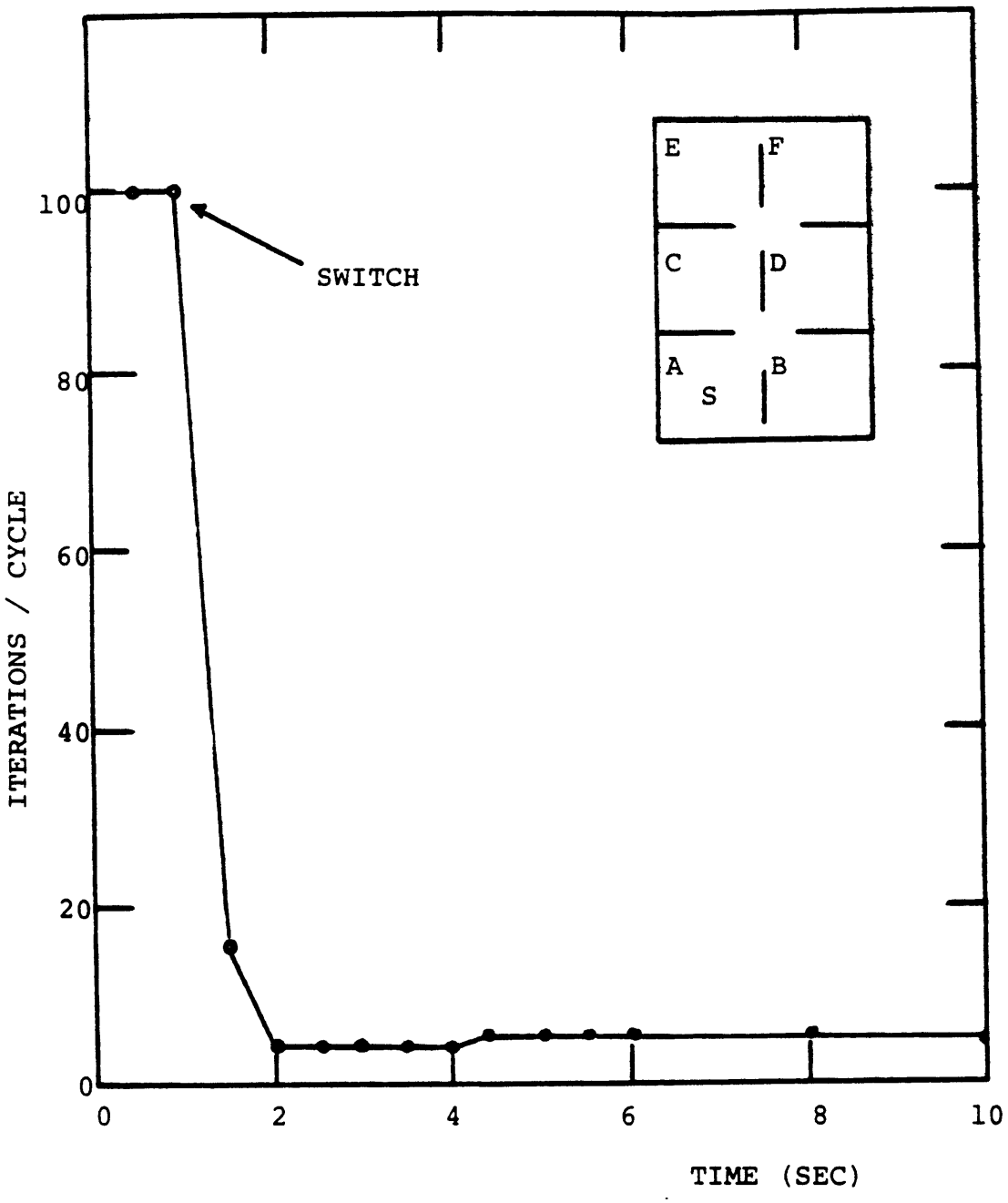

FIGURE 4.8: SWITCHING PROBLEM GEOMETRY AND CONVERGENCE BEHAVIOR

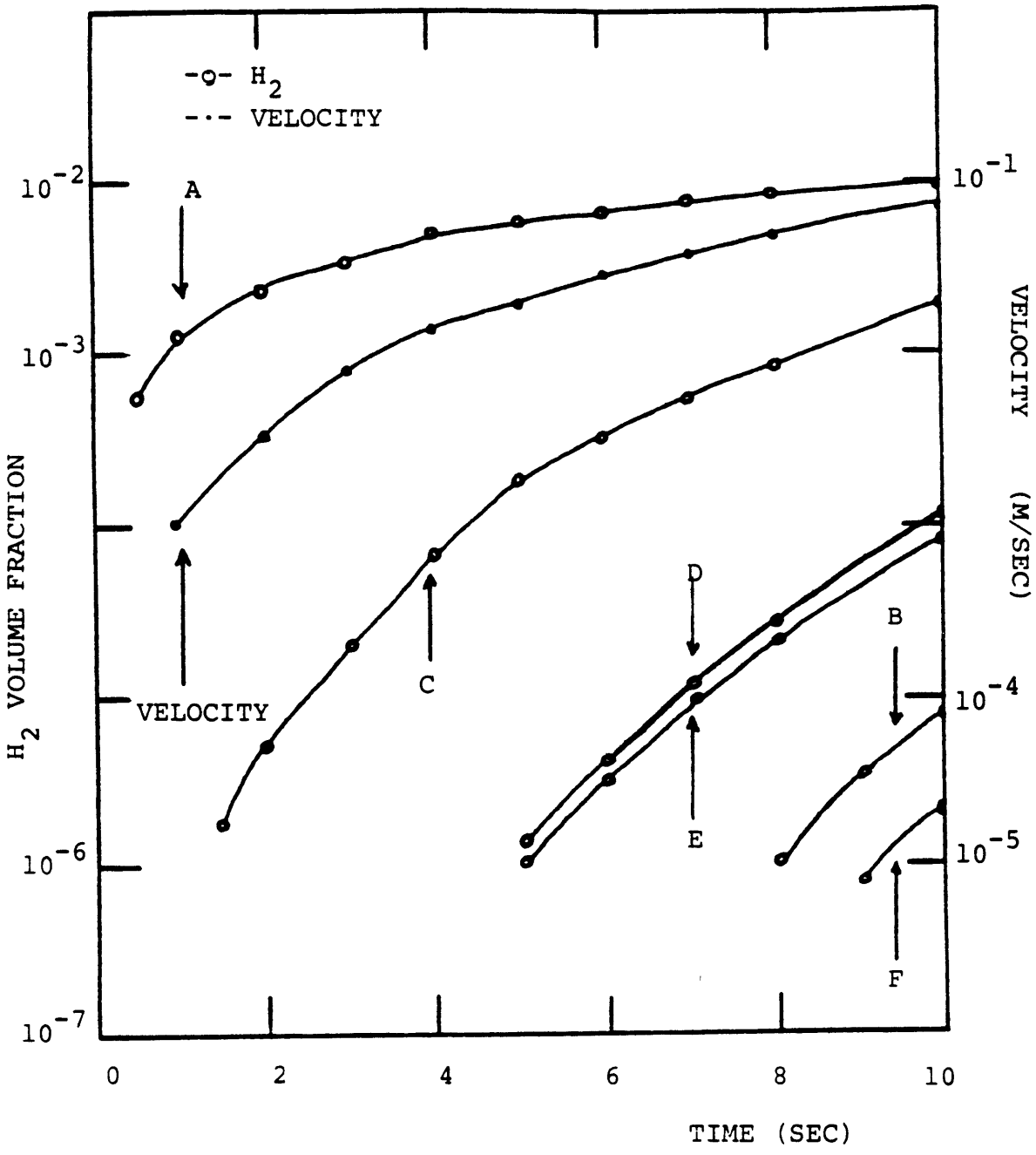

FIGURE 4.9: DEVELOPMENT OF VELOCITY AND HYDROGEN FIELDS IN SWITCHING PROBLEM

TIME= 1 SECOND

FLOW

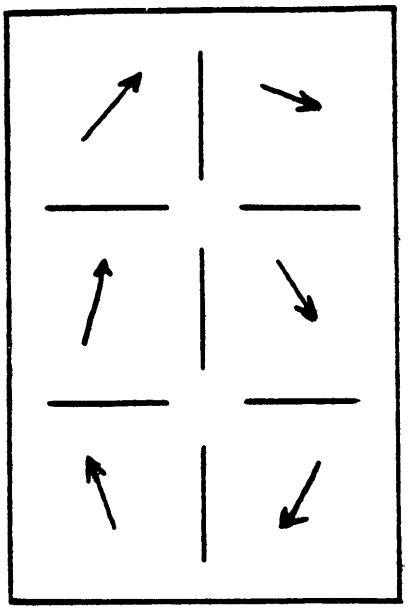

H_2 FRACTION

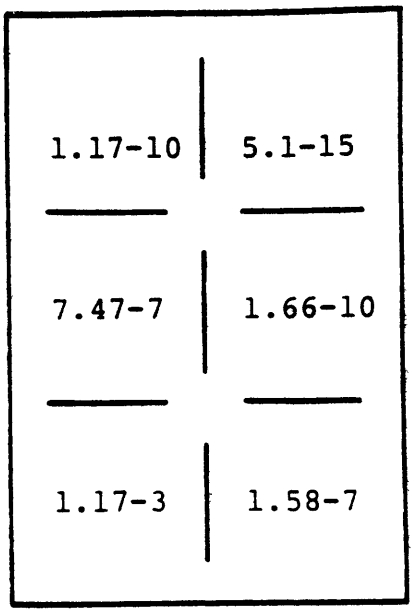

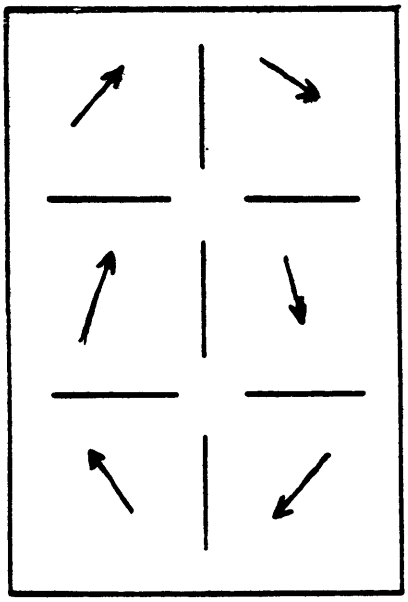

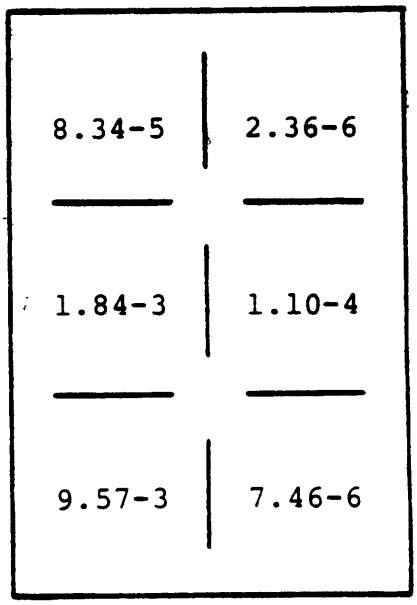

TIME= 10 SECONDS

FIGURE 4.10: FLOW AND HYDROGEN FIELDS AT 1 AND 10 SECONDS

error-free computer program is not documented here. The effort consists of careful planning, thorough review of coding, numerous debugging runs and extensive comparison of calculated results with hand calculations and known analytical solutions. The end product of this process is a useable but unvalidated tool. Validation is demonstrated by comparison of computed predictions with experimental data. The two chief sources of empirical data are large scale experiments performed at the Battelle Frankfurt Institute and the Handford Engineering Development Laboratory. Prior to the result presentations for each simulation group, a brief overview of the testing programs and facilities are provided.

4.3.1 Battelle Frankfurt Tests

This subsection is divided into two parts. First the facility and relevant tests are reviewed. Following this a number of simulations and comparisons based on particular BF tests are reported. These tests are particularly useful in code validation because many emphasized a separate-effects approach which allows for straightforward interpretation.

4.3.1.1 Facility and Testing Program Review

The hydrogen mixing tests performed at the Battelle Frankfurt (BF) test facility provide many of the principal test cases for the model validation. Given the central role of these tests, this subsection is included in order to provide

a brief description of this experimental program with special emphasis upon relevant tests. This is not a project review and should not be used as a source of experimental data. The original works cited in the references should be used for those purposes.

The BF experimental program involved the investigation of hydrogen behavior in prototypic light water reactor containment geometries during extended periods. Phase I and Phase II testing will be described. The purpose of the program is to provide basic phenomenological data and also to generate benchmark data for analytical model validation (particularly the lumped parameter RALOC code). The thermal hydraulic conditions of the first two testing phases are limited to slow injection rates typical of the post-blowdown period of a hypothetical event without steam effects. The basic test facility is illustrated schematically in Figure 4.11. There is a central cylindrical region which may be physically divided by a horizontal orifice plate. The central region can be connected to four additional chambers which occupy bordering radial locations. Finally, this partially connected assembly resides in a larger room. Figure 4.12 provides a perspective view of the facility and illustrates the compartment geometry and potential junction locations. Junction flow areas are shown in Figure 4.13. Injection source location can be changed and the assembly is instrumented for data acquisition of pressures,

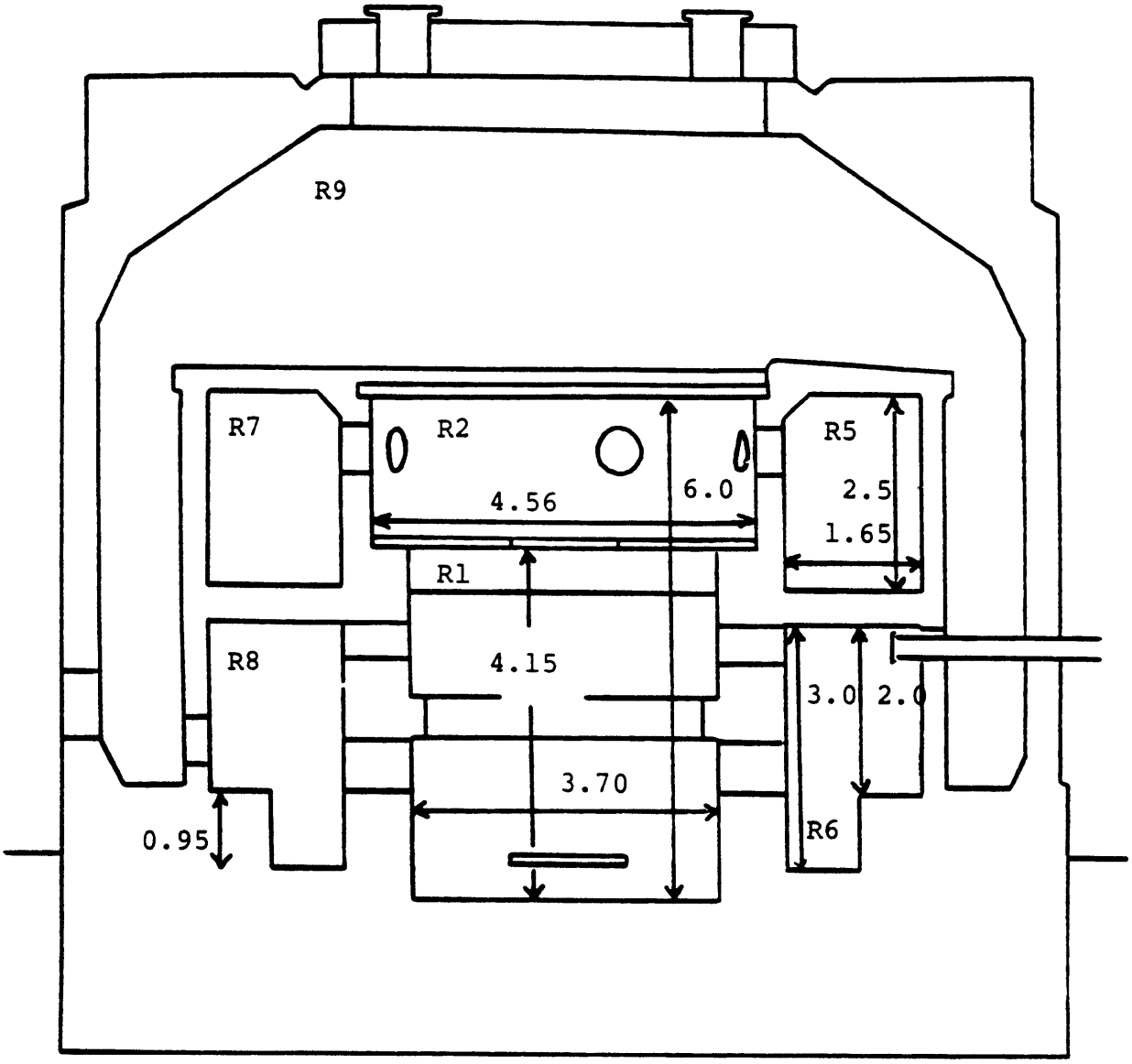

FIGURE 4.11: BATTELLE FRANKFURT FACILITY SCHEMATIC

(ALL DIMENSIONS IN METERS)

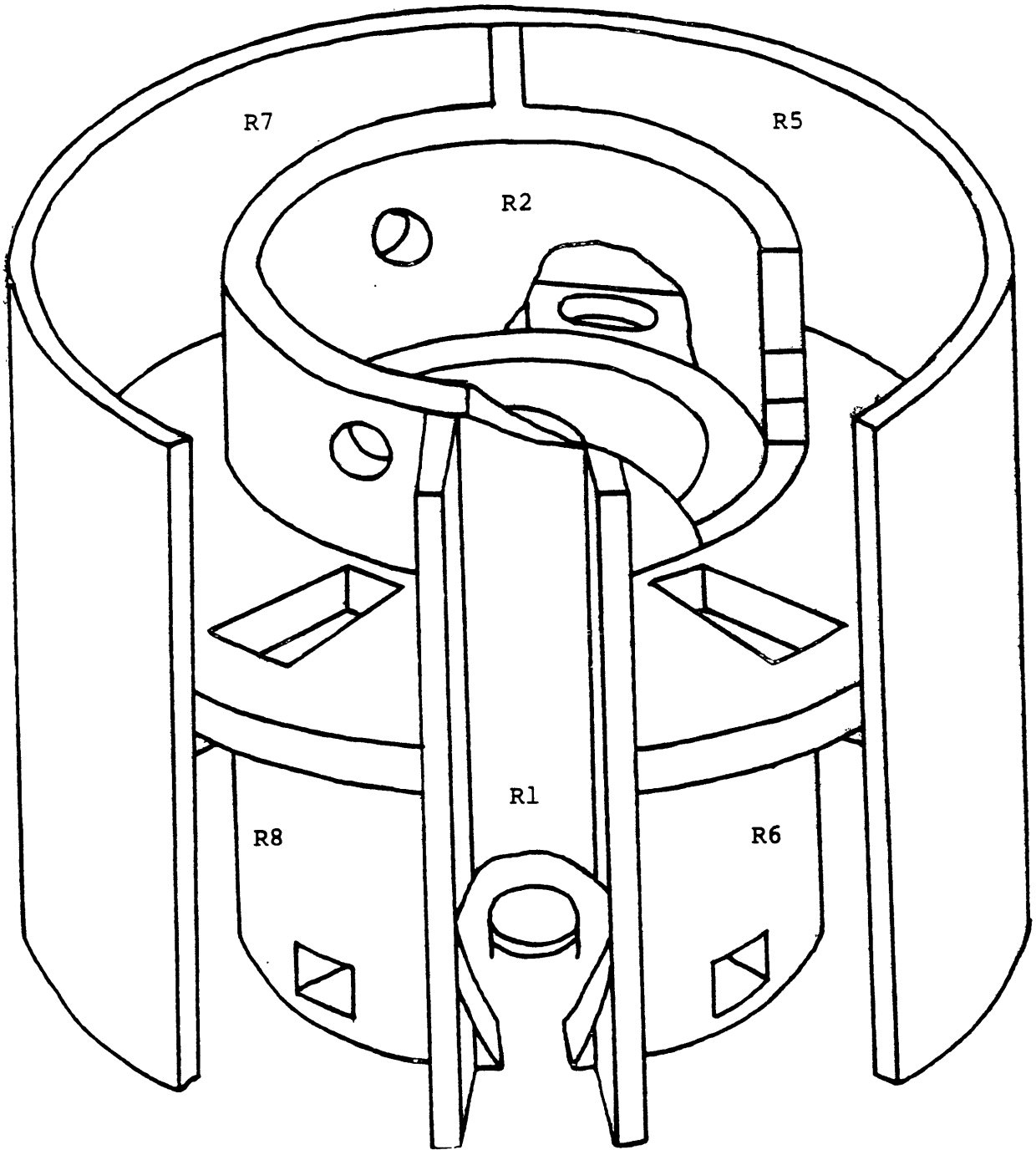

FIGURE 4.12: THREE DIMENSIONAL VIEW OF BATTELLE FRANKFURT FACILITY

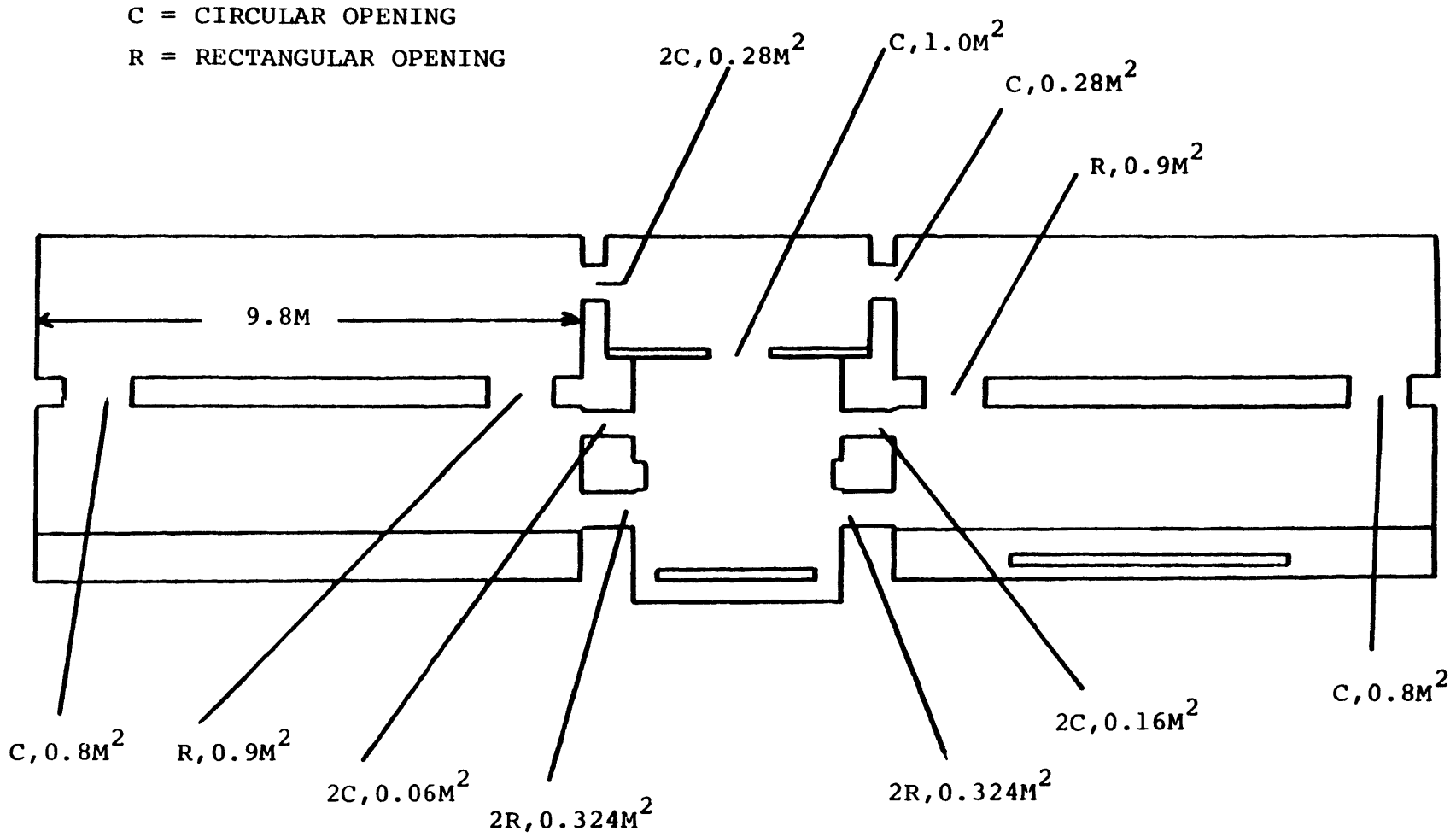

FIGURE 4.13: ROOM CONNECTION ARRANGEMENT AND SIZES FOR BATTELLE FRANKFURT FACILITY

temperatures, hydrogen concentrations, flow rates, etc. as is illustrated in Figure 4.14. The source itself is a pad covered with a porous cloth through which premixed gas mixtures are passed. This is also shown in Figure 4.14. The hydrogen measurement probe and its associated circuitry are depicted in Figure 4.15. Basically, the probe is a catalytic device in which a gas sample is nearly completely burned liberating heat which in turn changes the electrical resistivity of the coil. The change in resistivity is proportional to the original gas sample hydrogen concentration. The reference coil serves to compensate for ambient temperature changes in the local probe vicinity. The data sampling rates were on the order of every 40 seconds. Use of these probes in a steam environment has not been tested.

The Phase I series consisted of 9 tests and involved only the central cylindrical region of the facility which has a net free volume of approximately 80 m^3 and two of the smaller horizontally connected compartments. Phase I tested the measurement and data acquisition equipment and provided useful information into hydrogen behavior in large compartments. A synopsis of this test series is provided in Table 4.3. Tests 1 through 6 involve the central cylindrical geometry. The flow rates in test 1 and 6 were corrected sometime into each test as indicated. Tests 7 through 9 were performed in the smaller horizontally connected compartments. This table also details the overall objectives of each test.

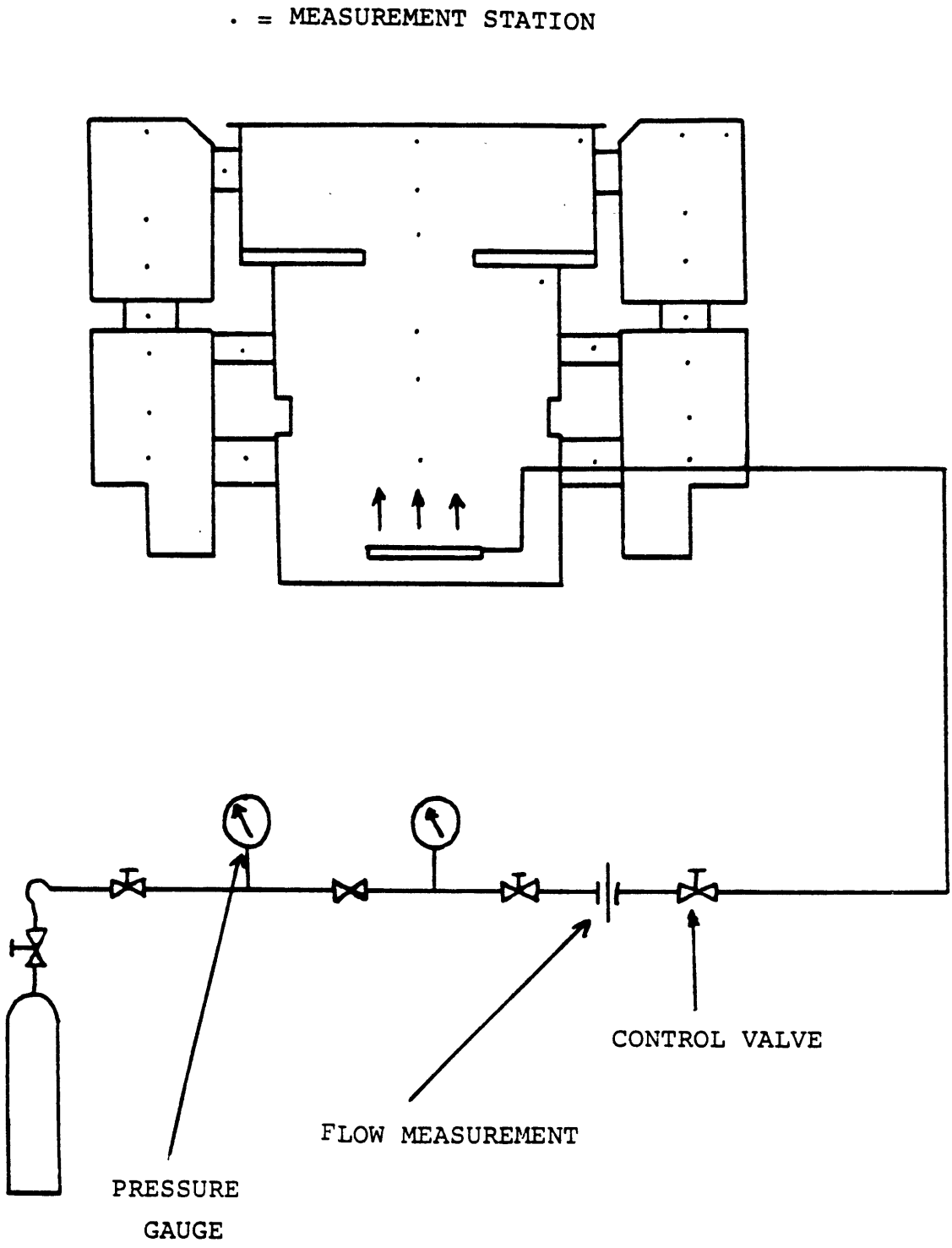

FIGURE 4.14: BATTELLE FRANKFURT SOURCE AND INSTRUMENTATION LOCATION SCHEMATICS

HYDROGEN MEASUREMENT DEVICE DIAGRAMS

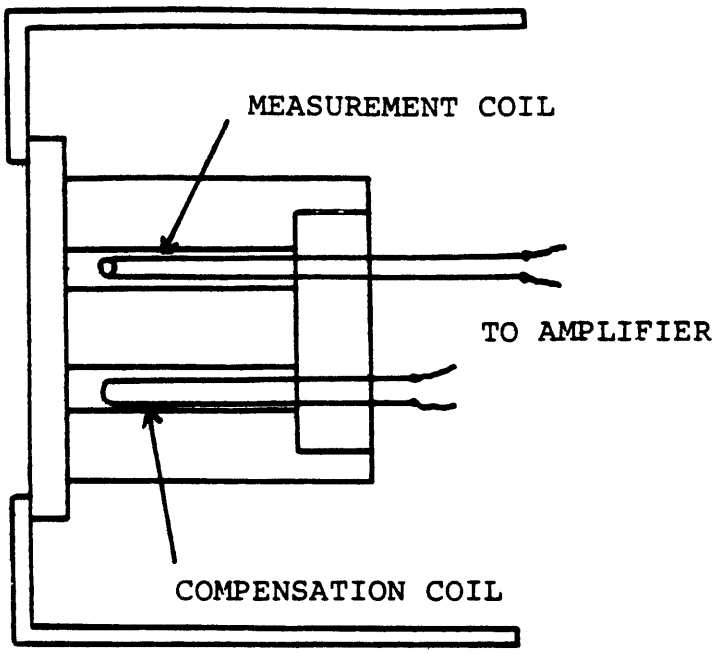

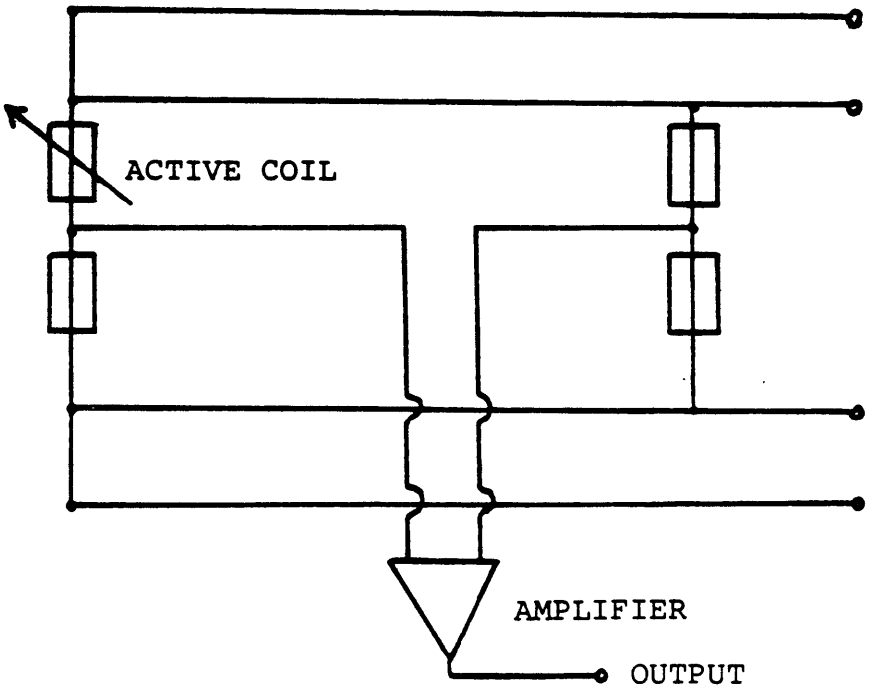

FIGURE 4.15

Table 4.3

Phase I Battelle Frankfurt Tests

	Test No. 1	Test No. 2	Test No. 3	Test No. 4	Test No. 5
Duration of release (sec)	1380 + 11220	13620	10320	7800	31200
Gas mixture N_2/H_2 (volume %)	68/32	34/66	34/66	34/66	34/66
Release rate (m^3/sec)	1.66E-3/ 7.55E-4	3.306E-4	3.389E-4	3.444E-4	1.417E-4
Total released volume (m^3)	2.3/2.272	4.51	3.49	2.67	4.44
Initial air volume (m^3)	70.8	71.9	71.4	71.9	71.8
Initial room temperature (°C)	18	17	17	22	19
Injection gas temperature (°C)	16/19	19	18.5	25	21
Orifice diameter (m)/ area (m^2)	-	1.13/1.0	0.62/0.3	-	-
Height of source above ground (m)	0.6	0.6	0.6	3.4	0.6
Test objective	Basic test density convection	Density convection with large orifice	Density convection with small orifice	Diffusion by change of source location	Replication of Test No. 1 with constant $\dot{m}$

Table 4.3 (cont'd)

	Test No. 6	Test No. 7	Test No. 8	Test No. 9
Duration of release (sec)	1080 + 6480	28800	37080	32400
Gas mixture N_2/H_2 (volume %)	34/66	34/66	34/66	34/66
Release rate (m^3/sec)	6.528E-4/ 2.722E-4	1.206E-4	1.286E-4	1.169E-4
Total released volume (m^3)	0.7/1.67	3.15	4.77	3.79
Initial air volume (m^3)	72.0	81.0	81.8	81.4
Initial room temperature (°C)	35/19	16	13	9
Injection gas temperature (°C)	19	14	12	7
Orifice diameter (m)/ area (m^2)	1.13/1.0	-/1.0	-/0.3	-/0.3
Height of source above ground (m)	0.6	0.25	0.25	1.5
Test Objective	Density convection with thermal layering	Basic test-different geometry	Convection & diffusion with small orifice	Change of injection location

The chief parametric investigations of this series involve injection rate, source location, orifice-size and placement, initial compartment temperature distribution, compartment geometry and orientation. The observations drawn from these tests are as follows.

The injection rate affected mixing in that rates below 6×10^{-4} m^3/sec resulted in very homogeneous mixtures while heterogeneities developed at faster rates. The concentration profile of Test No. 4 in which the source was located at the geometry mid-height exhibited a distinct difference between the upper and lower portions. The upper portion contained a nearly homogeneous mixture while a gradient existed below. In fact, the lower region behavior was compared to a pure one-dimensional diffusional problem. From this analysis the BF personnel estimated a binary H_2/air diffusion coefficient ranging from 6×10^{-5} to 6.3×10^{-5} m^2/sec which compares very well with literature value around 6.1×10^{-5} m^2/sec. Similar results were obtained in the horizontally-connected geometry. These findings indicate that a source located in an unfavorable location can induce substantial non-uniform concentrations if convective effects are supressed.

Two different orifice sizes were used in both geometries. The cylindrical geometry data indicates that a phenomena which might be called a "critical orifice size" exists such that larger openings have little effect on intercompartmental mixing while small openings cause stratification and

retardation of mixing. The effect of orifice size is less noticeable in the horizontal geometry where concentration differences between compartments is nearly proportional to orifice area. (In quantitative terms, at 15000 seconds into each experiment, a difference of 0.4% was observed in the 1.0 m^2 case (No. 7) while a difference of 1.2% was seen in the 0.3 m^2 case (No. 2).)

In test No. 6 an initial compartment temperature inversion is introduced in order to test the effects of the stratification on hydrogen transport. A dramatic difference in hydrogen concentration is observed between the two compartments. For example at 5000 seconds, the average concentrations of the upper and lower portions of the vessel are 1% vs 3.5%, respectively. The measurement station at the orifice also exhibited interesting behavior. Periodically, a rapid inflow to the upper compartment would occur indicating times when the buoyancy force of the lighter mixture overcame the blockage effect of the physical contraction and the thermal inversion. Nevertheless, these periodic inflows are not sufficient to substantially homogenize the vessel concentrations. Finally, the main finding in the area of compartment geometry and orientation is that the vertically connected compartments (cylindrical region) benefit from the buoyancy-induced convection to a significantly greater degree than the horizontally-joined geometry where small local convective and diffusion driven transport drive the flow.

The Phase II tests utilize multi-compartment geometries with longer term tests and more complex objectives. Phase II tests are also useful in the testing of lumped parameter models (see 4.4). Table 4.4 provides an overview of this testing program. These are four main parametric tests related to Phase II. They are assessments of the effect of a horizontally and vertically connected multi-room geometries, effect of various compartmental temperature distributions, reduction of injection rate with concurrent extention of testing period and finally, the use of helium as an alternative for hydrogen in order to allow higher concentrations in later tests.

The major empirical findings are the following. First, homogeneous concentrations within compartments result when the initial compartmental temperature distribution is uniform ($\Delta T < 2°C$) but thermal inversions do cause local concentration heterogeneities. However, the multi-compartment geometry aids in breaking down inversions due to the greater potential for destabilizing natural convective paths to develop. Local humidity has a distinct effect such that high humidity seems to favor local hydrogen accumulation. Third, the initial convection pattern has an important effect on the course of the transient. Fourth, air blowers or recirculation fans seem to provide effective mixing and finally, helium seems to be a reasonable substitute for hydrogen but the measurement system requires upgrading.

Table 4.4

List of Tests - Phase II

Parameter Test No.	Temperature Temp. Gradient	Injec. Loc. H_2	m_{H_2} m^3/h	Injec. Loc. He	m_{He} m^3/h	Individual Objective
10	CT	R1	1.5	-	-	Diffusion through convection without thermal effect
11	CT	-	-	R1, bottom	1.0*	Same as 10, suitability of helium as test gas
12	CT	R1	0.3	-	-	Same as 10, effect of injection rate
13	constant	R1	1.5	-	-	Same as 10, with hindering through thermal inversion, however
14	constant	R1	1.5	-	-	Same as 13, except for 6 additional sampling probes
15	constant	R1	0.3	-	-	Same as 12, effect of injection rate
16	constant	R1	1.5	-	-	Same as 14, noticeable eventual breakthrough, however
17	constant	R6	1.5	-	-	Effect of the injection location
18	variable	R1	1.5	-	-	Effect of the location of the heater coil
19	constant	R1	1.5	R1 bottom	2.0	Same as 13, except for breakthrough forced by the injection
20	variable	R1	0.3	-	-	Observation of Temp. Equalization
21	variable	-	-	-	-	Same as 20, except without H_2 injection

Table 4.4 (cont'd)

Parameter Test No.	Temperature Temp. Gradient	Injec. Loc. H_2	m_{H_2} m^3/h	Injec. Loc. He	m_{He} m^3/h	Individual Objective
22	constant	R1	1.5	R1, bottom horizontal	3.0	Same as 19, except for higher He injection rate (intermixing)
23	constant	R1	1.5	-	-	Same as 13, except intermixing by concentration fan v = 15 m^3/hr

Gen.: Injection gas 67% H_2 (or He)/33% N_2; max. hydrogen concentration 4%
Location of the overflow openings according to enclosed drawing (closed opening represented intersector)
* changed according to discussion report of 10/18/79

Table 4.5 is provided as an overall summary of the Phase I and II testing programs. Also included in this table is a compilation of tests which have been calculated using other analytical models and the model developed in this work.

4.3.1.2 Simulations Based On Selected Experiments

A number of simulation runs are reported in this section to demonstrate the slow mixing model's predictive capability of single phase mixing experiments. Two Phase I Battelle Frankfurt tests are emphasized. Both were conducted in the central cylindrical region of the facility with an orifice plate in place between the upper and lower regions. The first simulation set is based on BF Test 2 (designated hereafter as BF2) during which a hydrogen/nitrogen mixture was introduced near the floor of the lower region and the initial atmosphere is isothermal. A number of short term simulations of this test and some "thought experiment" variations on it are reported. First, a simulation of the first 200 seconds of the test is reported. Second, the same problem but without an orifice plate is studied. This open geometry case is also used for study of numerical procedure optimization and turbulence model behavior. Third, a complete closed orifice simulation is described to act as a point of comparison with the previous two results.

Table 4.5

BF Testing/Simulation Overview

	Test Numbers																						
	1	2	3	4	5	6	7	8	9	10	11	12	13	14	15	16	17	18	19	20	21	22	23
Convection	✓	✓	✓		✓	✓	✓	✓	✓	✓	✓	✓	✓	✓	✓	✓			✓			✓	✓
Diffusion				✓			✓	✓		✓	✓	✓	✓	✓	✓	✓	✓	✓	✓	✓	✓	✓	✓
Orifice Size		✓	✓					✓															
Thermal Stratification						✓				✓	✓		✓	✓		✓			✓	✓	✓	✓	✓
Injection Rate					✓							✓			✓				✓			✓	
Source Location				✓					✓								✓	✓					
He vs H_2											✓											✓	
Heater Coil																			✓				
Calculated by	1 3 5	12 34 57	2 5	2 3 5	5	12 4 76				4		1 76	1		6				4				

Notes

Test 5 - Same as 1, except $\dot{m}$ corrected.
Test 13 - Thermal inversion.
Test 14 - Same as 13, but additional sampling points.
Test 16 - Inversion varied to cause breakthrough.
Test 21 - H_2 not used.
Test 23 - Same as 13, except fan used.

Calculated by:

1 - Jahn (GRS) - RALOC
2 - Trent et.al. (BNWL) - Tempest
3 - Travis et.al. (LANL) - HMS
4 - Buxton et.al. (Sandia) - RALOC
5 - KWU model
6 - Thurgood (BNWL) - COBRANC
7 - LIMIT (MIT)

BF Test 6 (BF6) is the second experiment emphasized in these single-phase slow mixing validation runs. This test is similar to BF2 except the injection rate is higher (by approximately a factor of two) and a stable thermal stratification existed prior to injection. A number of both short- and long-term test simulations are reported. The first set of results are based on a coarse mesh model. The coarse mesh limits the spatial definition of the inversion behavior. It also amplifies numerical diffusion effects in areas of significant intermesh crossflow as is typical of inversion interfaces. The second simulation demonstrates the predictive accuracy gained by optimizing the mesh definition, modelling solid heat sinks and reducing numerical dispersion.

The coarse mesh model of the BF facility used in all simulations save for the final BF6 series of calculations is depicted in Figure 4.16. A 32 node, two-region problem zone is defined assuming two-dimensional axisymmetry along the centerline. In all cases the lower three left-hand cells are source cells. Five particular cells are designated with letters (A through E) which denote areas which are referenced in the resultant figures. Finally, a selected group of hydrogen and temperature sensor locations are designated by numbers. These are also used in subsequent figures to allow easier simulation/empirical data comparison.

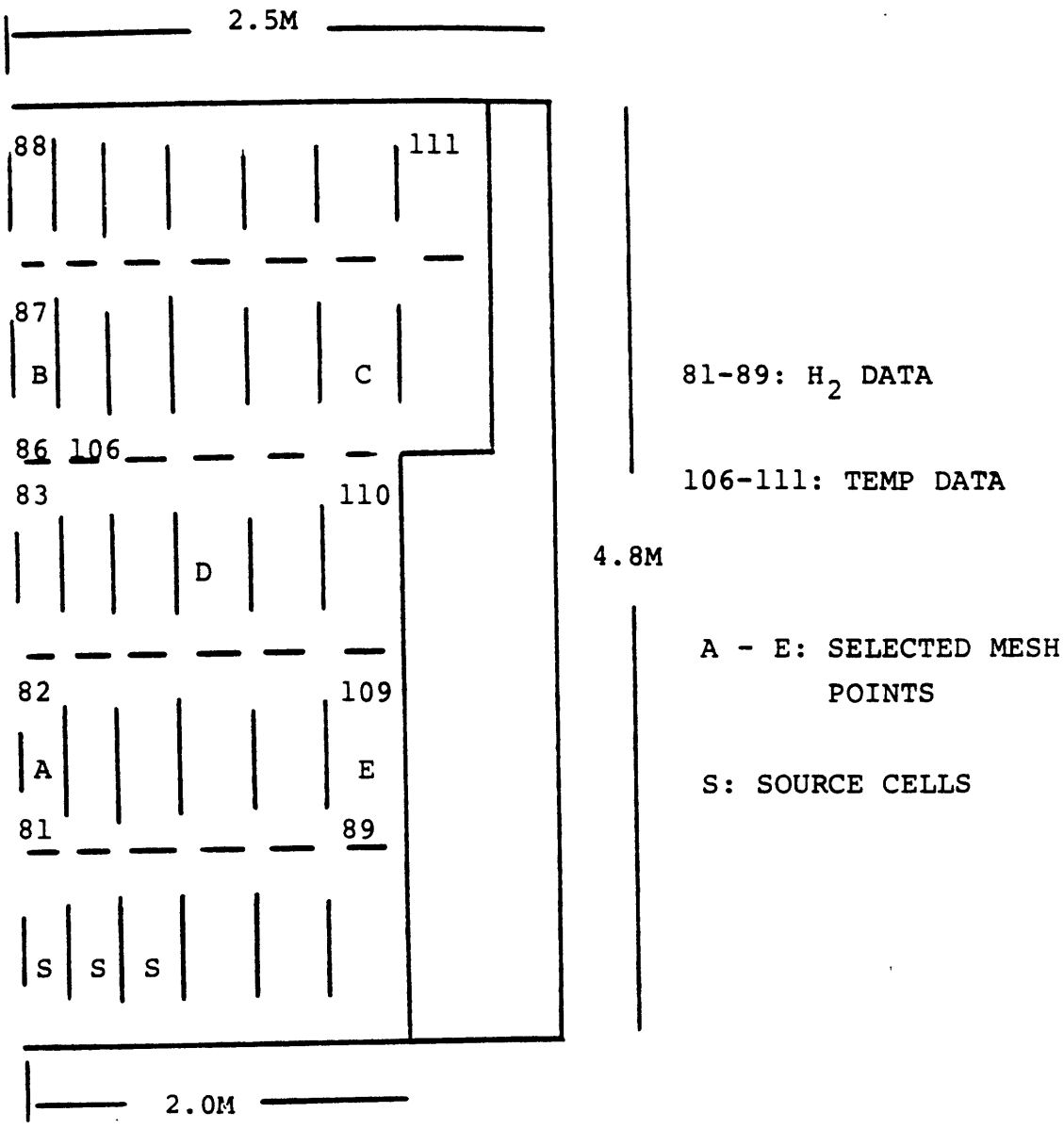

FIGURE 4.16: BASIC 32 NODE MODEL OF BATTELLE FRANKFURT INNER VESSEL USED IN MOST SIMULATIONS

4.3.1.2.1 Scenario Based On BF2

This simulation describes the first 200 seconds of the BF2 test. A minor difference between the simulation and experiment is that while the source introduction was spatially uniform (radially) in the test, the simulation assumed a slightly skewed (bias away from centerline) definition. The assymmetry was small (10% or so) and should not inhibit useful comparison. An initially uniform air atmosphere at a temperature of 17°C is assumed to exist, into which a 19°C 66%/34% (by volume) H_2/air flow is introduced at a rate of 1.19 m^3/hr. A laminar isothermal flow field is assumed. Figures 4.17, 4.18 and 4.19 depict the predicted velocity and hydrogen concentration fields at 20, 100 and 200 seconds, respectively. At 20 seconds the circulation induced by the lighter hydrogen is developing in the lower region, while the upper region is as yet unaffected save for a small net inflow due to the expansion present in the lower region. The H_2 profile reflects this scenario. The flow fields at 100 and 200 seconds are very similar. The developed velocity field involves a strong central jet of hydrogen-rich flow which continues through the orifice region into the upper region. The central flow causes shear driven (due to walls and orifice plate) recirculations in both regions. A number of other interesting observations are noted. The mixture becomes stably stratified away from the central region in both the upper and lower regions. The shear driven

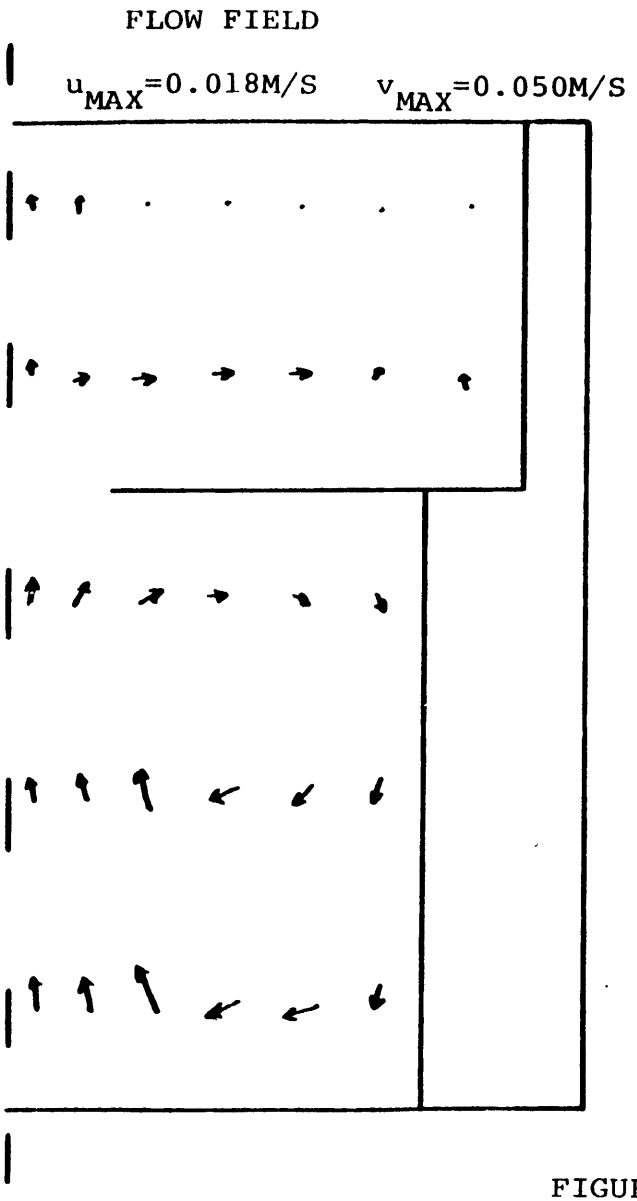

H_2 VOLUME FRACTION

3.1-13	8.3-13	3.2-16	7.4-20	5.9-24	1.7-28	1.2-33
1.5-9	5.3-9	3.9-12	1.2-15	1.6-19	3.5-24	1.6-28
1.1-6	4.9-6	1.3-5	1.9-7	9.5-10	1.2-12	---
8.3-5	2.5-4	4.1-4	4.5-4	1.1-6	5.6-9	---
1.1-3	1.6-3	1.5-3	2.6-6	1.1-8	2.4-11	---

FIGURE 4.17: BF2 SIMULATION AT 20 SECONDS

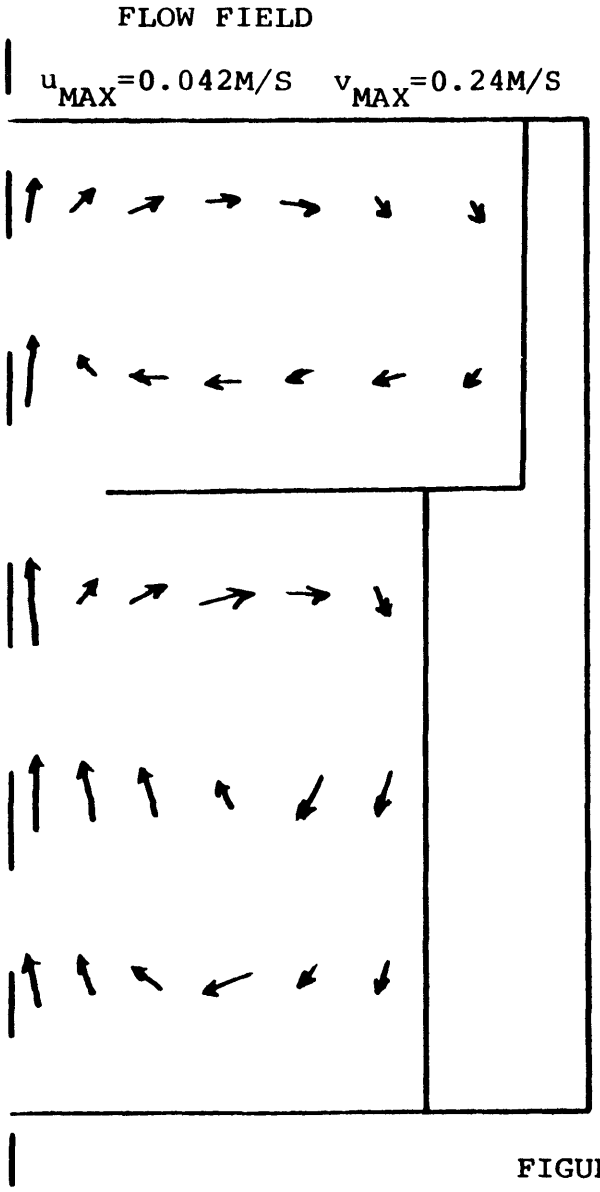

H_2 VOLUME FRACTION X 1000

2.0	1.0	0.85	0.49	0.10	5.8-3	7.9-5
2.0	0.06	0.02	0.03	3.7-5	8.7-5	5.9-7
2.0	0.88	0.84	0.81	0.86	0.88	---
2.1	1.5	0.70	0.44	0.63	0.77	---
2.3	1.7	1.1	0.18	0.26	0.41	---

FIGURE 4.18: BF2 SIMULATION AT 100 SECONDS

FLOW FIELD

u_{MAX}=0.054M/S v_{MAX}=0.26M/S

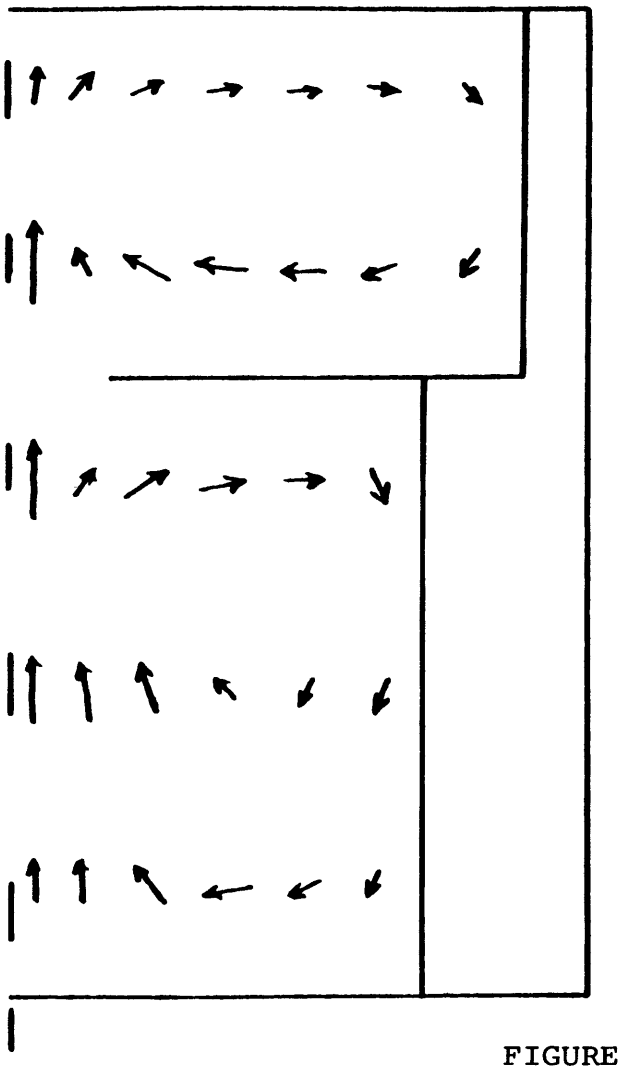

H_2 VOLUME FRACTION X 1000

2.6	1.5	1.2	1.0	0.94	0.87	0.73
2.6	0.27	0.31	0.36	0.43	0.53	0.59
2.7	1.3	1.3	1.2	1.2	1.1	---
2.8	2.1	1.3	0.94	1.0	1.0	---
2.9	2.3	1.7	0.76	0.80	0.86	---

FIGURE 4.19: BF2 SIMULATION AT 200 SECONDS

recirculation produces a hydrogen gradient along the principal flowpaths.

The development history of the velocity field is shown in Figure 4.20. Also plotted is the Courant time step size. The velocity profile requires roughly 50 seconds to develop and thereafter remains relatively unchanged. The hydrogen volume fraction transients at five selected locations are plotted in Figure 4.21. The concentration gradient peak at the centerline is also evident in this figure. The behavior of point D is noteworthy in that it is not monotonic. The physical explanation of the behavior is as follows. The lower region major recirculation loops develop faster than that of the upper region. Secondly, the buoyant central plume takes some time to penetrate the orifice and reach the facility ceiling where it will turn and cause clockwise flow in the upper region. Prior to the development of the upper region flow field, relatively hydrogen rich flow is directed at D. After the upper circulation commences, hydrogen-free atmosphere is pumped down into the lower region through the right half of the orifice. This dilutant stream is entrained in the lower recirculation and is convected to D. This depression is transitory since eventually the dilutant effect diminishes as the upper region gains hydrogen.

The actual experiment ran for a few hours. However, the short-term predictions can be compared to early data

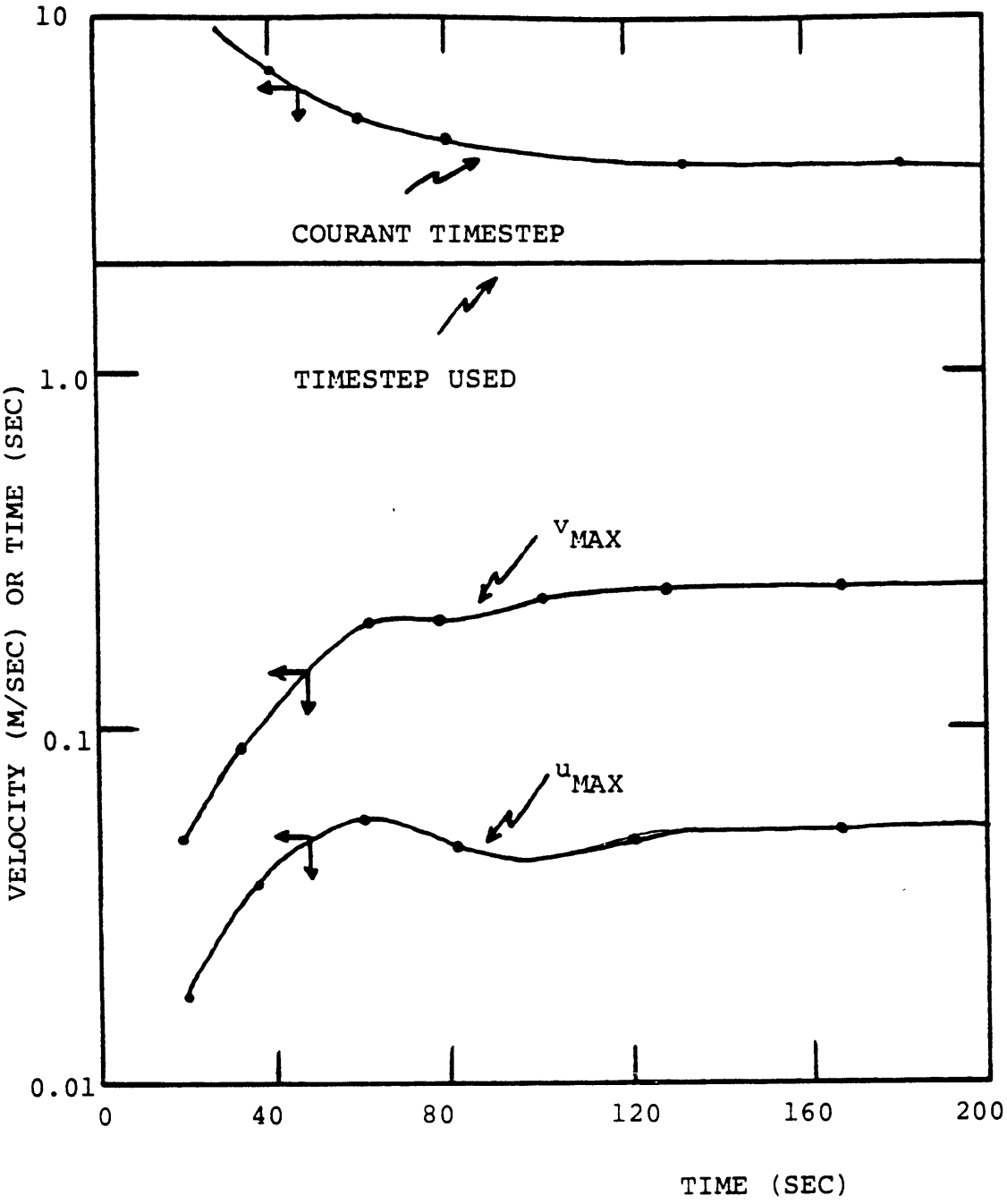

FIGURE 4.20: DEVELOPMENT OF VELOCITY FIELD DURING BF2 SIMULATION

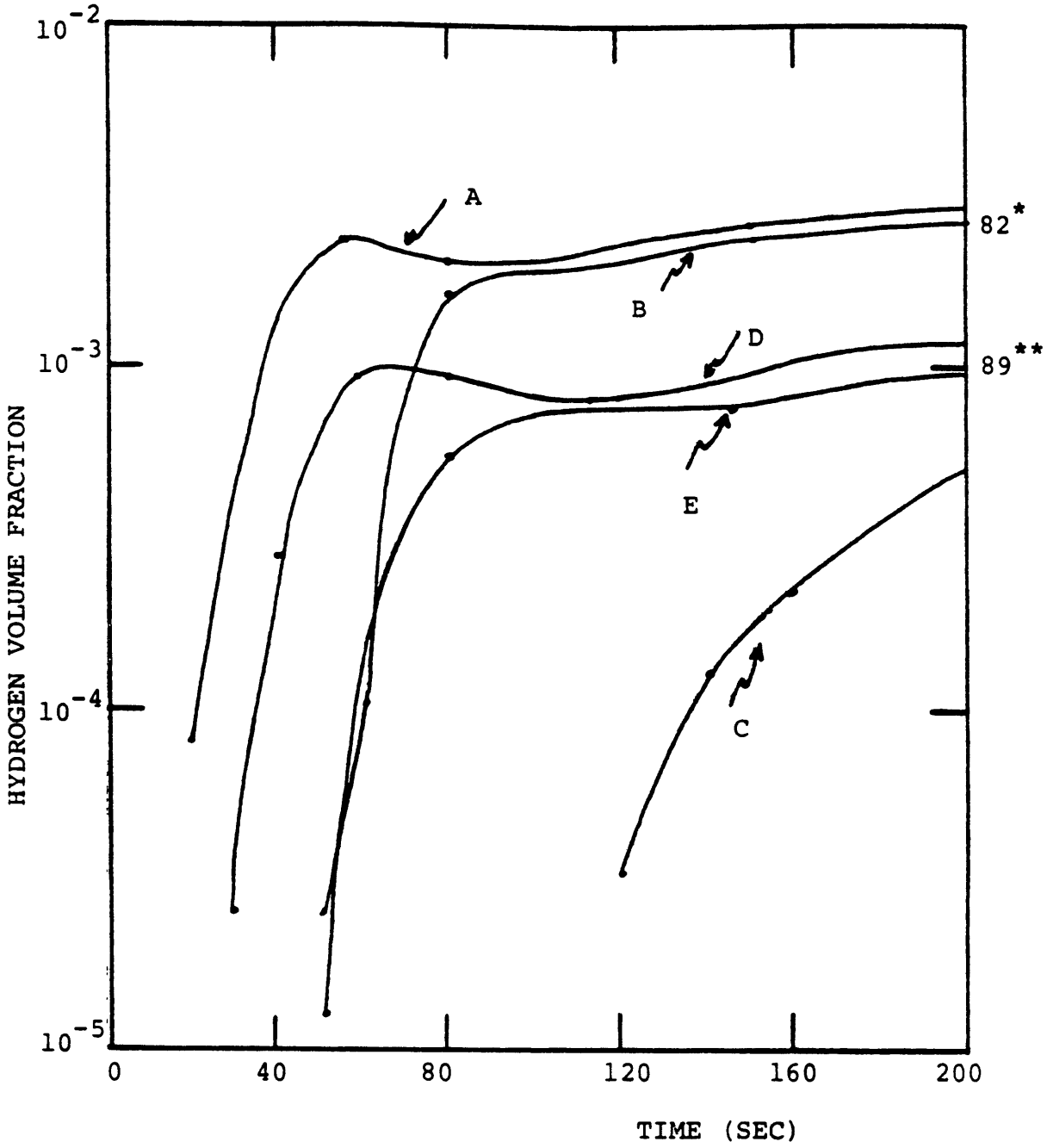

*APPROXIMATE READING AT MEASUREMENT POINT 82

**APPROXIMATE READING AT MEASUREMENT POINT 89

FIGURE 4.21: HYDROGEN CONCENTRATION TRANSIENTS

measurements. The measured hydrogen concentrations at sensor locations 82 and 89 are indicated in Figure 4.21. Good agreement is seen. Further extrapolation of the short-term predictions indicate good physical agreement with the general findings of BF2.

4.3.1.2.2 Completely Open Compartment

This simulation is identical to the previous one except the orifice plate is completely removed. This case is similar to the BF Test 1 except that different source flow rates are used. This problem is discussed to illustrate the effect of the orifice upon the physical phenomena and the computational effort involved. The flow field and H_2 concentration profile at 100 seconds is depicted in Figure 4.22. When this figure is compared to Figure 4.18 it is seen that the open geometry leads to more uniform hydrogen concentrations with small axial and radial gradients. An extreme example of this difference is the upper left node of the domain where the hydrogen concentrations are 7.6-4 and 7.9-8, respectively, in the two cases. The velocity field develops at nearly the same rate as in the previous case and the terminal velocity magnitudes were similar in both cases. The development of the flow field is illustrated in Figure 4.23. Nevertheless, significant differences between the fully open and orificed geometry are evident. The velocity magnitudes are nearly 20% higher in the open geometry demonstrating the flow resistance afforded by the

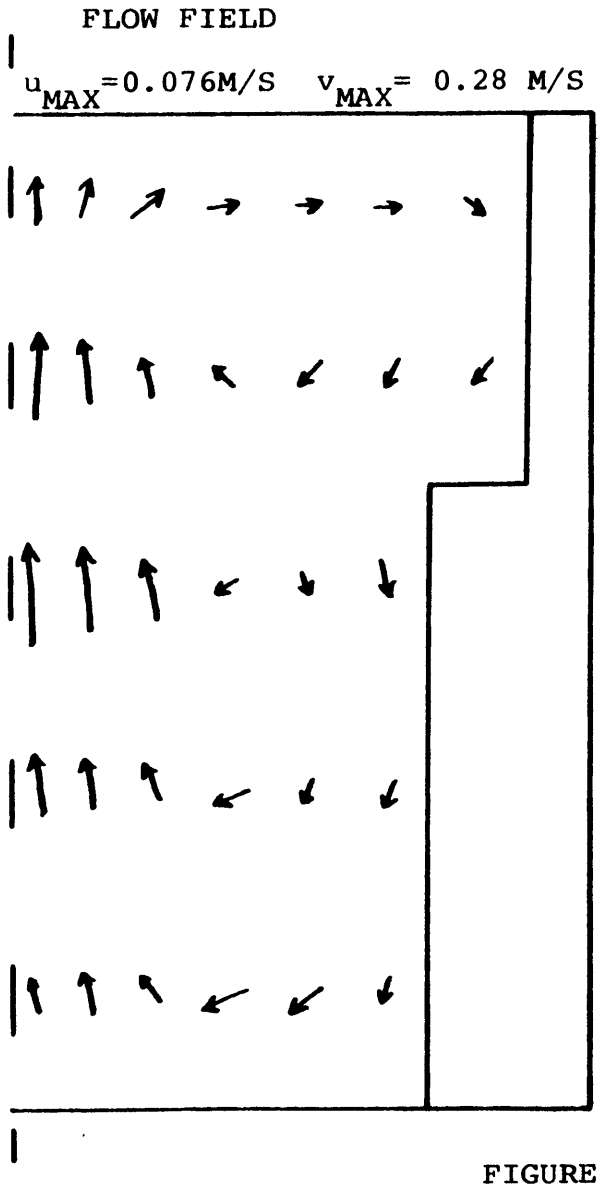

H_2 VOLUME FRACTION X 1000

1.9	1.4	1.1	0.87	0.77	0.77	0.76
1.9	1.1	0.47	0.29	0.37	0.50	0.61
1.9	1.0	0.42	0.20	0.21	0.20	---
2.0	1.2	0.51	0.09	0.11	0.09	---
2.2	1.5	0.90	0.03	0.03	0.03	---

FIGURE 4.22: OPEN FACILITY SIMULATION AT 100 SECONDS

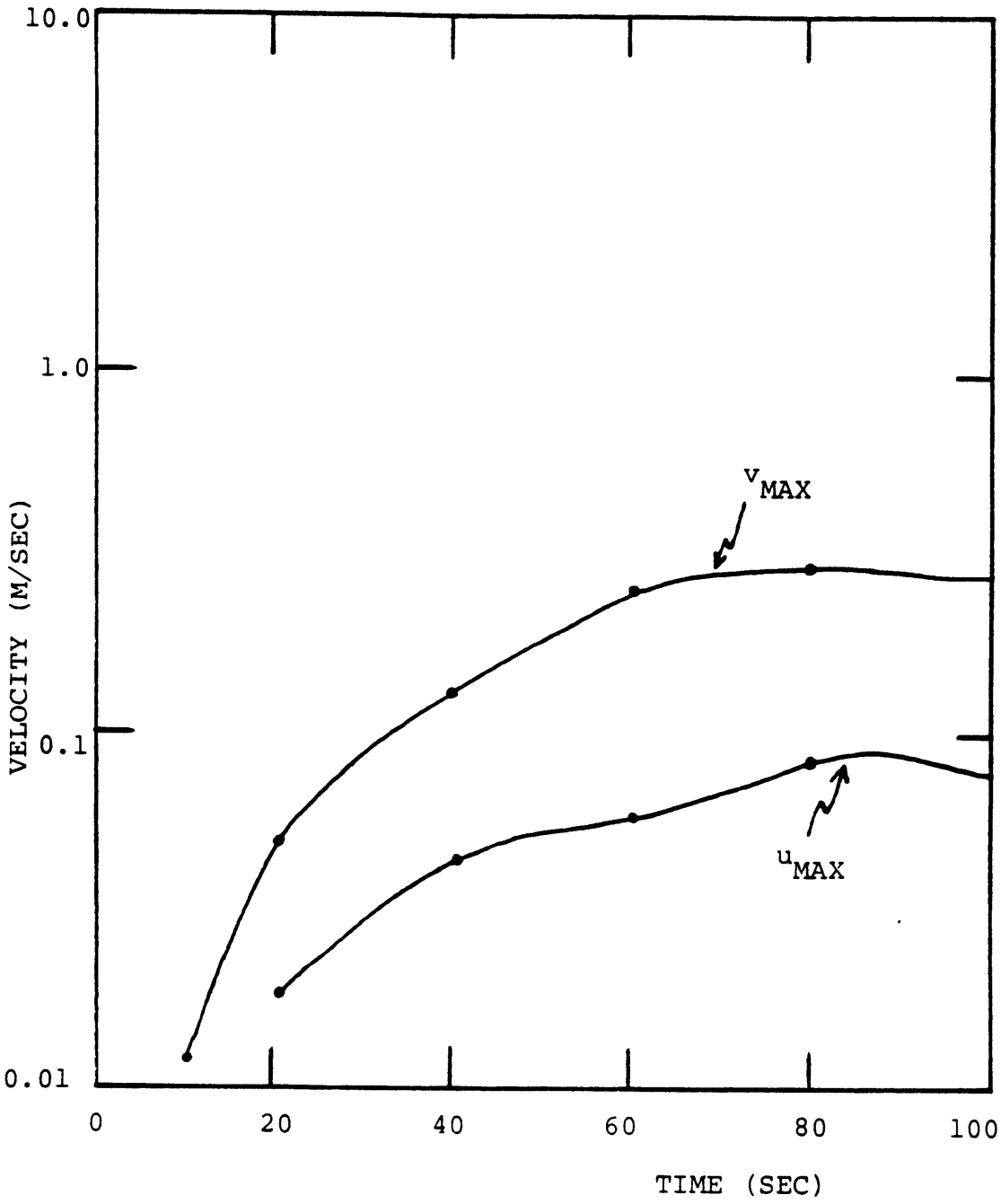

FIGURE 4.23: DEVELOPMENT OF VELOCITY FIELD DURING OPEN FACILITY SIMULATION

orifice. The stable stratification of the non-source regions spans the entire height of the facility. The "shelf-region" of the upper volume causes a slight upward velocity trajectory which inhibits the formation of a large single recirculation region but instead two distinct upper and lower circulations develop.

The hydrogen concentration transients of five selected locations are presented in Figure 4.24. It is interesting to note that point D displays similar qualitative behavior as seen before. The physical scenario however, is a bit different in that this transitory depression of hydrogen abundance is caused by the location of D in the border region to two low flow recirculation foci. The orifice effect is also clear in that all centerline locations lead other regions regardless of elevation.

As described in Chapter 3, successive over-relaxation is employed in the SMAC solution procedure. The degree of over-relaxation is a free parameter selected by the analyst. The results of a sensitivity study of this value for BF-type transients was performed using this scenario as the benchmark. The results of the study are summarized in Table 4.6.

Table 4.6

Over-relaxation Factor	Average Iterations Per Cycle
1.5	41
1.7	31
1.8	27
1.9	33

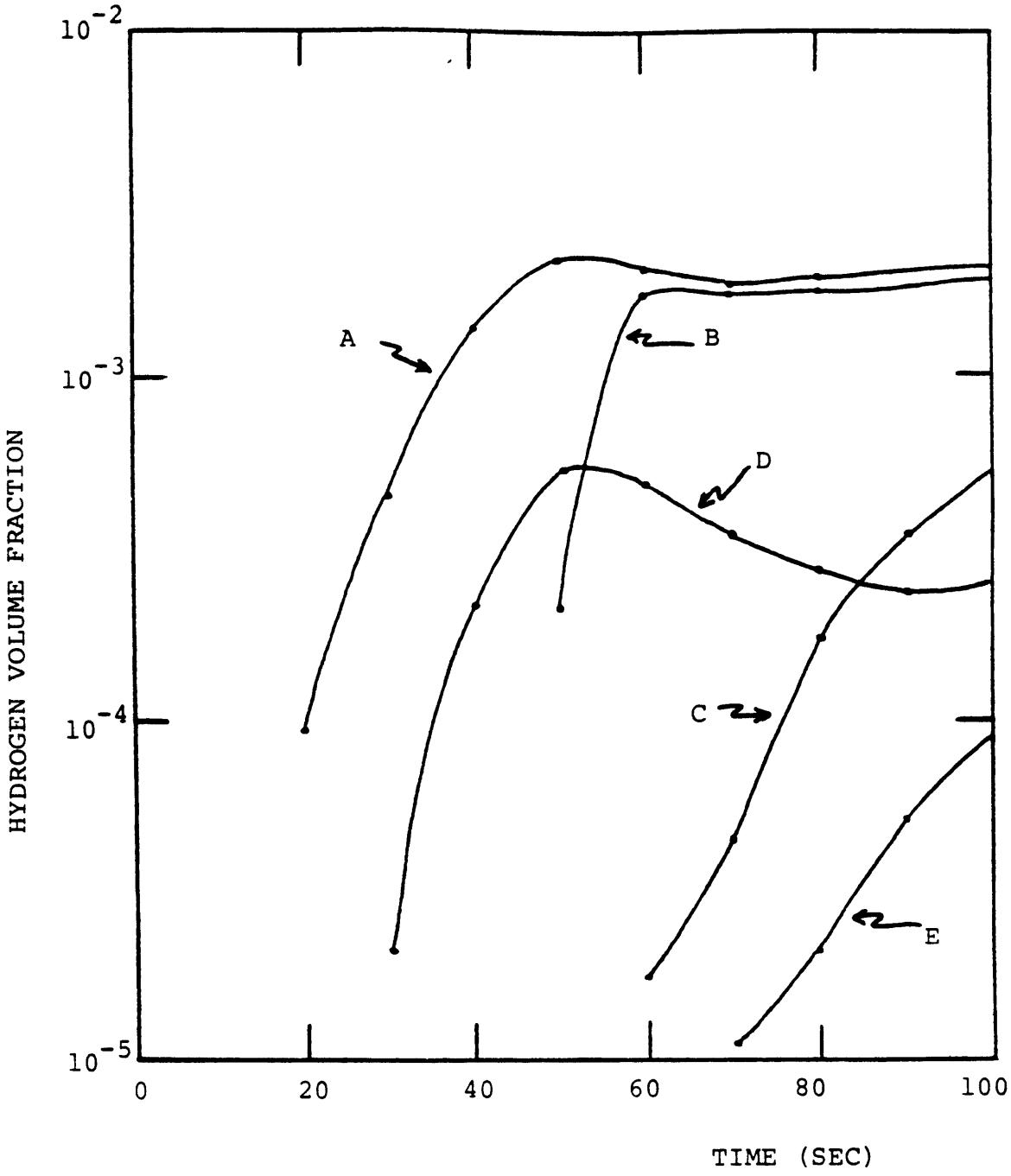

FIGURE 4.24: HYDROGEN CONCENTRATION TRANSIENTS DURING OPEN FACILITY SIMULATION

The optimized over-relaxation factor of 1.8 is then used in all subsequent runs having a similar nodalization. In all cases, identical physical results accrued.

Turbulent diffusion is not physically dominant in these relatively low flow tests. This is apparent when convective and diffusional velocities are compared. Consider this open-facility simulation. The radial (u-component) velocities are of the order of 10^{-2} m/sec. The diffusional velocity is the product of the diffusivity and gradient. The maximum predicted concentration gradients are on the order of 1/m which would require a diffusivity of 10^{-2} m^2/sec to produce an effect comparable to the convective transport. A simulation using an initially uniform turbulence field corresponding to mass diffusivities of approximately 10^{-4} m^2/sec showed the diffusional effect to be negligible even though this level of turbulent diffusion enhances overall diffusion by a factor of 10 (i.e., $D^T/D^m=10$). The behavior of the predicted turbulent kinetic energy, dissipation and turbulent diffusivity is depicted in Figure 4.25. This low flow transient illustrates a case when a turbulence model applicable to transitional flow is desirable.

4.3.1.2.3 Completely Closed Orifice

The final case in this BF2-based series involves a completely closed orifice (i.e., single lower region problem). Figure 4.26 shows the hydrogen and flow field at 100 seconds. In this short time a very uniform concentration field has developed. The flow field developed faster than

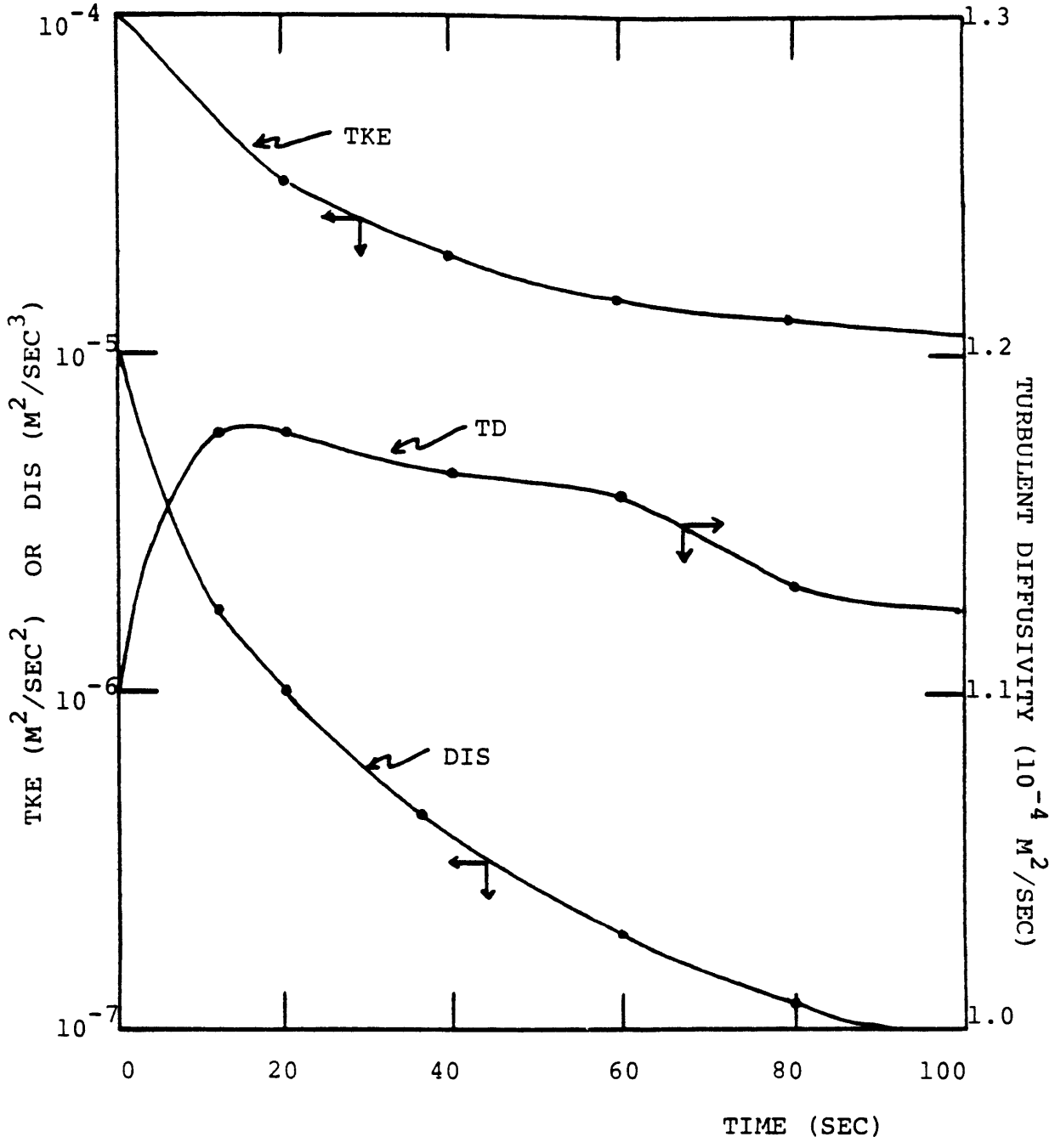

FIGURE 4.25: BEHAVIOR OF TURBULENCE PARAMETERS DURING OPEN FACILITY SIMULATION

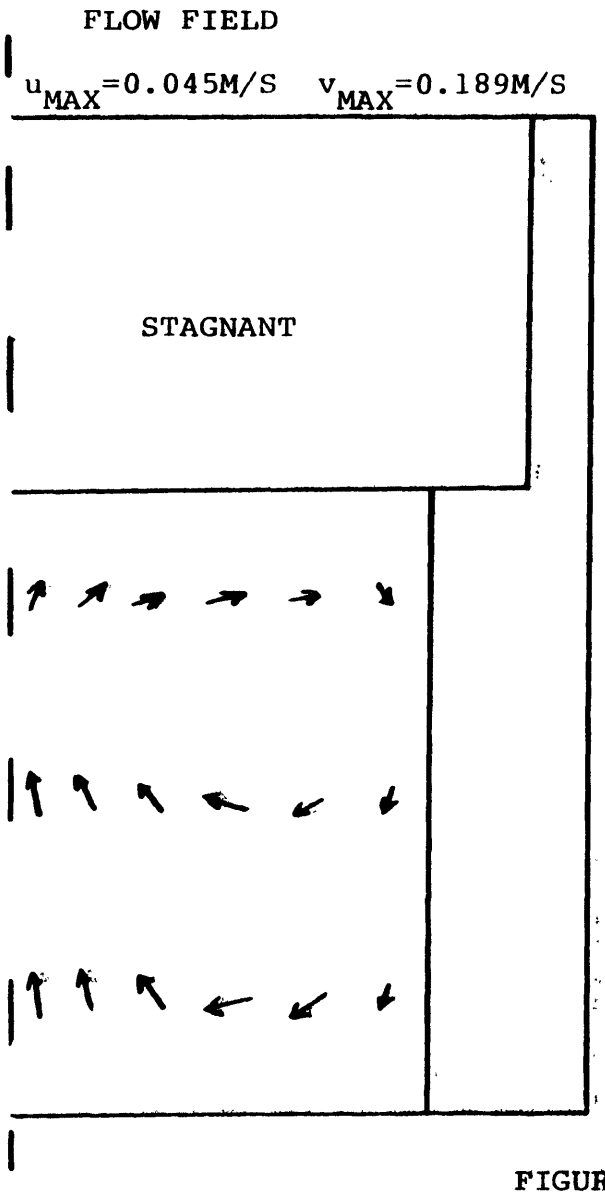

H_2 VOLUME FRACTION X 1000

0	0	0	0	0	0	0
0	0	0	0	0	0	0
2.1	1.6	1.3	1.1	1.1	0.98	---
2.1	1.4	0.67	0.50	0.70	0.83	---
2.3	1.7	1.1	0.18	0.27	0.44	---

FIGURE 4.26: CLOSED FACILITY SIMULATION AT 100 SECONDS

in the previous two cases (elapsed time of about 30 seconds), but the magnitude of the axial velocity components are less than the previous simulations due to the retarding effects of the enclosing walls.

4.3.1.2.4 BF Test No. 6 Simulation I - Coarse Mesh

This test was performed in the same geometry as the BF2 test. However, a stable thermal atmospheric inversion was introduced prior to hydrogen injection. The upper region was heated to approximately 35°C while the lower region's temperature was 19°C. These are approximate temperature values as the exact temperature distribution was not measured. A 66/34 H_2/N_2 mixture was introduced in the lower region at an initial rate of approximately 2.3 m^3/hr. At 1080 seconds this rate was reduced to 0.9 m^3/hr which was maintained until 7460 seconds at which time all injection was terminated. The simulation reported here uses laminar flow modelling (turbulence model not employed), no heat sinks are modelled, and the coarse 32 node mesh discretization. The limitations of these assumptions are illustrated in the reported results.

The flow and hydrogen fields at 20,100 and 200 seconds are depicted in Figures 4.27, 4.28, 4.29, respectively. A comparison with the calculated fields for the BF2 and completely closed orifice predictions at 100 seconds is enlightening. The BF6 result is distinctly different from the BF2

FLOW FIELD

u_{MAX}=0.034M/S v_{MAX}=0.087M/S

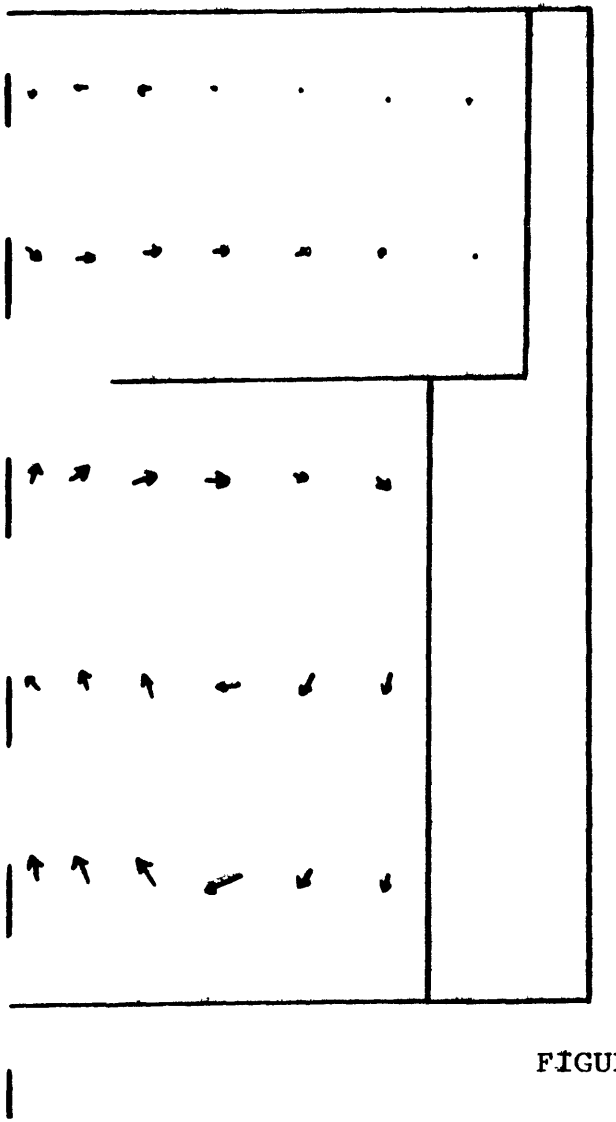

H_2 VOLUME FRACTION

1.5-12	1.3-12	4.5-13	2.2-16	2.3-20	7-25	4.4-30
7.6-8	6.4-8	4.6-10	7.7-13	2.7-16	2-20	4.5-25
8.8-5	9.1-5	6.1-5	2.6-6	3.2-8	8.6-11	---
1.2-3	1.2-3	9.1-4	1.7-4	8.2-6	7.5-8	---
3.5-3	3.2-3	2.0-3	1.0-5	1.6-7	7.2-10	---

FIGURE 4.27: BF6 SIMULATION AT 20 SECONDS

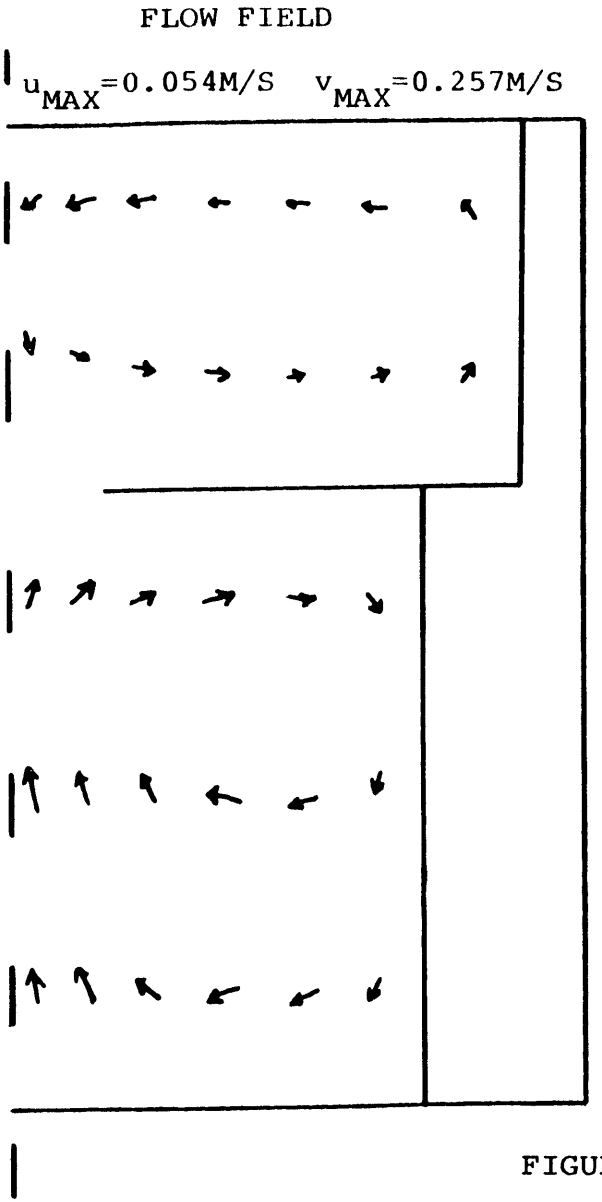

H_2 VOLUME FRACTION X 1000

0.0037	.0046	.0058	.0075	0.010	0.014	0.013
0.39	0.19	0.12	0.088	0.072	0.064	0.034
4.4	3.2	2.5	2.3	2.1	1.9	---
4.5	2.6	1.4	1.4	1.6	1.6	---
5.0	3.5	2.3	0.71	0.72	0.95	---

FIGURE 4.28: BF6 SIMULATION AT 100 SECONDS

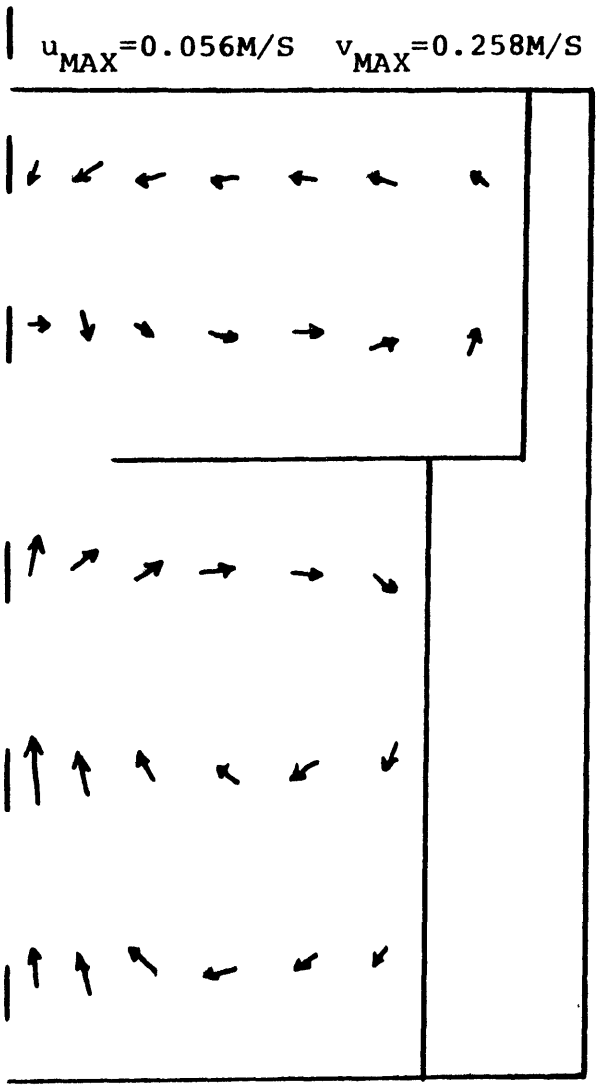

H_2 VOLUME FRACTION X 1000

0.049	0.056	0.062	0.070	0.079	0.091	0.098
0.65	0.37	0.27	0.21	0.19	0.17	0.13
6.2	5.0	4.4	4.1	3.9	3.7	---
6.3	4.3	3.2	3.2	3.4	3.4	---
6.7	5.1	3.9	2.3	2.3	2.6	---

FIGURE 4.29: BF6 SIMULATION AT 200 SECONDS

simulation. The general flow pattern shows the lower region involved in the hydrogen transport with its resultant circulation while the upper region shows a small counterclockwise circulation and very little hydrogen inflow. The counterclockwise upper flow is caused by the flow diversion of the central plume from its vertical trajectory by the inversion layer. The inversion layer effect is further evidenced in the inverse hydrogen stratification predicted in the upper region. In fact the BF6 flow pattern is very similar to the completely-closed orifice simulation described previously. The hydrogen field reflects the same in that the BF6 concentration profile of can be predicted by doubling the simulated profile of the closed geometry. This is completely consistent given the initial BF6 injection rate is roughly twice that assumed in the closed facility simulation.

Hydrogen concentration transients for the five selected locations during this early period (0-200 seconds) are plotted in Figure 4.30. The predicted concentration of 0.63% at A (200 seconds) compares very well with the measured value of 0.65 ± 0.05%. The development of the velocity field is depicted in Figure 4.31. Local mixture densities are reported in Figure 4.32. The lower region exhibits lower mixture density due to hydrogen inflow and some transient heating due to thermal mixing at the orifice. The upper region density increases due to the influx of cooler,

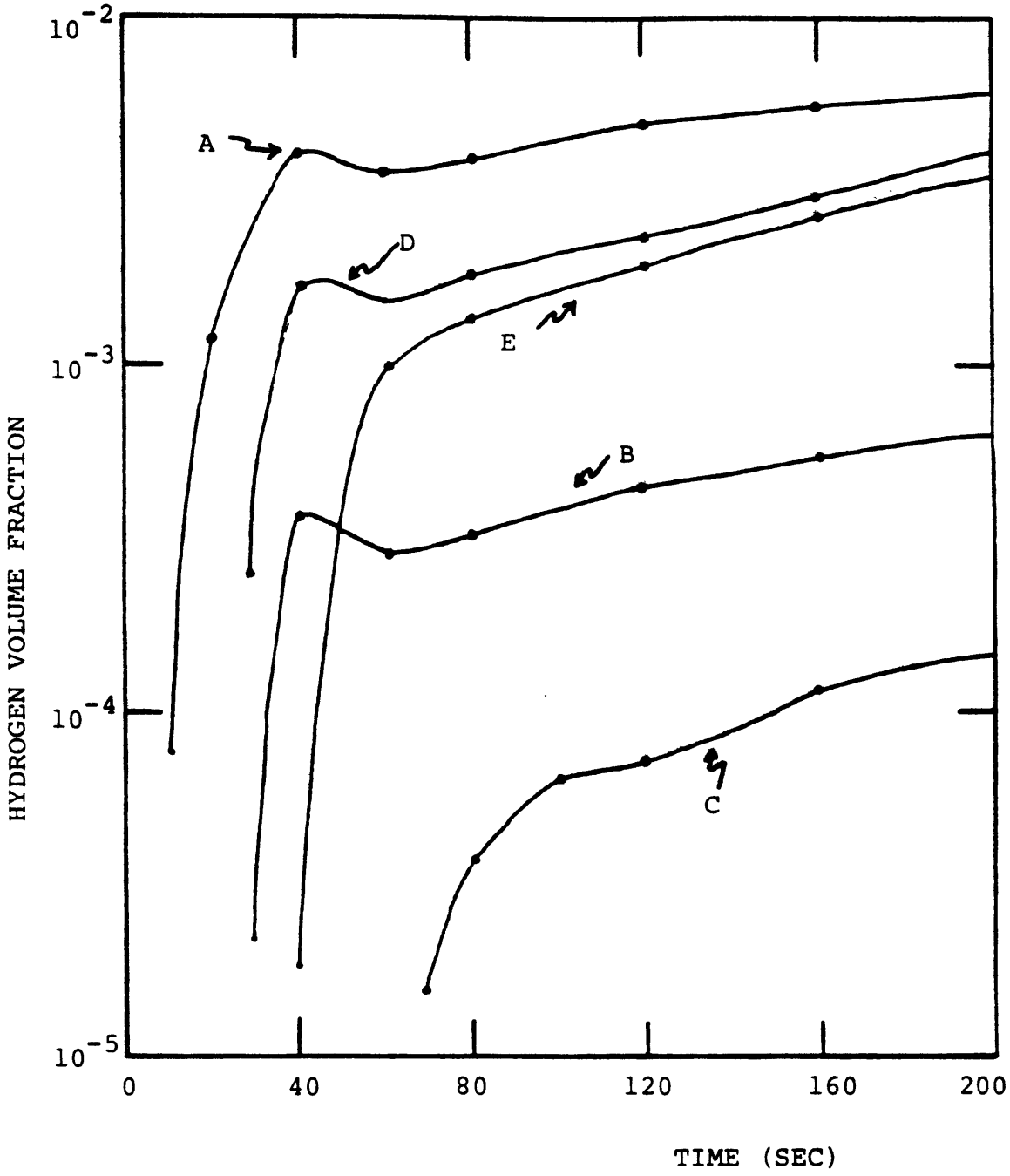

FIGURE 4.30: HYDROGEN CONCENTRATION TRANSIENTS DURING FIRST 200 SECONDS OF BF6 SIMULATION

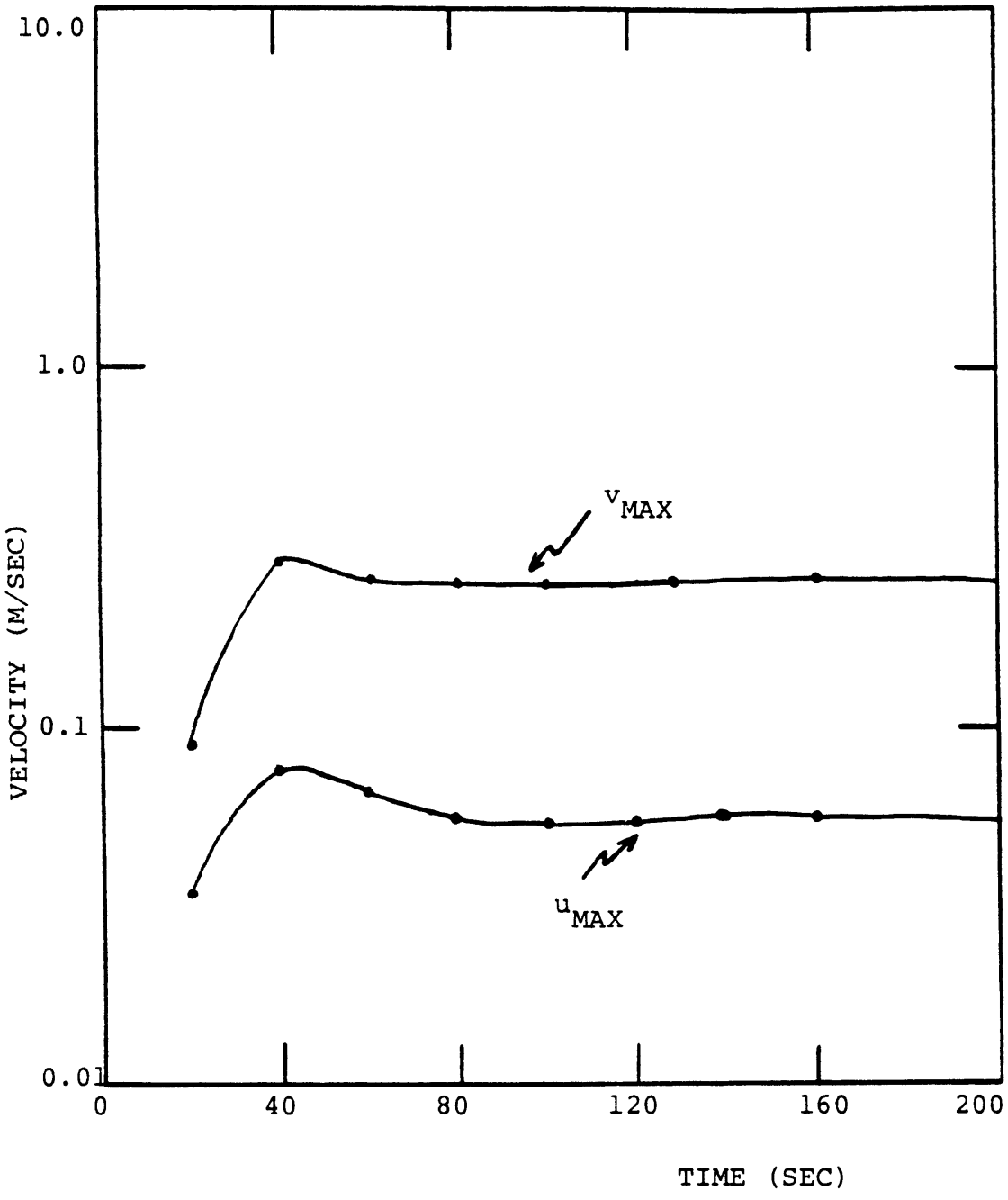

FIGURE 4.31:VELOCITY FIELD DEVELOPMENT DURING FIRST 200 SECONDS OF BF6 SIMULATION

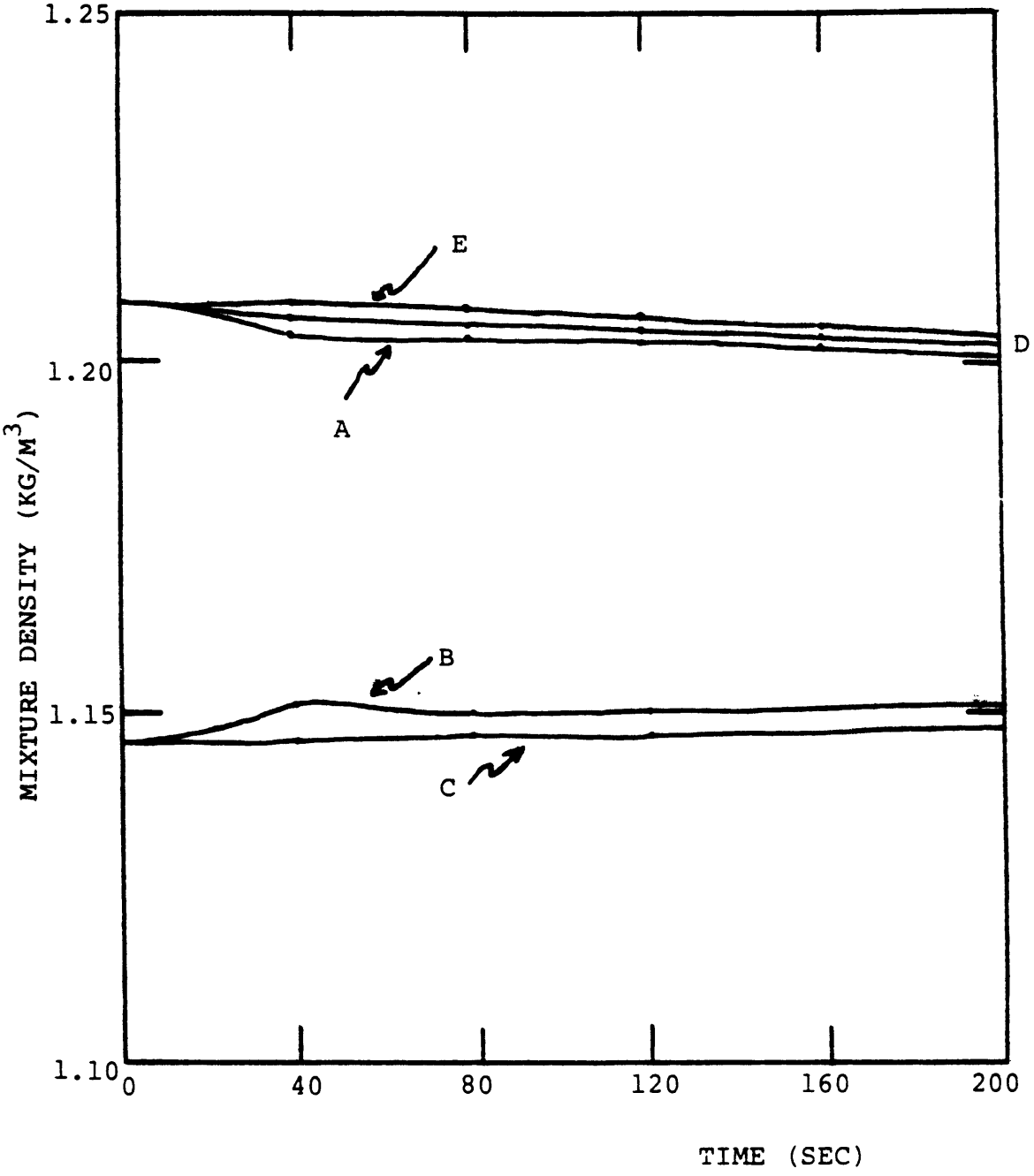

FIGURE 4.32: MIXTURE DENSITY TRANSIENTS DURING FIRST 200 SECONDS OF BF6 SIMULATION

hydrogen-starved air.

The predicted field at 2000 seconds (see Figure 4.33) is qualitatively similar to the 200 second prediction. However, the lower region hydrogen profile is distinctly homogeneous compared to earlier times but the inversion remains apparent. The magnitude of the maximum vertical velocity has decreased from 0.257 to 0.186 m/sec indicating the decreasing buoyancy effect as the global condition gains hydrogen. The 4000 second fields shown in Figure 4.34 are distinctly different from the 2000 second prediction. The flow pattern is not characterized by a central and vertical plume that penetrates the intrafacility height. The counterclockwise upper circulation has been replaced by a clockwise flow. The velocity magnitude has increased and hydrogen is nearly uniformly mixed. No inversion is apparent. The field is nearly identical to the isothermal BF2 test.

The hydrogen volume fraction transient for points A and B are compared to data from the comparable sensor locations for the first 5000 seconds of the test in Figure 4.35. The code predictions agree well with empirical data until roughly 2000 seconds when the code predicts the breakdown of the inversion while in reality the inversion remained in place. Mixture temperature and density at points A and C are plotted in Figures 4.36 and 4.37, respectively. A comparison of the temperature at C with temperature measurement station 106 data shows the predictions exhibit a

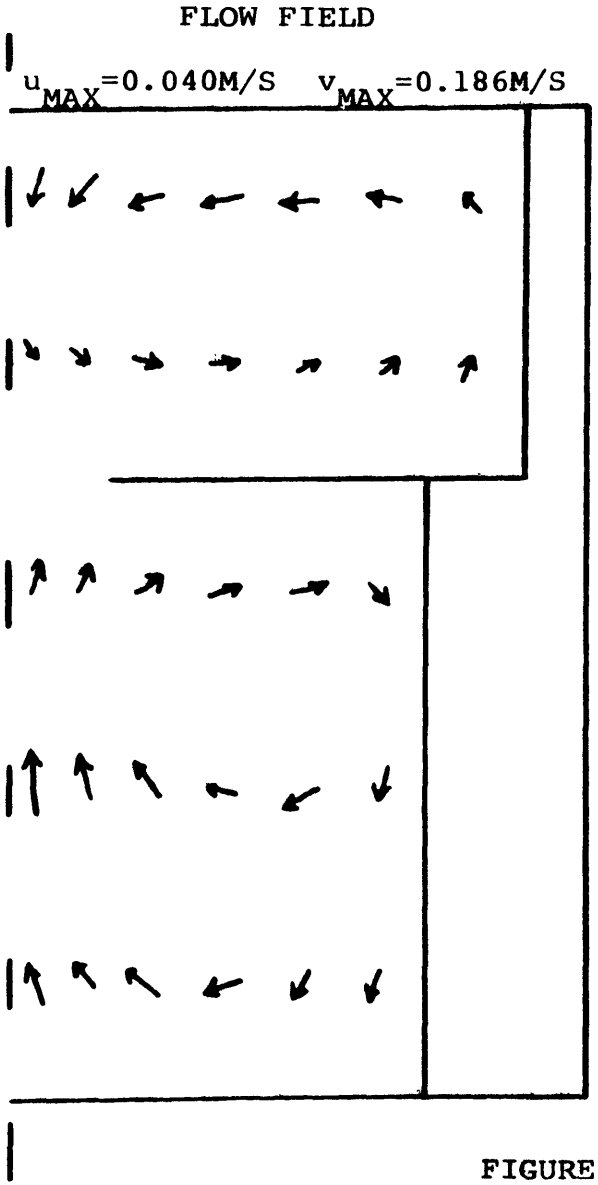

H_2 VOLUME FRACTION X 100

0.51	0.52	0.52	0.53	0.53	0.54	0.55
0.82	0.68	0.63	0.61	0.59	0.58	0.56
2.4	2.3	2.3	2.2	2.2	2.2	---
2.4	2.3	2.2	2.2	2.2	2.2	---
2.4	2.3	2.3	2.2	2.2	2.2	---

FIGURE 4.33: BF6 SIMULATION AT 2000 SECONDS

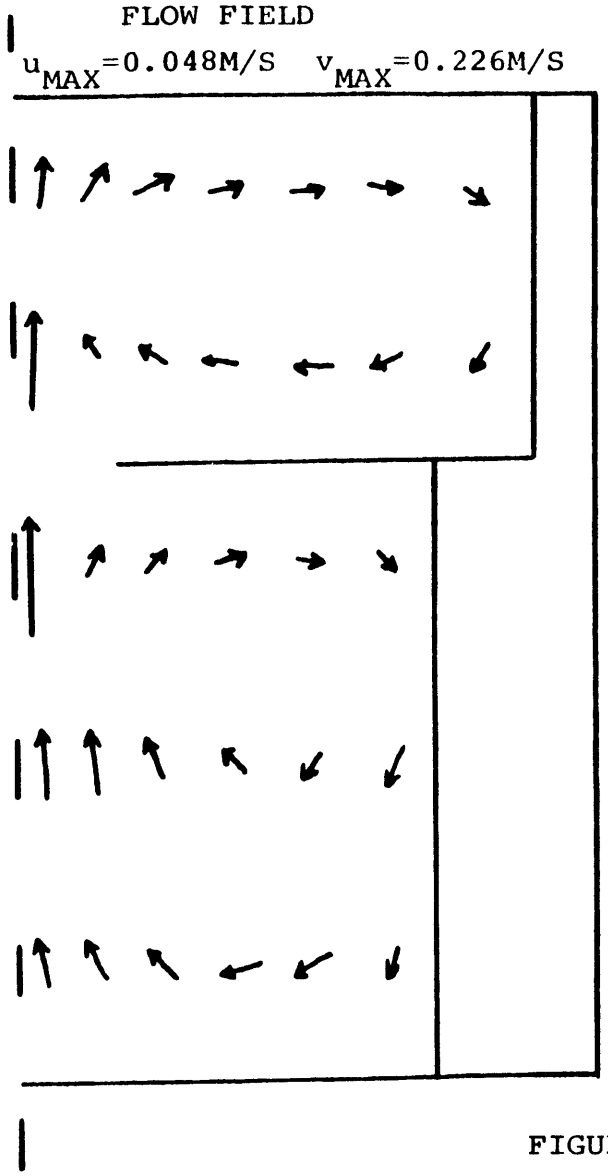

H_2 VOLUME FRACTION X 100

2.6	2.5	2.5	2.5	2.5	2.5	2.5
2.6	2.4	2.4	2.4	2.4	2.4	2.4
2.6	2.5	2.5	2.5	2.5	2.5	---
2.6	2.6	2.5	2.5	2.5	2.5	---
2.7	2.6	2.5	2.4	2.4	2.4	---

FIGURE 4.34: BF6 SIMULATION AT 4000 SECONDS

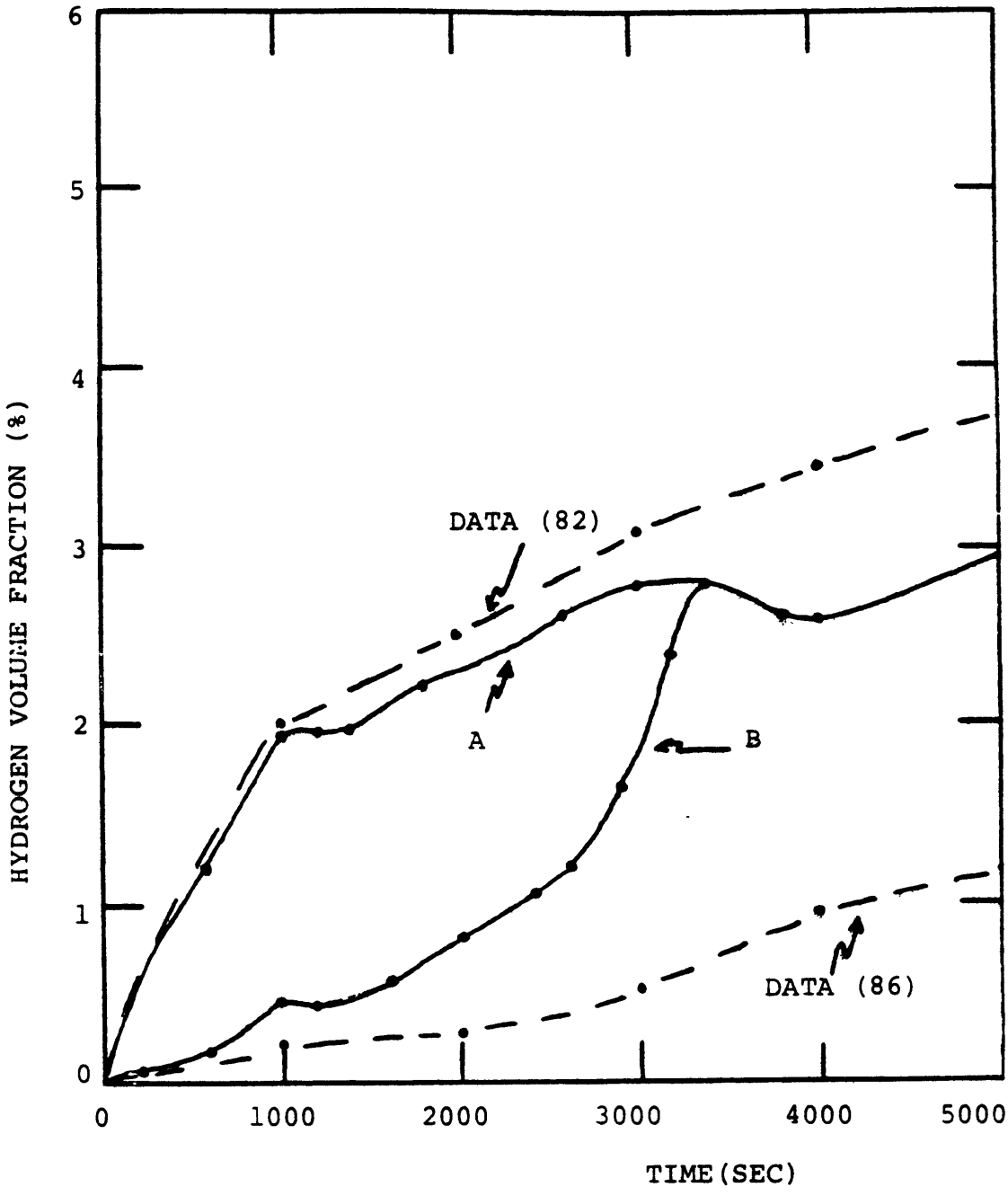

FIGURE 4.35: COMPARISON OF MEASURED VS PREDICTED H_2 CONCENTRATIONS DURING 32 NODE BF6 SIMULATION

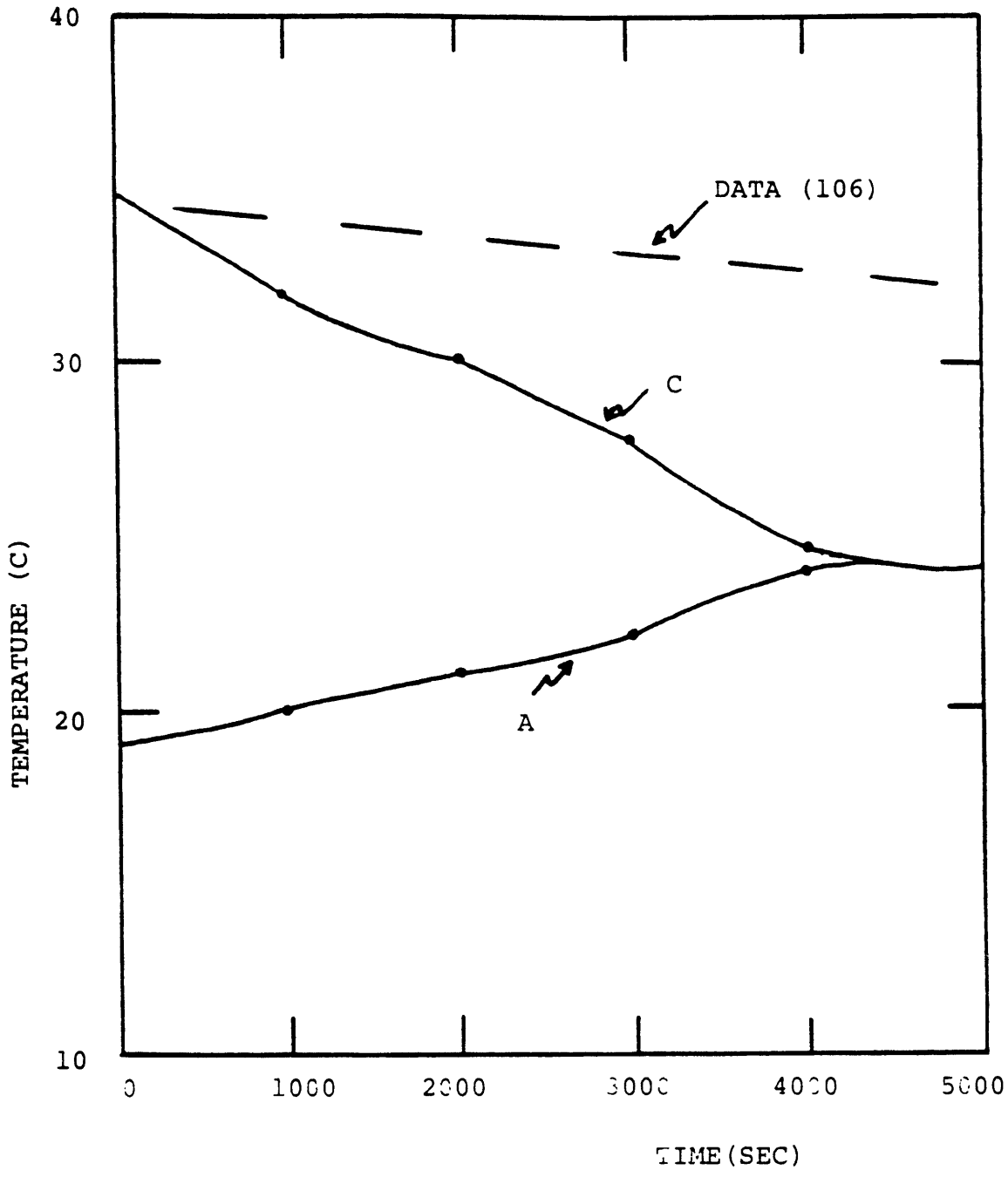

FIGURE 4.36: COMPARISON OF MEASURED VS PREDICTED TEMPERATURES DURING 32 NODE BF6 SIMULATION

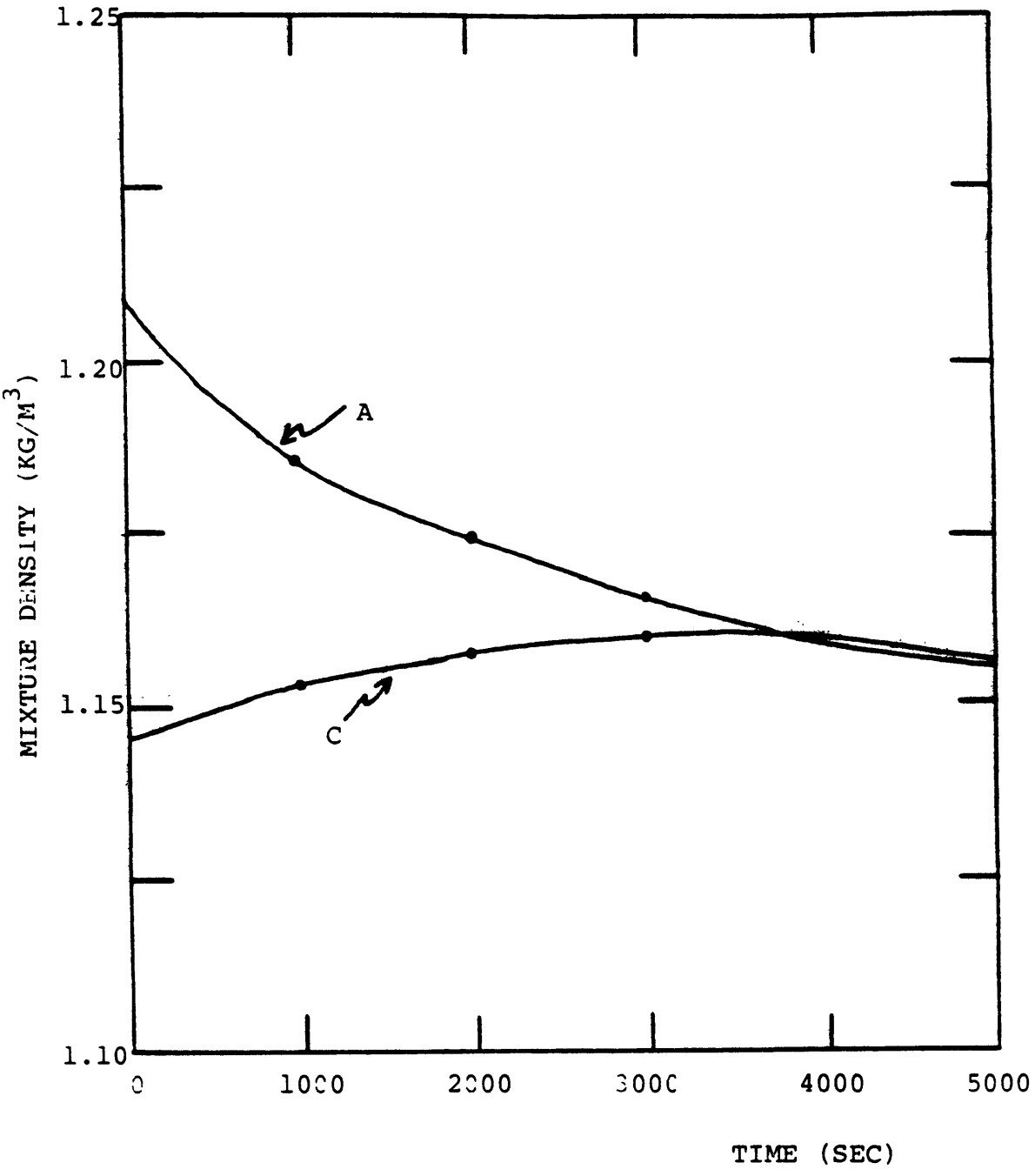

FIGURE 4.37: MIXTURE DENSITY TRANSIENT DURING BF6 SIMULATION

substantially faster thermal mixing transient. The mixture density plots mirror this effect. Clearly, the inversion breakdown allows the plume penetration into the orifice region. The plot of orifice region vertical velocities in Figure 4.38 clearly illustrates this bimodal behavior. The orifice region Froude number based on the following similitude

$$Fr = \frac{v}{\sqrt{g\frac{\delta\rho}{\rho}L}} \qquad (4.1)$$

is reported in Table 4.7. This further demonstrates the diminishing inverse buoyancy effect.

Table 4.7

Orifice Froude Number

Time(s)	Fr
0	0
200	.035
400	.040
600	.048
800	.055
1000	.063
1200	.049
2000	.078
3000	.20
4000	3.0

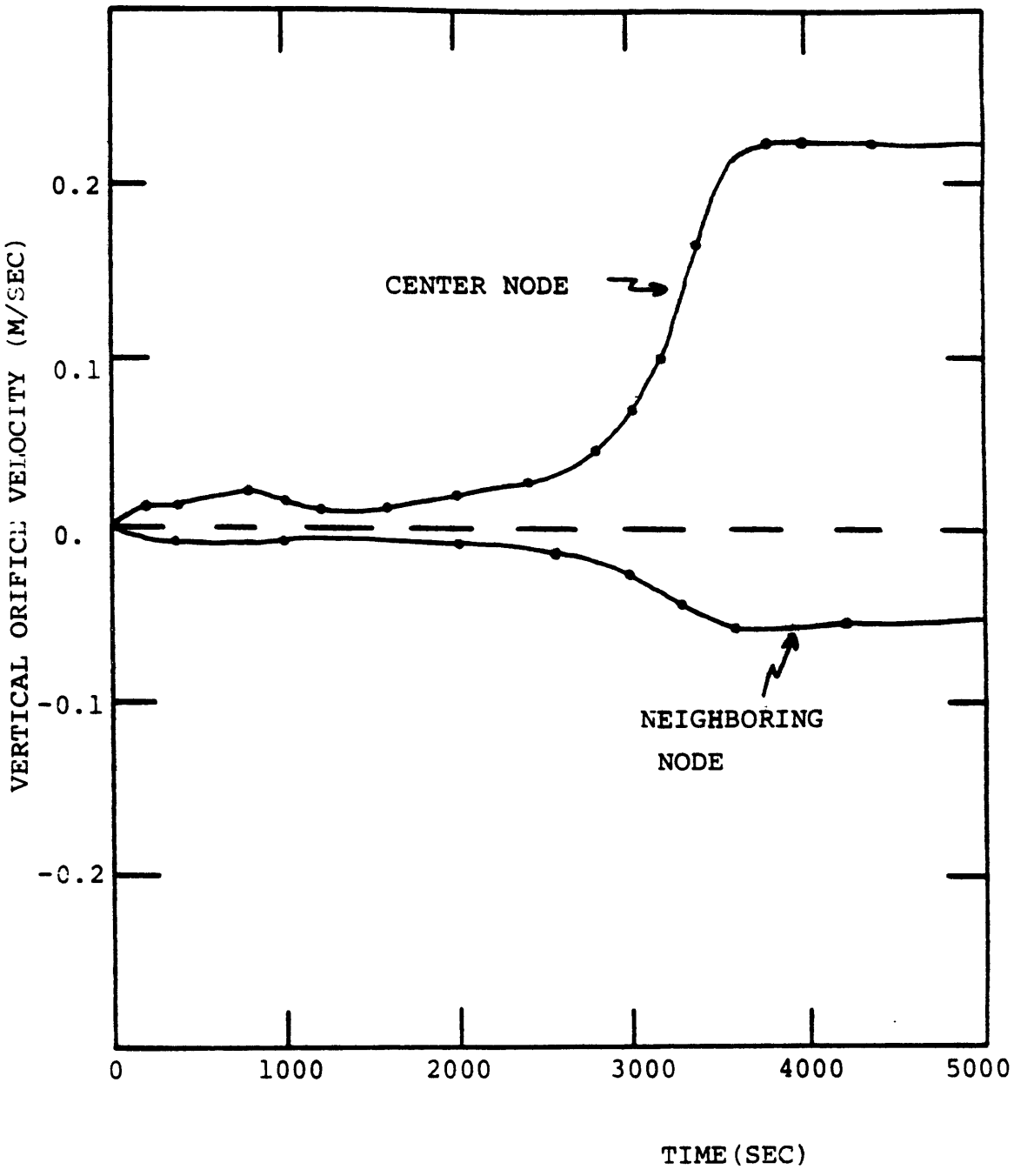

FIGURE 4.38: BEHAVIOR OF ORIFICE REGION VERTICAL FLOW DURING BF6 SIMULATION

A number of effects can be identified to explain the discrepancies between predictions and measurements. First, the lack of heat sink modelling neglects the thermal storage capacity of the concrete walls which in turn would retard the thermal transient. Second, the laminar flow assumption causes the central hydrogen-rich plume to be narrower in the initial period of the test. This higher hydrogen concentration causes enhanced buoyancy in the central core and thus earlier flow penetration in the orifice region. Third, the buoyancy effect embodied in the body force term of the momentum equation is based on a reference state. The reference state for this simulation was not updated to reflect the rising hydrogen concentration. This effect can mispredict buoyant velocities by as much as 25%.

Fourth, and most significant, the use of a very coarse mesh leads to an inaccurate prediction of the velocity field near the inversion layer (orifice region) and also causes high numerical diffusion. Figure 4.39 is a map of the estimated numerical diffusion coefficients at 1000 seconds. These constants are much higher than physical diffusive effects and are highest in the distinctly crossflow region near the orifice. As a confirmatory study of this conclusion the thermal inversion decay transient was interpreted as a transient slab conduction problem. The resultant thermal diffusivity computed is roughly 19×10^{-3} m^2/sec which is in excellent agreement with the computed numerical

NUMERICAL DIFFUSIVITY MAP AT 1000 SECONDS

(M^2/SEC)

11.5-3	11.5-3	6.8-3	3.5-3	1.1-3	1.6-3	3.6-3
19.9-3	15.2-3	8.1-3	4.1-3	1.3-3	1.9-3	4.1-3
21.7-3	29.3-3	17.9-3	7.7-3	5.8-3	9.8-3	
6.8-3	17.1-3	16.2-3	10.3-3	7.6-3	8.9-3	
17.9-3	19.4-3	7.3-3	4.4-3	2.6-3	3.2-3	

MOLECULAR DIFFUSIVITY - 0.10-3 M^2/SEC

TURBULENT DIFFUSIVITY - 1.00-3 M^2/SEC

FIGURE 4.39: COMPARISON OF MOLECULAR, TURBULENT AND NUMERICAL DIFFUSIVITIES AT 1000 SECONDS INTO BF6 SIMULATION

diffusivities (average 21 x 10^{-3} m^2/sec). The improved prediction of the test using techniques to diminish the limitations reported in this simulations is shown in the next section.

4.3.1.2.5 BF Test No. 6 Simulation II - Model Improvements

A second simulation of BF6 is reported which is formulated to address the shortcomings of the first calculation. The major model improvements are: a finer mesh, partial correction of numerical diffusion, better definition of initial thermal stratification, use of turbulence model and modelling of heat sinks. The problem nodalization is presented in Figure 4.40. A 50 node discretization with two vertical heat sinks (concrete) is used. The closer mesh spacing of the orifice region allows for more accurate velocity field definition. Periodic reference state update is employed to more accurately evaluate buoyancy effects. The partial numerical diffusion correction scheme discussed in Chapter 3 is also invoked.

The first 5000 seconds of the test are simulated. Figure 4.41 depicts the flow field during this period. The qualitative characteristics of the field did not change over this interval and nothing in the velocity transient indicated that the flow was making a transition to the non-inversion pattern. The flow is characterized by a strong central plume causing a clockwise recirculation

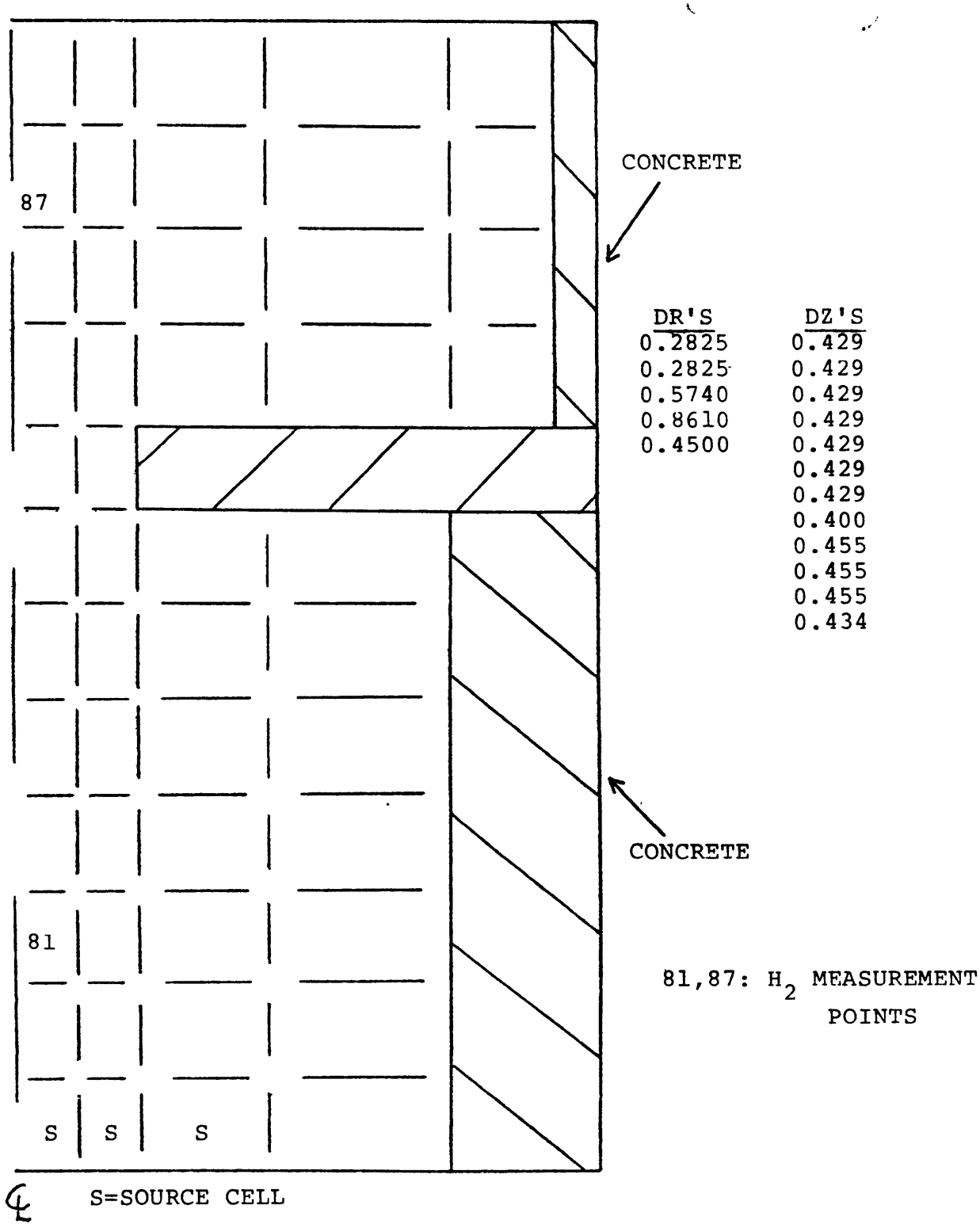

FIGURE 4.40: 50 NODE MODEL FOR BF6 SIMULATION

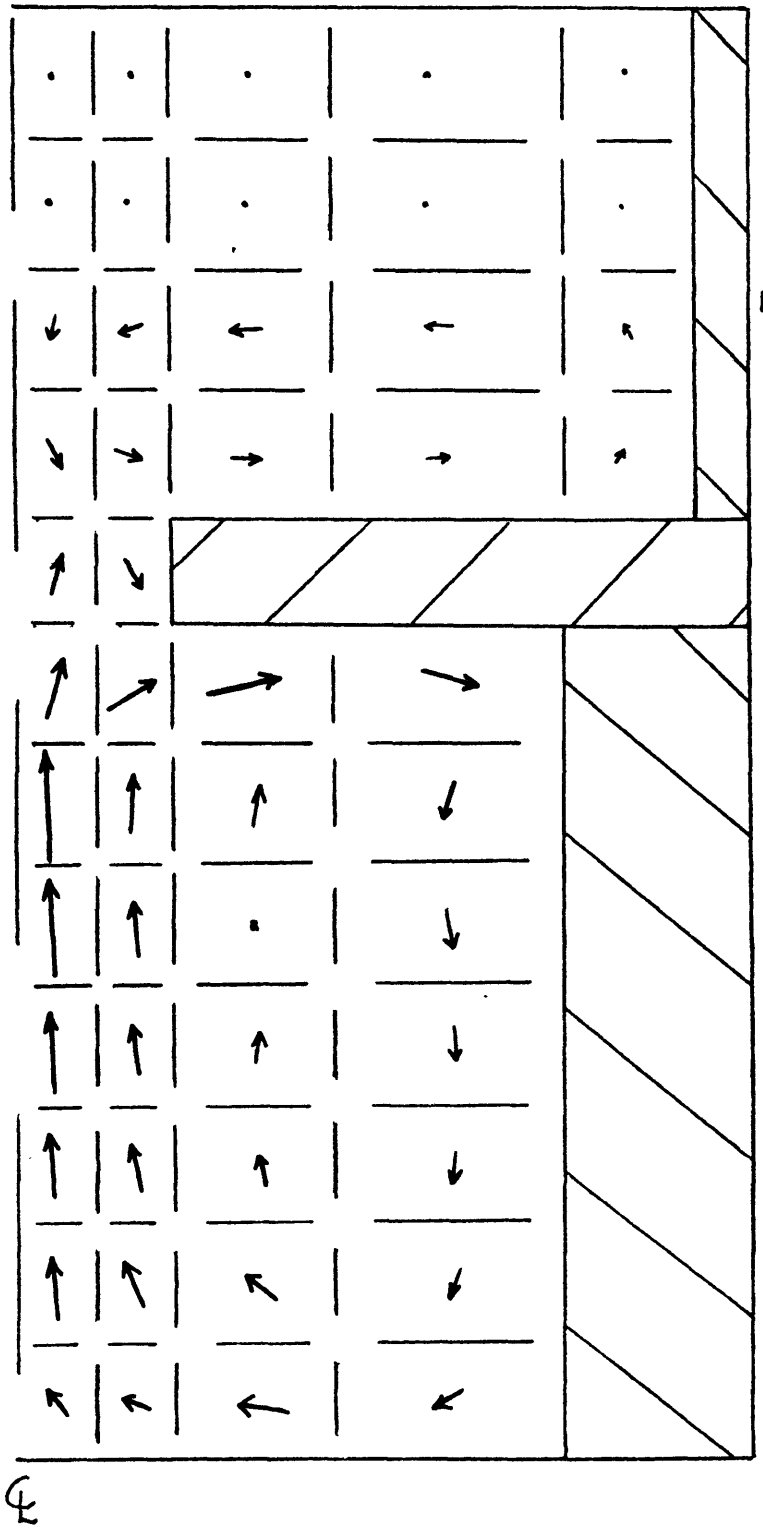

VELOCITY HISTORY

t (s)	Umax (m/s)	Vmax (m/s)
1000	0.0870	0.2419
2000	0.0649	0.1798
3000	0.0645	0.1790
4000	0.0642	0.1783
5000	0.0639	0.1776

FIGURE 4.41: VELOCITY PROFILE AND TIME HISTORY DURING 50 NODE BF6 SIMULATION

in the lower region. The upper region admits very little hydrogen and experiences a small counterclockwise recirculation predominantly in the lower elevations of the upper compartment. The quantitative data describing the velocity field are also summarized in Figure 4.41. The decrease in the steady state vertical components around 1000 seconds is due to a reduction in the source flow at that time.

Figures 4.42 through 4.44 illustrate the predicted hydrogen concentration profiles at 1000, 3000 and 5000 seconds, respectively. The inversion blocks the hydrogen build-up in the upper region throughout the simulation. Also, the convective and diffusive (including turbulence) transport homogenizes the lower region distribution. The temperature profiles depicted in Figures 4.45 through 4.47 reflect the same physical circumstances. An additional effect helping to stabilize the inverse thermal stratification is the interaction of the concrete heat slabs.

Figure 4.48 presents a comparison of the code predictions of the hydrogen transients at two representative locations in the lower and upper regions with the measured data. Much better agreement is noted in contrast to the previous coarse mesh laminar simulation. The upper region predictions remain in good agreement throughout the calculation. The predicted lower region concentrations fall below the measurements by as much as 1 volume percent. This lack of quantitative agreement is also noted by

H_2 VOLUME FRACTIONS X 1000

0.03	0.04	0.03	0.03	0.04
0.10	0.10	0.11	0.12	0.12
0.50	0.50	0.51	0.54	0.59
1.58	1.08	0.83	0.74	0.67
12.34	11.76			
12.41	11.64	11.15	11.00	
12.43	11.41	10.71	10.84	
12.46	11.38	10.62	10.69	
12.55	11.48	10.74	10.55	
12.72	11.64	10.84	10.42	
13.01	11.94	11.03	10.26	
13.65	12.75	11.80	10.05	

FIGURE 4.42: HYDROGEN VOLUME FRACTION PROFILE AT 1000 SECONDS INTO 50 NODE BF6 SIMULATION

H_2 VOLUME FRACTION X 100

0.05	0.05	0.05	0.05	0.05
0.08	0.08	0.09	0.09	0.09
0.19	0.19	0.20	0.20	0.21
0.34	0.28	0.25	0.24	0.23
2.03	1.96			
2.04	1.99	1.97	1.96	
2.04	1.99	1.95	1.95	
2.05	1.99	1.95	1.95	
2.05	1.99	1.95	1.94	
2.06	2.00	1.96	1.93	
2.08	2.02	1.97	1.92	
2.11	2.06	2.01	1.91	

FIGURE 4.43: HYDROGEN VOLUME FRACTION PROFILE AT 3000 SECONDS INTO 50 NODE BF6 SIMULATION

H_2 VOLUME FRACTION X 100

0.17	0.17	0.16	0.17	0.17
0.23	0.24	0.24	0.25	0.25
0.45	0.45	0.46	0.46	0.47
0.75	0.62	0.55	0.53	0.51
2.77	2.62			
2.78	2.71	2.70	2.69	
2.78	2.73	2.69	2.69	
2.78	2.73	2.68	2.68	
2.79	2.73	2.69	2.67	
2.80	2.74	2.69	2.67	
2.81	2.75	2.71	2.66	
2.85	2.80	2.75	2.65	

FIGURE 4.44: HYDROGEN VOLUME FRACTION PROFILE AT 5000 SECONDS INTO 50 NODE BF6 SIMULATION

TEMPERATURE IN °C

308.08	308.07	308.08	308.08	308.06
307.93	307.94	307.93	307.93	307.96
307.03	307.02	307.00	306.97	306.91
305.75	306.39	306.65	306.74	306.81
292.83	293.36			
292.81	292.94	292.87	292.86	
292.81	292.80	292.79	292.86	
292.81	292.80	292.80	292.85	
292.81	292.81	292.81	292.84	
292.81	292.81	292.81	292.83	
292.81	292.81	292.81	292.83	
292.81	292.81	292.81	292.81	

FIGURE 4.45: TEMPERATURE PROFILE AT 1000 SECONDS INTO BF6 SIMULATION

TEMPERATURE IN °C

307.75	307.75	307.75	307.74	307.71
307.37	307.37	307.35	307.36	307.36
305.83	305.82	305.81	305.78	305.72
304.86	305.30	305.49	305.57	305.62
293.34	293.74			
293.31	293.41	293.36	293.35	
293.31	293.30	293.30	293.35	
293.31	293.31	293.30	293.34	
293.31	293.31	293.31	293.33	
293.31	292.31	293.31	293.33	
293.31	293.31	293.31	293.33	
293.31	293.31	293.31	293.31	

FIGURE 4.46: TEMPERATURE PROFILE AT 3000 SECONDS INTO BF6 SIMULATION

TEMPERATURE IN °C

307.11	307.10	307.11	307.10	307.07
306.53	306.51	306.50	306.50	306.50
304.55	304.55	304.53	304.49	304.42
303.17	303.81	304.08	304.18	304.27
294.00	294.62			
293.97	294.12	294.04	294.04	
293.97	293.96	293.96	294.04	
293.97	293.97	293.96	294.02	
293.97	293.97	293.97	294.00	
293.97	293.97	293.98	294.00	
293.97	293.97	293.98	293.99	
293.97	293.97	293.97	293.98	

FIGURE 4.47: TEMPERATURE PROFILE AT 5000 SECONDS INTO BF6 SIMULATION

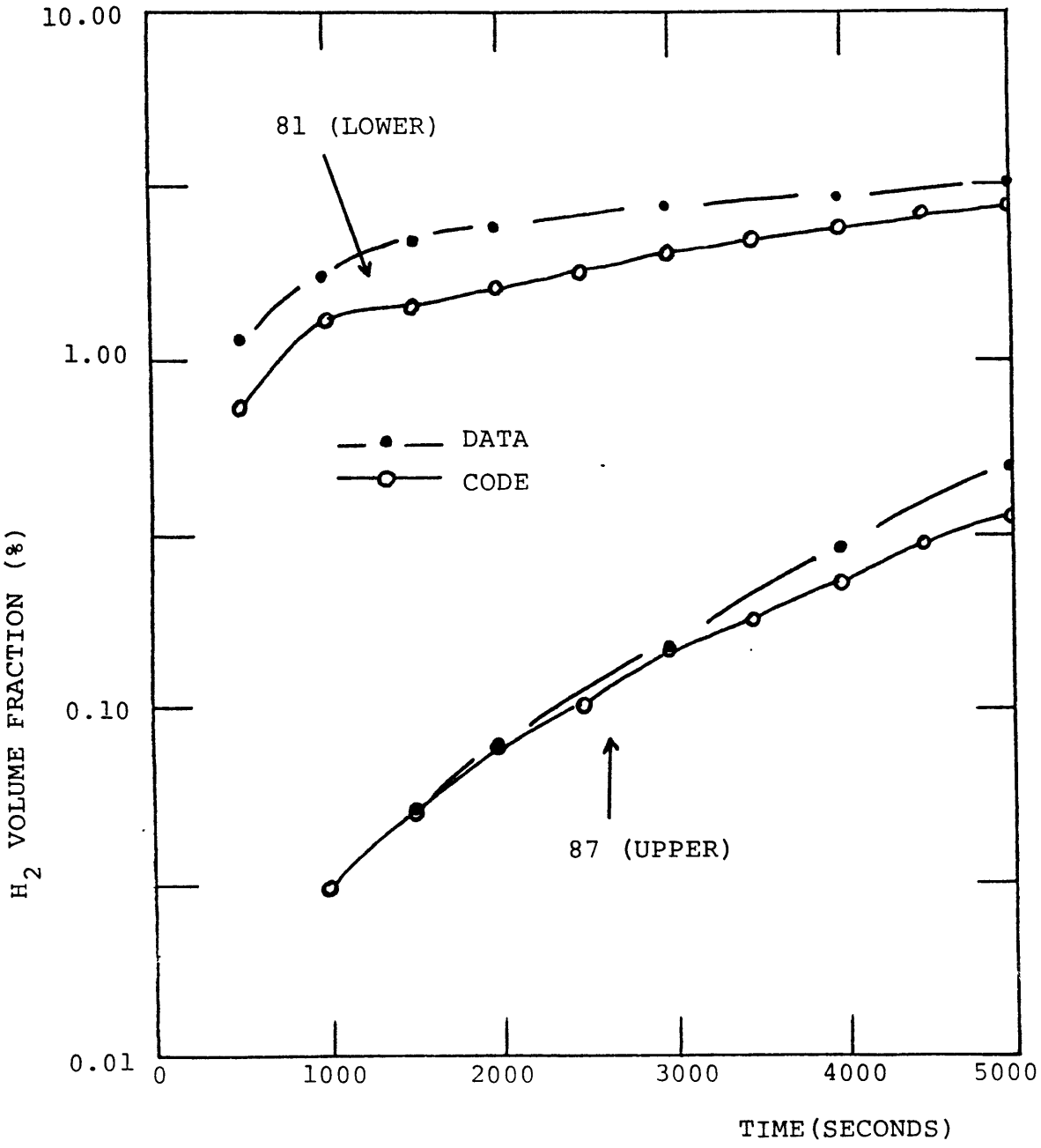

FIGURE 4.48: COMPARISON OF MEASURED AND PREDICTED HYDROGEN CONCENTRATIONS DURING 50 NODE BF6 SIMULATION

Thurgood [67] and Trent [64] which suggests a possible error in the measurement of source flow during the experiment.

The maximum vertical and horizontal velocity components are plotted vs. time in Figure 4.49. The two most important characteristics observed are the development period of approximately 100 seconds and the transition to a new lower vertical component which is caused by the reduction in the hydrogen injection rate. Finally, Figure 4.50 is a comparison of the orifice region Froude numbers of this result and the previous simulation. The substantially different behaviors verify the physical characteristics of the two calculations. In summary, the second finer mesh simulation utilizing turbulence modelling, accounting for solid heat sinks/sources, periodic reference state update and partial numerical diffusion correction is a much more accurate model of the BF6 test.

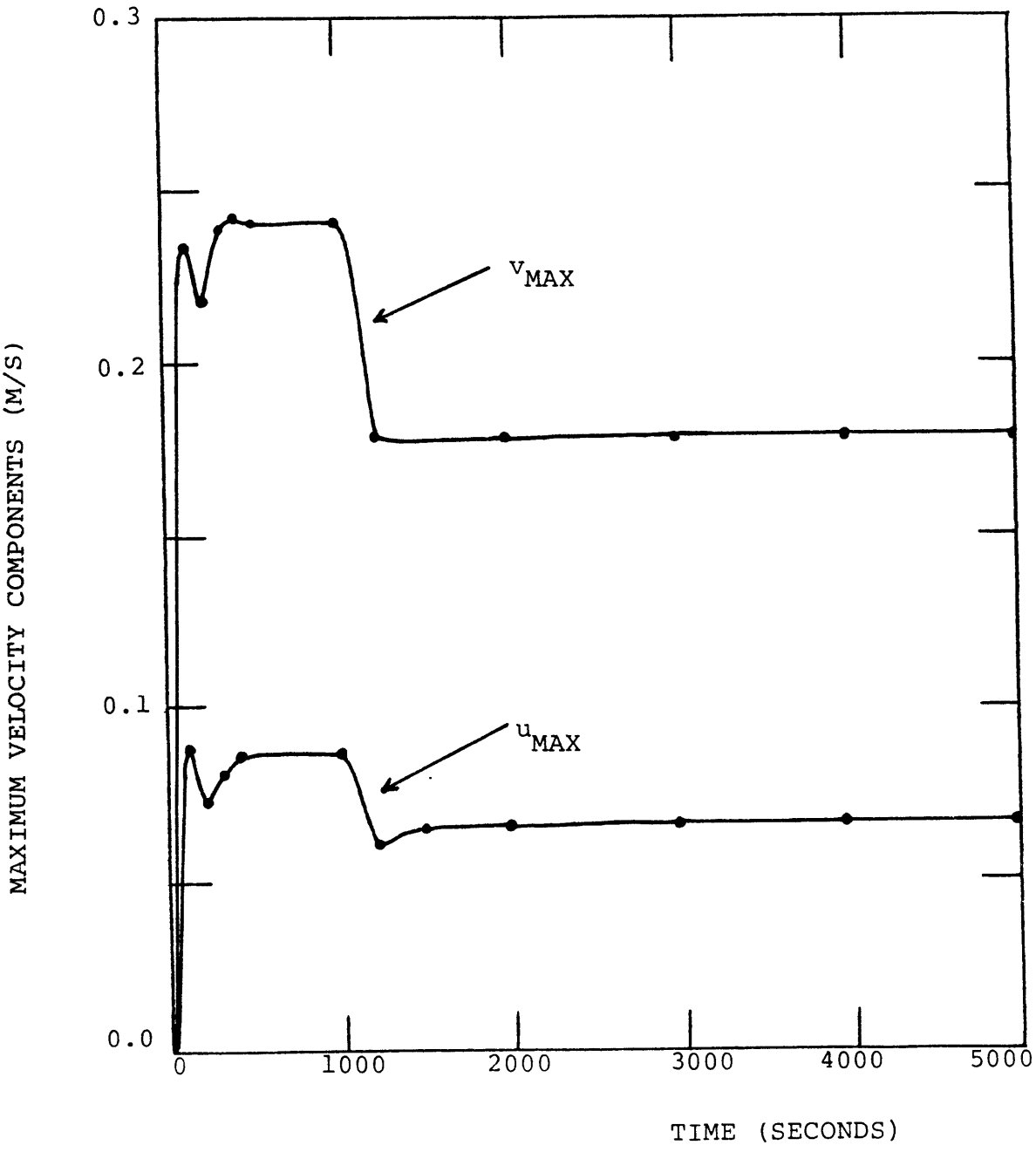

FIGURE 4.49: DEVELOPMENT HISTORY OF VELOCITY FIELD DURING 50 NODE BF6 SIMULATION

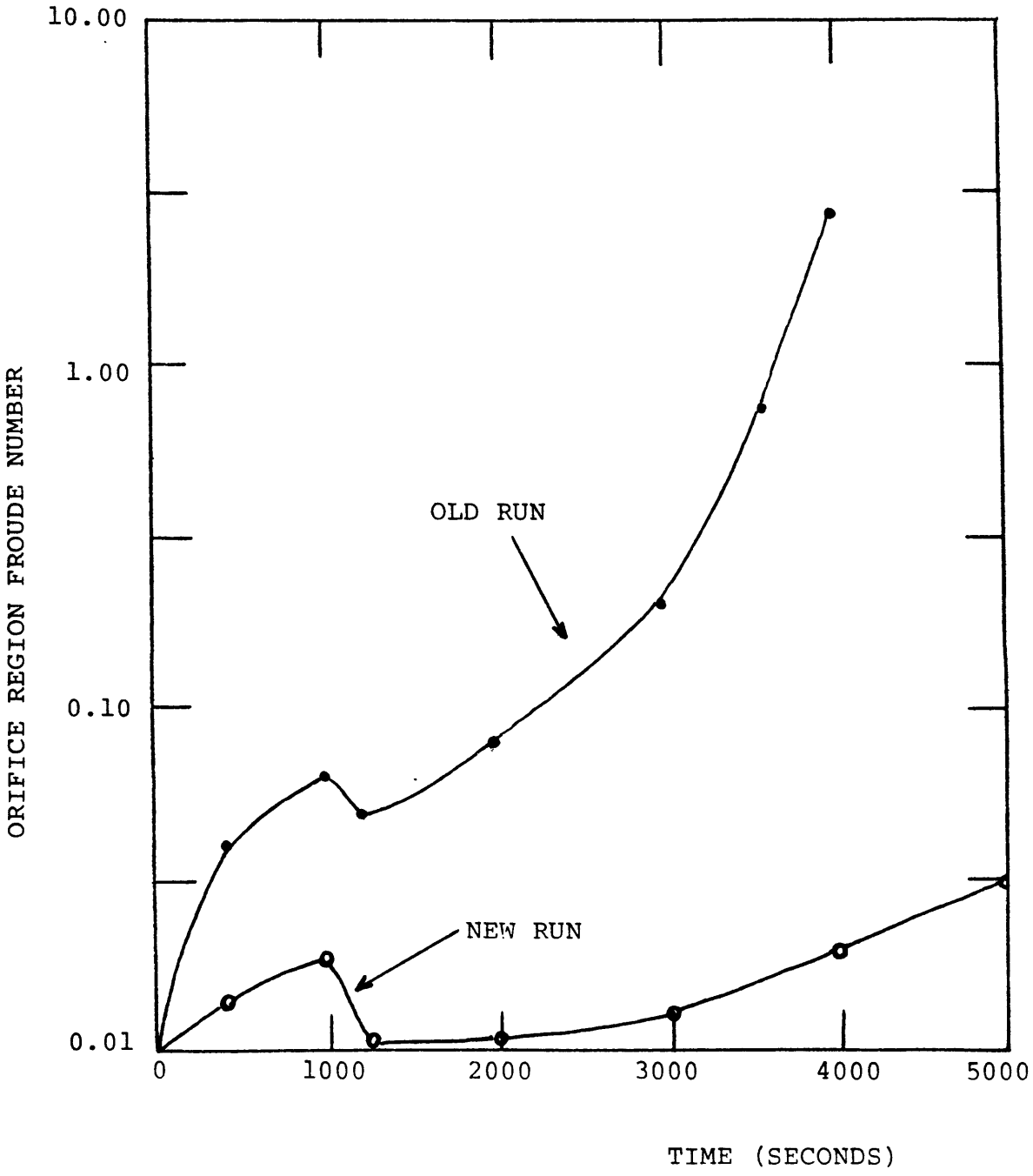

FIGURE 4.50: COMPARISON OF ORIFICE REGION FROUDE NUMBERS OF THE TWO BF6 SIMULATIONS

4.3.2 Hanford Engineering Development Laboratory Tests

The hydrogen mixing tests performed at the Hanford Engineering Development Laboratory (HEDL) are representative of events in which hydrogen is injected at higher rates than typical of a degrading core events. One example is a release from a pipe break in the reactor coolant system early in the postulated event. The facility and tests are conducted to be representative of actual containment conditions including the presence of steam, complex geometrical arrangements and containment air recirculation systems. The tests are performed in the HEDL Containment Systems Test Facility (CSTF). Given the complexity of the tests, their simulation is more difficult and costly. The physical regimes encountered test the validity bounds of the slower mixing model.

4.3.2.1 Facility and Testing Program Review

The facility and associated features are depicted in Figures 4.51 and 4.52. The underlying modelling criteria are based on scale modelling of a Pressurized Water Reactor (PWR) ice condenser containment. The large vessel is 20.4 m high, 7.6 m in diameter with a free volume of 850 m^3. Detailed design and testing data are provided by Bloom et al. and Bloom and Claybrook. The vessel is compartmentalized so that the lower region can simulate the lower compartment of an ice condenser contain ent. This lower test volume is approximately 150 m^3 in volume and occupies 300° of the

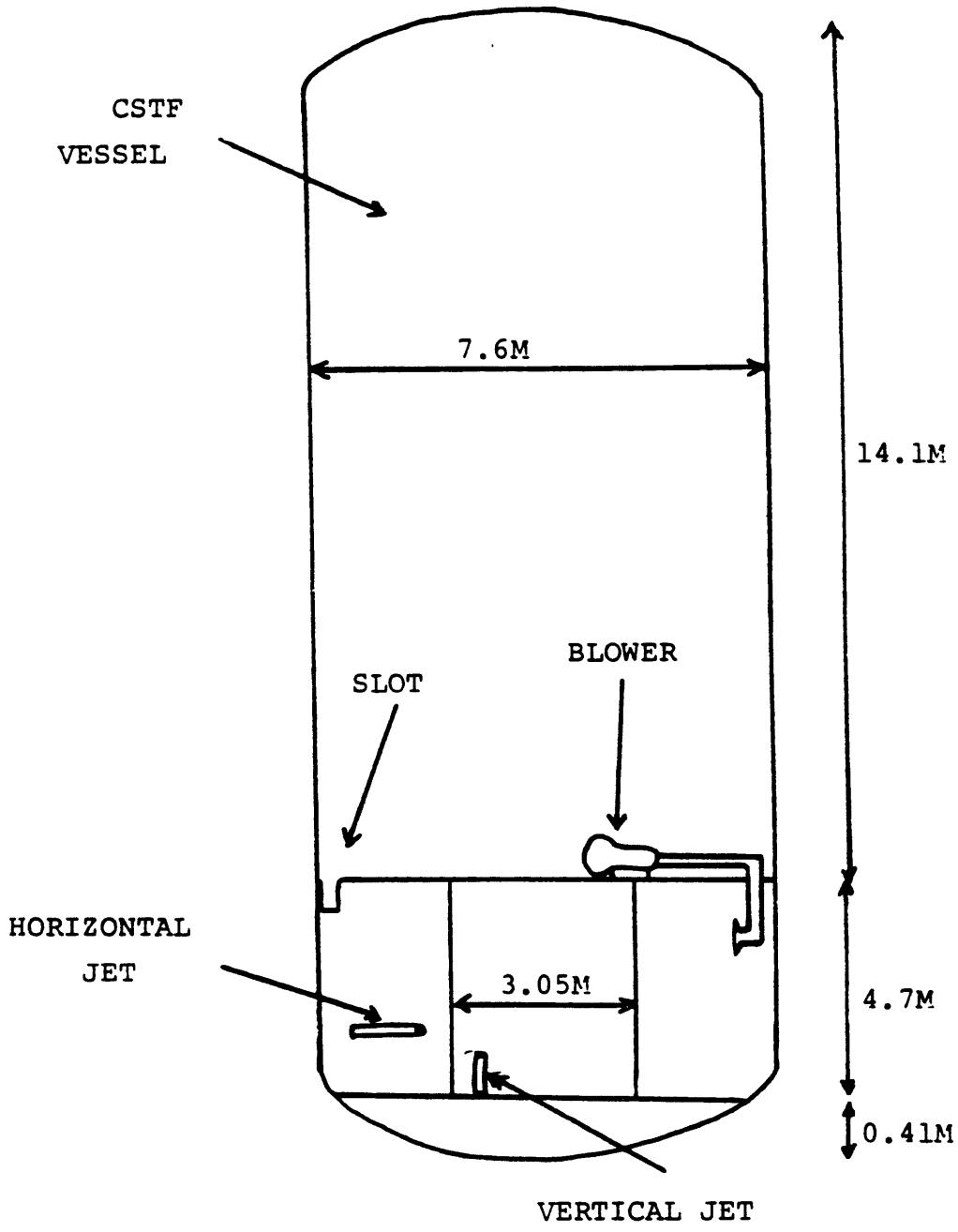

FIGURE 4.51: HEDL FACILITY SCHEMATIC

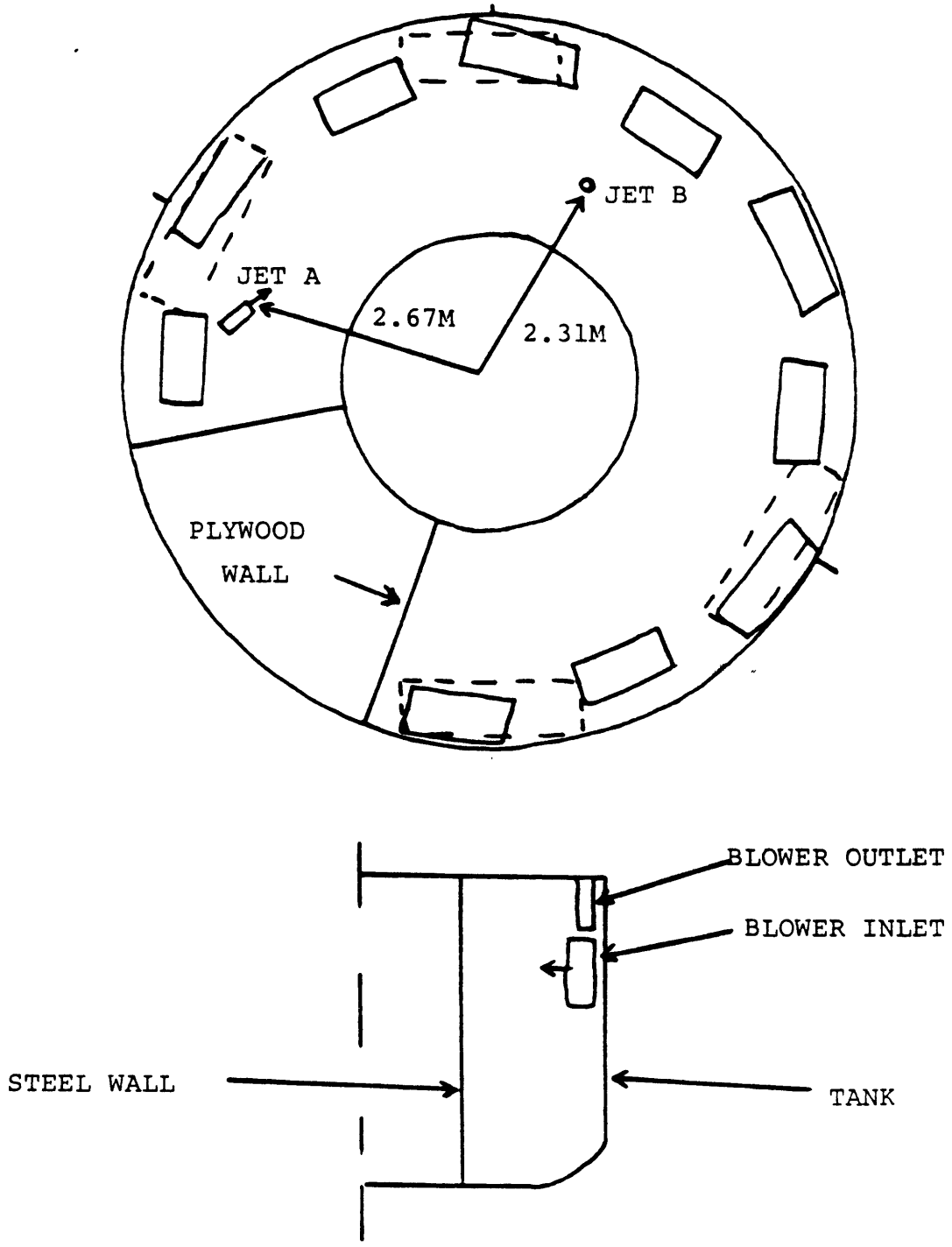

FIGURE 4.52: CROSS SECTIONAL SCHEMATIC OF HEDL FACILITY

annular region. The central core of the lower region represents the reactor cavity.

Air blowers which circulate the atmosphere from the upper to the lower region are included in the facility as shown in Figure 4.51. The four air blower openings operate at a total flowrate of 1.8 m^3/sec. Twenty-four return flow paths from the lower to the upper compartment are situated in the manner depicted in Figure 4.52. These represent partially open ice condenser bays. The test compartment does not contain any obstacles representative of vessels, piping and other structure. The facility is extensively instrumented with temperature, velocity and hydrogen sensors (i.e., thermocouples, film anemometers and gas analyzers).

Three sets of tests define the experiment matrix as shown in Table 4.8. The first series of tests (HM-P1 through P4) were performed to test the effect of the air recirculation system and initial thermal conditions. The second series involved the introduction of either hydrogen or helium in the form of a high velocity gas-steam horizontal jet. The jet size was scaled to represent a 2 inch break in a real system. The jet location which is labelled "Jet A" in Figure 4.51 is centered in the annulus at 275 (azimuthal) at a height of 1.5 m. The final two tests involved the injection of a vertical gas-steam jet at location "Jet B" which is located at 180° at a height of 1.2 m. The vertical jet tests are scaled to represent a release from the rupture

Table 4.8

HEDL Hydrogen Mixing Test Matrix

Test	Initial Gas/ Gas Temp (^{o}C)	Recirc Flow (m^3/sec)	Source	Gas Flow (kg/sec)	Steam Flow (kg/sec)	Jet Orientation
HM-P1	AIR/29	0	none	NA	NA	NA
HM-P2	AIR/29	1.73	none	NA	NA	NA
HM-P3	AIR/66	0	none	NA	NA	NA
HM-P4	AIR/66	1.73	none	NA	NA	NA
HM-1	AIR/66	0	HE-STM	0.0066	0.205	Horizontal
HM-2	AIR/66	0	HE-STM	0.0133	0.410	Horizontal
HM-3	AIR/66	1.73	HE-STM	0.0066	0.205	Horizontal
HM-4	AIR/66	1.73	HE-STM	0.0133	0.410	Horizontal
HM-5*	N_2/66	1.73	H_2-STM	0.0066 (planned) 0.0050 (actual)	0.410	Horizontal
HM-6**	AIR/66	1.73	HE-STM	0.0066	0.205	Vertical
HM-7	AIR/66	1.73	HE-STM	0.0066	0.410	Vertical

*designated as EPRI Standard Problem HEDL A

**designated as EPRI Standard Problem HEDL B

disk of the pressurizer relief tank. Tests HM-5 and HM-6 are designated Standard Problems HEDL A and HEDL B by the EPRI/HEDL hydrogen assessment research program.

The qualitative empirical observations are now summarized. In the absence of a jet source (i.e., preliminary tests) measured natural circulation velocities are on the order of .1 m/sec to .3 m/sec depending upon initial thermal conditions, while velocities with recirculation fans operating range from 0.15 to 0.45 m/sec over the same thermal condition spectrum. The enhanced mixing characteristic of higher thermal gradients are expected to be more typical of the actual containment post accident environment. The gas release simulations produced the largest concentration gradients for horizontal gas releases coupled with no forced recirculation. The jet momentum influenced flow far from the injection location especially in the case of vertical jets. Finally, helium is shown to be a valid simulant for hydrogen. In summary, these more complex tests reinforce lessons learned from the Battelle Frankfurt tests and also demonstrate the important mixing effects of the source configuration, ventilation system operation and initial thermal conditions.

4.3.2.2 Simulations Based On Selected Tests

Of the two HEDL tests designated as standard problems, the vertical jet case (Case B - HM6) is utilized for a

validation calculation. This test is chosen since it produced the more significant spatial variations in gas concentrations. In addition, helium was used in HEDL B and this analysis demonstrates the code's ability to model hydrogen simulant gases. Helium flow is modelled as a hydrogen flow of half the mass flow rate so that the similitude of the buoyancy introduced is maintained. The one-half factor arises from the ratio of the two gases' molecular weights. An implicit assumption in this approach is that the helium jet is a small contributor to the source flow's momentum source contribution since halving the gas mass flow reduces the momentum flux. The validity of this assumption is demonstrated in the following calculation.

$$\text{Momentum of steam jet} = .24\frac{kg}{sec} \times 80\frac{m}{sec} = 19.2 \text{ kg-m/sec}^2$$

$$\text{Momentum of actual helium jet} = .0068\frac{kg}{sec} \times 80\frac{m}{sec} = 0.5 \text{ kg-m/sec}^2$$

$$\text{Momentum of assumed hydrogen jet} = 0.5 \times 0.5 = 0.25 \text{ kg-m/sec}^2$$

$$\text{Total momentum of actual jet} = 19.7 \text{ kg-m/sec}^2$$

$$\text{Momentum of simulated jet} = 19.45 \text{ kg-m/sec}^2.$$

As is seen this model introduces an error of 1.2% in the momentum source. An additional assumption is that hydrogen transport properties are similar to those of hydrogen.

The HEDL facility contains recirculation blowers which enhance mixing between the upper and lower volumes. An ancillary model is developed to represent this blower effect

by user-defined blower-cells which exhibit source/sink characteristics. Hydrogen, air and the resultant energy mixing effects are expressed through the following model equations:

$$\frac{\partial \rho_a}{\partial t} = \frac{Q}{V}[\rho_{ao}-\rho_a] \ , \tag{4.1}$$

$$\frac{\partial \rho_h}{\partial t} = \frac{Q}{V}[\rho_{ho}-\rho_h] \ , \text{ and} \tag{4.2}$$

$$\frac{\partial \rho e}{\partial t} = \frac{Q}{V}[(\rho e)_{ao}+(\rho e)_{ho}-(\rho e)_a- (\rho e)_h] \ . \tag{4.3}$$

These equations are solved implicitly after the overall mass and energy transport equations are solved. The model input specification assumes knowledge of the time dependent behavior of inlet blower flowrate, temperature, hydrogen and air densities. These have been ascertained from the experimental data reports. The blower characteristics of HEDL B are summarized in Table 4.9. This modelling approach can possibly be used when more complex fan cooler component simulations are undertaken.

Before performing a detailed continuum analysis of HEDL B, a simple hand calculation based on a well-mixed single region lumped parameter model is reported. This exercise serves two purposes; first, it validates the data utilized in the blower model and second, it tests the validity of the helium/hydrogen modelling approach. Both

Table 4.9

HEDL B Blower Specification

Time (sec)	Air Density (kg/m^3)	Hydrogen Density (kg/m^3)	Temperature (°K)	Flow* (m^3/sec)
0	1.1303	0.0	308.0	0.433
90	1.1052	0.0	315.0	0.433
270	1.1017	0.00078	316.0	0.433
330	1.0896	0.00104	319.5	0.433
630	1.0712	0.00234	325.0	0.433
690	1.0695	0.00260	325.5	0.433
870	1.0795	0.00270	322.5	0.433

*flow of one blower (total = 4 x 0.433 = 1.733)

HEDL A and B are simulated in this manner and the calculated results are compared to the experimental gas concentration data in Figure 4.53. As is evident, excellent agreement is noted especially in the horizontal jet case (HEDL A). Of course, the axial stratification and azimuthal asymmetry of the vertical jet case cannot be predicted by a lumped model. Nevertheless, these results validate the blower and mass source data and also demonstrate the usefulness of simplified analysis to parameterize more complex calculations.

The problem mesh nodalization is depicted in Figure 4.54. The 80 node mesh is used as a compromise between the desire for accuracy and the need to perform an economical

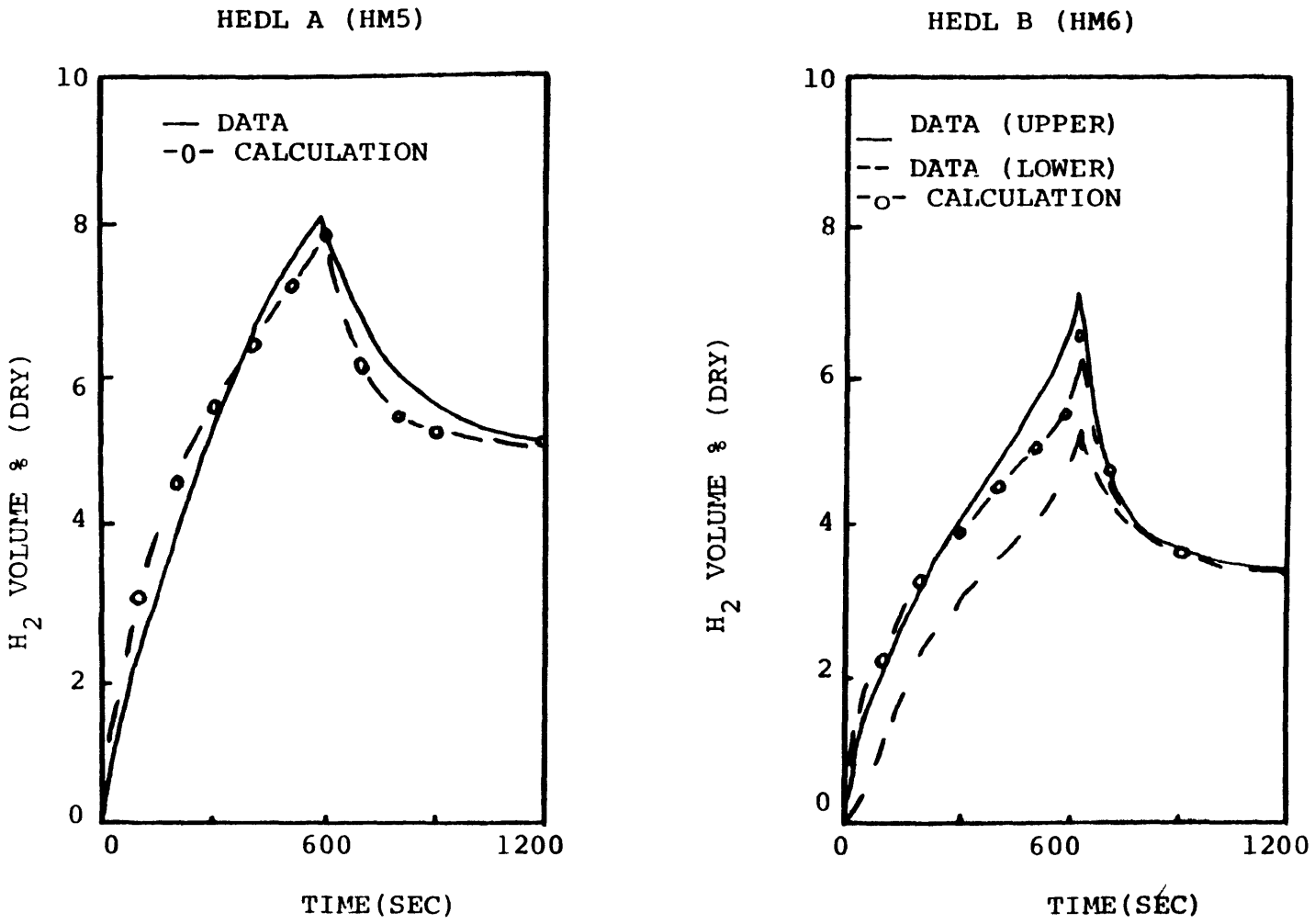

FIGURE 4.53: COMPARISON OF LUMPED PARAMETER ANALYSIS RESULTS TO DATA FOR TESTS HEDL A AND HEDL B

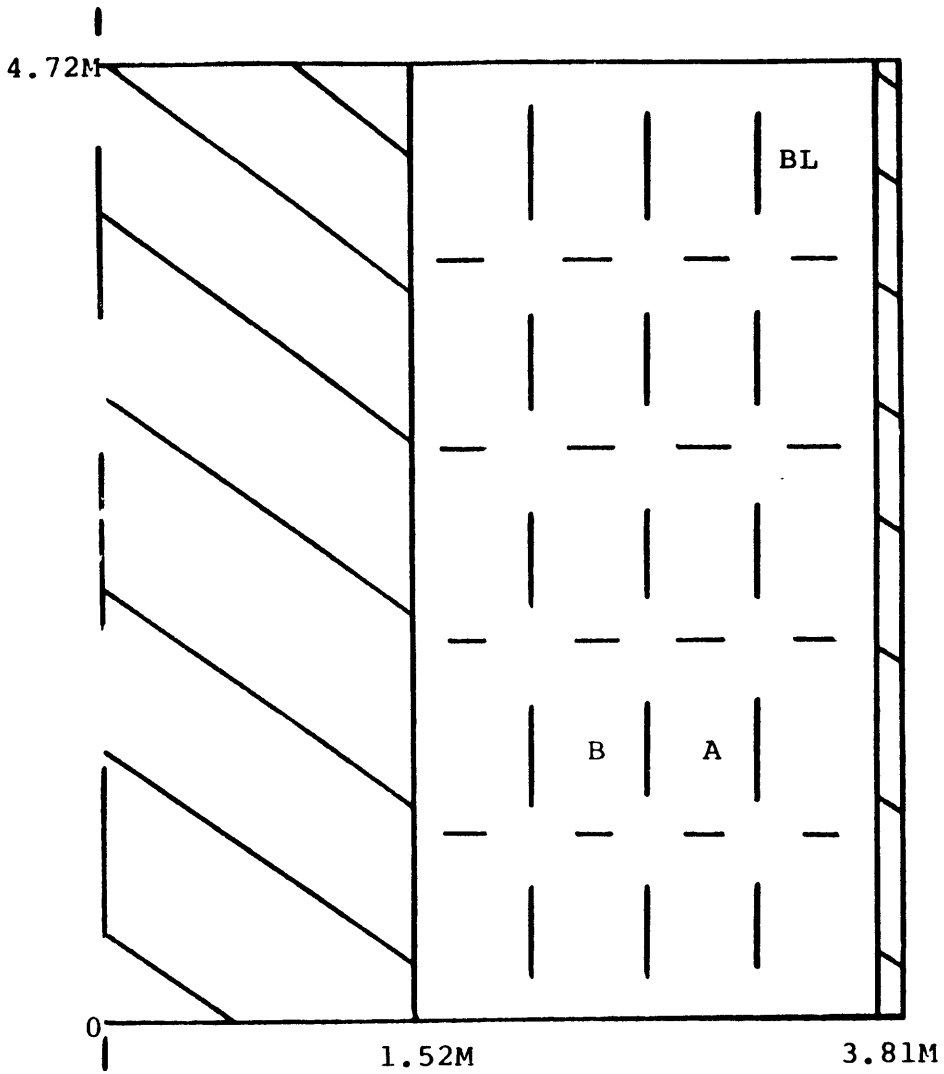

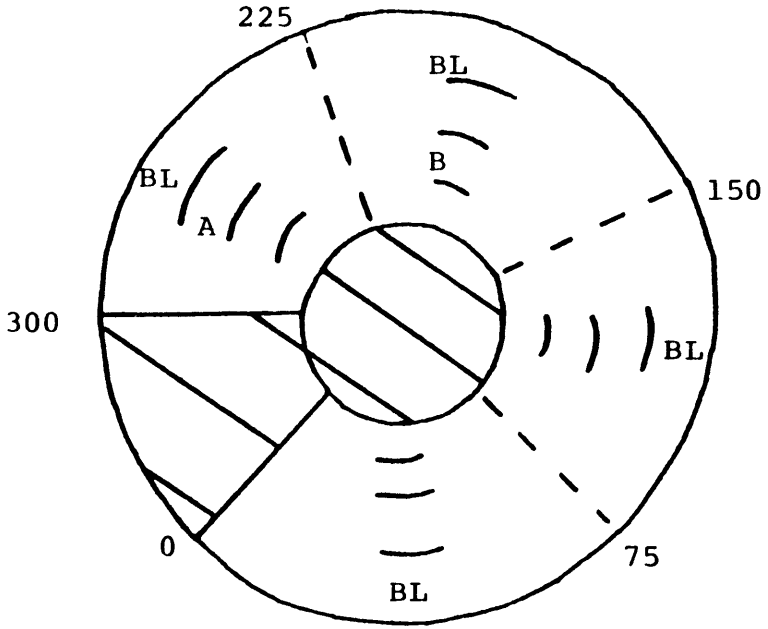

δR=0.57M
δZ=0.94M
$\delta\theta$ =75

BL=BLOWER CELL
A=JET A CELL
B=JET B CELL

FIGURE 4.54: 80 NODE MODEL OF HEDL FACILITY

computation. All four upper right hand cells are designated as blower cells. The initial volume is assumed to be filled with air at 338.15°K. The jet flow temperature varies from 373°K to 388°K over the course of the injection. A jet velocity of 80 m/sec is assumed and the jet effect is treated as a momentum source in the source cell. This approach while incapable of providing spatial resolution of the near jet flow field allows for an economical way to represent a jet in a coarse spatial mesh. The turbulence model is used as well as the enhanced containment heat transfer package. The heat sink model is the steel tank outer surface. The inner cylinder boundary as well as the 60° wood block are modelled as insulated surfaces.

Though the jet injection continued for over 600 seconds (H_2 injection actually began at 45 seconds after jet was initiated), only the first 300 seconds of the test are simulated. The two main reasons for the abbreviated simulation are calculational cost and the fact that the characteristics of the predictions are apparent by the 300 second point. Figures 4.55 and 4.56 depict the flow and thermal fields at 50 seconds in the jet and a non-jet azimuthal regions, respectively. The flow field depicted in these figures represent the two-dimensional resolution (in the r-z plane) of the velocity vectors. Azimuthal velocity components at the cell back and front faces are noted in the diagram. The non-jet region exhibits a

FLOW FIELD*

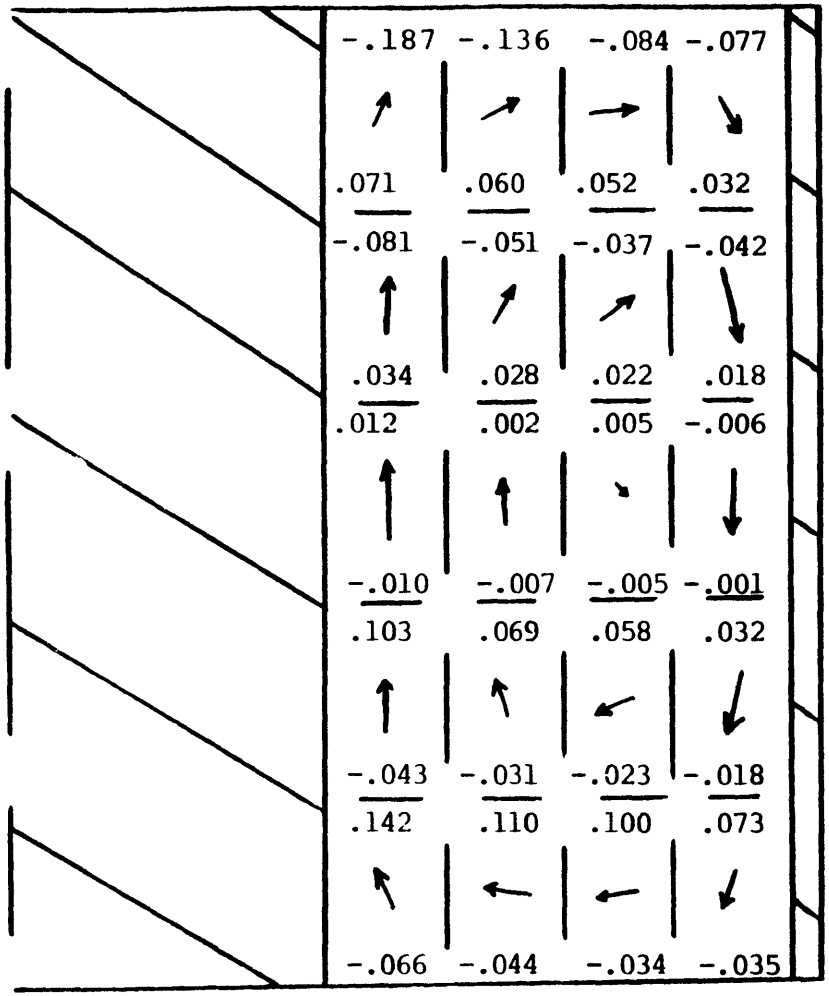

u_{max} = .24 m/s v_{max} = .52 m/s w_{max} = .19 m/s

TEMPERATURE FIELD

320.2	319.7	318.7	312.9
310.8	311.9	311.8	312.7
309.3	308.7	312.7	312.3
308.6	309.2	310.0	311.7
308.9	309.5	310.0	310.8

* Flow vectors correspond to r-z velocity. Values given at cell top and bottom are front and back face azimuthal velocity components, respectively.

FIGURE 4.55: FLOW AND TEMPERATURE FIELDS IN NON-JET (K=3) REGION AT 50 SECONDS INTO HEDL B SIMULATION

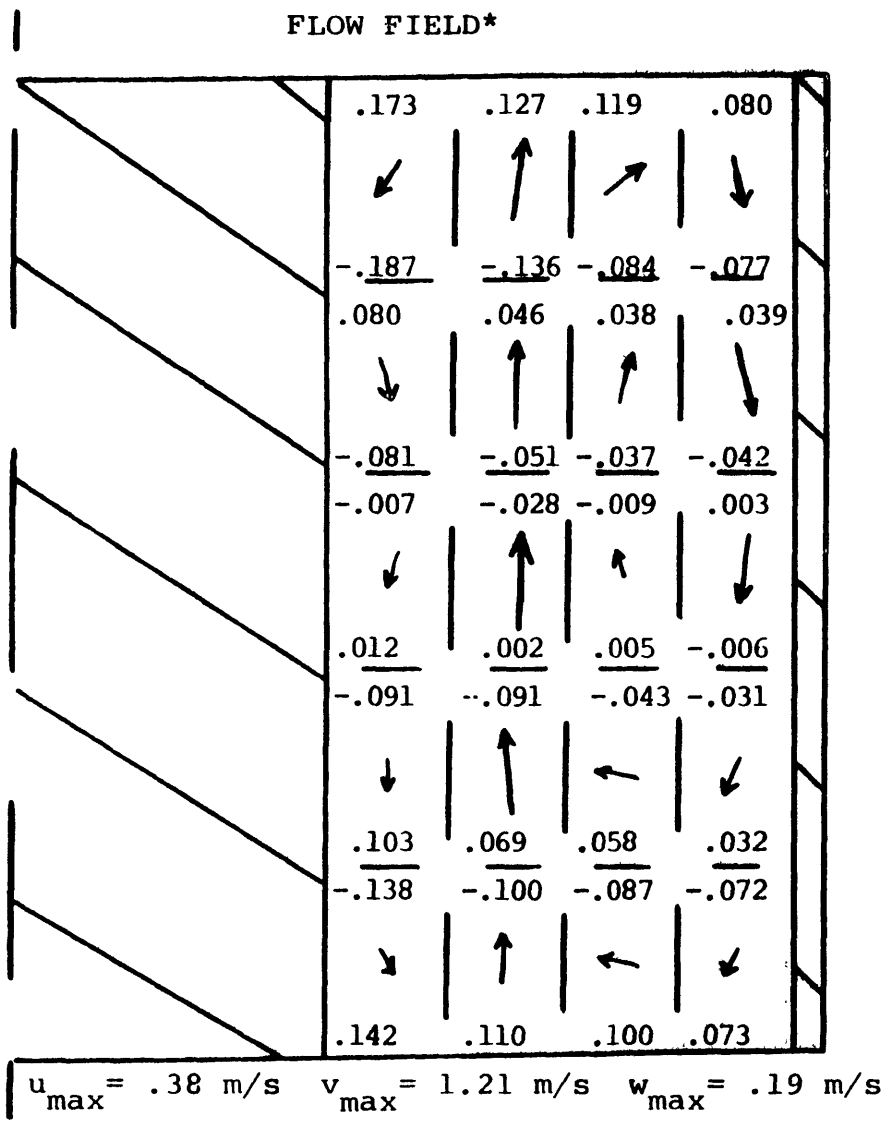

TEMPERATURE FIELD

342.2	342.6	341.7	336.9
336.8	342.2	340.0	337.3
332.6	342.3	337.1	337.4
326.0	342.6	334.2	337.1
314.6	320.8	329.3	333.3

* Flow field follows convention of previous figure.

FIGURE 4.56: FLOW AND TEMPERATURE FIELDS IN JET (K=4) REGION AT 50 SECONDS INTO HEDL B SIMULATION

clockwise recirculation due to the blower cells and the presence of the neighboring jet. The azimuthal field reflects the diversion of the jet when it strikes the upper boundary. All three non-jet regions exhibited qualitatively similar fields. The near-jet azimuthal region is distinctly different. The central jet dominates the flow causing local recirculation and reentrainment in the near jet region. The coarse mesh is seen to inhibit good jet resolution. The temperature field in the near-jet region reflects the higher temperature of the incoming stream. Though not shown the water density follows a similar profile.

Figures 4.57 and 4.58 depict analogous flow and temperature fields at 300 seconds. Three qualitative differences are observed between these plots and the predictions at 50 seconds. First, the jet vertical velocity is about 100% greater while the non-jet vertical and radial components are similar to the previous levels. The temperature profile in both zones is more uniform but still reflects the buoyancy of the warmer mixture. Third, the azimuthal velocity components have decreased by over 50%. This is reflected in the temperature fields which exhibit heightened azimuthal gradients. This final effect significantly influences the hydrogen concentration predictions.

Figure 4.59 is a plot of both predicted and measured hydrogen volume fraction (dry-no steam included in fraction)

FLOW FIELD*

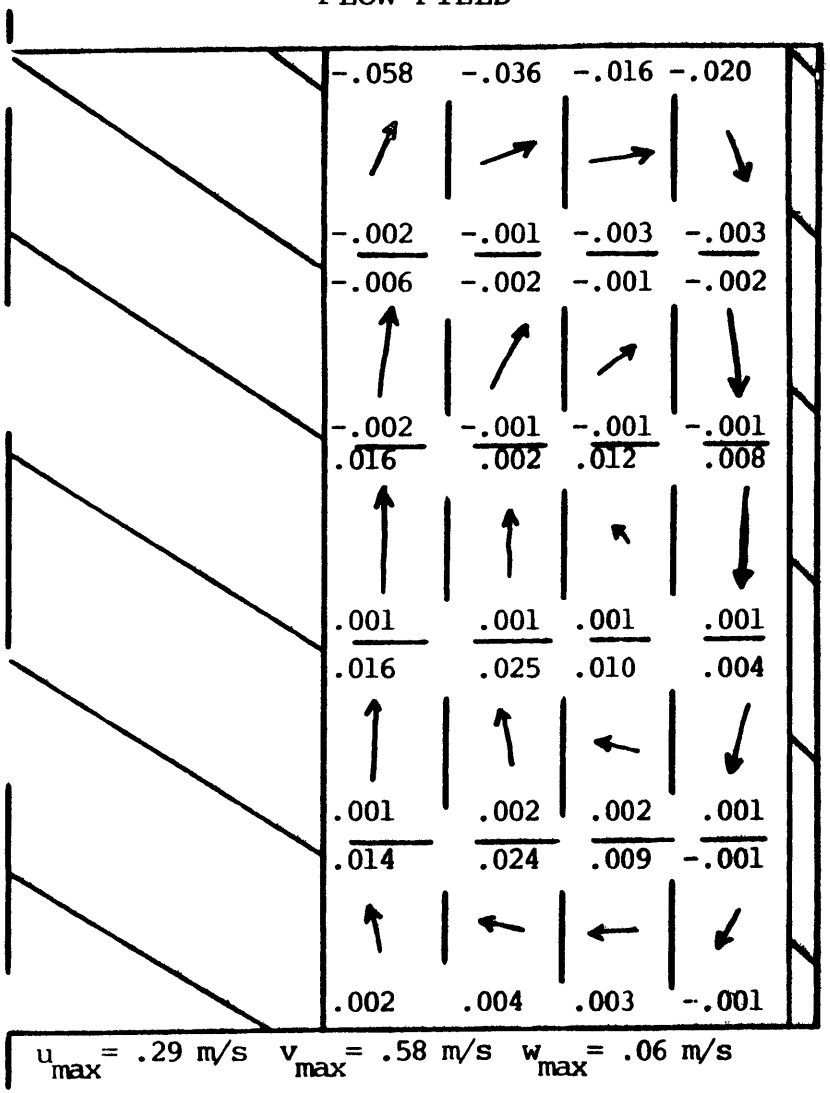

TEMPERATURE FIELD

335.8	335.3	335.1	331.0
331.5	331.4	331.5	331.2
331.3	331.4	331.3	331.2
331.2	331.3	331.3	331.3
331.2	331.3	331.4	331.4

* Flow field follows convention of previous figure.

FIGURE 4.57: FLOW AND TEMPERATURE FIELD IN NON-JET REGION (K=3) AT 300 SECONDS INTO HEDL B SIMULATION

FLOW FIELD*

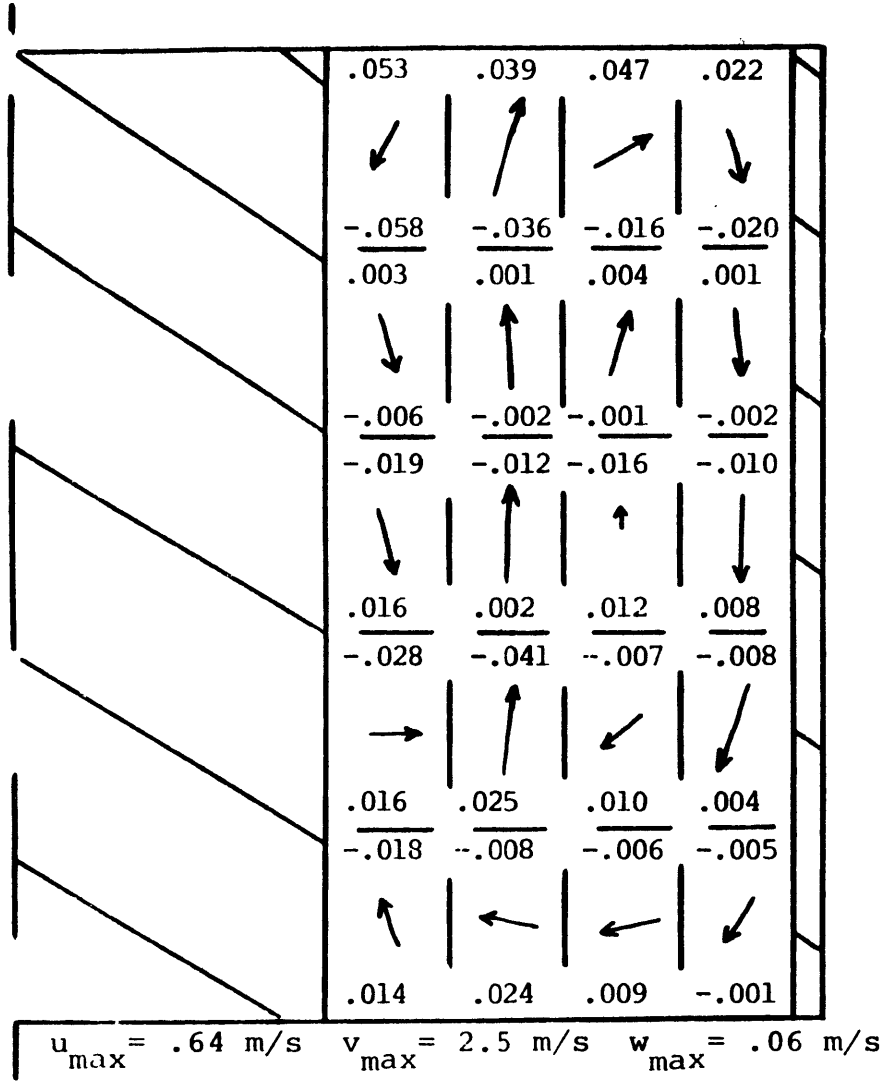

u_{max} = .64 m/s v_{max} = 2.5 m/s w_{max} = .06 m/s

TEMPERATURE FIELD

360.8	360.8	360.7	358.3
360.8	360.8	360.1	358.9
360.5	360.9	359.5	358.8
358.9	361.1	358.8	358.8
357.9	358.4	358.7	358.7

* Flow field follows convention of previous figure.

FIGURE 4.58: FLOW AND TEMPERATURE FIELDS IN JET (K=4) REGION AT 300 SECONDS INTO HEDL B SIMULATION

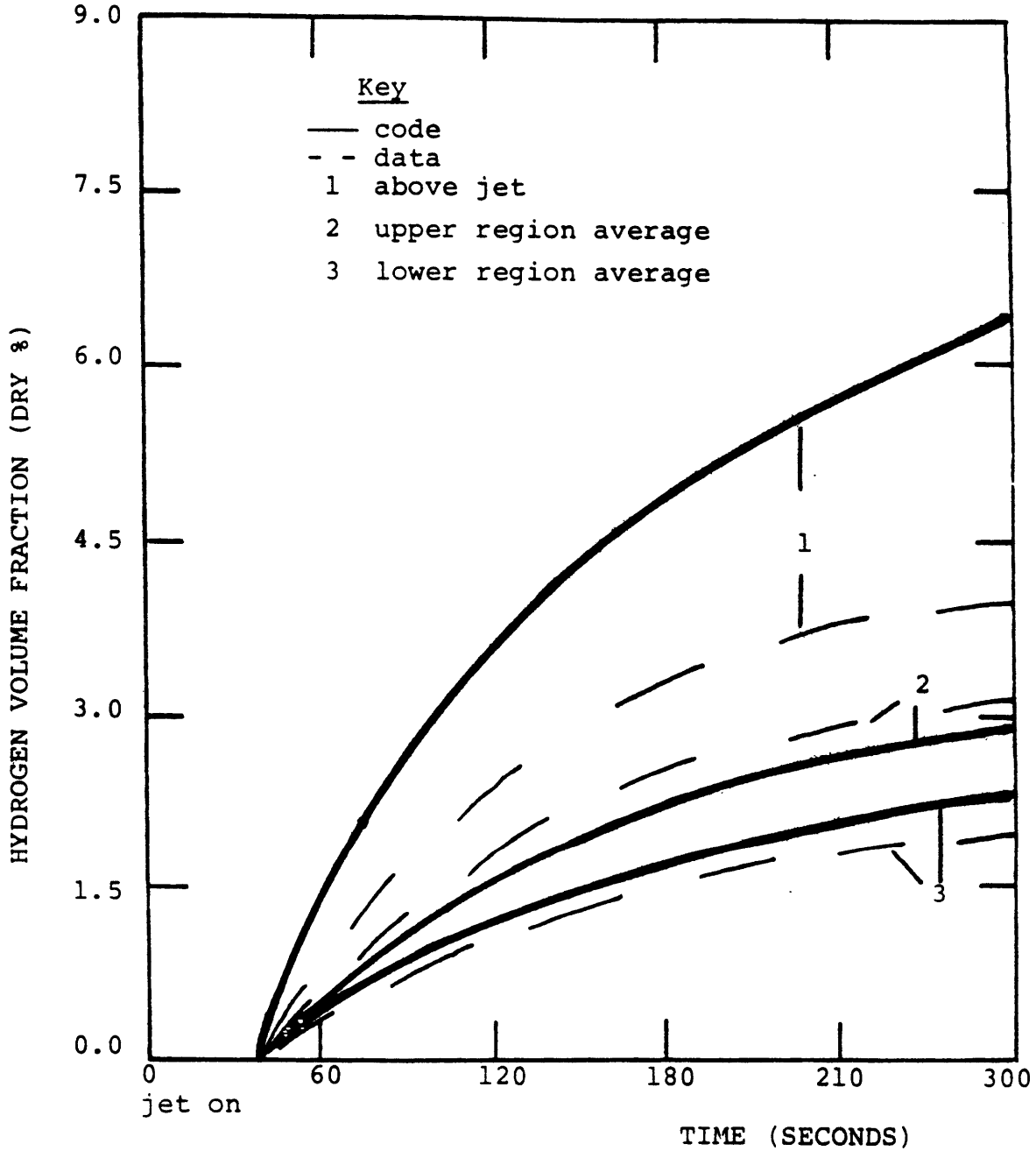

FIGURE 4.59: HYDROGEN VOLUME FRACTION PREDICTIONS VS DATA DURING HEDL B EXPERIMENT

during the first 300 seconds of the injection. Three pairs of curves are included. Type 1 curves are the volume fractions at the upper elevation in the jet region. Curves 2 and 3 are azimuthally-averaged concentrations at the upper and lower axial elevations. The agreement of the averaged data is good. The code predicts a larger degree of homogenization but the axial stratification is still apparent. The near-jet data are in the least agreement. At 300 seconds, the code results are nearly twice as large as the measurements. In general, the hydrogen concentrations in the near-jet region are 2-3 times larger than in other azimuthal zones. Probable causes of this disagreement in azimuthal homogenization are addressed below. The plots of normalized maximum velocity components versus time provided in Figure 4.60 is helpful in understanding this simulation. The axial and radial velocities exhibit similar behavior in that they reach a peak and then slowly decrease. The azimuthal component reaches a peak and then decays, with some oscillation, to more depressed levels. The azimuthal convective mixing is decreasing in time.

After detailed data analysis of this simulation, three effects are identified as contributors to the underprediction of azimuthal mixing. These effects are not independent and indeed may act synergistically. The coarse mesh, especially in the azimuthal direction, leads to inaccurate specification of parameter profiles. This is especially

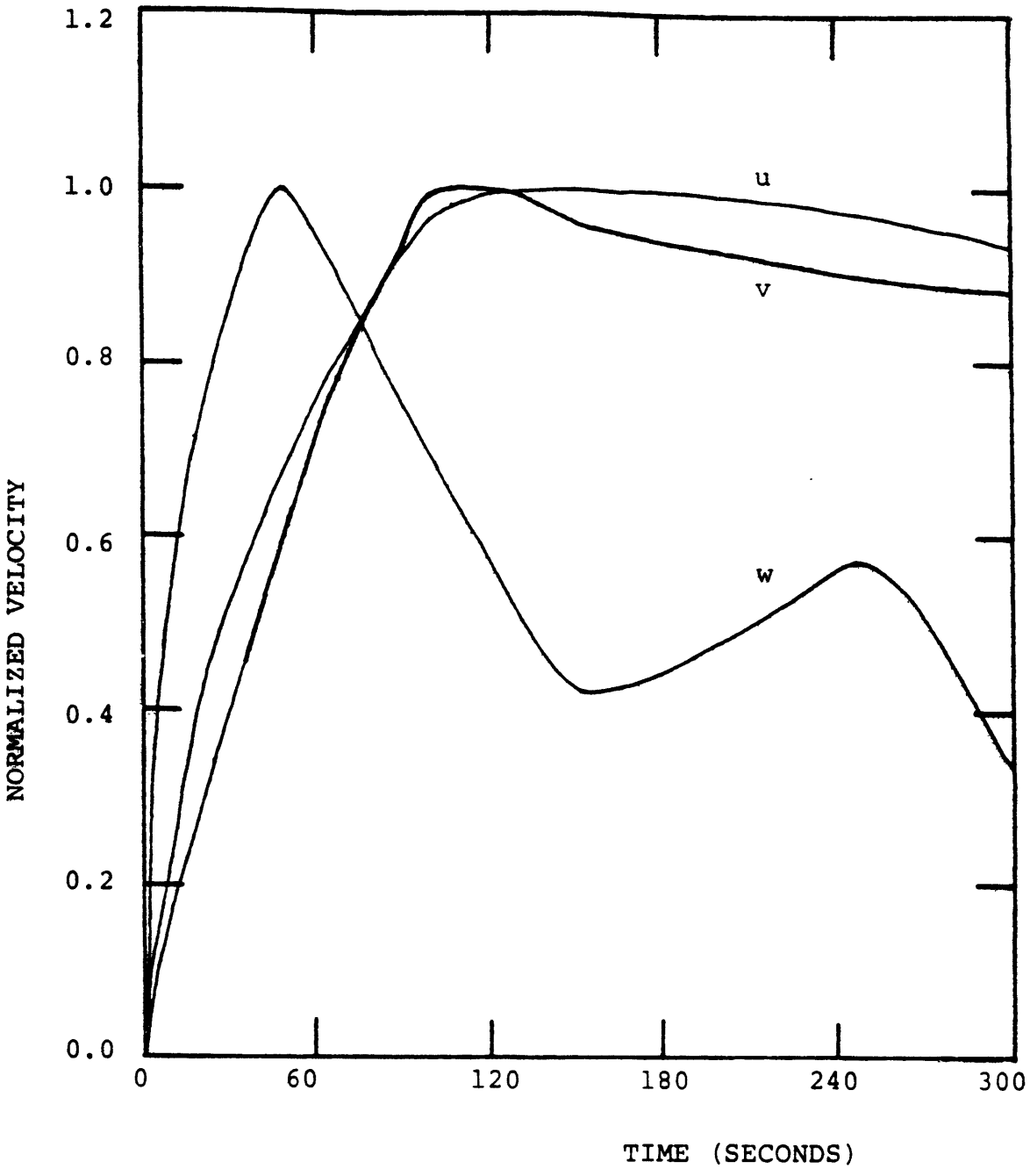

FIGURE 4.60: BEHAVIOR OF NORMALIZED VELOCITY COMPONENTS DURING HEDL B SIMULATION

important in the evaluation of second derivatives which describe diffusional processes. Given the dimensions of the problem, the radial second differences and the azimuthal second differences can be estimated as follows.

$$\text{radial second difference} \sim \frac{1}{.25^2} \sim 16 \text{ , and}$$

$$\text{azimuthal second difference} \sim \frac{1}{(2 \times 1.3)^2} \sim 0.15 \text{ .}$$

Thus, the very coarse azimuthal resolution can depress the importance of diffusional effects. The effect causes inaccuracies in the diffusion of both hydrogen and momentum. The momentum diffusion, driven by molecular and turbulent viscosity, is an important mechanism for promoting the development and sustenance of the azimuthal field. With decreasing viscosity, the jet will become increasingly two-dimensional. The second related cause is an inaccurate specification of turbulence levels. The input levels corresponded to TKE levels of 10^{-4} m^2/s^2 which is small compared to the estimated jet region levels of 10^{-2} - 10^{-3} m^2/s^2 . This effect will also inhibit diffusional transport. Finally, the blower model utilized while accurate in an integral sense does not accurately describe the mixing and momentum source of the recirculation flow. A more accurate description of these types of devices would enhance the quality of their predicted local effect.

Despite these limitations, the overall simulation is a success especially given the model and the discretization used. The local thermodynamic state algorithm behaved quite well showing excellent convergence even in cells with over 50% water (by mass). The average hydrogen concentration predictions showed general agreement with the data and sources of inaccuracy are reasonably well categorized.

A second simulation is reported which addresses a few of the limitations noted above. A 96 node three dimensional model is utilized as depicted in Figure 4.61. The azimuthal nodalization is increased by 50% while the axial mesh spacing is increased slightly. The input data are similar to the first simulation except for refinement of the source and blower conditions based on more detailed experimental measurement data. This input refinement led to a somewhat different timing sequence such that the basic transient events are: blowers on (0 s), steam on (15 s) and hydrogen on (100 s). Therefore the results of this run cannot be compared with the preceding data in regards to time. Figures 4.62 and 4.63 depict the velocity and temperature fields at 50 seconds in the non-jet and jet regions, respectively. These fields are very similar to the 80 node simulation in this time frame. The higher temperature steam jet is seen to dominate the dynamics in both the near-jet flow and thermal fields. Figures 4.64 and 4.65 depict analogous predictions in the

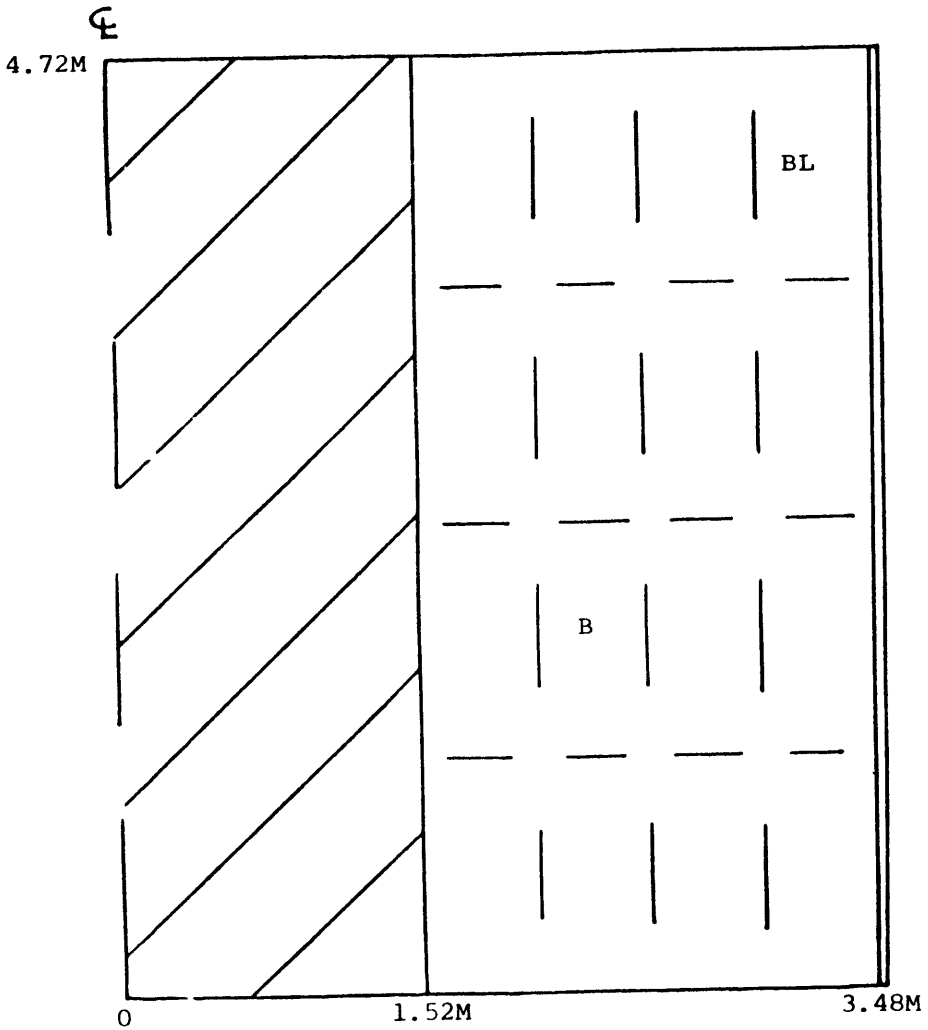

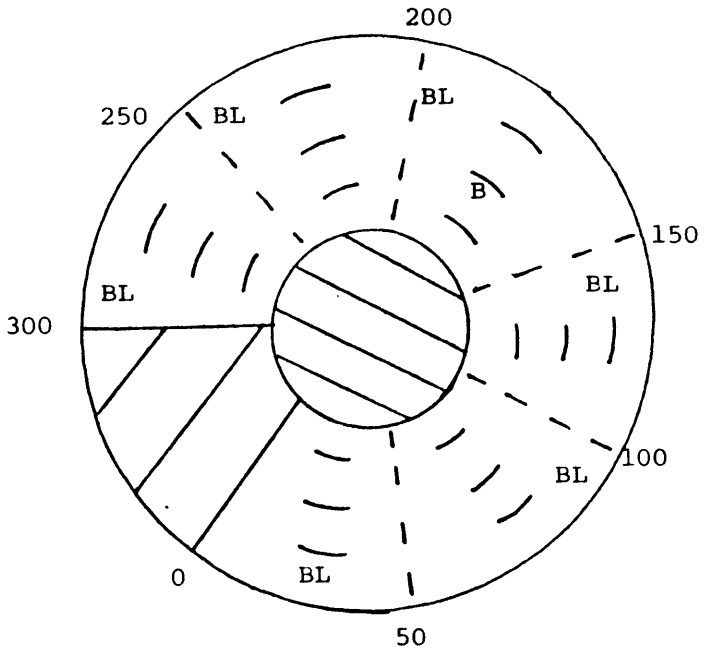

δR = 0.57M
δZ = 1.18M
$\delta\theta$ = 50°

BL = Blower Cell
B = JET B

FIGURE 4.61: 96 NODE MODEL OF HEDL FACILITY

FLOW FIELD*

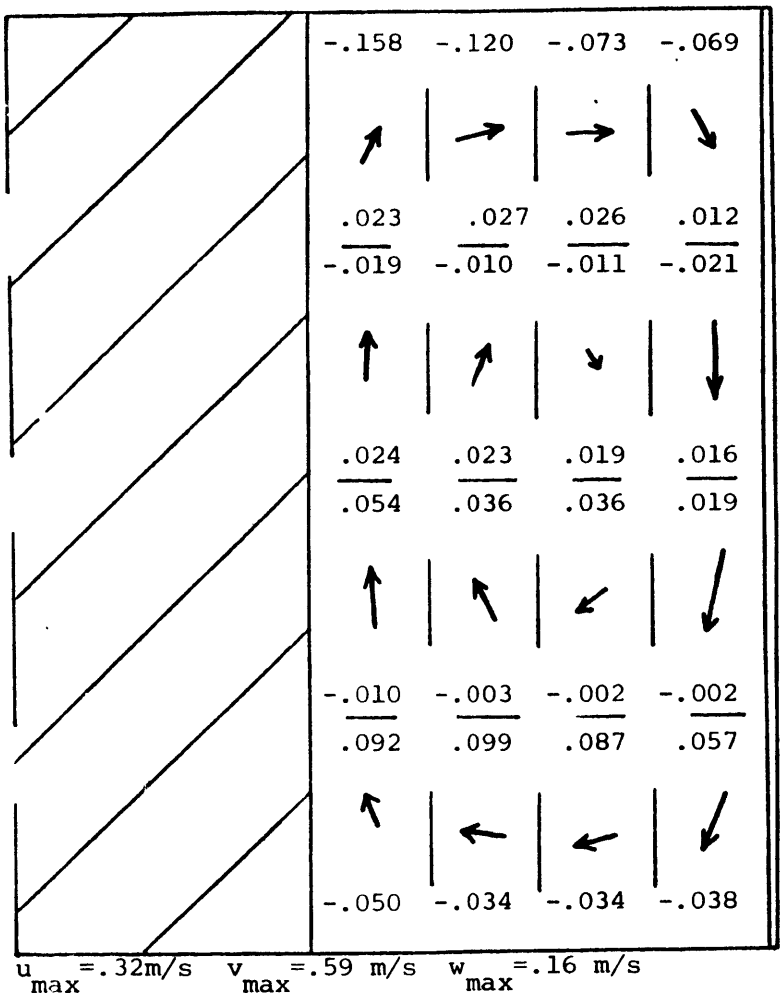

TEMPERATURE FIELD

328.1	327.2	329.0	310.5
322.7	321.9	322.4	313.1
321.2	319.4	318.0	314.1
319.8	318.2	318.0	315.5

*Flow field follows convention of previous HEDL figures.

FIGURE 4.62: FLOW AND TEMPERATURE FIELDS IN NON-JET REGION AT 50 SECONDS INTO 96 NODE HEDL B SIMULATION

FLOW FIELD*

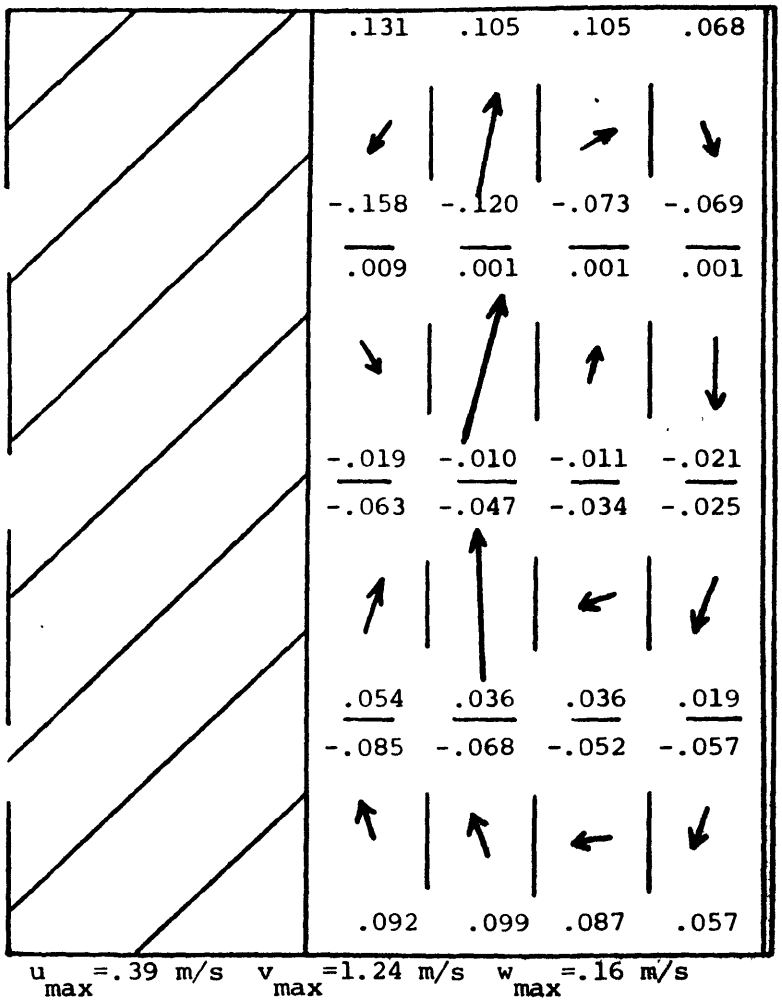

TEMPERATURE FIELD

336.4	335.6	332.0	322.6
329.1	334.6	326.6	321.0
316.8	336.3	316.2	319.4
317.7	313.9	313.1	315.8

*Flow field follows convention of previous HEDL figures.

FIGURE 4.63: FLOW AND TEMPERATURE FIELDS IN JET REGION AT 50 SECONDS INTO 96 NODE HEDL B SIMULATION

FLOW FIELD*

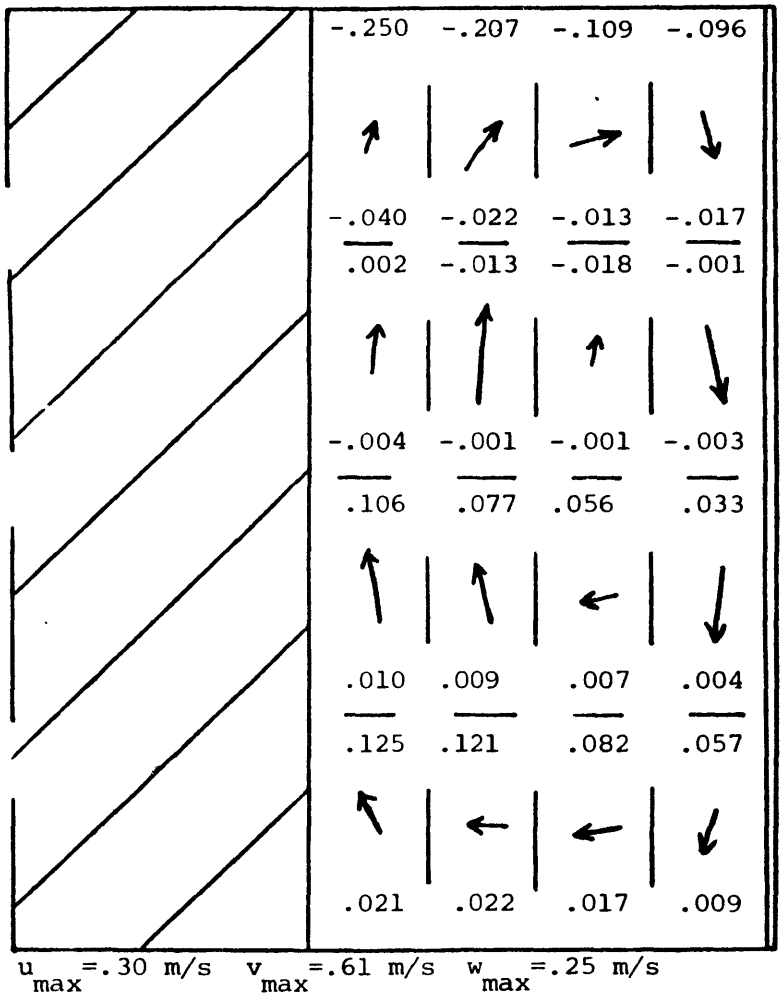

TEMPERATURE FIELD

354.1	350.0	349.5	345.4
341.6	342.3	342.1	345.1
341.8	342.7	343.1	344.7
341.9	342.9	343.0	344.0

*Flow field follows convention of previous HEDL figures.

FIGURE 4.64: FLOW AND TEMPERATURE FIELDS IN NON-JET REGION AT 350 SECONDS INTO 96 NODE HEDLB SIMULATION

FLOW FIELD*

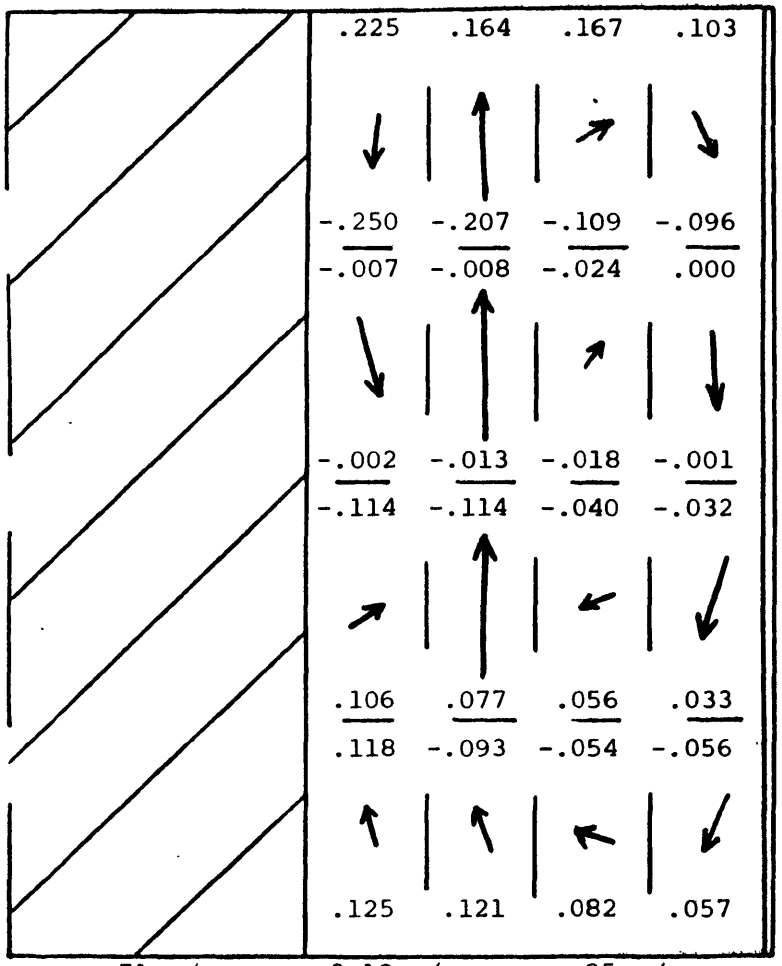

TEMPERATURE FIELD

360.4	359.7	359.9	358.2
360.2	359.5	358.7	358.1
354.4	359.5	357.6	357.9
352.4	355.1	356.6	357.2

*Flow field follows convention of previous HEDL figures.

FIGURE 4.65: FLOW AND TEMPERATURE FIELDS IN JET REGION AT 350 SECONDS INTO 96 NODE HEDL B SIMULATION

same regions at 350 seconds (end of simulation). In the non-jet region, the shear caused by the jet leads to a peaked axial velocity component away from the left side boundary. This influence of the jet in planes away from the source region is not observed in the coarser azimuthal nodalization calculation. The jet region fields are qualitatively similar to previous results but show better jet resolution and increased entrainment.

Figure 4.66 depicts the predicted and measured hydrogen volume fractions during the first 350 seconds of the experiment. As compared to the 80 node simulation, this result shows improved agreement with data especially in the region average data. The code still underpredicts azimuthal mixing but the disagreement has decreased by roughly 50%. The two reasons identified for this improvement are the decreased azimuthal node spacing and better source definition. Nevertheless the remaining disagreement reinforces the need for further increased nodalization and an improved blower model. The transient behavior of the three normalized velocity components shown in Figure 4.67 indicates that the azimuthal component is starting to behave more congruently with the axial and radial velocities.

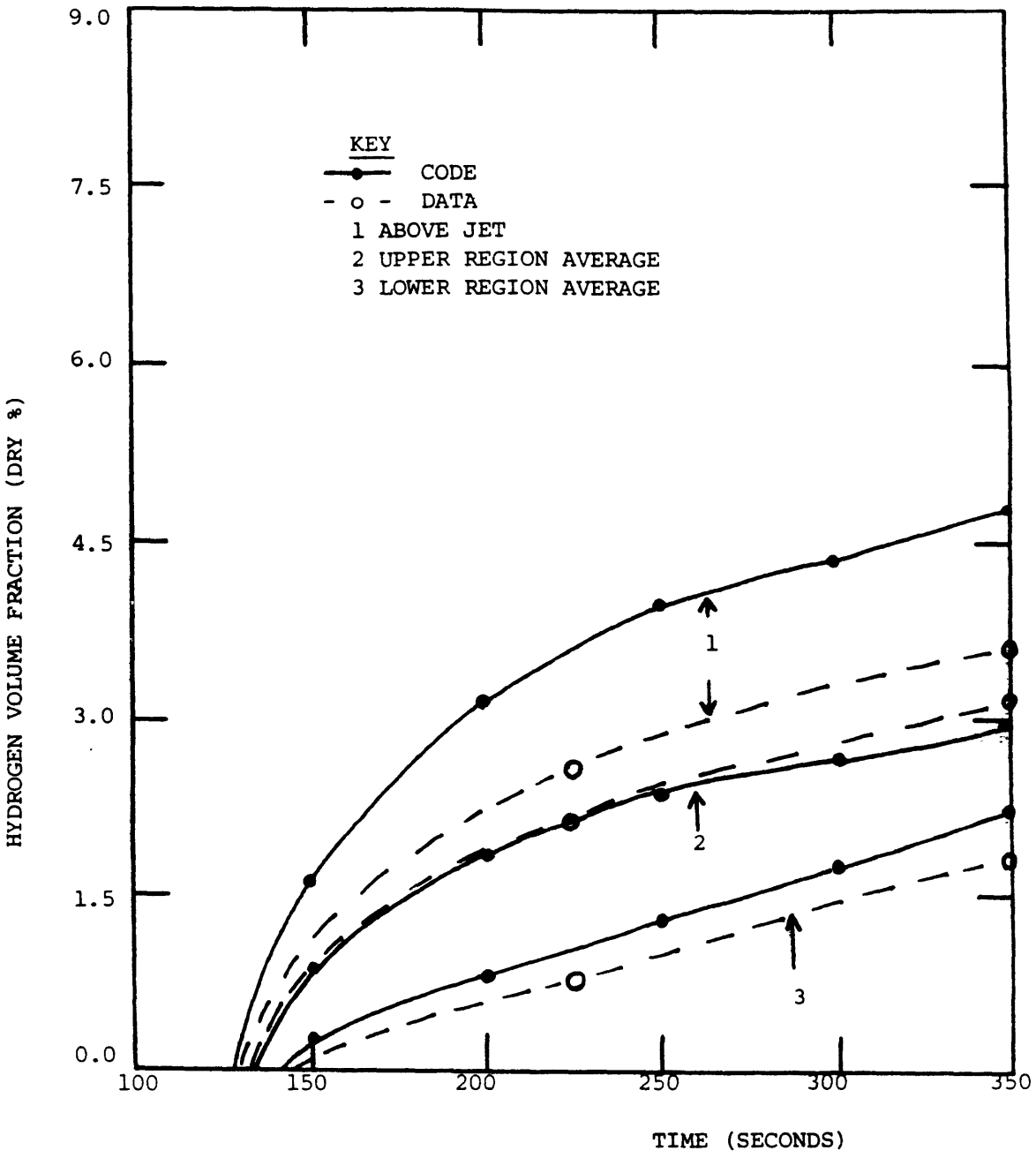

FIGURE 4.66: HYDROGEN VOLUME FRACTION PREDICTIONS VS DATA DURING 96 NODE HEDL B SIMULATION

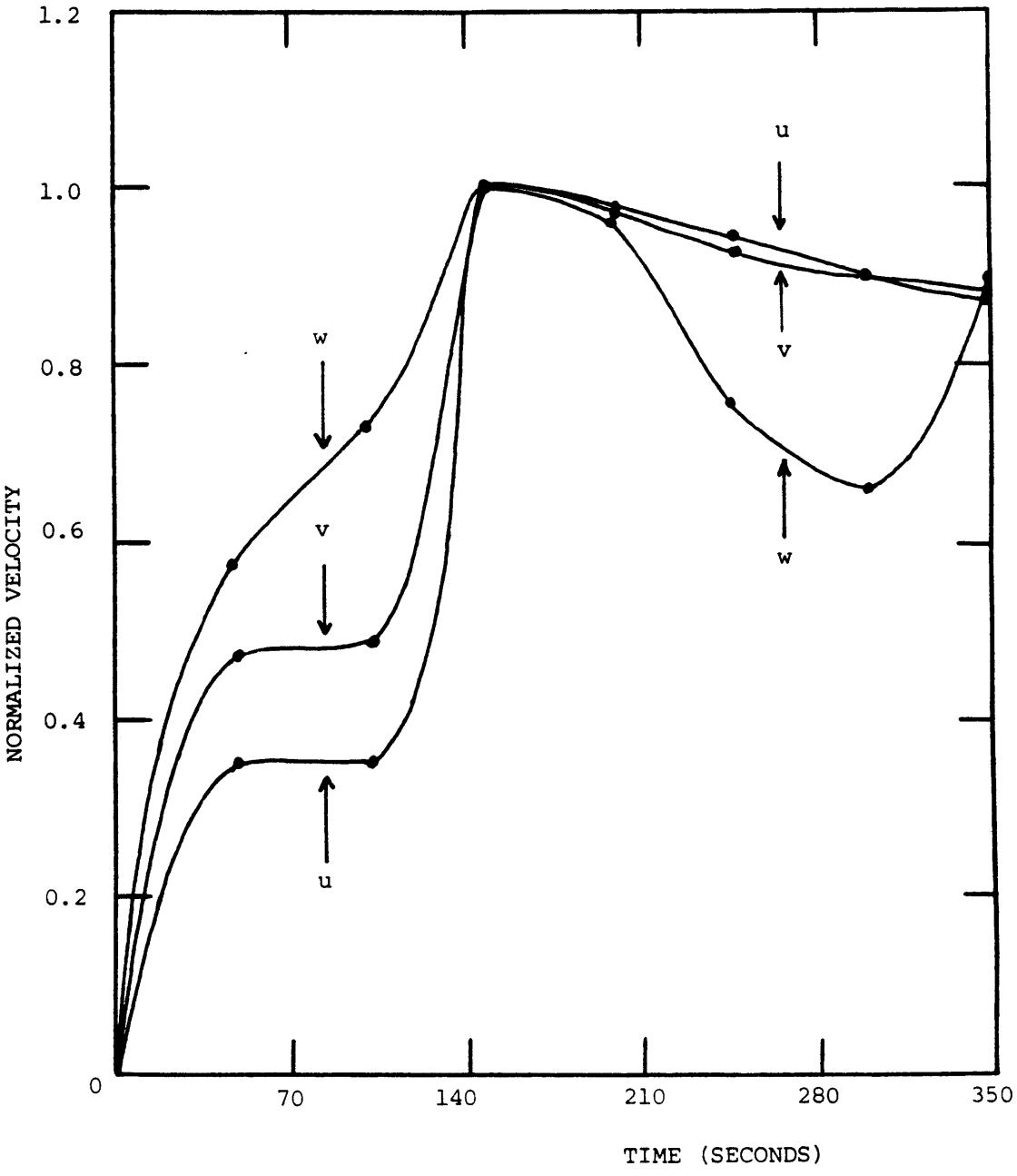

FIGURE 4.67: BEHAVIOR OF NORMALIZED VELOCITY COMPONENTS DURING 96 NODE HEDL B SIMULATION

4.4 Lumped Parameter Model Results

The development of the lumped parameter capability is not a central part of this work and is based on well-known methods. As such, the model is used in a few sample calculations to demonstrate that it has been implemented correctly. The results reported here are ascertained using the full nodal model. Experience with the original BEACON lumped/continuum calculations has shown that such coupled simulations are susceptible to time step instabilities if the bounding lumped regions' global state changes quickly. Also, using the continuum options to model internodal flow paths as is required by the original formulation is computationally inefficient and sometimes physically inappropriate.

The first simulation is a simple three region problem in which air is injected into one compartment. Each volume is 1 m^3, connected in tandem fashion (1→2→3) and at an initial state of 289.15°K and atmospheric pressure. Air of the same temperature is injected into room 1 at a rate of 10^{-3} kg/sec. The code's predictions for the average compartmental state is compared to the exact solution in Table 4.10. Excellent agreement is noted.

The second problem is a six region multiconnected geometry as defined in Figure 4.68. The room sizes and flowpath characteristics resemble the BF facility. Hydrogen and air are introduced in the lower central compartment at

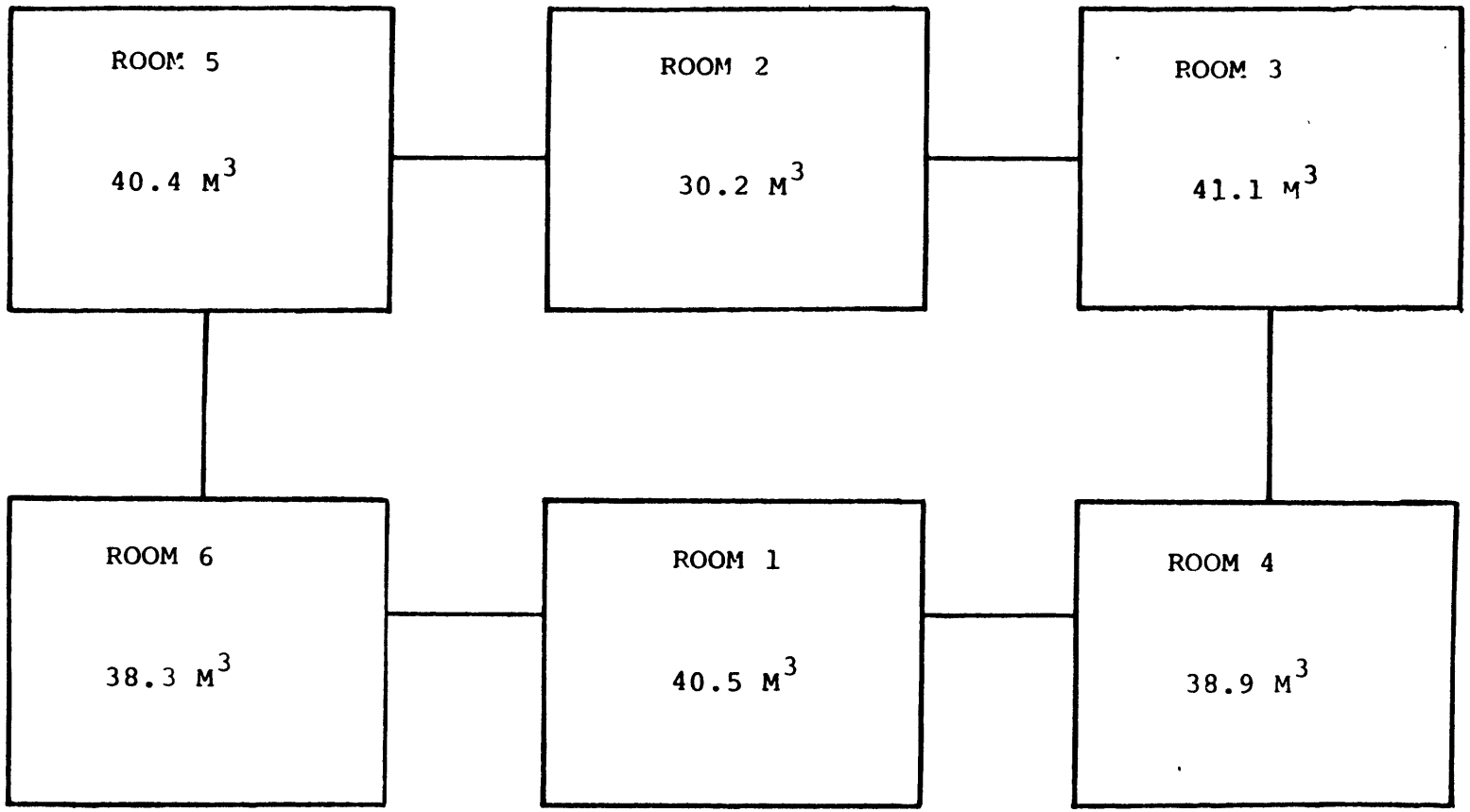

FIGURE 4.68 : PROBLEM GEOMETRY AND CONNECTION LOGIC FOR SIX ROOM LUMPED PARAMETER PROBLEM

Table 4.10

Comparison of Code Predictions to Exact Results for Three Region Air Injection Problem at 20 Seconds

Parameter	Exact	Code
Pressure (N/m^2)	102128	102128
Temperature (°K)	289.788	289,787
Density (kg/m^3)	1.22787	1.22788

rates of 5.0×10^{-6} and $3.7\ 10^{-5}$ kg/sec, respectively. A 10000 second simulation is reported which utilized a constant time step of 5 seconds. The computed hydrogen volume fraction transients are depicted in Figure 4.69.

This multiroom simulation is similar to the BF12 test except for the disconnection of regions 1 and 2. The BF12 data indicated more homogeneous hydrogen profiles. This is due to the connection between rooms 1 and 2. Attempts at simulating this configuration with its potential for recirculating flow paths produced results very sensitive to junction characteristic input. This highlights the inherent weakness of nodal methods in that the inexact specification of junction loss coefficients and inertias significantly affect predictions. Automatic time step control is also required if flow rates become large enough to cause instabilities. Second, the vertical streaming of a more buoyant gas such as hydrogen through a relatively stagnant

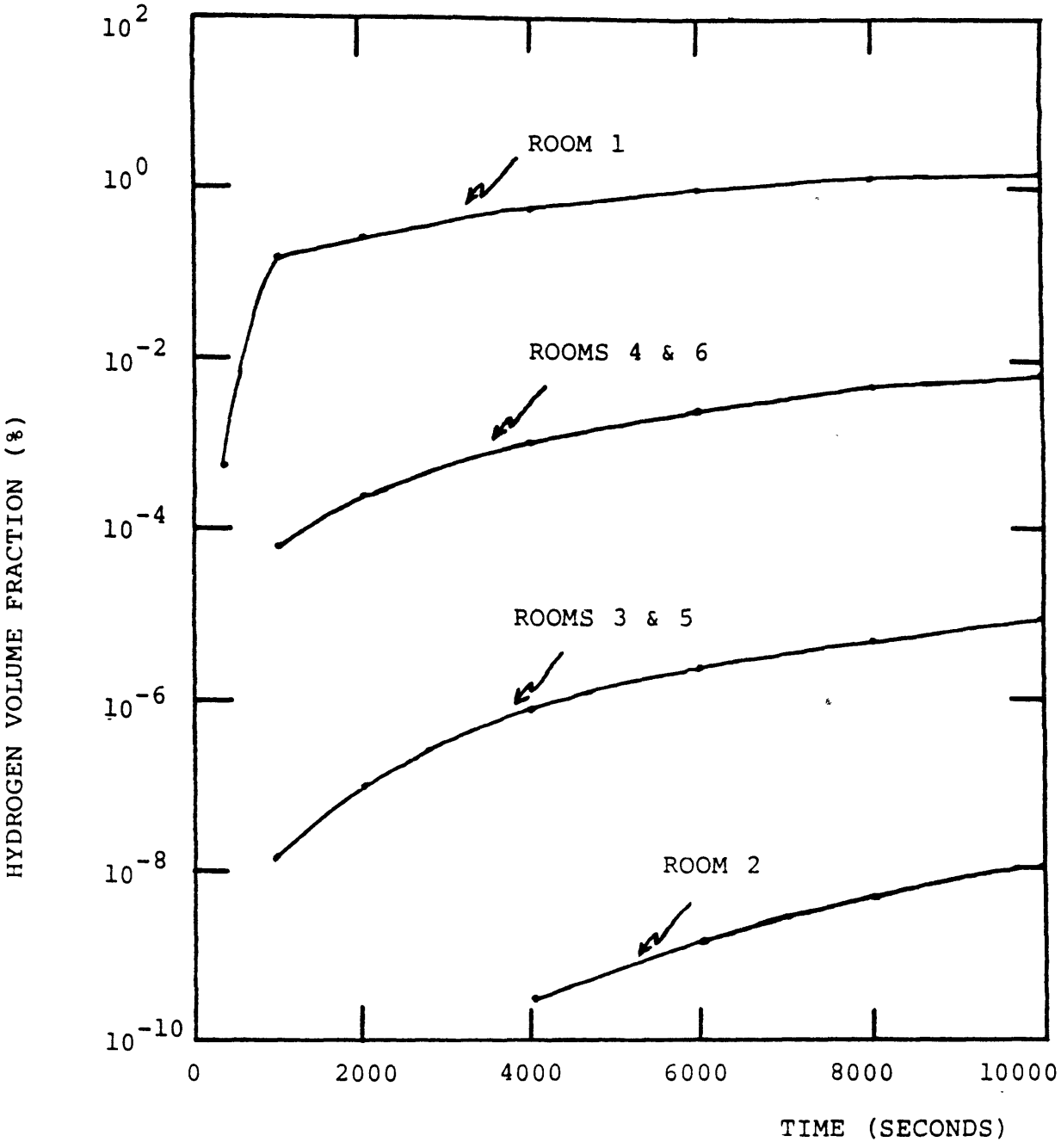

FIGURE 4.69: ROOM HYDROGEN CONCENTRATION TRANSIENTS FOR LUMPED PARAMETER PROBLEM

region without good mixing into an upper vertically connected region cannot be predicted by nodal methods such as that utilized here. The inaccuracy arises from the well-mixed assumption implicit in the nodal formulation.

Overall, the reported results demonstrate the usefulness of this added capability. Its present limitations include the inability to treat vertical streaming, the need for a versatile time step control logic and better definition criteria for junction characteristics.

4.5 Discussion of Results

The results reported are a representative sample of calculations which demonstrate the capabilities and limitations of the analytical models described herein as they are embodied in a computer code named LIMIT. In general, a versatile computational tool with a wide range of applicability is demonstrated. Before addressing the performance of the three major modelling options, a general observation is made. Over the course of this developmental effort, no clearly advantageous choice between implementing a fully general model applicable to lumped and continuum analyses of varying time scales or using the phenomenon-specific approach presented here became apparent. The former approach is designed to accommodate all significant phenomena no matter which dominate in a particular situation. This minimizes the chances of neglecting important effects. However this route pays the price of greater complexity, less computational

efficiency and certain inaccuracies due to the unavoidable extension of ancillary models. The approach used in this work is more efficient, less complex and has the potential for greater problem specific accuracy. Nevertheless, the analyst is required to have a good a prior understanding of the problem to make a proper choice. Further, certain physical situations are not clearly placed within the validity bounds of any one modelling option. The HEDL problem is a good example of such a situation.

The modified BEACON equation set or rapid blowdown transient model is shown to be applicable to physical situations dominated by two-phase effects. Predictions of transients of this nature are both reasonable and well-behaved. The current version of this model has inherited the original BEACON code sensitivity to very high or low (nearly single phase) flows. The coupled phasial equations and especially the interphasial exchange models are most suspect. The model also consumes large amounts of computational resources (see 4.7).

The continuum slow mixing model is the most useful for many pertinent analyses. The Battelle Frankfurt based simulations demonstrate that it is most accurate in situations where local states are true perturbations of a reference state and compressibility effects are small. Some unique features of the model formulation which help relax the usual incompressible assumption constraints are a

conservative formulation of certain transport equations, a thermodynamic model which can treat a condensible component and periodic reference state update. The two major limitations of the model are the Courant time step and numerical diffusion. Both constraints require the use of a fine mesh and a commensurate amount of computation time. The simulation of the BF6 test demonstrates the importance of these considerations. Nevertheless, the model can be confidently utilized in this type of simulation if the computing resources are expended. The HEDL based problems test the validity bounds of the slow mixing model and invoke most of the new ancillary models. Given the coarse mesh and basic incompressible formulation, the results compare well with data at least qualitatively. Most significant is the demonstrated ability of the thermodynamic model to treat problems in which water occupies a significant mass fraction (~50%). The HEDL simulation also demonstrates the full 3-D cylindrical spatial definition of the model. Numerical diffusion remains a source of inaccuracy in these simulations as is evidenced by the predicted hydrogen concentration axial gradients being less sever than the measured data.

The lumped parameter model, especially in its completely nodal (no continuum regions) formulation, allows numerous economical scoping calculations. The results of such sensitivity or global state computations are useful to either define the scenarios worthy of more detailed continuum

analysis or provide a means of testing modelling hypotheses. The problems reported show that the LIMIT lumped model is properly formulated and produces physically reasonable results. Of course, the well-mixed nodal assumption does limit the applicability range of the model. For example, such phenomena as vertical streaming of buoyant hydrogen through a compartment without radial mixing cannot be predicted.

4.6 Model Capabilities vs Other Approaches

Of the analytical tools currently being applied to hydrogen transport analysis, six methods in addition to this work are worthy of additional comment. Specifically these are: KWU lumped parameter analysis, the RALOC program as utilized by German researchers [54] and at Sandia National Laboratory [56], the MAPHY code [57] developed in Japan, TEMPEST [63] utilized at Battelle Northwest Laboratory (BNWL), HMS [65] developed at Los Alamos National Laboratory, COBRA-NC [67] employed at BNWL and the LIMIT code. The major analytical features of these methods are summarized in Table 4.11.

On the basis of a limited survey, the following comparative critique is presented. The KWU method is a manual calculation informally reported in a BF experimental progress report. As is expected, it is of limited use but does provide quick order of magnitude assessment. The RALOC and

Table 4.11

Representative Hydrogen Transport Models

Feature	Model						
	KWU (Hand Calculated)	RALOC (GRS or Sandia)	MAPHY (Japan)	TEMPEST (BNWL)	HMS (LANL)	COBRA-NC (BNWL)	LIMIT (MIT)
Continuum				X	X	X	X
Lumped Parameter	X	X	X		X	X	X
Two-Phase Effects		X	X		X	X	X
Blowdown					X	X	X
Turbulence Model				2 Equat. k-ε		Eddy Viscosity	2 Equat. k-ε
Multi-Compartments		X	X			X	X
Fan Coolers/Sprays		X	X			X	X
Chemical Reactions	No	?	?	No	?	?	?

MAPHY codes are quite similar. Both are based on nodal lumped parameter formulations and offer limited spatial definition capability. They are both good nodal tools but have difficulty handling problems involving many regions due to the stiff coupling of the governing differential equations. TEMPEST is a single region (but multi-material) continuum code based on a strict incompressible flow formulation. Its predictive ability of slow single phase problems is noteworthy but a rather fine mesh discretization is required. The lack of a multicompartment capability as well as the omission of a condensible field limits its usefulness in analyzing more complex transients involving realizstic geometries and steam injection.

HMS, COBRA-NC and the MIT method are the most versatile and appropriate tools. The HMS program has been successfully applied to the solution of benchmark problems. The lack of a lumped parameter option, detailed turbulence model and multicompartment option are significant limitations but overall the HMS code embodies a worthwhile approach. COBRA-NC is more versatile and has been used to accurately reproduce selected empirical results. The continuum model based on a two-fluid two phase model is very accurate but seems inappropriately complex for the economical analysis of longer quasi-homogeneous transients. However, the single model formulation avoids the model choice inherent in the MIT code. The COBRA turbulence model may not be adequate

for analyzing transients dominated by turbulent diffusive transport.

The capabilities of the current work's method in the areas of problem versatility, computational efficiency, reduction of numerical diffusion and proper heat/mass transfer modelling are unique. Two negative aspects of this work are the need to enhance the transition between applicable continuum models and greater validation. Nevertheless, the current version of the MIT program compares quite favorably with other alternatives. Finally, while the analysis of post-chemical reaction flow is not of central interest to this work (see Appendix C for preliminary discussion), the direct extension of any of these methods to this more complex regime is questionable.

4.7 Computational Effort Analysis

An important goal of this research is to produce an analysis tool which is relatively economical to employ. A major disadvantage of most other tools used in hydrogen transport modelling is that utilization in a production mode operation in which budgetary and computing facility limitations are present is not achievable if useful predictions are required. The LIMIT code is a good first step in achieving cost efficient yet accurate simulation. Table 4.12 illustrates the computational effort required for the simulations reported earlier. The cost and running time figures

Table 4.12

Representative Computational Costs

Type	Problem Duration (s)	Number of Cells[1]	CPU Time (s)	CPU Time/ Duration-Cell	Approximate Cost[2] ($)
FAST	0.2	100	651	32.55	60.
SLOW-BF	8000.0	32	5033	0.020	360.
SLOW-HEDL	200.0	80	3332	0.208	225.
LUMPED	10000.0	6	56	0.00093	11

Notes: 1. Fluid Cells

2. Based on 0.7 SBU/CPUs, weekend priority, includes printing and tapes costs on a CDC CYBER-176.

presented are approximate values utilizing a CYBER-176 computer on a commercial basis. The rapid transient model is clearly the most resource consuming as is expected. The cost efficiency of the slower mixing model is noted. The HEDL jet type analysis is seen to be an order of magnitude greater than BF type transients and the economy of the lumped model is clearly demonstrated.

More detailed analysis of the slower mixing model behavior indicates the following qualitative observations. If Courant numbers are limited to 0.5, the number of pressure iterations required to attain a divergence free flow field is 10-20. Approximately 15 pressure iterations require the same amount of computation as the remaining non-iterative calculations. That is, if a computational cycle involved 30 iterations and used 9 seconds of computing time, 3 seconds are spent solving the passive transport equations and the tilde phase of the momentum equation solution while 6 seconds are used in the flow field selective over-relaxation iteration. Finally, the total transient computing time using the slower mixing model is proportional to the number of fluid cells raised to the approximately 1.25 power. For example, if an 80 node HEDL computation requires 1000 seconds, a 100 node simulation of the same problem would utilize roughly 1300 seconds of CPU time.

5.0 Conclusions and Recommendations

5.1 Conclusions

The analytical models and the computer program which embodies them described in this work are shown to fulfill the need to accurately model hydrogen gas transport in nuclear reactor containment buildings. Though hydrogen safety is the central focus of the research, the tool itself is potentially applicable to a much broader range of analyses. The validation and demonstration calculations presented in Chapter 4 illustrate the code's capabilities and limitations.

The general conclusion drawn from this work is that a versatile basic tool has been produced. Some more specific concluding observations are now presented and suggestions for future work are contained in the following section.

The use of two different continuum models depending upon the dominant physical phenomena is shown to be an effective way to achieve economical yet useful results. This flexibility allows the analyst to match the tool to the problem's requirements. Two weaknesses of this approach must be remembered. First, the analyst must make a choice based on engineering judgment. Second, certain applications may straddle the boundary of the two models' applicability. The modified two-fluid BF\CON equation set is not recommended for longer transients or physical situations which are single-phase in nature.

The lumped parameter modelling capability (especially the pure nodal model) provides a very useful option. The principal applications of this model are situations where spatial resolution is less important than global state changes. The demonstration problems show not only its efficiency but also its limitations. Modelling flow junction characteristics (loss coefficients, inertias, etc.) always involves approximation. Also, the well-mixed volume assumption cannot account for preferential component transport such as hydrogen or steam streaming induced by local buoyancy or jet effects.

The slow mixing model is shown to be an adequate physical representation of most problems of interest. The incompressible flow field assumption allows for economical numerical solution due to the decoupling of the conservation equations. A certain degree of compressibility is introduced however in the formulation of the buoyancy forces and the energy conservation equations. Nevertheless, experience has shown that application of this method to truly compressible problems leads to significant mispredictions.

Numerical diffusion especially due to the donor cell treatment of convective terms has been shown to be a very important consideration. The use of coarse mesh spacing in the interest of economy aggravates the false diffusion problem. The failure to properly predict the breakdown of atmospheric inversions is a problem caused by this effect.

A partial improvement in this regard is the use of a numerical diffusivity correction and the utilization of optimized problem meshes. However, a complete solution to this problem save for the brute force approach of very fine mesh spacing and small time steps is not achieved.

The local thermodynamic state determination model and calculational logic has proved to be quite successful. The specific successive substitution algorithm is stable and converges to a desirable accuracy quickly. Its application to other situations of similar characteristics such as moist plumes is strongly suggested.

The validation and demonstration simulations reported provide a good degree of confidence in the code's ability to predict real physical situations. The Battelle Frankfurt simulations tested the physical regime of single-phase, pure plume behavior. The simulation of tests in which a neutrally stratified pre-test atmosphere existed is accurate even when coarse mesh spacing is utilized. The mixing in thermally stratified fields is not accurately predicted (first simulation of BF6) if coarse mesh spacing is used and numerical diffusion is not corrected.

The application of the slow mixing model to the HEDL experiments tests the validity boundary of the model. Modelling a high velocity steam/gas jet as a distributed momentum source is a useful approximation. Its major limitation is that a detailed knowledge of the near-jet flow field is compromised. A recirculation blower model is

described which adequately represented the test facility ventilation system. Nevertheless, a more versatile fan cooler is desirable. The thermodynamic state model performed reasonably well except for some predictions near the steam jet. Finally, the overall prediction of hydrogen concentrations is seen to be acceptable considering the relatively coarse discretization. However, application of the method in its present form to problems exhibiting stronger compressibility and phase change effects should be done with proper caution.

The overall code characteristics and its computational efficiency compare quite well with other methods. Simulations of significant problems can be accomplished at reasonable cost. The major limitation of both the rapid and slow mixing models is the Courant time step stability restriction. This is especially so in longer slowly varying transients.

5.2 Recommendations For Future Work

This work represents the first major step in an ongoing research project and as expected further effort is desirable. The areas of proper diffusion modelling is being addressed in a related effort and some of the benefits of that work are incorporated into the current program. The area of ancillary effects modelling such as heat transfer, surface mass transfer, containment sprays and fan cooler models are

also under development. Four additional topics are recommended for future consideration.

First, model improvement in a number of specific instances is recommended. The need and possible methods of extending the so-called slow mixing model to problems exhibiting more significant compressibility is advisable. If the need is demonstrated the main options are either modification of the existing solution method or implementation of a new scheme. The former choice is the more straightforward while the latter has greater potential for achieving significant improvement. The relaxation of the time step limitations as well as the potential for fully correcting false diffusion both suggest the investigation of implicit methods. Appendix D is provided as a starting point for such an investigation. The general area of code streamlining and optimization are worthy of additional effort. A potential running time reduction of roughly 20% could probably be accrued from a careful reprogramming program.

The second area of suggested future work is additional model validation. The current effort is limited to a few selected simulations. Comparison predictions with the more complex (and expensive to run) BF and HEDL experiments would afford greater confidence in the method and also illuminate problem areas requiring improvement. An important aspect of this work is to accomplish it in a more economical situation than the commercial computer time rates imposed on the present development.

The application of the model to actual containment design and licensing problems is the third recommended topic. The purpose of the code is for it to be employed in real world applications and a systematic performance of such analyses is of definite benefit.

Finally, the methods developed and implemented can be extended to other analysis areas. A few suggested areas are containment fission product transport, general post-accident containment response and analysis of non-nuclear combustible gas problems. The general area of modelling reacting flows is addressed in Appendix C. The potential for extension to these areas is conceptual at this time and can only be accurately assessed by a systematic study.

6.0 References

1. R.W. Bergstrom and W.A. Chittenden, "Reactor-Containment Engineering: Our Experience To Date," Nucleonics 17, pp. 86-93, April 1959.

2. G.W. Keilholtz, "Annotated Bibliography of Hydrogen Considerations in Light-Water Power Reactors," ORNL-NSIC-120, February 1976.

3. L. Baker, Jr. and L.C. Just, "Studies of Metal-Water Reactions at High Temperatures III-Experimental and Theoretical Studies of the Zirconium-Water Reaction," ANL-6548, December 1964.

4. L. Baker, Jr. and R.D. Ivins, "Analyzing the Effects of a Zirconium-Water Reaction," Nucleonics 23, pp. 70-74, July 1965.

5. J.M. Genco and G.E. Raines, "Metal Water Reactions During a Loss-of-Coulant-Accident--The Zirconium-Steam Reaction," ANS Transactions 9, pp. 555-556, October 1966.

6. M.J. Bell et al., "Post-LOCA Hydrogen Generation in PWR Containments," ANS Transactions 13, pp. 203-204, June 1970.

7. H.E. Zittel, "Radiolytic Hydrogen Generation After Loss-of-Coolant Accidents in Water Cooled Power Reactors," Nuclear Safety 13, pp. 459-467, November 1972.

8. W.D. Fletcher et al., "Post-LOCA Hydrogen Generation in PWR Containments," Nuclear Technology 10, pp. 420-427, April 1971.

9. J.R. Lopata, "Control of Containment H_2 Levels Evolved from Zinc Primers during a LOCA," Power Engineering 78, pp. 48-51, November 1974.

10. J.O. Henrie and A.K. Postma, "Analysis of the Three Mile Island (TMI-2) Hydrogen Burn," Proceedings of the Second International Meeting on Nuclear Thermal Hydraulics, pp. 1157-1170, January 1983.

11. G. Langer et al., "Experimental Investigation of Hydrogen Distribution in a Containment of a Light Water Reactor Following a Coolant Loss Accident," BF-63.363-3, Battelle Institute e.V. Frankfurt, translated October 1980.

12. "Experimental Investigation of the Hydrogen Distribution in a Model Containment (Preliminary Experiments Phase II)," BF-R-64.036-1, Federal Ministry for Research and Technology, Bonn, July 1980.

13. G.R. Bloom et al., "Hydrogen Distribution In a Containment With a High-Velocity Hydrogen-Steam Source," HEDL-SA-2682, October 1982.

14. G.R. Bloom and S.W. Claybrook, "Standard Problems On Hydrogen Mixing and Distribution," Westinghouse Hanford Company, March 1982.

15. R. Zinnari and C. Nahum, "Research Activities on the Hydrogen Behavior Inside BWR Containment after LOCA Developed Under the CNEM-AMN Agreement," Sandia Hydrogen Workshop, January 1981.

16. M.P. Sherman et al., "The Behavior of Hydrogen During Accidents in Light Water Reactors," NUREG/CR-1561, SAND 80-1495, 1980.

17. M. Hertzberg and K.L. Cashdollar, "Flammability Behavior and Pressure Development of Hydrogen Mixtures in Containment Volumes," Proceedings of the Second International Meeting on Nuclear Thermalhydraulics, pp. 29-37, January 1983.

18. J.C. Cummings et al., "Hydrogen Combustion Results From the Sandia Intermediate Scale (VGES) Tank and the Sandia Critical-Tube-Diameter Test Facility," Proceedings of the Second International Meeting on Nuclear Thermalhydraulics, pp. 1212-1218, January 1983.

19. R. Jaung et al., "Detonability of Containment Building Atmospheres During Core-Meltdown Accidents," Proceedings of the Second International Meeting on Nuclear Thermalhydraulics, pp. 1171-1177, January 1983.

20. R.K. Kumar et al., "Combustion of Hydrogen at High Concentrations Including the Effect of Obstacles," Proceedings of the Second International Meeting on Nuclear Thermalhydraulics, pp. 1203-1211, January 1983.

21. Code of Federal Regulations, Title 10, Part 50.

22. W.R. Butler et al., "Regulatory Perspective On Hydrogen Control For LWR Plants," Sandia Hydrogen Workshop, January 1981.

23. C.J. Boyd et al, "A Probabilistic Risk Assessment Perspective of the Impact of Hydrogen on PWR Safety," Sandia Hydrogen Workshop, January 1981.

25. L. Thompson, "Hydrogen Combustion and Control," EPRI Journal, pp. 56-58, May 1982.

26. R.D. Richtmeyer and K.W. Morton, Difference Methods for Initial Value Problems, Second Edition, Wiley, New York, 1967.

27. P.J. Roache, Computational Fluid Dynamics, Hermosa, Albuquerque, 1976.

28. C.W. Hirt, "Heuristic Stability Theory for Finite-Difference Equations," J. Comp. Physics, 2, 1968.

29. S.V. Patankar, Numerical Heat Transfer and Fluid Flow, Hemisphere, New York, 1980.

30. V.H. Ransom and J.A. Trapp, "Applied Mathematical Models in Nuclear Thermal Hydraulics," Proceedings of the Second International Meeting on Nuclear Thermal-hydraulics, pp. 99-110, January 1983.

31. E. Isaacson and H.B. Keller, Analysis of Numerical Methods, Wiley, New York, 1966.

32. F.H. Harlow and A.A. Amsden, "Multifluid Flow Calculations at All Mach Numbers," J. Comp. Physics 16, pp. 1-19, 1974.

33. W.C. Rivard and M.D. Torrey, "K-FIX: A Computer Program for Transient Two-Dimensional, Two-Fluid Flow," LA-NUREG-6623, April 1977.

34. M. Ishii, Thermo-Fluid Dynamic Theory of Two-Phase Flow, Collection de la Direction des Etudes et Recherches d'Electricite de France, 1975.

35. A.A. Amsden and F.H. Harlow, "The SMAC Method: A Numerical Technique for Calculating Incompressible Fluid Flows," LA-4370, May 1970.

36. J. Douglas and J.E. Gunn, "A General Formulation of Alternating Direction Methods," Num. Math 6, pp. 428-453, 1964.

37. W.R. Briley and H. McDonald, "Solution of the Multi-dimensional Compressible Navier Stokes Equations by a Generalized Implicit Method," J. Comp. Physics 24, 372-397, 1977.

38. W.R. Briley and H. McDonald, "On the Structure and Use of Linearized Block Implicit Schemes," J. Comp. Physics 34, pp. 54-73, 1980.

39. K.Y. Huh, Treatment of Physical and Numerical Diffusion in Fluid Dynamic Simulations, Ph.D. Thesis, Department of Nuclear Engineering, MIT, August, 1983.

40. K.V. Roberts and N.O. Weiss, "Convective Difference Schemes," Math of Comp. 20, No. 94, pp. 271-99, 1966.

41. J.E. Fromm, "Practical Investigation of Convective Difference Approximations of Reduced Dispersion," High Speed Computing in Fluid Dynamics, The Physics of Fluids, Supplement 2, ed. F.N. Frenkiel and K. Stewartson, 1969.

42. G.D. Raithby, "A Critical Evaluation of Upstream Differencing Applied to Problems Involving Fluid Flow," Comp. Methods in Appl. Mech. and Eng. 9, pp. 75-103, 1976.

43. G.D. Raithby, "Skew Upstream Differencing Scheme for Problems Involving Fluid Flow," Comp. Methods in Appl. Mech. and Eng. 9, pp. 153-164, 1976.

44. S.H. Chang, Comparative Analysis of Numerical Methods for the Solution of Navier-Stokes Equations, Ph.D. thesis, M.I.T. Department of Nuclear Engineering, May 1981.

45. J. Weisman and A. Tentner, "Application of the Method of Characteristics to Solution of Nuclear Engineering Problems," Nucl. Science and Eng. 78, pp. 1-29, 1981.

46. J.K. Dukowicz and J.D. Ramshaw, "Tensor Viscosity Method for Convection in Numerical Fluid Dynamics," J. Comp. Physics 32, pp. 71-79, 1979.

47. B.E. Launder and D.B. Spalding, Mathematical Models of Turbulence, Academic Press, London, 1972.

48. J.L. Lumley, "Second Order Modelling of Turbulent Flows," from Prediction Methods for Turbulent Flows, W. Kollman, ed., Hemisphere, New York, 1980.

49. W. Rodi, "Turbulence Models for Environmental Problems," from Prediction Methods for Turbulent Flows, W. Kollman, ed., Hemisphere, New York, 1980.

50. T.A. Porsching et al., "Stable Numerical Integration of Conservation Equations for Hydraulic Networks," Nucl. Science and Eng. 43, pp. 218-225, 1971.

51. D.W. Hargroves et al., CONTEMPT-LT/028--A Computer Program for Predicting Containment Pressure-Temperature Response to a Loss-of-Coolant Accident, NUREG/CR-0252, TREE-1279, August 1978.

52. L.J. Metcalfe et al., CONTEMPT4/MOD4--A Multicompartment Containment System Analysis Program, TREE-NUREG-1202, February 1978.

53. H.L. Jahn, "RALOC--A New Model for the Calculation of Local Hydrogen Concentrations in Subdivided Containments Under LOCA Aspects," Thermal Reactor Safety Topical Meeting, Idaho 1977.

54. H.L. Jahn, "Hydrogen Distribution in Subcomparted Containments: Analysis and Experiments," Water Reactor Safety International Meeting, 1980.

55. L.D. Buxton et al., "Transport of Gases in LWR Containments," presented November 1981 at Sandia National Laboratories.

56. L.D. Buxton, "Assessment of RALOC-Mod 1 With 1980 Updates," SAND 82-2005C, October 1982.

57. T. Fujimoto et al., "Development of Mixing Analysis Computer Code on Behavior of Hydrogen in Subcompartmented Containment Vessel After LOCA," Sandia Hydrogen Workshop, October 1982.

58. M. Fischer et al., "The Multi-Compartment-Code WAVCO, Developed to Analyze the Behavior of Non-Condensables During Hypothetical Accidents," Proceedings of the Second International Meeting on Nuclear Thermal-hydraulics, pp. 1058-1063, January 1983.

59. A.L. Camp et al., "HECTR: A Computer Program for Modelling the Response to Hydrogen Burns in Containments," SAND 82-1964C, 1982.

60. G.J.E. Willcutt, Jr. and R.G. Gido, "Mixing of Radiolytic Hydrogen Generated Within a Compartment Following a LOCA," NUREG/CR-0304, LA-7421-MS, August 1978.

61. G.J.E. Willcutt, Jr. et al., "Hydrogen Mixing in a Closed Containment Compartment Based on a One-Dimensional Model with Convective Effects," NUREG/CR-1575, LA-8429MS, September 1980.

62. C.R. Broadus et al., BEACON/Mod 3: A Computer Program for Thermal Hydraulic Analysis of Nuclear Reactor Containments--Users Manual, NUREG/CR-1148, April 1980.

63. D.S. Trent, "Computation of Hydrogen Distribution Using the Tempest Code," BNWL Report at EPRI H_2 Workshop, October 1981.

64. D.S. Trent and L.L. Eyler, "Application of the TEMPEST Computer Code for Simulating Hydrogen Distribution in Model Containment Structures," Sandia Hydrogen Workshop, October 1982.

65. J.R. Travis et al., "Modelling of H_2 Migration In LWR Containments," LA-UR-81-3171, October 1981.

66. J.R. Travis, "HMS: A Model for Hydrogen Migration Studies In LWR Containments," LA-UR-82-2702, October 1982.

67. M.J. Thurgood, "Application of COBRA-NC to Hydrogen Transport," Sandia Hydrogen Workshop, October 1982.

68. C.T. Crowe et al., "The Particle-Source-In Cell (PSI-Cell) Model for Gas Droplet Flows," Journal of Fluids Engineering, ASME Transactions 99, pp. 325-332, June, 1977.

69. F.H. Harlow and A.A. Amsden, "Numerical Calculation of Multiphase Fluid Flow," J. Comp. Physics 17, 1974.

70. Handbook of Tables for Applied Engineering Science, R.E. Bolz and G.L. Tuve, ed., Chemical Rubber Company, 1970.

71. M. Corradini, "Turbulent Condensation On A Cold Wall In The Presence Of A Noncondensible Gas," Proceedings of the Second International Meeting on Nuclear Thermal-hydraulics, pp. 1102-1110, January 1983.

72. B. Covelli et al., "Simulation of Containment Cooling With Outside Spray After a Core Meltdown," Nuclear Eng. and Design 69, pp. 127-137, 1982.

73. R.B. Bird et al., Transport Phenomena, Wiley, New York, 1960.

74. O. Hinze, Turbulence, Second Edition, McGraw-Hill, New York, 1980.

75. C.R. Wilke, "Diffusional Properties of Multicomponent Gases," Chemical Eng. Progress 46(2), pp. 95-106, February 1950.

76. G.D. Stubley et al., "Simulation of Convection and Diffusion Processes by Standard Finite Difference Schemes and by Influence Schemes," Comp. Math. Appl. Mech. and Engr. 35, pp. 153-168, 1982.

77. R.G. Gido et al., "COMPARE and BEACON vs. Battelle-Frankfurt Tests," LA-MS-9461, 1982.

APPENDIX A

COMPUTER APPLICATION TOPICS

A.1 General Principles

The development of analytical models is only part of the process of creating useful computational tools. The correct and efficient implementation of these models in computer programs is as important. The purpose of this appendix is to review the methods utilized in this work in order to document the process and also provide guidance to future workers. This discussion is not meant to present a compendium of detailed coding changes. Acquisition, installation and modification involve substantial time and effort especially if the work involves the use of software not directly compatible with the available computer systems. Some insight into this process is provided in the next section.

The inclusion of the model changes derived in the main body of this work necessitated extensive modification of the code. A review of the modifications from a programming standpoint is presented in A.3. A unique feature of executing larger programs on CDC equipment is the concept of segmented loading. Basically, this feature allows efficient computer core memory utilization through the active storage of only those software modules

which are required for execution at a particular time. The specific loading logic for the revised program is specified in A.4. After a code is developed, most of its use is in a production execution mode. Therefore various production mode options are addressed in section A.5.

Finally, future work may require the application of the code on a non-CDC system. The overall experience accrued in this work leads to a cautionary note that such a change involves a significant amount of time, effort and detailed knowledge of both CDC and the new host system both from a hardware and software viewpoint. Nevertheless the final section of this appendix points out some of the more important areas in this regard.

A.2 Acquisition, Installation and Modification

The BEACON code was chosen as the foundation for this work for the technical reasons presented in the main body of this work. Another positive aspect is that it was available at relatively little expense on a timely basis from the National Energy Software Center (NESC). From a computer applications standpoint, the code's most negative feature is its incompatibility with non-Control Date Corporation

(CDC) systems. The code was developed at the Idaho National Engineering Laboratory (INEL) using a CDC-7600 computer with software specification compatible with either SCOPE 2.1 or NOS/BE operating systems. Specifically, the code takes advantage of the overlay segmented loading particular to CDC, utilizes the CDC UPDATE utility in its source file management, and employs variable large and small core memory (LCM and SCM) allocation. Finally many input/output (I/O) and data management tasks are accomplished using the CDC-version of the INEL Environmental Subroutine Library.

MIT has no formal access to CDC machines and hence alternative computational plans are necessary. The two major options are to transform the code to an IBM (MIT)-compatible version or use CDC machines on a commercial basis. The former option is very costly in terms of time, effort and money and the latter alternative is pursued in this work. The available commercial CDC equipment is a CYBER-176 machine with a NOS operating system. A review of tne CDC commercial charge schedule reveals that while most costs are comparable, disk storage space is much more expensive for the CDC system. Therefore after the code was received at MIT, many changes were made using IBM systems. Of course the code could only be

modified but not tested. Subsequent compilation, debugging, modification and execution is done on the CDC system. Figure A.1 provides an overview of this process.

The direct installation of the code onto the CYBER-176 is also not a straightforward procedure. The NOS system is not completely equivalent to the SCOPE 2.1 or NOS/BE systems. Hence a substantial amount of machine-specific software study and modification is required. As part of this effort the job control language, program compilation, program loading and execution software is revised. One major set of changes relate to the environmental library. Many of these routines are not called by BEACON and some are written in a non-compatible form. Therefore, this library is edited such that only those routines called by the code are saved. It is also necessary to delete certain output data plotting options. The environmental library routines compiled and used by the code are listed in Table A.1. Finally, all use of quotation marks (") must be eliminated from routine CVI since it is not compatible with NOS-based COMPASS (CDC assembly language).

The FTN/176 Extended Fortran 4 compiler is needed to compile and execute the program. Other compilers such as FTN are not applicable. Further the compiler

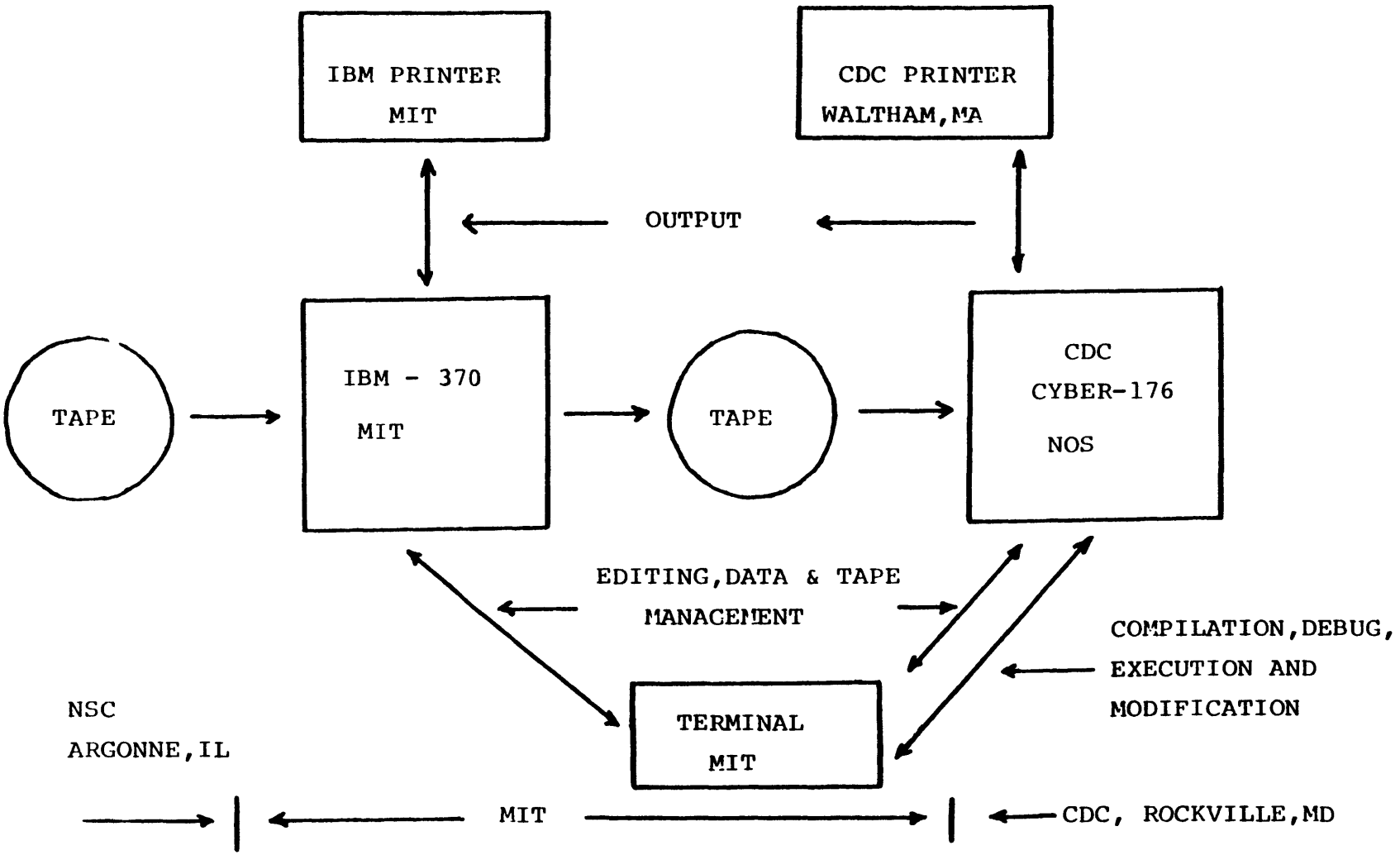

FIGURE A.1: BASIC COMPUTER APPLICATION MODES OF OPERATION

Table A.1

Environmental Library Routines Retained

For Use With Modified Code

CVI*	IDFIND	SHIFT
CVIERC	INITIAL	ZEROUT
DELETE	INP	FTBMXJ
DMPLST	INPPCK	CPL
DSCRIB	INPUPK	CPV
ERROR	INP2	DROLHP
FABEND	INP5	DROLPH
FTBEXP	INP6	HEADERX
FTBFTB	INP8	LCNTGS
FTBMEM	LINK	LCONTG
FTBOUT	LOCATE	REMTM
FTBMV2	MODE	THCV
FTBRDC	MOVE	TL
FTBRSV	SHFTLK	VISCL

*COMPASS programming modified

must operate in a STATIC mode. Finally the user must explicitly expand LCM and SCM prior to loading the object code since the default memory specifications of the FTN/176 compiler are not sufficient to properly store the code and its data.

Utilization of the CDC UPDATE utility and subroutine library object code storage may seem more cumbersome than direct source file editing and compilation but their use allows more economical code development and testing. In order for the procedures to be used, the program must be stored in the following form. First a file containing the entire code in an UPDATE Program Library format is required. Second, a compiled object code file of a subroutine library is needed. Third, a compiled object code version of the main program, BEACON, is needed as well as the environmental subroutines. The detailed mechanics of performing changes are addressed in the LIMIT user's manual [A-1].

A.3 Brief Review of Modifications

Both the original and modified codes are very large Fortran programs consisting of hundreds of subroutnes and tens of common blocks. Any subroutine-specific accounting of all modifications is not appropriate here. Table A.2 summarizes the modification effort. The majority of the modified

Table A.2

Modification Summary

	Original Code	Changed	Deleted	Added	New Total
Common Blocks	25	15	0	5	30
Routines	213	66	14	31	230

routines and common blocks are altered to either accommodate hydrogen as a constituent or handle new calculations arising from the optional 3-D or lumped parameter models. All the 14 deleted subroutines involve plotting options that are not executable on a CYBER-176 system. Actually these lines are merely "commented-out" and can easily be retrieved by future workers if it is so desired. A list of the deleted routines is provided in Table A.3. The logic structure of the slower mixing computation is shown schematically in Figure A.2. The modular "top down" structure allows for easy understanding and modification.

A.4 Segmented Loading

Due to the size of the code it is loaded into the core of the CDC machine in a segmented manner in order to efficiently utilize storage. The segmented loading utility allows only those parts of a software package which are required by each other for proper execution to reside in core concurrently. The segmented loading directions in this work is shown in Figure A.3. The changes noted describe the differences between this loading directive and that of the original code (Figure 70 of BEACON manual). Also shown is the "load tree" which results when these directives are utilized. The tree diagram indicates that the main program is always in core (the trunk of the "tree") but the four main branches (BCNINP, PRINT, KFIXT, and HTCNTL) never reside in

Table A.3

Plotting Subroutines Deleted From the Modified Code Execution Procedures

ADV	MOVPAR
CPLOTS	OCPLT
DRV	PLT
FIXLBL	PLOTS
FLMPLT	POBPLT
PLMPLTB	PPLOTS
FRAME	VPLOTS

FIGURE A.2: SLOW MIXING SUBCODE CODING STRUCTURE

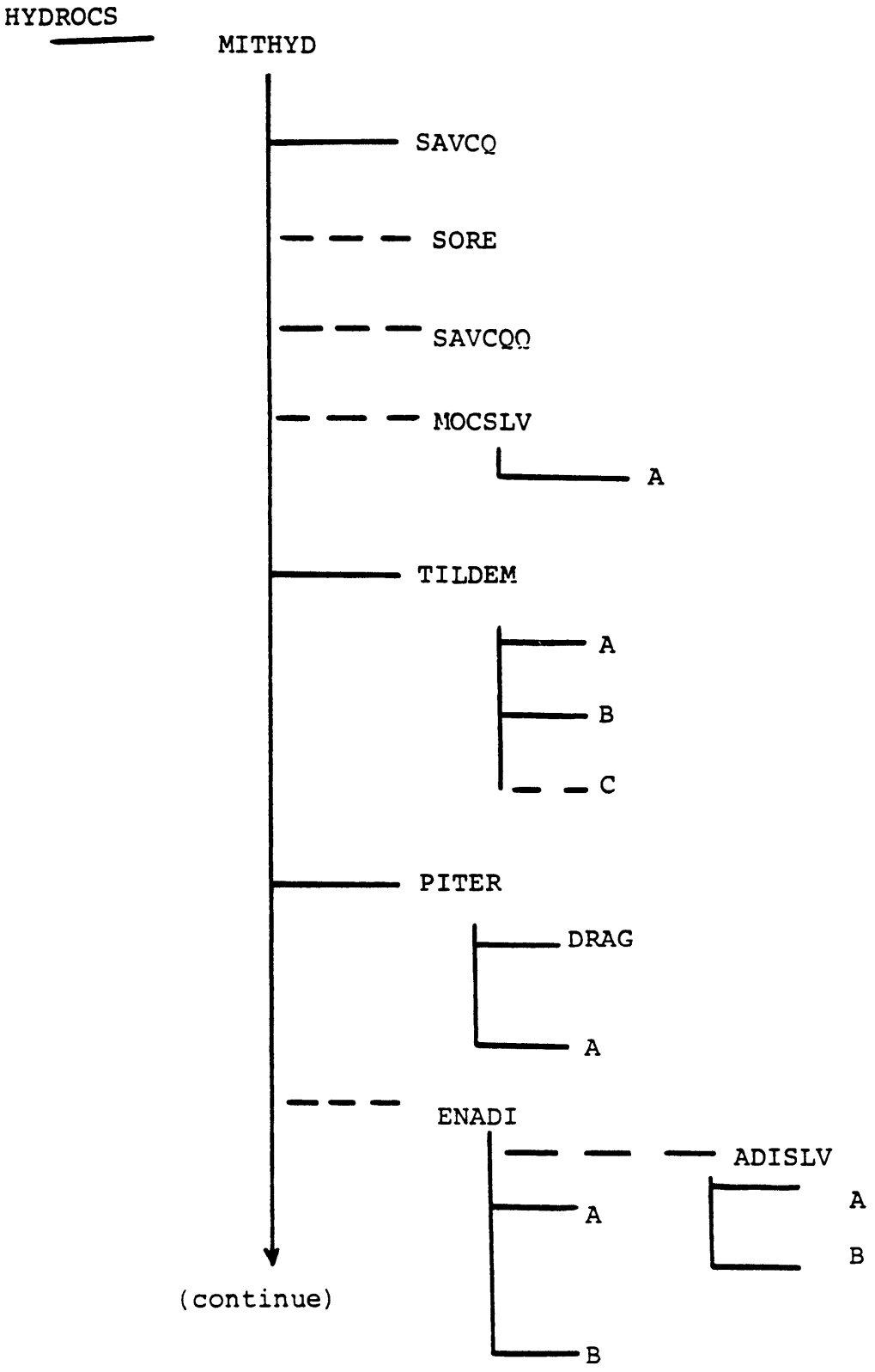

FIGURE A.2 (continued)

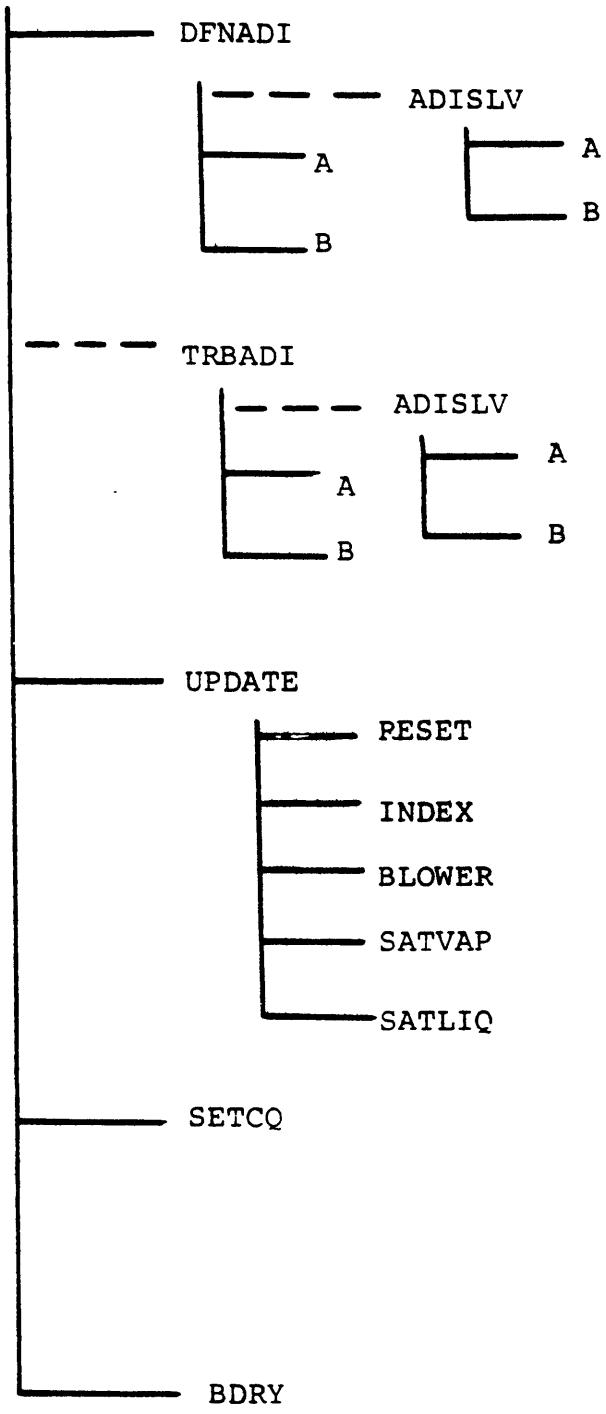

FIGURE A.2 (continued)

——— DIRECT CALL

----- CONDITIONAL TRANSFER

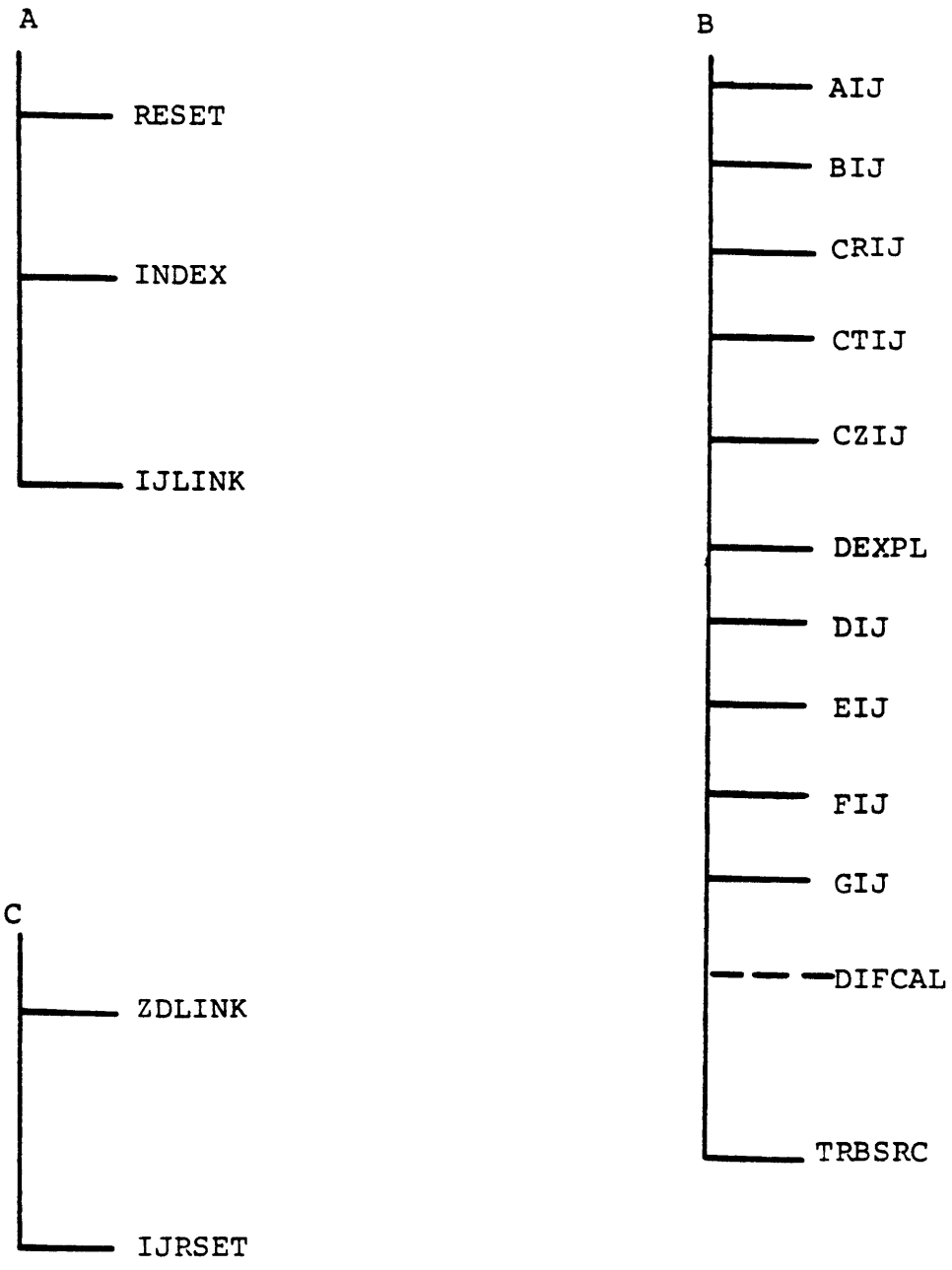

```
*                BEACON HYDROGEN - MIT SEGLOAD DIRECTIVES                    CHANGE
BCNPGM   TREE     BEACON-(BCNINP-(KCHINP-(INP,MESINP,LNKINP),HTINP),PRINT,      1
,KFIXT,HTCNTL)
BEACON  INCLUDE   HYDROCS,IJLINK,RESET,INITAL FLMTHK,STANTN,IPHMT               2
INP     INCLUDE   PGMINP,SOLINP,SETC,KASET1
MESINP  INCLUDE   CELINP,OCINP,BDYINP,VELINP,RFINP,FLMINP,ZDINP
LNKINP  INCLUDE   SCINP,CELCHK,CELMAP,IJMAP,OPINP,FLINP
HTINP   INCLUDE   HTCOM,HT1INP
PRINT   INCLUDE   PRINT,ZDPRNT,FBPRNT,FLMDBP,HTOUT                            1
KFIXT   INCLUDE   TILDE,BETAS,ITER,ICONV,ZEROD,SORE,ZDSORE,FLMDRV,FLMSAV,     3
,WALTRN,FLMSURF,MITHYD                                                        4
HTCNTL  INCLUDE   HTBCDN,HT1SST,HT1TDP
        GLOBAL    STP.END,FCL.C,Q8.IO.
        GLOBAL    KSC,PLTCOM,PPCOM,MMCOM,ZDCOM,MANDE,SCCOM,CNTLCOM
        GLOBAL    GLOBAL,IJCOM,TABCOM,EOSCOM,SCALAR,INPCOM
        GLOBAL    TRBCOM,MOMCOM,DFNCOM                                        5
        GLOBAL    HTNCOM,BLOCOM                                               5
        GLOBAL    FTB,FLMCOM,PHCOM,FLCOM,FAST
        LEVEL
        TREE      DUMMY
DUMMY   GLOBAL    DUMCOM
        END       BEACON
```

TREE DIAGRAM

```
*BEACON
 ?
 ?_BCNINP
 ??
 ??_KCHINP
 ???
 ???_INP
 ???
 ???_MESINP
 ???
 ???_LNKINP
 ??
 ??_HTINP
 ?
 ?_PRINT
 ?
 ?_KFIXT
```

(continued)

```
 ?
 ?_HTCNTL
```

EXPLANATION OF CHANGES

1 - deletion of plotting routines
2 - deletion of PACKZZ (EL)
3 - deletion of PLMDBP (plotting)
4 - inclusion of MITHYD in KFIXT branch
5 - new global common blocks

FIGURE A.3: SEGMENTATION LOADING DIRECTIVES AND RESULTING LOAD TREE

core concurrently. Further information is available in CDC documentation of the LOADER utility (particularly LDSET and LOAD commands).

A.5 Production Mode Execution

The successful execution of the code in a production (i.e. no modifications) mode requires at least three pieces of software. The first is compiled object code of the main program, subroutines and environmental library. These may reside in one to three files. Splitting them into three has an advantage if modifications are required (see below). The second item is the segmentation loading directive file (see A.4). Finally, input data defining the desired simulation must be specified.

The utilization of three separate files for storage of the main program, subroutines and environmental library, respectively, allows the user to employ the procedures described in section 3 of the code's users manual to accomplish code changes. Briefly this storage mode coupled with storage of the code in an UPDATE program library format allows piecewise code modification and recompilation thereby minimizing costs.

A.6 Application on a Non-CDC System

The conversion of the program to a form compatible with a non-CDC system is a formidable task. This is especially true if the new host system is IBM. The problems can be grouped into two major categories. First and foremost are system software and hardware differences. The system level problem areas are segmented loading, dynamic memory allocation and the environmental subroutine library. The latter two are closely related. Second, the Fortran coding itself requires straightforward but extremely tedious editing given the code's size (≈40000 lines). The switch to non-segmented loading basically requires a much larger core allocation. This is also true of non-dynamic memory allocation. The memory allocation problems are complicated by the extensive use of environmental library routines to read, manipulate, reconfigure and retrieve data.

In general, CDC Fortran is more flexible than IBM Fortran. Some specific differences are now enunciated.

1. All equivalenced arrays must be explicitly dimensioned.
2. Maximum number of characters defining a variable must be reduced from 7 to 6. This is a major problem.

3. Data storage overlaying such as the "Level 2" specification of all CELCOM variables is not allowed and host-system specific overlaying must be formulated.
4. Plotting routines are not transferable. This is also true of the IGS post-processing plot package.
5. Multiple equal signs are unacceptable.
6. Hollerith variable size is limited to 4 characters on IBM while CDC allows larger specification. This disturbs not only naming but also logic functions.

[A-1] V.P. Manno and M.W. Golay, Users Manual for the LIMIT Code - Hydrogen Analysis in Reactor Containments, MIT Energy Laboratory, MIT-EL-83-010, September, 1983.

Appendix B: Input Decks For Reported Simulations

The input data decks reported in this appendix correspond to a number of simulations reported in Chapter 4. Some problems were run with earlier versions of the code and as such slight differences in format may exist. If one wishes to use these specifications, the user should consult the users manual to verify the validity of each entry. The files included are listed below.

DATA DECK	DESCRIPTION (REFERENCE)
DATA1	air/water blowdown (4.2.1)
DATA2	H_2 /water blowdown (4.2.2)
DATA3	BF2 using BEACON (4.2.3)
DATEST	switching test (4.2.4)
DATA3A	basic BF2 model (4.3.1)
DATBF6	32 node BF6 model (4.3.1)
DNBF6	49 node BF6 model (4.3.1)
HEDLB	80 node HEDL B model (4.3.2)
ROOM6	6 room lumped problem (4.4)

```
 83/04/14. 11.25.21.
PROGRAM   DATA1

**     INPUT FILE FOR SAMPLE PROBLEM 1
00100   ' SAMPLE PROBLEM 1- PROBLEM 2 FROM BEACON/MOD 3 MANUAL'
**     BASIC PROBLEM INPUT
00110   0.0 0.2 0.001 SEC 10.0 20 XEQ USERDEF
00120   0.001 0.1 0.0025 2.0
00130   AUTODT 1 0.1 1.5 1.0E10
00140   PRINT NOPRINT PRINT NOPRINT NOPRINT
**      00150 CHANGED TO DELETE PLOTTING REQUEST
00150   NOPLOTS
00220   1 1.0E4 0.0 0.0 0.0
00230   0 0.0 0.0 1.0E4
00240   LASL PT LBF/IN2 DEGR FT SEC-1
**     EULERIAN REGION INPUT
11005    'TOPDOWN VIEW OF ROOM COMPARTMENTS'
11000   CARTSN 11 14 1.0 1.0 10.0 FT 0.0 0.0
11010   NOSLIP NOSLIP NOSLIP NOSLIP
**     XHYD=0.0 IS ADDED AS 12TH ENTRY OF CARDS M1101-M1199
11101   MIXTURE 2 2 8 5 0 14.7 600.0 600.0 0.9 1.0 0.0
11102   MIXTURE 2 6 4 9 0 14.7 600.0 600.0 0.9 1.0 0.0
11103   MIXTURE 2 10 6 15 0 14.7 600.0 600.0 0.9 1.0 0.0
11104   MIXTURE 7 10 8 12 0 14.7 600.0 600.0 0.9 1.0 0.0
11105   MIXTURE 9 10 12 15 0 14.7 600.0 600.0 0.9 1.0 0.0
**     OBSTACLE CELL INPUT
11401   NOSLIP 9 2 12 5
11402   NOSLIP 5 6 12 9
11403   NOSLIP 7 13 8 15
**     SPECIFIED BOUNDARY INPUT
11501   INFLOW 2 1 8 1
**     XHYD=0.0 IS ADDED AS 7TH ENTRY OF CARDS M1601-M1699
11601   MIXTURE 14.7 600.0 600.0 0.5 1.0 0.0
11701   0.0 10.0 0.0 10.0
11502   OUTFLOW 13 10 13 15
.
READY.
```

DATA1A: AIR-WATER BLOWDOWN

```
 83/02/10. 13.58.23.
PROGRAM   DATA2

**     INPUT FILE FOR SAMPLE PROBLEM 2
00100   ' SAMPLE PROBLEM 2- MODIFIED BEACON SP2 WITH H2 INFLOW'
**     BASIC PROBLEM INPUT
00110   0.0 0.2 0.001 SEC 10.0 20 XEQ USERDEF
00120   0.001 0.1 0.0025 2.0
00130   AUTODT 1 0.1 1.5 1.0E10
00140   PRINT NOPRINT PRINT NOPRINT NOPRINT
**      00150 CHANGED TO DELETE PLOTTING REQUEST
00150   NOPLOTS
00220   1 1.0E4 0.0 0.0 0.0
00230   0 0.0 0.0 1.0E4
00240   LASL PT LBF/IN2 DEGR FT SEC-1
**     EULERIAN REGION INPUT
11005    'TOPDOWN VIEW OF ROOM COMPARTMENTS'
11000   CARTSN 11 14 1.0 1.0 10.0 FT 0.0 0.0
11010   NOSLIP NOSLIP NOSLIP NOSLIP
**     XHYD=0.0 IS ADDED AS 12TH ENTRY OF CARDS M1101-M1199
11101   MIXTURE 2 2 8 5 0 14.7 600.0 600.0 0.9 1.0 0.0
11102   MIXTURE 2 6 4 9 0 14.7 600.0 600.0 0.9 1.0 0.0
11103   MIXTURE 2 10 6 15 0 14.7 600.0 600.0 0.9 1.0 0.0
11104   MIXTURE 7 10 8 12 0 14.7 600.0 600.0 0.9 1.0 0.0
11105   MIXTURE 9 10 12 15 0 14.7 600.0 600.0 0.9 1.0 0.0
**     OBSTACLE CELL INPUT
11401   NOSLIP 9 2 12 5
11402   NOSLIP 5 6 12 9
11403   NOSLIP 7 13 8 15
**     SPECIFIED BOUNDARY INPUT
11501    INFLOW 2 1 8 1
**     XHYD=1.0 IS ADDED AS 7TH ENTRY OF CARDS M1601-M1699
**     NOTE INFLOW IS NOW ALL HYDROGEN
11601   MIXTURE 14.7 600.0 600.0 0.5 0.0 1.0
11701   0.0 10.0 0.0 10.0
11502   OUTFLOW 13 10 13 15
.
READY.
old,dabf12
READY.
```

DATA2: H_2/WATER BLOWDOWN

```
PROGRAM   DATA3

**     INPUT FOR SAMPLE PROBLEM 3
00100   ' BATTELLE TEST NO. 2- 16 NODE MODEL'
**     BASIC PROBLEM INPUT
00110   0.0 10000.0 0.1 SEC 10.0 1 XEQ USERDEF
00120   0.1 1.0 1.0 5.0 5.0 100.0 100.0 10000.0
00130   AUTODT 0 0.9 2.0 20.0
00140   PRINT NOPRINT NOPRINT NOPRINT NOPRINT PRINT
00190   2 0
00200   1.0 0.0001 0.0001 100 5 0
00220   1 1.0E-50 0.0 0.0 0.0
00230   0 0.0 0.0 1.0E-50
00240   LASL PT LBF/IN2 DEGC M SEC-1
**     EULERIAN REGION DATA
11005   ' MESH 1 - UPPER PORTION OF VESSEL '
11000   AXISYM 4 2 1.0 1.0 0.0 M 0.0 1.0
11010   SLIP NOSLIP NOSLIP NOSLIP
11020   0.25 0.315 0.685 1.2
11030   0.8 1.0
11050   NOFILM
11101   MIXTURE 2 2 5 3 0 14.7 17.0 17.0 0.99 1.00 0.0
21005   ' MESH 2 - LOWER PORTION OF VESSEL '
21000   AXISYM 4 2 1.0 1.0 0.0 M 0.0 1.0
21010   SLIP NOSLIP NOSLIP NOSLIP
21020   0.25 0.315 0.685 0.75
21030   1.0 2.02
21050   NOFILM
21101   MIXTURE 2 2 5 3 0 14.7 17.0 17.0 0.99 1.00 0.0
**     SOURCE ADDITION - SIX SOURCES,ONE AIR AND ONE HYDROGEN
**     ADDED TO EACH OF 3 LOWER LEFT CELLS OF MESH 2
**    SOURCE MODELLING CHANGED
**     NOW SPECIFIED INFLOW
21501   INFLOW 2 1 4 1
21601   MIXTURE 14.7 19.0 19.0 1.0 0.882 0.118
21701   0.0 6.734E-05 0.0 6.734E-05
**     COUPLING BETWEEN TWO MESHES - REPRESENTS OROFICE
006001 BOTTOM 1 2 2 2 2 2 3 2
.
READY.
```

DATA3: BF2 USING BEACON

```
list

 83/04/14. 11.42.29.
PROGRAM   DATEST

** TEST DATA FOR SWITCHING CHECK
00100   ' SWITCHING TEST CASE '
00110   0.0 10.0 0.5 SEC 10.0 1 XEQ USERDEF 0 1.0E+10
00120   0.5 2.0 1.0 10.0
00130   CONST 20 0.5 1.25 10.0
00140   PRINT NOPRINT PRINT NOPRINT NOPRINT NOPRINT
00190   1 0 10.0
00200   1.0 0.00010 0.00010 100 20 0
00220   1 1.0E+04 0.0 0.0 0.0
00230   0 0.0 0.0 1.0E+04
00240   LASL PT LBF/IN2 DEGC M SEC-1
00400   0 1.0 1.8 1.0E-20 1.0E-20 1.0E-20 1.0E-20
00410   0.000 1.44 1.92 1.44 200.0 1.0 1.3
00420   0 0.0 0.0 0.0 0.0
11005   ' TEST MESH '
11000   CARTSN 2 3 1.0 1.0 1.0 M 0.0 1.0 0 1.221206
11010   SLIP SLIP SLIP SLIP
11050   NOFILM
11101   AIR 2 2 3 4 0 14.7 16.0
3010  HYD 1 2 2 003011 0.0 DEGREES 1.0 1.0 1.0 0.0
3011  SEC KG/SEC J/KG M SEC-1
3012  0.0 1.0E-04 4.124E+06 0.0
3013  10.0 1.0E-04 4.124E+06 0.0
.
READY.
```

DATEST:SWITCHING TEST

```
83/04/14. 11.33.07.
PROGRAM   DATA3A

**     INPUT FOR SAMPLE PROBLEM 3A
00100   ' BF2 OPEN -  RELAX=1.8 TURB  - 32 NODES '
**     BASIC PROBLEM INPUT
00110   0.0 100.0 2.0 SEC 10.0 1 XEQ USERDEF 1 1.0E+06
00120   2.0 20.0 10.0 100.0 20.0 200.0 200.0 10000.0
00130   AUTODT 75 0.5 1.25 50.0
00140   PRINT NOPRINT PRINT NOPRINT NOPRINT PRINT
00190   2 0
00200   1.0 .000025 .000025 100 1000 0
00220   1 1.0E-50 0.0 0.0 0.0
00230   0 0.0 0.0 1.0E-50
00240   LASL PT LBF/IN2 DEGC M SEC-1
**       NEW INPUT CARDS
00400   0 1.0 1.80 1.0 1.0 1.0 1.0
00410   0.090 1.44 1.92 1.44 200.0 1.0 1.3
**     EULERIAN REGION DATA
11005   ' MESH 1 -  LOWER REGION '
11000   AXISYM 6 3 1.0 1.0 0.0 M 0.0 1.0 1 1.216997
11010   SLIP SLIP SLIP SLIP
11020   0.2825 0.2825 0.3092 0.3401 0.3741 0.4115
11030   1.0 1.0 1.0
11050   NOFILM
11101   AIR 2 2 7 4 0 14.7 17.0
11201   2 2 7 4 0. 0. 0. 0. 1.0E-04 1.0E-05
21005   ' MESH 2 - UPPER REGION '
21000   AXISYM 7 2 1.0 1.0 0.0 M 0.0 1.0 1 1.216997
21010   SLIP SLIP SLIP SLIP
21020   0.2825 0.2825 0.3092 0.3401 0.3741 0.4115 0.4501
21030   1.0 0.8138
21050   NOFILM
21101   AIR 2 2 8 3 0 14.7 17.0
21201   2 2 8 3 0. 0. 0. 0. 1.0E-04 1.0E-05
**     SOURCE ADDITION - SIX SOURCES,ONE AIR AND ONE HYDROGEN
**     ADDED TO EACH OF 3 LOWER LEFT CELLS OF MESH 1
3010   AIR 1 2 2 003011 0.0 DEGREES 0.0657 1.0 1.0 0.0
3060   AIR 1 3 2 003011 0.0 DEGREES 0.2701 1.0 1.0 0.0
3110   AIR 1 4 2 003011 0.0 DEGREES 0.6642 1.0 1.0 0.0
3011   SEC KG/SEC J/KG M SEC-1
3012   0.0 1.367E-04 2.934E+05 0.0
3013   10000.0 1.367E-04 2.934E+05 0.0
3160   HYD 1 2 2 003061 0.0 DEGREES 0.0657 1.0 1.0 0.0
3210   HYD 1 3 2 003061 0.0 DEGREES 0.2701 1.0 1.0 0.0
3260   HYD 1 4 2 003061 0.0 DEGREES 0.6642 1.0 1.0 0.0
3061   SEC KG/SEC J/KG M SEC-1
3062   0.0 1.828E-05 4.181E+06 0.0
3063   10000.0 1.828E-05 4.181E+06 0.0
**       COUPLING
006001   TOP 1 2 4 6 2 2 2 6
.
READY.
o
```

DATA3A: BASIC BF2 MODEL

```
PROGRAM   DATBFG

**     INPUT FOR SAMPLE PROBLEM  BF 6
00100   ' BF TEST  6.  - 32 NODES '
**     BASIC PROBLEM INPUT
00110    0.0 10.0 2.0 SEC 10.0 1 XEQ USERDEF 1 1.0E+06
00120   2.0 20.0 20.0 200.0 200.0 8000.0
00130   AUTODT 50 0.5 1.25 50.0
00140   PRINT NOPRINT PRINT NOPRINT NOPRINT PRINT
00145   62 0
00190   2 0
00200   1.0 .000100 .000100 100 4000 0
00220   1 1.0E-50 0.0 0.0 0.0
00230   0 0.0 0.0 1.0E-50
00240   LASL PT LBF/IN2 DEGC M SEC-1
**       NEW INPUT CARDS
00400   0 1.0 1.80 1.0 1.0 1.0 1.0
00410   0.000 1.44 1.92 1.44 0.9 1.0 1.3
00420   0 0.0 7.0E-05 7.0E-05 0.0
**     EULERIAN REGION DATA
11005   ' MESH 1 -  LOWER REGION '
11000   AXISYM 6 3 1.0 1.0 0.0 M 0.0 1.0 1 1.180391507
11010   SLIP SLIP SLIP SLIP
11020   0.2825 0.2825 0.3092 0.3401 0.3741 0.4115
11030   1.0 1.0 1.0
11050   NOFILM
11101   AIR 2 2 7 4 0 14.7 19.0
21005   ' MESH 2 - UPPER REGION '
21000   AXISYM 7 2 1.0 1.0 0.0 M 0.0 1.0 1 1.180391507
21010   SLIP SLIP SLIP SLIP
21020   0.2825 0.2825 0.3092 0.3401 0.3741 0.4115 0.4501
21030   1.0 0.8191
21050   NOFILM
21101   AIR 2 2 8 2 0 14.7 35.0
21102   AIR 2 3 8 3 0 14.7 33.339376
**     SOURCE ADDITION - SIX SOURCES,ONE AIR AND ONE HYDROGEN
**     ADDED TO EACH OF 3 LOWER LEFT CELLS OF MESH 1
3010   AIR 1 2 2 003011 0.0 DEGREES 0.10443 1.0 1.0 0.0
3060   AIR 1 3 2 003011 0.0 DEGREES 0.31328 1.0 1.0 0.0
3110   AIR 1 4 2 003011 0.0 DEGREES 0.58229 1.0 1.0 0.0
3011   SEC KG/SEC J/KG M SEC-1
3012   0.0 2.700E-04 2.09706E+05 0.0
3013   1075.0 2.700E-04 2.09706E+05 0.0
3014   1085.0 1.126E-04 2.09706E+05 0.0
3015   7560.0 1.126E-04 2.09706E+05 0.0
3016   7565.0 1.000E-30 2.09706E+05 0.0
3017   8000.0 1.000E-30 2.09706E+05 0.0
3160   HYD 1 2 2 003061 0.0 DEGREES 0.10443 1.0 1.0 0.0
3210   HYD 1 3 2 003061 0.0 DEGREES 0.31328 1.0 1.0 0.0
3260   HYD 1 4 2 003061 0.0 DEGREES 0.58229 1.0 1.0 0.0
3061   SEC KG/SEC J/KG M SEC-1
3062   0.0 3.610E-05 2.97632E+06 0.0
3063   1075.0 3.610E-05 2.97632E+06 0.0
3064   1085.0 1.505E-05 2.97632E+06 0.0
3065   7560.0 1.505E-05 2.97632E+06 0.0
3066   7565.0 1.000E-30 2.97632E+06 0.0
3067   8000.0 1.000E-30 2.97632E+06 0.0
**      COUPLING
006001  TOP 1 2 4 2 2 2 2 2
.
READY.
```

DNBF6: 32 NODE BF6 MODEL

```
 83/06/14. 11.02.27.
PROGRAM   DNBF6

**     INPUT FOR SAMPLE PROBLEM  BF 6
00100   ' BF TEST  6.  - 49 NODES - HEAT SINKS - RESTART '
**     BASIC PROBLEM INPUT
00105  NOREAD 0 NOWRITE 0 NOCOPY
00110   0.0 5000.0 1.0 SEC 10.0 1 XEG USERDEF 1 1.0E+06
00120  25.0 200.0 300.0 500.0 500.0 8000.0
00130  AUTODT 25 0.5 1.25 50.0
00140  PRINT NOPRINT PRINT NOPRINT NOPRINT PRINT
00145  62 0
00190  2 0
00200  1.0 .000100 .000100 100 100 0
00220  1 1.0E-50 0.0 0.0 0.0
00230  0 0.0 0.0 1.0E-50
00240  LASL PT LBF/IN2 DEGC M SEC-1
**      NEW INPUT CARDS
00400  -1 0.5 1.8 1.0E-20 1.0 1.0 1.0E-20
00410  0.090 1.44 1.92 1.44 0.9 1.0 1.3
00420  0  3.0E-05  7.0E-05  7.0E-5  0.0
**     EULERIAN REGION DATA
11005   ' MESH 1 -  LOWER REGION '
11000  AXISYM 5 5 1.0 1.0 0.0 M 0.0 1.0 1 1.204604 1 1.0
11010  SLIP SLIP SLIP SLIP SLIP SLIP
11020  0.2825 0.2825 0.3673 0.4774 0.5903
11030  0.5 1.0 0.9 0.4 0.2
11050  NOFILM
11101  AIR 2 2 6 4 0 14.7 18.0 18.0 1.0 1.0 0.0 2 2
11102  AIR 2 5 6 5 0 14.70000379 23.0 23.0 1.0 1.0 0.0 2 2
11103  AIR 2 6 6 6 0 14.70001158 26.0 26.0 1.0 1.0 0.0 2 2
11201  2 2 4 5 0.0 0.0 0.0 0.0 0.0025 0.0012 2 2 0.0
21005   ' MESH 2 - UPPER REGION '
21000  AXISYM 6 4 1.0 1.0 0.0 M 0.0 1.0 1 1.137284 1 1.0
21010  SLIP SLIP SLIP SLIP SLIP SLIP
21020  0.2825 0.2825 0.3673 0.4774 0.5903 0.45
21030  0.2 0.3 0.5 0.8138
21050  NOFILM
21101  AIR 2 2 7 3 0 14.70002338 35.0 35.0 1.0 1.0 0.0 2 2
21102  AIR 2 4 7 4 0 14.70002057 37.0 37.0 1.0 1.0 0.0 2 2
21103  AIR 2 5 7 5 0 14.70002282 39.0 39.0 1.0 1.0 0.0 2 2
21202  2 2 7 5 0.0 0.0 0.0 0.0 0.0 0.0 2 2 0.0
**     SOURCE ADDITION - SIX SOURCES,ONE AIR AND ONE HYDROGEN
**     ADDED TO EACH OF 3 LOWER LEFT CELLS OF MESH 1
3010   AIR 1 2 2 003011 0.0 DEGREES 0.09182 1.0 1.0 0.0 1 0.0
3060   AIR 1 3 2 003011 0.0 DEGREES 0.27545 1.0 1.0 0.0 1 0.0
3110   AIR 1 4 2 003011 0.0 DEGREES 0.63273 1.0 1.0 0.0 1 0.0
3011   SEC KG/SEC J/KG M SEC-1
3012   0.0 2.700E-04 2.09706E+05 0.0
3013   1075.0 2.700E-04 2.09706E+05 0.0
3014   1085.0 1.126E-04 2.09706E+05 0.0
3015   7560.0 1.126E-04 2.09706E+05 0.0
3016   7565.0 1.000E-30 2.09706E+05 0.0
3017   8000.0 1.000E-30 2.09706E+05 0.0
3160   HYD 1 2 2 003061 0.0 DEGREES 0.09182 1.0 1.0 0.0 1 0.0
3210   HYD 1 3 2 003061 0.0 DEGREES 0.27545 1.0 1.0 0.0 1 0.0
3260   HYD 1 4 2 003061 0.0 DEGREES 0.63273 1.0 1.0 0.0 1 0.0
3061   SEC KG/SEC J/KG M SEC-1
3062   0.0 3.610E-05 2.97632E+06 0.0
3063   1075.0 3.610E-05 2.97632E+06 0.0
3064   1085.0 1.505E-05 2.97632E+06 0.0
3065   7560.0 1.505E-05 2.97632E+06 0.0
3066   7565.0 1.000E-30 2.97632E+06 0.0
```

DNBF6 (continued)

```
**      COUPLING
006001  TOP 1 2 6 2 2 2 2 2
**     HEAT SINKS
1000001  M WATT DEGC
1000002  -1 SEC 10.0
1000000  WATT/M-DEGC J/M3-DEGC WATT/M2-DEGC
1000101  0.94 1.93E+06
1000201  2.5
1010000  ' CONCRETE IN LOWER REGION '
1010001  3 2 2.0 1.0 100 0.01 0.0
1010002  MULTI 1 6 2 6 6 DUMMY 0 0 0 0 0
1010003  M 3.0 RIGHT NONE
1010200  0 1
1010201  2 2.65
1010301  1 2
1010401  0.0 2
1010601  20.0 3
1010009  1 1 0 0
1020000  ' CONCRETE IN UPPER REGION '
1020001  3 2 2.45 1.0 100 0.01 0.0
1020002  MULTI 2 7 2 7 5 DUMMY 0 0 0 0 0
1020003  M 1.8138 RIGHT NONE
1020200  0 1
1020201  2 2.65
1020301  1 2
1020401  0.0 2
1020601  37.3 3
1020009  1 1 0 0
.
READY.
```

```
PROGRAM   HEDLB

00100  ' HEDL B SIMULATION 100 NODE 3D MODEL '
**  RESTART SPECS
00105  NOREAD 0 WRITE 2 NOCOPY
**  BASIC INPUT DATA
00110  0.0 700.0 0.1 SEC 10. 1 XEG USERDEF 3 1.0E+10
00120   50.0 100.0 100.0 900.0
00130  AUTODT 10 0.5 1.25 10.0
00140  PRINT NOPRINT PRINT NOPRINT NOPRINT PRINT
00150  1 0 10.0
00200  1.0 0.00010 0.00010 100 50 0
**  DUMMY INTERPHASIC PARAMETERS
00220  1 0.0 0.0 0.0 0.0
00230  0 0.0 0.0 0.0
00240  LASL PT LBF/IN2 DEGC M SEC-1
**  NEW INPUT CARDS
00400  0 1.0 1.8 1.0 1.0 1.0 1.0E-20
00410  0.090 1.44 1.92 1.44 0.9 1.0 1.3
00420 0 3.3E-05 6.0E-04 3.3E-05 0.0
**  BLOWER MODEL
00500  4
00510  5 6 2 7
00511  0.0  1.1303  0.0  308.0  0.43333
00512  90.0  1.1052  0.0  315.0  0.43333
00513  270.0  1.1017  0.00078  316.0  0.43333
00514  330.0  1.0896  0.00104  319.5  0.43333
00515  630.0  1.0712  0.00234  325.0  0.43333
00516  690.0  1.0695  0.00260  325.5  0.43333
00517  870.0  1.0795  0.00270  322.5  0.43333
00520  5 6 3 7
00521  0.0  1.1303  0.0  306.0  0.43333
00522  90.0  1.1052  0.0  315.0  0.43333
00523  270.0  1.1017  0.00078  316.0  0.43333
00524  330.0  1.0896  0.00104  319.5  0.43333
00525  630.0  1.0712  0.00234  325.0  0.43333
00526  690.0  1.0695  0.00260  325.5  0.43333
00527  870.0  1.0795  0.00270  322.5  0.43333
00530  5 6 4 7
00531  0.0  1.1303  0.0  308.00  0.43333
00532  90.0  1.1052  0.0  315.0  0.43333
00533  270.0  1.1017  0.00078  316.0  0.43333
00534  330.0  1.0896  0.00104  319.5  0.433333
00535  630.0  1.0712  0.00234  325.0  0.43333
00536  690.0  1.0695  0.00260  325.5  0.43333
00537  870.0  1.0795  0.00270  322.5  0.43333
00540  5 6 5 7
00541  0.0  1.1303  0.0  306.0  0.43333
00542  90.0  1.1052  0.0  315.0  0.43333
00543  270.0  1.1017  0.00078  316.0  0.43333
00544  330.0  1.0896  0.00104  319.5  0.43333
00545  630.0  1.0712  0.00234  325.0  0.43333
00546  690.0  1.0695  0.00260  325.5  0.43333
00547  870.0  1.0795  0.00270  322.5  0.43333
**   CONTINUUM REGION INPUT
11005  ' HEDL B FACILITY - 80 NODES'
11000  AXISYM 4 5 1.0 1.0 1.52 M 0.0 1.0 1 1.04425 4 1.0
11010  SLIP SLIP SLIP SLIP SLIP SLIP
11020  0.5725 0.5725 0.5725 0.5725
11030  0.944  0.944  0.944  0.944  0.944
11040  0.20833  0.20833  0.20833  0.20833
11050  NOFILM
11101  AIR 2 2 5 6 0 14.7 65.0 65.0 1.0 1.0 0.0 2 5
11201  2 2 5 6 0.0 0.0 0.0 0.0 1.0E-04 1.0E-06 2 5 0.0
```

HEDLB: 80 NODE HEDLB MODEL

```
**  HYDROGEN - STEAM JET
03010  STEAM 1 3 3 03011 0.0 DEGREES 1.0 1.0 1.0 0.0 4 0.0
03011  SEC KG/SEC J/KG M SEC-1
03012    0.  0.24167  2.6678E+06  80.
03013   630.  0.24167  2.7033E+06  80.
03014   690.  0.0 2.70332E+06 0.0
03015  900.  0.0  0.0  0.0
03060  HYD 1 3 3 03061 0.0 DEGREES 1.0 1.0 1.0 0.0 4 0.0
03061  SEC KG/SEC J/KG M SEC-1
03062    0.  0.000000  5.3528E+06  0.0
03063   45.  0.0 5.3528E+06  0.0
03064   90.  0.003375  5.339E+06  80.
03065  585.  0.003375  5.553E+06  80.
03066  630.  0.00783  5.553E+06  80.0
03067 690.  0.000000  5.553E+06 0.0
03068  900.0  0.0 5.553E+06 0.0
**   HEAT SINK DATA
1000000  BTU/HR-FT-DEGF  BTU/FT3-DEGF  BTU/HR-FT2-DEGF
1000001  M  WATT  DEGK
1000002  -1  SEC  5.0
1000101  30.0  55.0
1010000  ' STEEL TANK '
1010001  3 2 3.81 0.0 100 0.01 0.0
1010002  MULTI 1 5 2 5 6 DUMMY 0 0 0 0 0
1010003  M  4.72  RIGHT NONE
1010200  0  1
1010201  2  3.83
1010301  1  2
1010401  0.0  2
1010601  338.15  3
1010009   22 22 0 0
.
READY.

READY.
```

HEDLB (continued)

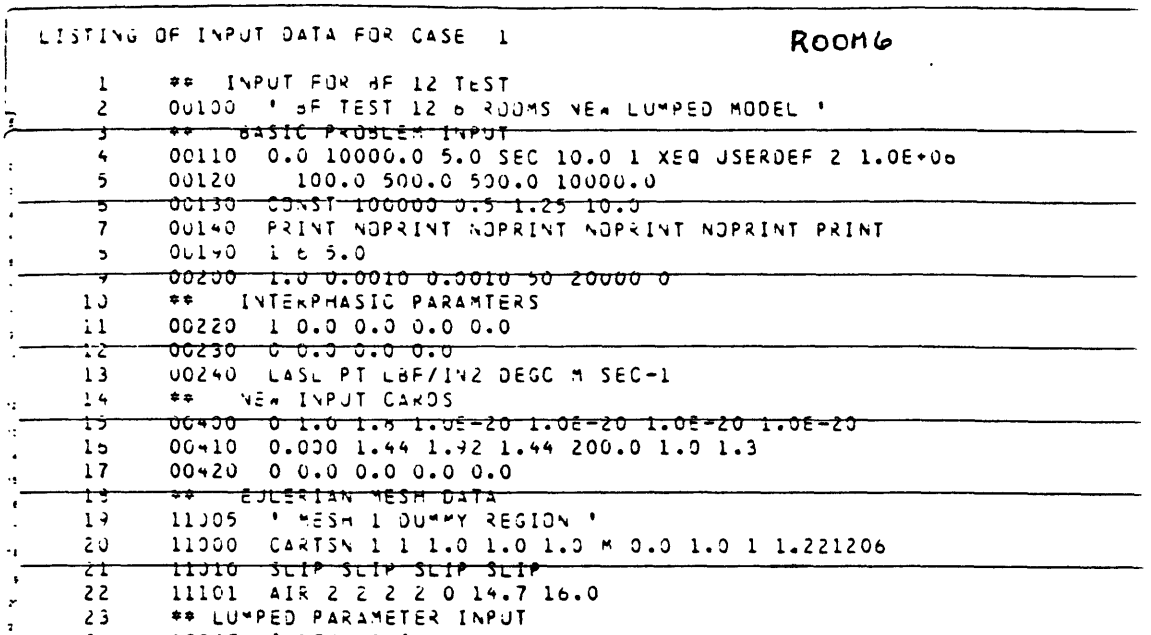

```
LISTING OF INPUT DATA FOR CASE  1                                ROOM6

    1    **  INPUT FOR BF 12 TEST
    2    00100  ' BF TEST 12 6 ROOMS NEW LUMPED MODEL '
    3    **   BASIC PROBLEM INPUT
    4    00110  0.0 10000.0 5.0 SEC 10.0 1 XEQ USERDEF 2 1.0E+06
    5    00120    100.0 500.0 500.0 10000.0
    6    00130  CONST 100000 0.5 1.25 10.0
    7    00140  PRINT NOPRINT NOPRINT NOPRINT NOPRINT PRINT
    8    00150  1 6 5.0
    9    00200  1.0 0.0010 0.0010 50 20000 0
   10    **   INTERPHASIC PARAMTERS
   11    00220  1 0.0 0.0 0.0 0.0
   12    00230  0 0.0 0.0 0.0
   13    00240  LASL PT LBF/IN2 DEGC M SEC-1
   14    **   NEW INPUT CARDS
   15    00400  0 1.0 1.5 1.0E-20 1.0E-20 1.0E-20 1.0E-20
   16    00410  0.000 1.44 1.92 1.44 200.0 1.0 1.3
   17    00420  0 0.0 0.0 0.0 0.0
   18    **   EULERIAN MESH DATA
   19    11005  ' MESH 1 DUMMY REGION '
   20    11000  CARTSN 1 1 1.0 1.0 1.0 M 0.0 1.0 1 1.221206
   21    11010  SLIP SLIP SLIP SLIP
   22    11101  AIR 2 2 2 2 0 14.7 16.0
   23    ** LUMPED PARAMETER INPUT
   24    12005  ' ROOM 1 '
   25    12000  ZEROD 40.5 M3 0.0 0.0 0.0
   26    12010  AIR 14.7 16.0
   27    22005  ' ROOM 2 '
   28    22000  ZEROD 30.2 M3 0.0 0.0 0.0
   29    22010  AIR 14.7 16.0
   30    32005  ' ROOM 5 '
   31    32000  ZEROD 41.1 M3 0.0 0.0 0.0
   32    32010  AIR 14.7 16.0
   33    42005  ' ROOM 6 '
   34    42000  ZEROD 38.9 M3 0.0 0.0 0.0
   35    42010  AIR 14.7 16.0
   36    52005  ' ROOM 7 '
   37    52000  ZEROD 40.4 M3 0.0 0.0 0.0
   38    52010  AIR 14.7 16.0
   39    62005  ' ROOM 8 '
   40    62000  ZEROD 38.3 M3 0.0 0.0 0.0
   41    62010  AIR 14.7 16.0
   42    **  SOURCE ADDITION TO ROOM 1
   43    3010  AIR 1 0 0 003011 0.0 DEGREES 1.0 1.0 1.0 0.0
   44    3011  SEC KG/SEC J/KG M SEC-1
   45    3012  0.0 3.7147E-05 2.90547E+05 0.0
   46    3013  1000000.0 3.7147E-05 2.90547E+05 0.0
   47    3060  HYD 1 0 0 003061 0.0 DEGREES 1.0 1.0 1.0 0.0
   48    3061  SEC KG/SEC J/KG M SEC-1
   49    3062  0.0 4.9667E-06 4.13804E+06 0.0
   50    3063  1000000.0 4.9667E-06 4.13804E+06 0.0
   51    **   NEW COUPLING SPECS
   52    009001  1 1 4 3.8 3.8 0.60 0.0
   53    009002  2 4 3 0.20 0.20 0.20 0.0
   54    009003  3 3 2 25.5 25.5 0.90 0.0
   55    009004  4 1 6 3.8 3.8 0.60 0.0
   56    009005  5 6 5 0.20 0.20 0.20 0.0
   57    009006  6 5 2 12.8 12.3 0.50 0.0
   58    .
```

ROOM6: 6 ROOM LUMPED PARAMETER MODEL

APPENDIX C
ANALYTICAL ASPECTS OF POSSIBLE EXTENTION TO CHEMICALLY REACTIVE FLOWS

C.1 Introduction

When one considers the progression of hydrogen related accidents in nuclear containments, five general phenomena are identified. The first is the hydrogen source behavior since its characteristics will define both the relevant time frames and bounding compositional end states. Once hydrogen appears the pre-chemical reaction flow transient will determine local fluid and thermodynamic conditions. The accurate prediction of this pre-chemical reaction phase is the focus of the main body of this work. Nevertheless, as hydrogen concentrations increase, ignition criteria and progression become important. Depending upon the local conditions and the strength of the ignition source, either a subsonic deflagration or a detonation will result. The purpose of this appendix is to briefly review the new physical and computational aspects of introducing chemical reactions to analytical models of hydrogen transport.

C.2 Important Phenomena

The three important physical processes are ignition phenomena, deflagration (subsonic combustion wave

propagation) and detonations. A brief discussion of each of these is presented.

C.2.1 Ignition Phenomena

At the relatively low pressures (a few atmospheres at most) and temperatures (less than 400°K) typical of the post-accident environment, a chemical reaction must be instigated by a significant ignition source. The containment however does contain equipment which can act as an inadvertent trigger (e.g., sparks from electric motors associated with pumps and valve operators). Due to the presence of these items, analysis studies which are not concerned with ignition, per se, may proceed under the assumption that an adequate ignition source is present. One possible calculational approach would be to artificially hold the temperature in a particular region at a high value typical of a postulated ignition source and use equations descriptive of the chemical reactions of interest.

For analyses in which ignition is of central importance such as studying deliberate igniter locations, greater modelling effort is required. Toong [C-1] points out that ignition criteria may be categorized by two independent quantities: critical power density and critical energy-deposition duration. A detailed chemical reaction analysis of the H_2-reaction mechanism is provided

by Lewis and von Elbe [C-2] who use fourteen separate reactions. As discussed earlier and theoretically explained by Lewis and von Elbe, the water vapor content of the mixture is of great importance since even a small amount significantly inhibits the reaction.

Good analytical treatment of ignition depends upon accurate quantitative rate descriptions. In this regard the works of Sawyer and Glassman [C-3] and Jensen and Jones [C-4] are noteworthy. The former provides the results of a detailed experimental investigation of the reaction of hydrogen with nitrogen dioxide, pure oxygen and mixtures of oxygen and nitric oxide. The latter work provides an extensive tabulation of rate constants especially applicable to flame propagation calculations. Local hydraulics including turbulence level must be included in such simulations. Ballal and Lefebvre [C-5] provide a discussion of the influence of flow parameters on both ignition and quenching phenomena. Nevertheless, due to the problem's complexity, detailed investigation of ignition phenomena must chiefly rely on experimental programs.

C.2.2 Deflagration Regime

The physical picture of this regime involves the burning of a combustible mixture such that subsonic propagation waves (flames) dominate the dynamics. The appropriate level of analytical sophistication depends upon the

spatial and temporal accuracy required. The range of desired detail may be qualitatively grouped into three categories. The crudest sort of analysis would involve a lumped parameter or large control volume approach with the addition of mass and energy source terms in the balance equations. The information provided from such an analysis should give a good qualitative picture of the change in the global thermodynamic state of a rather large region. For example, the overall pressure and temperature rise in a particular containment room may be estimated by this method. (The previously referenced HECTR code is an example of this approach.)

The lumped parameter approach gives little insight into spatial details. In regions with non-uniform geometries, flow patterns and ignition source locations, more accurate procedures must be invoked. Such approaches are based on the solution of continuum equations augmented by chemical kinetic models. It is clear that the greater information content of the analysis is achieved at the expense of greater phenomenological modelling and computational effort. This is especially true in turbulent flow fields in which the coupling of the fluid dynamics and chemistry is important.

The third category of deflagration analysis addresses the detailed structure of the flame and its propagation behavior. This level of detail is not as of much interest

in the nuclear safety area as the reacting flow analysis. Toong provides a theoretical discussion of premixed flame behavior which describes the physics in terms of an eigenproblem, with propagation speed being the eigenvalue. While laminar flames are well understood and predicted by current methods, turbulent flame propagation remains an area of extensive research.

In the laminar regime, analytical solutions based on a boundary layer approach are useful. Of particular note is the effect of chemical reaction on the temperature profile in the boundary layer. Reitz [C-6] has reported a numerical solution based on an explicit computational technique using a one-dimensional Lagrangian mesh. His equation set is based on Lewis number equal to one and neglecting radiation, body force and bulk-viscosity effects. The two-step (time level splitting) technique is shown to be more efficient yet as accurate as more complex methods.

The turbulent flame literature is vast and only a few particular works are referenced here. The work of Spalding [C-7] is significant because of its survey nature and the knowledge of the author in the area of computational turbulence. Kennedy and Plumb [C-8] have presented a turbulence boundary layer analysis to describe buoyancy controlled wall flames. They employ a rather sophisticated three parameter turbulence closure model: k (turbulent

kinetic energy), ε (dissipation of K), and G (root mean square fluctuation of mixture density). The authors include the third transport equation for G in order to account for the contribution of compositionally-induced buoyancy in the turbulent processes. This additional equation adds an additional algebraic closure relation of the form,

$$\langle u'T' \rangle = C(G\sigma k)^{\frac{1}{2}} , \qquad (C.1)$$

where C is an empirical constant ($\tilde{=}$ 0.5).

Pergament and Fishburne [C-9] performed an empirical and analytical investigation of hydrogen/air diffusion flames in a pilot ignition cylindrical burner geometry. Using a stream function-vorticity approach, they modelled turbulence effects using a zero equation or algebraic model. This model produces qualitatively correct results but mispredicts the flame's structural characteristics and they recommend a more complex model. They also report some improved values for rate expressions which are reproduced in Table C.1.

C.2.3 Detonations

Detonations of any type are to be strictly avoided in nuclear containments. If hydrogen concentration is kept below 20% by volume, detonations should not be a problem. If they should occur however, the central concern is the strength of the supersonic detonation wave and potential

Table C.1

Important Hydrogen-Air-Water Reaction Steps and Associated Rate Expressions (from [C-9])

Reaction	Rate Coefficients (molecule-cm-sec)
$H + OH + M \longleftrightarrow H_2O + M$	$1.0 \times 10^{-28} T^{-2}$
$O + H + M \longleftrightarrow OH + M$	3.0×10^{-32}
$O + O + M \longleftrightarrow O_2 + M$	$5.0 \times 10^{-30} T^{-1} \exp(-340/RT)$
$H + H + M \longleftrightarrow H_2 + M$	$5.0 \times 10^{-30} T^{-1}$
$OH + O \longleftrightarrow H + O_2$	4.0×10^{-11}
$OH + H \longleftrightarrow H_2 + O$	$1.4 \times 10^{-14} T \exp(-7000/RT)$
$OH + H_2 \longleftrightarrow H_2O + H$	$1.0 \times 10^{-17} T^2 \exp(-2900/RT)$
$OH + OH \longleftrightarrow H_2O + O$	$1.0 \times 10^{-11} \exp(-1100/RT)$

structural damage. Toong provides physical insight into the processes with the underlying findings that while propagation may seem steady macroscopically, the dynamics of the fluid-chemical coupling is through unsteady, three dimensional wave interactions. The three major concepts to be considered in detonation studies are structure, sustenance and stability. Many workers have reported calculational tools of varying complexity and two are mentioned as representative (Cohen et al. [C-10] and Oran et al. [C-11,C-12]). Both are based on a one dimensional compressible flow solution coupled to chemical kinetics models using a Lagrangian approach. Oran reports good spatial definition of the shock front due to the minimal numerical diffusion and no use of artificial viscosities in the hydrodynamic solution scheme. The intrinsic difficulty arising from simulating processes of significantly different time scales (chemistry and flow) is addressed through the use of fractional step techniques. In contrast to the relatively small numbers of non-equilibrium reaction steps (order of 10) used in deflagration analysis, Oran et al. used over 40 reaction steps to simulate H_2 detonation shocks in a shock tube geometry. The need for such extensive chemical kinetic modelling is due to the shorter time scales associated with sonic flow problems.

C.3 Flow Modelling

As discussed in C.2, if spatial resolution and quantitative accuracy are important, the analyst is forced to solve the continuum problem. In this subsection some approaches proposed by workers in the field will be highlighted. Following this, a proposed analytical modelling approach is presented. This regime can itself be qualitatively divided into two flow-types: flows which are essentially non-reactive but are strongly influenced in a passive way (e.g., thermally-induced buoyancy) due to proximity to a stationary flame, and truly reactive flows involving flame propagation.

C.3.1 Flows Near a Stationary Flame

The presence of a flame affects the local flow field in a number of ways. The principal effect is strong buoyancy especially if the flame is in lower regions. Second, the products of combustion are introduced into the field thus changing its physical characteristics such as thermal diffusivity and viscosity. A good overview of various aspects of fire in enclosed spaces is provided by Emmons [C-13] who divides the phenomena into four spatial zones: the fire, the plume, hot layer and junctions to other regions. The physically reasonable constituitive equations are somewh-t different in each region. Of course, one may formulate general equations which are

universally applicable but this is not always the most fruitful approach since limiting the range of applicability (if appropriate to the problem) may enhance accuracy through the use of refined modelling and simplify computation.

The regime far from the fire may be considered a weakly buoyant flow. The underlying physical assumptions of weakly buoyant flows is the local density variations are small compared to a reference state. Analysis of these flows may be performed using techniques such as that developed in this work. As local state changes become larger, the underlying perturbation assumption becomes invalid and a fully compressible problem must be solved.

In the modelling of strongly buoyant flows characterized by substantial density variations, the inclusion of a physically accurate turbulence model is of importance. One approach is to include a production term in the turbulent kinetic energy (k) equation due to buoyancy and also include a similar effect in the dissipation (ε) equation. While this is less complex than the addition of a third turbulence equation (as suggested by Kennedy and Plumb), it may be equally accurate since the use of empirically derived (and therefore applicability limited) closure constants is lessened. Morton [C-14] describes the region directly above the fire in terms of a strongly buoyant plume. In this region he states that two important

physical ramifications are the inclusion of radiation as a significant heat transfer mechanism and proper modelling of turbulent entrainment. Two major conclusions drawn by Morton are: entrainment into very hot plumes is depressed when compared to cooler plumes which implies a weakly buoyant model would underestimate flame height; and the strongly buoyant plume spreads less than a weakly buoyant one due to the large upward accelerations of the central core of the plume.

C.3.2 Reactive Flows

A number of computational tools for the solution of reactive flow problems have been proposed. Two representative approaches will be described in this subsection. The reader is referred to the original works for detailed information. Given the complex geometries typical of a nuclear containment, a Eulerian formulation is more appropriate when setting up problems. Both these tools are Eulerian in nature. Both methods also use a similar spatial discretization such that mass density, energy and other parameters are defined at the cell center while velocity and momentum flux are defined at the cell boundaries. This is consistent with this work's approach.

The first method was developed at the Los Alamos National Laboratory using a modified ICE method. Butler and O'Rourke [C-15] described the initial formulation which is used in a program called RICE. The chemical kinetic

modelling including turbulence is based on the work of Rivard et al. [C-16]. The RICE code was modified by Westbrook [C-17] who changed the computational scheme to be more physically consistent with reactive flow problems. The second model is based on an extension of the SIMPLE algorithm to reactive flow and is described by Hjertager [C-18]. This methodology is utilized in the FLAKS code.

The basic model specifications are summarized in Table C.2. Both methods solve the compressible equations. The momentum equations are nearly the same and it is noted that bulk viscosity effects are included in the molecular shear stress tensor. The RICE code conserves internal energy and includes viscous dissipation while the FLAKS program conserves enthalpy but neglects dissipation.

The treatment of turbulence is distinctly different. The RICE approach uses an eddy diffusivity turbulence model (0-equation) while the FLAKS code uses a k-ε model. This k-ε model does not include any turbulence production due to buoyancy and effective similarity moduli (Pr and Sc numbers) are employed. The FLAKS component equations are based on the assumption of a single step irreversible reaction of fuel (fu) to products of combustion. The two quantities actually calculated are fuel mass fraction and mixture fraction. The RICE chemical kinetics are more general in that the user describes the relevant processes in terms of a number of finite rate processes using a rate

Table C.2

Two Representative Models

Model	RICE Code	FLAKS Code
Mixture mass	$\frac{\partial \rho}{\partial t} + \underline{\nabla}\cdot\rho\underline{u} = \underline{\nabla}\cdot D^T\underline{\nabla}\rho$	$\frac{\partial \rho}{\partial t} + \underline{\nabla}\cdot\rho\underline{u} = 0$
Mixture momentum	$\frac{\partial \rho\underline{u}}{\partial t} + \underline{\nabla}\cdot\rho\underline{u}\,\underline{u} = -\underline{\nabla}P + \underline{\nabla}\cdot\underline{\sigma}^m + \underline{\nabla}\cdot\underline{\sigma}^T$ σ^m includes bulk viscosity	$\frac{\partial \rho\underline{u}}{\partial t} + \underline{\nabla}\cdot\rho\underline{u}\,\underline{u} = -\underline{\nabla}P + \underline{\nabla}\cdot(\underline{\sigma}^m+\underline{\sigma}^T)$ σ^m includes bulk viscosity
Mixt re energy	$\frac{\partial \rho e}{\partial t} + \underline{\nabla}\cdot\rho e\underline{u} = -P(\underline{\nabla}\cdot\underline{u}) + \underline{\sigma}^m : \underline{\nabla}\,\underline{u}$ $+ \underline{\nabla}\cdot(k^m\underline{\nabla}T + \Sigma\rho h_\ell D_\ell^m \underline{\nabla}\frac{\rho_\ell}{\rho}) + q_c$ $+ e\underline{\nabla}\cdot D^T\underline{\nabla}\rho$ ℓ = reaction component	$\frac{\partial \rho h}{\partial t} + \underline{\nabla}\cdot\rho\underline{u}h = \frac{DP}{Dt} + \underline{\nabla}\cdot\frac{\mu^m+\mu^T}{\sigma_h}\underline{\nabla}h + q_c$ σ_h = effective P_R number
Component transport	$\frac{\partial \rho_k}{\partial t} + \underline{\nabla}\cdot\rho_k\underline{u} = \underline{\nabla}\cdot\rho D_k^m\underline{\nabla}\frac{\rho_k}{\rho} + S$ $+ \underline{\nabla}\cdot D^T\underline{\nabla}\rho_k$	$\frac{\partial \rho m_{fu}}{\partial t} + \underline{\nabla}\cdot\rho\underline{u}m_{fu} = \underline{\nabla}\cdot\frac{\mu^m+\mu^T}{\sigma_{fu}}\underline{\nabla}m_{fu} + S_{fu}$ $\frac{\partial f\rho}{\partial t} + \underline{\nabla}\cdot\rho\underline{u}f = \underline{\nabla}\cdot\frac{\mu^m+\mu^T}{\sigma_f}\nabla f$ σ = effective SC number
Turbulence	constant eddy diffusivity	2 equation k-ε model --no buoyancy effects

Table C.2 (cont'd)

Model	RICE Code	FLAKS Code
Chemical kinetics	numerous finite rate processes	single irreversible reaction
	reaction rate $\sim KT^{a}e^{-A/RT}$ (RR) for each reaction	fuel → products
	S $\sim$ ΣRR X stoichiometry factors	$S_{fu} \sim$ turbulence level x concentration
	$q_c \sim$ ΣRR X heat release of reaction	$q_c \sim S_{fu}$ x enthalpy of reaction
	time step splitting used for rapid processes	
Numerical method	modified Implicit Continuous-fluid Eulerian (ICE)	Semi-Implicit Method for Pressure Linked Equations (SIMPLE)
	w/energy equation in iteration loop	w/energy equation not in iteration loop
	w/ρ estimate on basis of temperature & composition changes	w/ρ estimate on basis of temperature change only
	w/explicit solution of component equations	w/implicit (block tridiagonal) energy, turbulence & component solutions

law as shown. The sum of the products of reaction rate and heat release constitute the energy source term. The FLAKS chemistry is significantly simpler in that mass source strength is computed on the basis of empirical constants and turbulence level.

The numerical techniques have some notable departures. The basic SIMPLE routine is kept intact in FLAKS such that the energy equation (as well as component and turbulent equations) solution is done outside of the major iterative loop. The iterative loop involves converging to a consistent velocity, pressure and density field with the estimated pressure correction due to state changes accomplished through an explicitly derived sound speed. This is similar to the original RICE version described by Butler and O'Rourke. However, Westbrook states that not including the energy equation in the iterative loop can cause inaccuracies due to the intimate coupling of energy and momentum transfer in reactive flows. He also suggests that the updated pressure estimate should be based not only on density effects (explicit sound speed approach) but also compositional changes.

Finally, the RICE authors also report an artificial deflagration wave thickening technique which alleviates the need for very fine calculational meshes. The FLAKS authors have reported physically reasonable simulations of shock tube problems and also furnace type environments. The RICE

authors have published simulations of combustion chambers and general obstacle flow geometries. For problems in which experimental data was available, most discrepancies were less than 20%.

The proper treatment of turbulence is of central importance in these problems. Neither model seems superior to the other in the cases reported. The limitations of an eddy diffusivity approach are well known. However, the use of a more complex model does not guarantee a commensurate accuracy gain since the closure constants were probably derived from incompressible pipe or duct flow which is phenomenologically distinct from reactive flows. On the basis of physical intuition, however, if one should go to a higher order model as has been done in FLAKS, buoyancy effects should be included since they are a dominant physical mechanism in flows of such heightened thermicity.

C.4 Outline of a Composite Model

The information presented in the previous sections can be used to outline a composite analytical model of reacting flows in a post-accident nuclear containment environment. The limitations of the model are the following. First, the hydrogen source strength and location are known a priori. Second, the model will not be used in detailed studies of deliberate ignition device placement and operation. As stated in C.2.1, such efforts should rely heavily on

experimental studies. Third, flame structure and small scale combustion-turbulence interaction are not modelled in greater detail than is required to produce reasonable macroscopic predictions. Finally, detonation wave propagation is not of central concern.

The desirable characteristics of a model falling within this scope are grouped into four categories - basic conservation equations, turbulence, chemistry and numerical method. The most important requirement of the conservation equations is their compressible formulation. Though this is a more difficult approach than a Boussinesq-type analysis, it is crucial for the correct prediction of the local state and its effect on chemical kinetics. Second, turbulence effects (augmentation of transport processes) should be included in the mass, momentum and energy balances since the strong buoyancy induced by exothermic reactions as well as the complex problem geometry make turbulent flow unavoidable. The inclusion of viscous dissipation should be carefully considered. It may be valid to neglect this term as done by Hjertager but an order of magnitude analysis would be helpful in justifying this approach. Since the problem involves at least four components (hydrogen, air, steam and liquid), the individual transport equations of the RICE code are favored. This is especially true when the rate effect of steam concentration is recalled. As such, evaporation and

condensation need be included in the model.

The question of proper turbulence modelling can not be fully answered given the present state of the art. The complex flow field itself does suggest the use of a more sophisticated model and buoyancy effects should be included. The basic problem physics calls for the inclusion of buoyancy since the time averaged equations contain terms involving the correlation of density and velocity (and density and temperature) fluctuations. While these terms are not usually important in thermal hydraulic problems, they are significant in turbulent reactive flows. The chemistry modelling should also properly reflect the dependence of the reaction rate on local steam concentration. Therefore, modelling the chemical kinetics through the use of rate equations as in the RICE formulation is desirable. An analysis of the relevant reaction steps in light of the expected global conditions may lead to significant simplification in this area such as reducing the required number of kinetic equations.

Numerical method selection remains part art and part science. Two general points do emerge from the material presented. The first involves the computational coupling of the energy equation to the momentum and continuity equations. Westbrook argues that since this coupling is physically strong, the numerics (embodied in the simultaneous nested iterative solution of the three) should

reflect the same. This is seen to be a valid constraint. Second, both the RICE and FLAKS programs were formulated so that the calculational time step was not limited by the sound speed. This is highly desirable for economical computation of subsonic flows and therefore should be employed. Again, Westbrook points out the pressure updating algorithm to accomplish this goal should include not only sound speed corrections but also compositional effects. The uncoupled solution of the remaining equations seems reasonable given the smaller degree of physical coupling involved.

The modelling framework described above should have an applicability range from pre-chemical reaction flow through strong deflagration propagation. Given this broad scope, the model developer should fine tune the appraoch if one physical regime is dominant. For example, the energy/momentum-continuity coupling may be relaxed to the ICE or SIMPLE method in pre-chemical reactive flow. Chemical kinetics can also be simplified and viscous dissipation neglected in certain situations. Such refinement would improve the computational efficiency of the analysis without much loss of accuracy.

C.5 Conclusions

A logical extension of the research effort reported in the main body of this work is to include chemical

reactions in the analytical models. A review of the state of the art leads to the conclusion that a physically reasonable modelling approach is difficult but achievable and some consideration of desirable model characteristics are addressed. Chief among these are - the momentum/energy transfer coupling should be tight; turbulence modelling must reflect the physical picture of a reacting flow especially through buoyancy; steam transport must be addressed in both the conservation and chemical kinetic formulations; the global state constraints may simplify the chemistry modelling; numerical technique should consistently reflect the physics; and ancillary modelling of particular effects such as phase change needs to be included.

C.6 References

[C-1] T.Y. Toong, Course 2.281 Notes, MIT Department of Mechanical Engineering, 1982.

[C-2] B. Lewis and G. von Elbe, Combustion, Flames and Explosions of Gases, Second Edition, Academic Press, New York, 1961.

[C-3] R.F. Sawyer and I. Glassman, "The Reaction of Hydrogen with Nitrogen Dioxide, Oxygen and Mixtures of Oxygen and Nitrogen Oxide," Twelfth Symposium (International) on Combustion, Combustion Institute, Pittsburgh, 1969.

[C-4] D.E. Jensen and G.A. Jones, "Reaction Rate Coefficients for Flame Calculations," Comb and Flame, 32, 1978.

[C-5] D.R. Ballal and A.H. Lefebvre, "The Influence of Flow Parameters on Minimum Ignition Energy and Quenching Distance," Fifteenth Symposium (International) on Combustion, Combustion Institute, Pittsburgh, 1975.

[C-6] R.D. Reitz, "Computations of Laminar Flame Propagation Using An Explicit Numerical Technique," Eighteenth Symposium (International) On Combustion, Combustion Institute, Pittsburgh, 1981.

[C-7] D.B. Spalding, "Mixing and Chemical Reaction in Steady Confined Turbulent Flames," Thirteenth Symposium (International) on Combustion, Combustion Institute, Pittsburgh, 1971.

[C-8] L.A. Kennedy and O.A. Plumb, "Prediction of Buoyancy Controlled Turbulent Wall Diffusion Flames," Sixteenth Symposium (International) on Combustion, Combustion Institute, Pittsburgh, 1977.

[C-9] H.S. Pergament and E.S. Fishburne, "Influence of Buoyancy on Turbulent Hydrogen/Air Diffusion Flames," Combustion Science and Technology, 18, 1978.

[C-10] L.M. Cohen et al., "A Computational Technique for the Evaluation of Dynamic Effects of Exothermic Reactions," Comb and Flame, 24, 1975.

[C-11] E.S. Oran et al., "Application of Time Dependent Numerical Methods to the Description of Reaction Shocks," Seventeenth Symposium (International) on Combustion, Combustion Institute, Pittsburgh, 1979.

[C-12] E.S. Oran et al., "Numerical Simulation of Detonations in Hydrogen-Air and Methane-Air Mixtures," Eighteenth Symposium (International) on Combustion, Combustion Institute, Pittsburgh, 1981.

[C-13] H.W. Emmons, "Fire," Sixth International Meeting of Applied Mechanics Proceedings, 1977.

[C-14] B.R. Morton, "Modeling Fire Plumes," Tenth Symposium (International) on Combustion, Combustion Institute, Pittsburgh, 1965.

[C-15] T.D. Butler and P.J. O'Rourke, "A Numerical Method for Two Dimensional Reacting Flows," Sixteenth Symposium (International) on Combustion, Combustion Institute, Pittsburgh, 1977.

[C-16] W.C. Rivard et al., "The Transient Dynamics of Chemically Reactive Gaseous Mixtures With Turbulence," Lecture Notes in Physics, 35, 1975.

[C-17] C.K. Westbrook, "A Generalized ICE Method for Chemically Reactive Flows In Combustion Systems," J. Comp. Physics, 29, 1978.

[C-18] B.H. Hjertager, "Simulation of Transient Compressible Turbulent Reactive Flows," Comb. Science and Technology, 27, 1982.

APPENDIX D

IMPORTANT CONSIDERATIONS FOR ASSESSING AN IMPLICIT SLOW MIXING SOLUTION SCHEME

The main body of this work has demonstrated the capabilities of the explicit slow mixing solution methodology. The explicit method does incur two important limitations--Courant time-step stability limit and incomplete numerical diffusion correction. An implicit formulation has the potential to address both these constraints. The relaxation of the Courant limit would allow more economical simulation while Huh [D-1] suggests that an implicit scheme could completely compensate for numerical diffusion with unconditional stability. The potential negative aspects of the implicit approach are increased computational effort, unknown stability limits when linearizations are required, increased programming complexity and potential unphysical (but stable) solution modes. The purpose of this appendix is to summarize the important points in this regard, describe one possible momentum equation treatment and provide guidance for future more detailed studies.

An implicit solution scheme requires substantially more computational work per time step than an explicit scheme due to the simultaneous nature of the implicit equations. The momentum equation is particularly limiting in this regard due to its vectorial nature and the non-

linearity of the convective terms. A fully implicit numerical formulation of the momentum equation leads to a very large non-linear set of coupled algebraic equations. The solution of such a set by either direct or iterative means is impractical for typical problem discretizations. A more fruitful approach is linearization of the convective terms and application of a fractional step method such as the Alternating Direction Implicit (ADI) scheme. A typical convective linearization is

$$u\frac{\partial u}{\partial x} \simeq u^n\left(\frac{u_{i+1}^{n+1}-u_i^{n+1}}{\delta x}\right) . \qquad (D.1)$$

While this linearization renders the problem tractable, it introduces a degree of explicitness which in turn compromises the unconditional stability of the method. A few investigators including Huh have found stability limits in the range of Courant numbers of 2 or 3. The passive transport equations (energy, components, turbulence) do not require any linearization approximation. The central question to be considered is to quantify the amount of effort required to carry out a single implicit cycle compared to 2 or 3 explicit cycles. One must keep in mind that an implicit treatment of the slow mixing model involves 30 directional sweeps (i.e., matrix inversions) per cycle.

A multipass ADI treatment of the transport equations has been presented in Chapter 3. The following formulation

is a potential momentum equation application. There are two aspects to the treatment of this equation. One is the proper choice of finite differencing. The second is choosing the proper directional sweep logic for the three component vector equation. Using the linearization proposed above and treating the pressure gradient, buoyancy forces, drag forces and momentum transport due to viscosity gradients as explicit momentum sources, the three directional momentum component equations can be formulated as follows. (Note that the same nomenclature and conventions of the main text are applied here.)

$$\delta u = A_u \delta u_{i+\frac{3}{2}} + B_u \delta u_{j+1} + F_u \delta u_{k+1} + (C_u^r + C_u^z + C_u^\theta)\delta u + G_u \delta u_{k-1} + D_u \delta u_{j-1} + E_u \delta u_{i-\frac{1}{2}} + \Delta u^E \qquad (D.2)$$

where $\delta u = u^{n+1} - u^n$,

$$A_u = \frac{2\delta t}{\delta r_+}\left[\left|u_{i+\frac{1}{2}}+u\right| - u_{i+\frac{3}{2}} - 2u + \frac{\mu_{i+1} r_{i+1}^\beta}{(r+\frac{\delta r}{2})\delta r_+ \rho_r}\right]^n ,$$

$$B_u = \frac{\delta t}{2\delta z}\left[\left|SR2v_{i+1}+SR1v\right| - (SR2v_{i+1}) + \frac{2(\mu_{j+1}+\mu)}{\delta z_+ \rho_r}\right]^n ,$$

$$F_u = \frac{\delta t}{(r+\frac{\delta r}{2})^\beta \delta\theta}\left[\tfrac{1}{2}\left|SR2w_{i+1}+SR1w\right| - \tfrac{1}{2}(SR2w_{i+1}+SR1w) + \frac{2\mu}{(r+\frac{\delta r}{2})^\beta \delta\theta_+ \rho_r}\right]^n ,$$

$$C_u^r = \frac{2\delta t}{\delta r_+}\left[-\left|u_{i+\frac{3}{2}}+u\right| - \left|u+u_{i-\frac{1}{2}}\right| - \frac{1}{\rho_r(r+\frac{\delta r}{2})^\beta}\left(\frac{\mu_{i+1}r_{i+1}^\beta}{\delta r_{i+1}} + \frac{\mu r^\beta}{\delta r}\right)\right]^n,$$

$$C_u^z = \frac{\delta t}{2\delta z}\left[-\left|SR2v_{i+1}+SR1v\right| - \left|SR2v_{i+1j-\frac{1}{2}}+SR1v_{j-\frac{1}{2}}\right| - (SR2v_{i+1}+SR1v) + (SR2v_{i+1j-\frac{1}{2}}+SR1v_{j-\frac{1}{2}}) - \frac{2}{\rho_r}\left(\frac{\mu_{j+1}+\mu}{\delta z_+} + \frac{\mu+\mu_{j-1}}{\delta z_-}\right)\right]^n,$$

$$C_u^\theta = \frac{\delta t}{2(r+\frac{\delta r}{2})^\beta \delta\theta}\left[-\left|SR2w_{i+1}+SR1w\right| - \left|SR2w_{i+1k-\frac{1}{2}}+SR1w_{k-\frac{1}{2}}\right| - (SR2w_{i+1}+SR1w) + (SR2w_{i+1k-\frac{1}{2}} + SR1w_{k-\frac{1}{2}}) - \frac{4}{\rho_r(r+\frac{\delta r}{2})^\beta}\left(\frac{\mu}{\delta\theta_+} + \frac{\mu_{k-1}}{\delta\theta_-}\right)\right]^n,$$

$$G_u = \frac{\delta t}{2(r+\frac{\delta r}{2})^\beta \delta\theta}\left[\left|SR2w_{i+1k-\frac{1}{2}}+SR1w_{k-\frac{1}{2}}\right| + (SR2w_{i+1k-\frac{1}{2}} + SR1w_{k-\frac{1}{2}}) + \frac{4\mu_{k-1}}{(r+\frac{\delta r}{2})^\beta \rho_r \delta\theta_-}\right]^n,$$

$$D_u = \frac{\delta t}{2\delta z}\left[\left|SR2v_{i+1j-\frac{1}{2}}+SR1v_{j-\frac{1}{2}}\right| + (SR2v_{i+1j-\frac{1}{2}}+SR1v_{j-\frac{1}{2}}) + \frac{2(\mu+\mu_{j+1})}{\rho_r \delta z_-}\right]^n,$$

$$E_u = \frac{2\delta t}{\delta r_+}\left[\left|u_{i-\frac{1}{2}}+u\right| + u_{i-\frac{1}{2}} + 2u + \frac{\mu r^{\beta}}{(r+\frac{\delta r}{2})^{\beta}\delta r \rho_r}\right]^n,$$

$$\Delta u^E = \left[\frac{\delta t}{\rho_r}M_u + A_u u_{i+\frac{3}{2}} + B_u u_{j+1} + F_u u_{k+1} + (C_u^r+C_u^z+C_u^\theta)u\right.$$

$$\left. + G_u u_{k-1} + D_u u_{j-1} + E u_{i-\frac{1}{2}}\right]^n, \quad \text{and}$$

$$M_u = \left[\frac{\rho_r^{\beta}}{r^{\beta}}(w^2-u^2) - \frac{\partial P}{\partial r} + \rho g_r + f_{Dr} + \frac{\partial \mu}{\partial r}\frac{\partial u}{\partial r} + \frac{\partial \mu}{\partial z}\frac{\partial v}{\partial r}\right.$$

$$\left. - \frac{\beta\mu u}{r^{2\beta}} + \frac{1}{r^{\beta}}\frac{\partial \mu}{\partial \theta}\left(\frac{\partial w}{\partial r} - \frac{\beta w}{r^{\beta}}\right) - \frac{2\beta\mu}{r^{2\beta}}\frac{\partial w}{\delta \theta}\right]^n.$$

$$\delta v = A_v \delta v_{i+1} + B_v \delta v_{j+\frac{3}{2}} + E_v \delta v_{k+1} + (C_v^r+C_v^z+C_v^\theta)\delta v$$

$$+ G_v \delta v_{k-1} + D_v \delta v_{j-\frac{1}{2}} + E_v \delta v_{i-1} + \Delta v^E, \qquad (D.3)$$

where $\delta v = v^{n+1}-v^n$,

$$A_v = \frac{\delta t}{2\delta r}\left[\left|Sz2u_{j+1}+Szlu\right| - (Sz2u_{j+1}+Szlu)\right.$$

$$\left. + \frac{4(r+\frac{\delta r}{2})^{\beta}\mu_+}{r^{\beta}\rho_r \delta r_+}\right]^n,$$

$$B_v = \frac{\delta t}{\delta z_+}\left[\left|v_{j+\frac{3}{2}}+v\right| - v_{j+\frac{3}{2}} - 2v + \frac{4\mu_{j+1}}{\rho_r \delta z_{j+1}}\right]^n,$$

$$F_v = \frac{\delta t}{2r^{\beta}\delta\theta}\left[\left|Sz2w_{j+1}+Szlw\right| - (Sz2w_{j+1}+Szlw)\right.$$

$$\left. + \frac{4\mu}{r^{\beta}\rho_r \delta\theta_+}\right]^n,$$

$$C_v^r = \frac{\delta t}{2\delta r}\Big[-\left|Sz2u_{j+1}+Szlu\right| - \left|Sz2u_{i-\frac{1}{2}j+1}+Szlu_{i-\frac{1}{2}}\right| - (Sz2u_{j+1}+Szlu) + (Sz2u_{i-\frac{1}{2}j+1}+Szlu_{i-\frac{1}{2}}) - \frac{4(r+\frac{\delta r}{2})^{\beta}}{r^{\beta}\rho_r}\left(\frac{\mu^+}{\delta r_+} + \frac{\mu^-}{\delta r_-}\right)\Big]^n,$$

$$C_v^z = \frac{\delta t}{\delta z_+}\Big[-\left|v_{j+\frac{3}{2}}+v\right| - \left|v_{j-\frac{1}{2}}+v\right| - \frac{4}{\rho_r}\left(\frac{\mu_{j+1}}{\delta z_{j+1}} + \frac{\mu}{\delta z}\right)\Big]^n,$$

$$C_v^{\theta} = \frac{\delta t}{2r^{\beta}\delta\theta}\Big[-\left|Sz2w_{j+1}+Szlw\right| - \left|Sz2w_{j+1k-\frac{1}{2}}+Szlw_{k-\frac{1}{2}}\right| - (Sz2w_{j+1}+Szlw) + (Sz2w_{j+1k-\frac{1}{2}}+Szlw_{k-\frac{1}{2}}) - \frac{4}{\rho_r r^{\beta}}\left(\frac{\mu}{\delta\theta_+} + \frac{\mu_{k-1}}{\delta\theta_-}\right)\Big]^n,$$

$$G_v = \frac{\delta t}{2r^{\beta}\delta\theta}\Big[\left|Sz2w_{j+1k-\frac{1}{2}}+Szlw_{k-\frac{1}{2}}\right| + (Sz2w_{j+1k-\frac{1}{2}} + Szlw_{k-\frac{1}{2}}) + \frac{4\mu_{k-1}}{r^{\beta}\rho_r\delta\theta_-}\Big]^n,$$

$$D_v = \frac{\delta t}{\delta z_+}\Big[\left|v_{j-\frac{1}{2}}+v\right| + v_{j-\frac{1}{2}} + 2v + \frac{4\mu}{\rho_r\delta t}\Big]^n,$$

$$E_v = \frac{\delta t}{2\delta r}\Big[\left|Sz2u_{i-\frac{1}{2}j+1}+Szlu_{i-\frac{1}{2}}\right| + (Sz2u_{i-\frac{1}{2}j+1}+Szlu_{i-\frac{1}{2}}) + \frac{4(r+\frac{\delta r}{2})^{\beta}\mu^-}{r^{\beta}\rho_r\delta r_-}\Big]^n,$$

$$\Delta v^E = [\ \frac{\delta t}{\rho_r} M_v + A_v v_{i+1} + B_v v_{j+\frac{3}{2}} + F_v v_{k+1} + (C_v^r + C_v^z + C_v^\theta) v$$
$$+ G_v v_{k-1} + D_v v_{j-\frac{1}{2}} + E_v v_{k-1}\ ]^n , \quad \text{and}$$

$$M_v = [- \frac{\rho_r \beta u v}{r^\beta} - \frac{\partial P}{\partial z} + \rho g_z + f_{Dz} + \frac{\partial \mu}{\partial r}\frac{\partial u}{\partial z} + \frac{\partial \mu}{\partial z}\frac{\partial v}{\partial z}$$
$$+ \frac{1}{r^\beta}\frac{\partial \mu}{\partial \theta}\frac{\partial w}{\partial z}\ ]^n .$$

$$\delta w = A_w \delta w_{i+1} + B_w \delta w_{j+1} + F_w \delta w_{k+\frac{1}{2}} + (C_w^r + C_w^z + C_w^\theta)\delta w$$
$$+ G_w \delta w_{k-\frac{1}{2}} + D_w \delta w_{j-1} + \Delta w^E , \qquad (D.4)$$

$$\delta w = w^{n+1} - w^n ,$$

$$A_w = \frac{\delta t}{2\delta r}[\,|S\theta 2 u_{k+1} + S\theta 1 u| - (S\theta 2 u_{k+1} + S\theta 1 u) + \frac{4(r+\frac{\delta r}{2})^\beta \mu}{r^\beta \delta r_+ \rho_r}] ,$$

$$B_w = \frac{\delta t}{2\delta t}[\,|S\theta 2 v_{k+1} + S\theta 1 v| - (S\theta 2 v_{k+1} + S\theta 1 v) + \frac{4\mu}{\rho_r \delta z_+}] ,$$

$$F_w = \frac{\delta t}{r^\beta \delta\theta_+}[\,|w_{k+\frac{3}{2}} + w| - w_{k+\frac{3}{2}} - 2w + \frac{4\mu_{k+1}}{r^\beta \rho_r \delta\theta_{k+1}}\ ] ,$$

$$C_w^r = \frac{\delta t}{2\delta r}[-|S\theta 2 u_{k+1} + S\theta 1 u| - |S\theta 2 u_{i-\frac{1}{2}k+1} + S\theta 1 u_{i-\frac{1}{2}}|$$
$$- (S\theta 2 u_{k+1} + S\theta 1 u) + (S\theta 2 u_{i-\frac{1}{2}k+1} + S\theta 1 u_{i-\frac{1}{2}})$$
$$- \frac{4}{r^\beta \rho_r}(\frac{\mu(r+\frac{\delta r}{2})^\beta}{\delta r_+} + \frac{\mu_{i-1}(r-\frac{\delta r}{2})^\beta}{\delta r_-})] ,$$

$$C_w^z = \frac{\delta t}{2\delta z}\left[-\left|S\theta 2v_{k+1}+S\theta 1v\right| - \left|S\theta 2v_{j-\frac{1}{2}k+1}+S\theta 1v_{j-\frac{1}{2}}\right| - (S\theta 2v_{k+1} + S\theta 1v) + (S\theta 2v_{j-\frac{1}{2}k+1}+S\theta 1v_{j-\frac{1}{2}}) - \frac{4}{\rho_r}\left(\frac{\mu}{\delta z_+} + \frac{\mu_{j-1}}{\delta z_-}\right)\right],$$

$$C_w^\theta = \frac{\delta t}{r^\beta \delta\theta_+}\left[-\left|w_{k+\frac{3}{2}}+w\right| - \left|w_{k-\frac{1}{2}}+w\right| - \frac{4}{\rho_r r^\beta}\left(\frac{\mu_{k+1}}{\delta\theta_{k+1}} + \frac{\mu}{\delta\theta}\right)\right],$$

$$G_w = \frac{\delta t}{r^\beta \delta\theta_+}\left[\left|w_{k-\frac{1}{2}}+w\right| + w_{k-\frac{1}{2}} + 2w + \frac{4\mu}{r^\beta \rho_r \delta\theta}\right],$$

$$D_w = \frac{\delta t}{2\delta z}\left[\left|S\theta 2v_{j-\frac{1}{2}k+1}+S\theta 2v_{j-\frac{1}{2}}\right| + (S\theta 2v_{j-\frac{1}{2}k+1}+S\theta 1v_{j-\frac{1}{2}}) + \frac{4\mu_{j-1}}{\delta z_- \rho_r}\right],$$

$$E_w = \frac{\delta t}{2\delta r}\left[\left|S\theta 2u_{i-\frac{1}{2}k+1}+ S\theta 1u_{i-\frac{1}{2}}\right| + (S\theta 2u_{i-\frac{1}{2}k+1}+S\theta 1u_{i-\frac{1}{2}}) + \frac{4\mu_{i-1}(r-\frac{\delta r}{2})^\beta}{r^\beta \delta r_+ \rho_r}\right]$$

$$\Delta w^E = \left[\frac{\delta t}{\rho_r} M_w + A_w w_{i+1} + B_w w_{j+1} + F_w w_{k+\frac{3}{2}} + (C_w^r + C_w^z + C_w^\theta) w + G_w w_{k-\frac{1}{2}} + D_w w_{j-1} + E_w w_{i-1}\right], \text{ and}$$

$$M_w = \left[-\frac{2\beta\rho_r wu}{r^\beta} - \frac{1}{r^\beta}\frac{\partial P}{\delta\theta} + f_{D\theta} + \frac{\beta\mu}{r^{2\beta}}\left(2\frac{\partial u}{\partial\theta} - w\right) + \frac{1}{r^\beta}\frac{\partial\mu}{\partial r}\left(\frac{\partial u}{\partial\theta} - \beta w\right) + \frac{1}{r^{2\beta}}\frac{\partial\mu}{\partial\theta}\left(\frac{\partial w}{\partial\theta} + 2\beta u\right) + \frac{1}{r^\beta}\frac{\partial\mu}{\partial z}\frac{\partial v}{\delta\theta}\right]^n.$$

The equations presented above define the basic matrix problem. However, the proper directional sweeping logic must be determined. A total of nine directional passes must be performed and a proper sequencing chosen. It is expected that the choice of sweep logic will affect not only accuracy but also stability.

Implementation of this solution logic into the LIMIT code is not a trivial exercise. An initial assessment of this aspect leads to the suggestion that two rather large subroutines are required. One would control the sweeping logic and perform the matrix inversion while the other calculates the direction and component dependent matrix coefficients and source terms. A final suggestion in this area is to allow the ADI solution to be optional.

The last major area requiring study is the overall question of unphysical solution behavior. The method proposed hasn't been used in any major applications and the potential for unphysical results has been identified by some workers [D-1]. The unknown subtleties must be better understood before this method can be applied to complex problems such as hydrogen mixing analysis.

[D-1] K.Y. Huh, Treatment of Physical and Numerical Diffusion in Fluid Dynamic Simulations, Ph.D. Thesis, MIT Department of Nuclear Engineering, August 1983.

Appendix E: Additional Remarks On the Solution of the Slow Mixing Model Energy Equation

Section 3.3.4.3 addresses the solution of the passive entity transport equations in the slow mixing continuum model. The general methodology described in that section can be specialized to the energy equation (i.e., Eq. 3.43) using the formulation presented here. In abbreviated form, the energy conservation equation is:

$$\frac{\partial \rho e}{\partial t} + C = D \,, \tag{E.1}$$

where C = convective terms and

D = diffusive (conduction) terms.

Expanding the temporal derivative and rearranging Eq. E.1 yields

$$\rho \frac{\partial e}{\partial t} = -C + D - e \frac{\partial \rho}{\partial t} \,. \tag{E.2}$$

For the other scalar transport equations which were formulated in an incompressible manner, the last RHS term of Eq. E.2 is approximated using the derivation presented in the discussion preceding Eq. 3.145, i.e.,

$$\frac{\partial \rho}{\partial t} \simeq \rho \, \underline{\nabla} \cdot \underline{u} \,. \tag{E.3}$$

However since the energy equation is cast in a conservative form, a more correct approach is to utilize the compressible continuity equation for the value of the temporal density derivation. Thus,

$$\frac{\partial \rho}{\partial t} \simeq -\underline{\nabla} \cdot \rho \underline{u} \ . \qquad \text{(E.4)}$$

Using the established nomenclature, the finite difference approximation for this term is

$$e\underline{\nabla} \cdot \rho \underline{u} \simeq e\Big[\frac{r^{\beta}_{i+\frac{1}{2}}(\rho\alpha_{+}+\rho_{i+1}\beta_{+}) - r^{\beta}_{i-\frac{1}{2}}(\rho_{i-1}a_{-}+\rho\beta_{-})}{r^{\beta}\delta r}$$

$$+ \frac{(\rho\gamma_{+}+\rho_{j+1}\delta_{+}) - (\rho_{j-1}\gamma_{-}+\rho\delta_{-})}{\delta z}$$

$$+ \frac{\lambda(\rho\varepsilon_{+}+\rho_{k+1}\sigma_{+}-\rho_{k-1}\varepsilon_{-}-\rho\sigma_{-})}{r^{\beta}\delta\theta}\Big] \ . \qquad \text{(E.5)}$$